University of Strathclyde
Department of Naval Architecture, Ocean & Marine Engineering

Three Dimensional Time Domain Simulation of Ship Motions and Loads in Large Amplitude Head Waves

by

Olgun Guven Hizir

A thesis presented in fulfilment of the requirements for the degree of
Doctor of Philosophy
Glasgow, UK
2015

This thesis is the result of the author's original research. It has been composed by the author and has not been previously submitted for examination which has led to the award of a degree.

Signed: Olgun Guven Hizir *Date: 10 April 2015*

DEDICATION

I want to dedicate this thesis to my father Burhan Hizir, my mother Sevda Hizir and my brother Toygun Hizir for their unconditional support and encouragement throughout my life.

Abstract

This PhD thesis presents the development of a practical computational tool named Large Amplitude RESponse (LARes), based on 3D quasi-non-linear time-domain technique, to predict ship motions and loads in large amplitude waves which can be accessible to ship designers.

Firstly, a linear 3-D Green source panel code (LARes L1) was developed to perform linear time-domain analysis ship motion and internal load simulations based on the frequency-domain hydrodynamic coefficients which were calculated in the linear PRECAL software. Linear simulations are validated with the linear time-domain PRETTI software results using rectangular barge geometry. The motions, internal loads, global and sectional hydrodynamic forces were agreed well with the linear PRETTI model results in zero and forward speed simulations.

Then, non-linear time-domain panel code (LARes L2) was developed in order to predict ship motions and loads in large amplitude waves using the Froude-Krylov nonlinearity level. At each time step, the exact wetted area of the ship surface under the wave profile was calculated and fed in the time-domain motion and load equations while the diffraction and radiation forces were kept as linear. The present program achieved good agreement with the non-linear PRETTI model results both for the barge and S175 container geometries at zero and forward speed conditions in small amplitude waves. Moreover, the S175 container ship results are compared with the available experimental data and agreed well with the experimental results in forward speed case. It has been observed that PRETTI code is over-estimating motion and load responses especially around the resonant frequency due to the surge motion influence in the memory forces evaluations. In the Froude-Krylov nonlinear level predictions, it has been observed that PRETTI diverges from the experimental results when the wave steepness is higher than 0.08 due to the linear radiation and diffraction forces.

Based on the same framework, a more advanced nonlinear time-domain panel code (LARes L3) was developed in order to investigate the effects of quasi-non-linear diffraction and radiation forces in large amplitude ship simulations. A new mesh generator was introduced in order to cut and correct the original panels under the still water level in the updated position of the ship after displacements and rotations. The quasi-non-linear diffraction and radiation forces were calculated at the pre-defined position cases and stored in a database. In order to lower the computational cost multi-dimensional integration and interpolation codes were generated. The S-175 containership was tested in 120 different position cases and resulting hydrodynamic coefficients and forces were stored in the database. The results of the LARes L3 model were compared with the available experimental data using the S-175 containership in forward speed. The computed motion responses showed a good agreement with the experimental data. Moreover, three of the developed models are compared with the experiments and their performances were investigated with respect to the increasing wave slope. In addition to that, the effect of the wave length and ship speed in large amplitude waves are investigated in detail. Non-linear behaviors of the codes were compared with the experimental results which showed a good agreement.

Finally, the Vertical Shear Force (VSF) and Vertical Bending Moment (VBM) responses were investigated in large amplitude motions. It was observed that, in the validation section, numerical model peak amplitudes showed well agreement with the experimental results, but they were observed to be shifted to the higher frequencies compared to the experimental results. The reason for that was attributed to the longitudinal mass distribution on the ship in the experimental setup which had not been provided in detail in the published experimental results.

Acknowledgements

First of all I would like to express my gratitude to my supervisor Prof. Atilla Incecik for his continuous support and encouragement. His critical decisions and positive attitudes during the research was the key factor in my success.

I would like to thank Prof. Osman Turan for his advices and efforts in my research. I will never forget his advices during the development and writing phase of the thesis which made the work more advance and meaningful.

I am very grateful to Prof. Mehmet Atlar for his recommendations and continuous moral support during my study. I had the opportunity to better understand the physical meaning of seakeeping with his experience in experiments.

I would like to specially to thank Prof. Tomoki Ikoma from Nihon University for his kind support in the development of my knowledge in my research.

I also would like to thank Dr. Yongwon Lee and Dr. Spyros Hirdaris from Lloyd’s Register for their continuous advices and encouragements during my research. I specially thank to Lloyd’s Register for the financial support they provided.

I am deeply indebted to Prof. Ismail Helvacioglu and Dr. Sebnem Helvacioglu for giving me kind advices, continuous technical and moral support.

I would like to express my gratitude to Dr. Paula Kellett for her kind friendship and her patience while proof reading my thesis. The design and English quality of the thesis is due to her hard work and attention.

I also would like to thank Dr. Johan Tuitman from TNO for his continuous technical support during my research.

I am very grateful to Prof. MD. Ozgur Yorbik, Prof. MD. Mehmet Arslan and Prof. MD. Onur Genc for their unconditional support and recommendations in my life.

I would like to thank people, who have continuously supported my study with their advices, Dr. Giuseppe Mortola, Dr. Zhi-ming Yuan, Dr. Serkan Turkmen, Dr. Emek Kurt.

I am grateful to Mrs. Thelma Will for her positive attitudes and her support in the administrative tasks. I'm also very thankful to all the people in the research centre of NAOME that helped and support me.

Table of Contents

Abstract ii

Acknowledgements iv

Table of Contents vi

List of Figures ix

List of Tables xiv

Nomenclature xv

1 Introduction 1

  1.1 Background 1

  1.2 Aims and Objectives 3

  1.3 Contribution to the field of study 4

  1.4 Contents of the Thesis 5

2 Literature Review 8

  2.1 Introduction 8

  2.2 Linear Wave-Rigid Body Interaction 9

    2.2.1 Steady Flow and Unsteady Flow Interaction 15

  2.3 Nonlinear Wave-Rigid Body Interaction 19

    2.3.1 Froude-Krylov Nonlinear Methods (Level 2) 23

    2.3.2 Body Nonlinear Methods (Level 3) 32

    2.3.3 Body-Exact (Weak-Scatter) Methods (Level 4) 36

  2.4 Rigid and Elastic Ship Experimental Studies 42

3 Theoretical Background for Motions and Loads 46

  3.1 Coordinate Systems 46

  3.2 General Description of the Frequency-Domain Boundary Value Problem. 49

    3.2.1 Internal Loads in the Frequency Domain Approach 60

  3.3 General Description of the Time-Domain Method 62

    3.3.1 Froude-Krylov and Restoring Forces 63

    3.3.2 Radiation Forces 65

    3.3.3 Diffraction Forces 69

    3.3.4 Internal Loads in the Time-Domain Approach 70

  3.4 Summary 72

4 Numerical Methods 73

4.1 Development of the Models 73

4.2 Data Input Tool 73

4.3 Dynamic Meshing Tool 74

4.4 Time Domain Nonlinear Equation Solver 81

4.5 Post Processor 82

4.6 Froude-Krylov Nonlinear (Level 2) Model 83

4.7 Body Nonlinear (Level 3) Model 85

4.7.1 Mesh Generation 87

4.7.2 Hydrodynamic Matrix Storage 91

4.7.3 Evaluation of Memory Functions 91

4.7.4 Evaluation of Interpolation 92

4.8 Summary 94

5 Validations 95

5.1 Introduction 95

5.2 Comparison of Time-domain Seakeeping Tools 95

5.3 Main Particulars of S-175 Container Ship 99

5.4 Validation of Motion Responses 100

5.4.1 Linear Motion Simulation Validations 100

5.4.2 Nonlinear Motion Simulation Validations 110

5.5 Validation of Load Responses 126

5.5.1 Linear Load Simulation Validations 127

5.5.2 Nonlinear Load Simulation Validations 132

5.6 Summary 142

6 Application of the Methodology in Motion 145

6.1 Introduction 145

6.2 Effect of the nonlinearity level in motion responses 145

6.3 Influence of the wave length on motion responses 161

6.4 Influence of speed on motion responses 167

6.5 Nonlinear behavior in motion responses 172

6.6 Nonlinearity in radiation and diffraction forces 175

6.7 Summary 184

7 Application of the Methodology to Predict Internal Load Responses 186
  7.1 Introduction 186
  7.2 Effect of the Nonlinearity Level on the Internal Load Responses 187
  7.3 Nonlinear Behavior in Vertical Load Responses 191
  7.4 Summary 200
8 Conclusions and Recommendations 202
  8.1 Introduction 202
  8.2 Novelty of the Research 202
  8.3 Contributions to the Research 203
  8.4 Achievements 205
  8.5 Conclusions 209
  8.6 Recommendations for the future works 211
References 213

List of Figures

Figure 3.1: Coordinate systems 47

Figure 3.2: Uniform base flow (left) and D-B flow (right) (Bunnik, 1999) 51

Figure 3.3: Uniform base flow (top) and D-B flow (bottom) comparison for heave and pitch responses at Fn=0.25 53

Figure 3.4: Comparison of the heave response for the Exact Forward Speed and Approximate Forward Speed formulations 58

Figure 3.5: Comparison of heave diagonal damping coefficients for the Exact Forward Speed and Approximate Forward Speed formulations 59

Figure 3.6: Sign convention for the hogging and sagging positions 60

Figure 3.7: Dynamic wave pressure distribution 64

Figure 3.8: Memory functions for S-175 ship at Fn=0.275 67

Figure 3.9: Infinite frequency added mass curve for S-175 ship at Fn=0.275 68

Figure 4.1 : Dynamic meshing approach 75

Figure 4.2: LARes discretization of the S-175 ship geometry 77

Figure 4.3: LARes S-175 ship geometry under waves in T_θ=0 degrees, H_w=5m 78

Figure 4.4: LARes S-175 ship geometry under waves in T_θ=4 degrees (left) T_θ=-4 degrees (right), H_w=5m 78

Figure 4.5: The formation of an element (Hess and Smith, 1962) 80

Figure 4.6: LARes L2 flowchart 84

Figure 4.7: LARes L3 flowchart 86

Figure 4.8: Rotated and meshed geometry of S-175 ship at -4 degrees of pitch rotation 88

Figure 4.9: Cutted panel correction close to the water surface 89

Figure 4.10: Diagonal damping coefficients for S-175 with and without the LID panels at Fn=0.25 90

Figure 4.11: LID panels comparison for S-175 ship for various pitch displacements. 90

Figure 4.12: Multi-dimensional memory functions integration 92

Figure 4.13: Multi-dimensional interpolation of memory functions 93

Figure 5.1: S-175 lines plan 99

Figure 5.2: S-175 Container ship mass distribution 99
Figure 5.3: Heave and pitch RAO of the barge at Fn=0.0 in head seas 101
Figure 5.4: Linear motion response of barge at ω=0.3 rad/s at H_w=1m Fn=0.0 102
Figure 5.5: Linear F-K forces at ω=0.3 rad/s and Hw=1m at Fn=0.0 103
Figure 5.6: Linear restoring of barge forces at ω=0.3 rad/s and H_w=1m at Fn=0.0. 103
Figure 5.7: Linear radiation forces of barge at ω=0.3 rad/s and H_w=1m at Fn=0.0. 104
Figure 5.8: Linear diffraction forces of barge at ω=0.3 rad/s, H_w=1m and Fn=0.0. 104
Figure 5.9: Linear heave and pitch RAO of the barge at Fn=0.164 in head seas 106
Figure 5.10: Linear motion response of barge at ω=0.66 rad/s, H_w=1m, Fn=0.164 107
Figure 5.11: Linear F-K forces of barge at ω=0.66 rad/s, Hw=1m, Fn=0.164 108
Figure 5.12: Linear restoring forces of barge at ω=0.66 rad/s, H_w=1m, Fn=0.164 . 108
Figure 5.13: Linear radiation forces of barge at ω=0.66 rad/s, H_w=1m, Fn=0.164 . 109
Figure 5.14: Linear diffraction forces of barge at ω=0.66 rad/s, H_w=1m, Fn=0.164 109
Figure 5.15: Nonlinear heave and pitch response functions of barge at H_w=1m, Fn=0.0 112
Figure 5.16: Nonlinear hydrodynamic force components of barge at ω=0.66 rad/s, H_w=1m, Fn=0.0 113
Figure 5.17: Nonlinear heave and pitch response functions of barge at H_w=1m, Fn=0.164 115
Figure 5.18: Nonlinear motion response of barge at ω=0.66 rad/s, H_w=1m, Fn=0.164 116
Figure 5.19: Nonlinear hydrodynamic force components of barge at ω=0.66 rad/s, H_w=1m, Fn=0.164 118
Figure 5.20: Nonlinear heave and pitch response comparison of S-175, Fn=0.0 120
Figure 5.21: LARes level 3 and level 2 hydrodynamic force components of S-175 at λ/L_{pp}=1.2, H_w/λ=1/120, Fn=0.0 122
Figure 5.22: Nonlinear heave and pitch response functions of S-175 at Fn=0.25, H_w/λ=1/120 123
Figure 5.23: LARes level 3 and level 2 hydrodynamic force components of S-175 at λ/L_{pp}=1.2, H_w/λ=1/120, Fn=0.25 125

Figure 5.24: Linear VSF (st 15) and VBM (st 10) responses of barge (Fn=0.0, β=180) 127

Figure 5.25: Linear VSF (st 15) and VBM (st 10) time history of barge at ω=0.66 rad/s at H_w=1m (Fn=0.0, β=180) 129

Figure 5.26: Linear sectional hydrodynamic force components comparison of barge forward of the midship section at ω=0.66 rad/s, H_w=1m (Fn=0.0, β=180) 130

Figure 5.27: Sectional hydrodynamic and inertial force components comparisons of barge forward of the midship section at ω=0.66 rad/s, H_w=1m (Fn=0.0, β=180).... 131

Figure 5.28: Nonlinear VSF (st 15) and VBM (st10) comparison of barge (Fn=0.0, β=180) 133

Figure 5.29: Nonlinear VSF (st 15) and VBM (st 10) time history of barge at ω=0.66 rad/s, H_w=1m (Fn=0.0, β=180) 134

Figure 5.30: Nonlinear sectional hydrodynamic force components comparison of barge forward of midship section at ω=0.66 rad/s, H_w=1m (Fn=0.0, β=180) 135

Figure 5.31: Sectional hydrodynamic and inertial force components comparisons of barge forward of midship section at ω=0.66 rad/s, H_w=1m (Fn=0.0, β=180) 136

Figure 5.32: Nonlinear VSF (st 15) and VBM (st 10) comparison of S-175 (Fn=0.0, β=180) 138

Figure 5.33: Nonlinear VSF (st15) and VBM (st 10) comparison of S-175 (Fn=0.25, β=180) 139

Figure 5.34: Nonlinear sectional hydrodynamic force components comparison of S-175 forward of the midship section at ω=0.5934 rad/s, H_w=1m (Fn=0.25, β=180) 141

Figure 5.35: Nonlinear sectional hydrodynamic force components comparison of S-175 forward of the midship section at ω=0.5934 rad/s, H_w=1m (Fn=0.25, β=180) 142

Figure 6.1: Variation of non-dimensional heave and pitch response with the wave steepness (Fn=0.20, λ/L=1.0) 149

Figure 6.2: Variation of non-dimensional heave and pitch response with the wave steepness (Fn=0.20, λ/L=1.2) 150

Figure 6.3: Variation of non-dimensional heave and pitch response with the wave steepness (Fn=0.20, λ/L=1.4) 151

Figure 6.4: Variation of non-dimensional heave and pitch response with the wave steepness (Fn=0.25, λ/L=1.0) 154

Figure 6.5: Variation of non-dimensional heave and pitch response with the wave steepness (Fn=0.25, λ/L=1.2) 155
Figure 6.6: Variation of non-dimensional heave and pitch response with the wave steepness (Fn=0.25, λ/L=1.4) 156
Figure 6.7: Variation of non-dimensional heave and pitch response functions with the wave steepness (Fn=0.275, λ/L=1.0) 158
Figure 6.8: Variation of non-dimensional heave and pitch response with the wave steepness (Fn=0.275, λ/L=1.2) 159
Figure 6.9: Variation of non-dimensional heave and pitch response with the wave steepness (Fn=0.275, λ/L=1.4) 160
Figure 6.10: Influence of wave length and wave steepness on the non-dimensional heave and pitch responses (Fn=0.20, λ/L=1.0, 1.2, 1.4) 163
Figure 6.11: Influence of wave length and wave steepness on the non-dimensional heave and pitch responses (Fn=0.25, λ/L=1.0, 1.2, 1.4) 164
Figure 6.12: Influence of wave length and wave steepness on the non-dimensional heave and pitch responses (Fn=0.275, λ/L=1.0, 1.2, 1.4) 165
Figure 6.13: Influence of speed and wave steepness on the non-dimensional heave and pitch responses (Fn=0.20, 0.25, 0.275, λ/L=1.0) 169
Figure 6.14: Influence of speed and wave steepness on the non-dimensional heave and pitch responses (Fn=0.20, 0.25, 0.275, λ/L=1.2) 170
Figure 6.15: Influence of speed and wave steepness on the non-dimensional heave and pitch responses (Fn=0.20, 0.25, 0.275, λ/L=1.4) 171
Figure 6.16: Positive, negative and mean values of non-dimensional heave and pitch responses (Fn=0.25, λ/L=1.2, 1.4) 174
Figure 6.17: Time history of comparison of radiation and diffraction forces and moments (Fn=0.25, λ/L=1.2, H_w=6m) 176
Figure 6.18: Influence of wave length and wave amplitude on the positive and negative peaks of the heave and pitch diffraction forces and moments (Fn=0.20, λ/L=1.0,1.2,1.4) 178
Figure 6.19: Influence of wave length and wave amplitude on the positive and negative peaks of the heave and pitch diffraction forces and moments (Fn=0.25, λ/L=1.0,1.2,1.4) 179

Figure 6.20: Influence of wave length and wave amplitude on the positive and negative peaks of the heave and pitch radiation forces and moments (Fn=0.20, λ/L=1.0,1.2,1.4) 181

Figure 6.21: Influence of wave length and wave amplitude on the positive and negative peaks of the heave and pitch radiation forces and moments (Fn=0.25, λ/L=1.0,1.2,1.4) 182

Figure 7.1: Variation of the amplitudes of the VBM amidships with the wave steepness (Fn=0.25, β=180) 189

Figure 7.2: Variation of the amplitudes of the VBM at station 15 with the wave steepness (Fn=0.25, β=180) 190

Figure 7.3: Positive, negative peaks and mean values of the VBM amidships as a function of wave steepness (Fn=0.25, λ/L_{pp}=1.0,1.2,1.4, β=180) 194

Figure 7.4: Positive, negative peaks and mean values of the VBM at station 15 as a function of wave steepness (Fn=0.25, λ/L_{pp}=1.0,1.2,1.4, β=180) 196

Figure 7.5: Positive, negative peaks and mean values of the VSF at station 15 as a function of wave steepness (Fn=0.25, λ/L_{pp}=1.0,1.2,1.4, β=180) 198

List of Tables

Table 2.1: Comparison of time-domain approaches (ITTC, 2011) ... 21
Table 2.2: Classification of time-domain seakeeping methods in the literature I ... 24
Table 2.3: Classification of time-domain seakeeping methods in the literature II ... 25
Table 4.1: Advantages & disadvantages of meshing methods ... 76
Table 5.1: Comparison of time-domain seakeeping tools ... 96
Table 5.2: S-175 main particulars ... 99

Nomenclature

Roman Symbols

L_{pp}	Length between perpendiculars
B	Breadth of the ship
T	Draft of the ship
$\overrightarrow{r_e}$	Displacement vector in hydrodynamic axis frame
$\overrightarrow{r_b}$	Displacement vector in body frame axis frame
T	Rotation matrix
U	Ship speed (m/s)
k	Wave number
Fn	Froude number
t	time
g	Acceleration of gravity
$\overrightarrow{n_J}$	Outward unit normal vector
m_j	Gradients of steady normal velocities
P	Pressure
C_o	Intersection between the body surface and the mean free surface
S	Mean wetted surface
S^*	Sectional mean wetted surface
g	Acceleration of gravity
F_j	Total oscillatory hydrodynamic force in the j^{th} direction
$F_{j,I}$	Incident wave force in the j^{th} direction
$F_{j,D}$	Diffraction force in the j^{th} direction
$F_{j,R}$	Radiation force in the j^{th} direction
M_{jk}	Mass matrix
A_{jk}	Global added-mass matrix
B_{jk}	Global damping matrix
C_{jk}	Global restoring matrix
K_{jk}	Memory functions matrix

V_3	Vertical Shear Force (VSF)
M_5	Vertical Bending Moment (VBM)
V_3	Vertical Shear Force (VSF)
R_j	Total radiation force
D_j	Total diffraction force
FK_j	Total Froude-Krylov force
H_j	Total restoring force
D_j	Total diffraction force
I_j^*	Sectional ship inertial forces and moments
$m(x)$	Sectional mass per unit length
x^*	Cut section position
$F_{j,D}^*$	Sectional diffraction force in the j^{th} direction
$F_{j,R}^*$	Sectional radiation force in the j^{th} direction
$F_{j,Res}^*$	Sectional restoring force in the j^{th} direction
$F_{j,I}^*$	Sectional incident wave force in the j^{th} direction
$F_{j,R}^*$	Sectional radiation force in the j^{th} direction
A_{jk}^{*h}	Sectional added-mass matrix
B_{jk}^{*h}	Sectional damping matrix
K_{jk}^{*h}	Sectional retardation functions matrix
C_{Res}^{*h}	Sectional restoring matrix
LCG	Longitudinal center of gravity
VCG	Vertical center of gravity

Latin Symbols

ζ	Incident wave elevation`
ζ_a	Incident wave amplitude
ω_e	Encounter frequency
ω_0	Incident wave frequency
β	Incident wave angle
ρ	Water density
ξ_j	Motion amplitude in jth direction
Φ_T	Total velocity potential
$\bar{\phi}_s$	Steady perturbation potential
ϕ_u	Unsteady potential
ϕ_I	Incident wave potential
ϕ_D	Diffraction potential
ϕ_j	Radiation potential
λ	Wave length
θ	Pitch rotation angle
$\ddot{\xi}_j$	Global acceleration

Chapter 1

Introduction

1.1 Background

Ship designers, builders and operators lack adequate tools for the prediction of ship responses in severe seas. This has resulted in a very conservative approach to ship design and the use of large “safety factors”. Ship structural frames and hence the ship weight are overestimated due to large safety factors and that resulted with less cargo capacity in order to satisfy the structural integrity of ships. Ship motions and loads in large waves are usually predicted using calculation tools based on a two or three dimensional small amplitude linear theory in frequency domain. Frequency domain calculations, has a shortcoming as the restriction of ship motions to small amplitudes compared to the ship dimensions. In order to find the motion responses and loads in severe sea conditions linear results needed to be extrapolated to required sea states. However, the extrapolation procedure violates the linear frequency domain approach and assumes that the motion is still sinusoidal disregarding the highly asymmetric vertical motions and loads experienced by the ship when subjected to large amplitude waves. It is a well-known fact that linear frequency domain calculation cannot predict the non-linear response patterns in large amplitude motion simulations.

Accuracy of the motion and loads response predictions depends on the ship hull form around the still water level. Fast ships like; container ships, frigates and some passenger ships have fine hull forms with small block coefficients. These types of ships have large bow flare profiles and large stern overhangs, therefore the vertical sections of the hull around the still water level varies significantly and the ship motions and loads will experience non-linear characteristics. This means that one needs to use time-domain prediction tools in order to evaluate non-linear motion equations. The complete non-linear treatment of the problem requires the calculation of the velocity potential which needs to satisfy both the body boundary and the free surface conditions simultaneously. Unfortunately, fully non-linear treatment of the boundary value problem has very high computational cost. Therefore it does not yield solutions appropriate for practical applications.

On the other hand, in order to develop a code to be used by ship designers, one needs to eliminate high computational costs and to maintain accuracy in large amplitude ship motion and load predictions up to an acceptable level. In this aspect, some practical tools have been developed based on the calculations of the hydrodynamic and hydrostatic forces at the instantaneous wetted position of the ship. However, in large majority of the previous works, radiation and diffraction forces are kept as linear in time domain ship motion simulations due to the high computational costs. Therefore, in order to design a fast and accurate tool to evaluate non-linear radiation and diffraction forces, a quasi-non-linear technique is adopted into the time domain motion equations. In the current study, 3D radiation and diffraction forces are evaluated using quasi-non-linear method based on the instantaneous position of the wetted hull under the mean water surface while the incident wave and restoring forces are evaluated under the instantaneous wetted ship profile at each time instant. In all calculations, consistency of the linear Boundary Value Problem (BVP) is ensured using the small scattered wave assumption which assumes scattered waves to be small compared to ship dimensions and motion response amplitudes.

In order to fulfil the aim of the study the in-house developed Large Amplitude Response (LARes) tool is developed in MATLAB software and the validations are performed using the benchmark ITTC S-175 container ship with highly nonlinear geometry at different forward speed cases with varying wave slopes in regular head seas. Motion and load responses are compared with large amplitude experimental results, in which the wave steepness is ranging from ka=0.01 to ka=0.12, and also with commercial PRETTI software (Van't Veer et al., 2009) for different forward speed cases. In order to verify and compare the numerical results, the experimental studies performed for International Towing Tank Conference (ITTC, 2010) and by Fonseca and Soares (2004) are used to compare nonlinear ship motion and load responses with respect to increasing wave slope. ITTC (2010) experiments are used to compare time-domain non-linear heave and pitch responses experienced by the ship in large amplitude waves for the forward speeds of Fn=0.20, Fn=0.25 and Fn=0.275. However, experiments of Fonseca and Soares (2004) are used to compare maximum and minimum peak points of the motion responses as well as the Vertical Shear Force (VSF) and Vertical Bending Moment (VBM) estimations at Fn=0.25. In the current research project, rigid ship motions are solved in time domain coupled equations of heave and pitch motions in head seas condition without taking into account viscous forces.

1.2 Aims and Objectives

The aim of the PhD thesis is to develop a practical computational tool, based on 3D quasi-non-linear time-domain technique, to predict ship motions and loads in large amplitude waves which can be accessible to ship designers. Main objectives of the research project can be summarized as follows:

1. Evaluation of the non-linear force components to account for:
    - Non-linear wave excitation forces (Froude-Krylov & Diffraction)
    - Quasi-non-linear time varying radiation forces which are calculated at the instantaneous wetted portion of ship under the still water level as the ship oscillates in large amplitude waves
    - Non-linear restoring forces.

2. Nonlinear evaluation of VSF and VBM in large amplitude waves.

3. Development of a practical computation tool accessible to ship designers, which will be applicable to the prediction of ship motions and loads in large amplitude waves, based on 3D frequency domain radiation and diffraction forces.

4. Investigation of the influence of quasi-non-linear radiation and diffraction forces in ship motion and load responses in large amplitude waves.

1.3 Contribution to the field of study

In the last decade, non-linear seakeeping methods have been very advanced in motions and loads calculation, but their efficiency has been very low and most of them are only solved by using super computers, which yield very high computational costs. Therefore, the current research aims to develop an efficient practical tool, which can be used by ship designers with an acceptable accuracy level in order to calculate non-linear motions and loads of the ships induced by large amplitude waves.

The original point of the research derives from the practical evaluation of 3D large amplitude ship motions and loads using Cummins's equations (Cummins, 1962) in the body-nonlinear level of nonlinearity. For this purpose, radiation and diffraction forces are pre-calculated with respect to the instantaneous wetted surface under the mean sea level with the linear potential flow three-dimensional (3D) hydrodynamic PREssure CALculation (PRECAL) software (Van't Veer, 2009) and stored in a database. Stored hydrodynamic forces and coefficients are interpolated for interim values of updated ship position at each time step and used in motion equations using impulse response functions (Cummins, 1962) with quasi-non-linear time-domain technique. The impulse-response formulation provides accurate results with a low computational cost in large amplitude ship motions and loads estimation. In order to evaluate quasi-non-linear radiation and diffraction forces:

- A database of pre-calculated range of ship positions accounting for the ship's varying submerged portion under the still water surface is generated and passed to PRECAL software.
- At each position, global and sectional complex diffraction forces, infinite frequency added mass and damping coefficients are evaluated.
- At each position, global and sectional memory functions are derived from damping curves.
- Pre-calculated global and sectional infinite frequency added mass and damping coefficients, diffraction forces, and memory functions are passed through the main motion equation at each time step.

1.4 Contents of the Thesis

This thesis starts with the critical review of the research which has been performed in linear and non-linear seakeeping analysis of rigid ships advancing in waves. In order to maintain the consistency in the previous works, literature review is divided into two sections: linear frequency-domain and nonlinear time-domain seakeeping analysis. Linear frequency domain seakeeping analysis section concentrates on the review and discussion on the steady flow approximations and zero and forward speed Green function evaluations. Nonlinear time-domain seakeeping section categorizes and reviews the previous work depending on the degree of the nonlinearity involved in hydrodynamic calculations. Moreover, in the nonlinear seakeeping section, the BVP is classified into three groups depending on the source type used in BVP solutions: transient Green source, Rankine source and Mixed-source formulations.

Chapter 3 describes the general approach and formulation of rigid ship motion and internal loads problem advancing at a constant speed in regular seas in frequency and time domain calculations. The chapter starts with the definition of the hydrodynamic axis frames, which has a crucial importance in the calculation of large amplitude responses. General description of the frequency domain BVP is provided in potential theory. Free surface and body boundary conditions derivations are provided in detail in order to derive the steady-flow components in the ship motions. Moreover, comparison of the double-body flow and uniform flow approaches are performed in the heave and pitch motion responses. Derivations of the time domain formulations are represented in terms of impulse response functions while free surface oscillations are derived using convolution integrals. Force components of the main motion and internal load equations are provided in detail in time domain approach with a focus on large amplitude motions. Vertical Shear Force (VSF) and Vertical Bending Moment (VBM) definitions are provided both frequency-domain and time-domain approaches in detail.

Chapter 4 describes the numerical procedures in order to solve nonlinear equations of motion in regular head seas. The flow charts of the Froude-Krylov (F-K) nonlinear and the introduced body-nonlinear method are provided in detail. In the development phase of the seakeeping models, focus is given to the advance meshing methods, their differences and variations. In order to eliminate the mathematical singularities in the panels close the still water level, automatic mesh correction code is generated. Moreover, a special attention is given to the waterplane area (LID) panels which are used to suppress the irregular frequencies in the frequency-domain BVP solution. In order to lower the computational cost of the simulations, multi-dimensional integration and interpolation codes are designed to be used in the body-nonlinear method predictions. Moreover, general solution approach for the proposed methodology is explained in detail.

Chapter 5 stands for the validation of motion and load estimations using the proposed methodology in regular seas in small amplitude waves. The chapter starts with the comparison of the time-domain LARes and PRETTI models with a special focus on the force components evaluation techniques. Global and sectional force components are compared with the PRETTI model in order to verify the accuracy of the force components. In order to verify the linear and nonlinear motion and force components barge geometry is used. Motion responses and VSF and VBM response comparisons at the midship section and at station 15 (1/4 L_{pp} from FP) for the S-175 container ship are performed using the available experimental data sets and the PRETTI model.

Chapter 6 provides the application of the proposed methodology in the motion responses. Motion response comparison of the LARes and PRETTI models are compared with the available experimental data sets in large amplitude waves. Motion response characteristics are investigated with respect to the increasing wave slope in three different forward speed (Fn=0.20, 0.25, 0.275) and three different wave length to ship length (λ/L_{pp}=1.0, 1.2, 1.4) combinations around the resonant frequency and compared against the experimental results. The influence of the wave length and ship speed on the motion responses in large amplitude waves is investigated detail in order to draw an overall conclusion. Nonlinear motion behaviour characteristics are investigated in detail focusing on the positive, negative peak values and also the mean value of the motion responses. Moreover, the investigation of the quasi-non-linear radiation and diffraction forces is performed and compared with the F-K nonlinear model in detail.

Chapter 7 describes the application of the proposed methodology in the internal load responses by comparing them with the LARes and PRETTI models and the available experimental data sets in large amplitude waves. VSF and VBM response characteristics at the mid-ship and station 15 (¼ Lpp from the forward perpendicular) positions are investigated with respect to the increasing wave slope at a forward speed of Fn=0.25 in three different wave length to ship length values (λ/L_{pp}=1.0, 1.2, 1.4) around the resonant frequency and compared against the experimental results.

Chapter 8 summarizes the achievements obtained using the proposed methodology and provides recommendations for the future research to develop the proposed methodology.

Chapter 2

Literature Review

2.1 Introduction

The main objective of this chapter is to review the previous works focus on the wave induced motions and loads on ships. The review starts with the leading linear theories and extends to the numerically more complicated and more advanced non-linear theories to predict ship motions and loads in a rough sea environment. In the present thesis, time-domain solution of radiation forces is obtained via convolution integrals in terms of impulse-response functions. The accuracy of time-domain solution is highly dependent on the frequency domain hydrodynamic coefficients. Hence, in the linear wave-body interactions section, frequency domain BVP solutions of previous works are reviewed. In the nonlinear wave-body interactions part, the contribution of each work is highlighted with respect to the nonlinearity levels that they implemented in the numerical calculations. Moreover, previous experimental studies in the field of wave-body interactions are also discussed with the aim of highlighting the main assumptions in rigid and elastic body models and experimental setups. Mainly, the literature review is divided into three main parts:

- Linear wave-rigid body interaction: here previous works related to linear seakeeping methods are reviewed putting the emphasis on the effect of steady and unsteady wave interactions, forward speed effect on the ship hydrodynamics using translating and/or pulsating source formulations and their limitations.
- Nonlinear wave-rigid body interaction: this section reviews the previous work which has been carried out in relation to nonlinear seakeeping methods. These are reviewed and sorted with respect to the nonlinearity levels implemented in the calculations.

- Experimental studies: here the experimental studies are highlighted with respect to their assumptions and model setups that were applied, and the motions and load responses on rigid bodies are reviewed.

2.2 Linear Wave-Rigid Body Interaction

Numerical computation of the forward speed ship motions problem has been of great interest to researchers for last three decades. Significant effort has been put in order to model wave-body interaction more accurately and in a computationally less expensive way. The BVP can be evaluated using two different methods, namely time-domain (transient method) and frequency domain method. Both of the methods may have several advantages and disadvantages for a particular problem. Time-domain analysis requires the evaluation of convolution integrals over all previous time steps of the fluid motion history. Therefore, time-domain methods take more computational time and memory to solve the BVP compared to frequency-domain methods. Forward speed time-domain Green's function simulation run time is in the same order as for zero-speed frequency domain simulation and its implementation is much simpler when compared to the more complex and time consuming forward speed frequency-domain methods (Liapis, 1986). Earlier work on ship motions is mostly based on frequency-domain methods due to a lack of computational resources.

During the second half of the 80s a research group called Cooperative Research Ships (CRS) developed linear potential flow 3D PRECAL software (Van't Veer, 2009) in order to predict ship motion and loads advancing with forward speed. The theoretical information about the PRECAL software will be presented in the methodology chapter. In the present thesis, PRECAL software is used to solve the forward speed linear BVP using the Approximate Forward Speed (AFS) and Exact Forward Speed (EFS) methods. A comparison of both methods will be examined in detail in the following chapters. In nonlinear calculations, forward speed hydrodynamic coefficients are derived using the AFS method due to its accuracy and fast computational time. In order to assess the effects of the AFS and EFS methods on the hydrodynamic coefficients and motion responses, previous works are reviewed and discussed below.

Dynamics of a vessel advancing in the sea was first studied by Froude (1861) and Krylov (1896). Hydrodynamic forces on a floating body were formulated taking into account inertial, restoring and first order incident wave force components. However, in their work steady–state forces originating from harmonic rigid body motion namely diffraction and radiation force components were not considered.

On the way to the modern seakeeping methods, researchers made significant developments in order to derive BVP accurately in order to solve wave-body interactions. Haskind (1946) was the first researcher to separate the velocity potential into the diffraction and radiation potentials. He applied the thin-ship theory in order to solve fluid-body interactions. Korvin-Kroukovsky (1955) used a slender-ship approach and applied strip theory method on the two dimensional sections while taking into account the interaction between transverse hull sections. St Denis and Pierson (1953) solved the problem in irregular seas using spectral analysis in which irregular sea was defined by the superposition of regular waves.

Cummins (1962) formulated an integro-differential equation to evaluate time domain responses of a ship with convolution integrals. In this equation, radiation forces are obtained via convolution integrals in terms of impulse-response functions. Ogilvie (1964) derived the relationship between frequency-domain coefficients and time-domain terms in the convolution term using Fourier transforms. In the present thesis, time domain ship motion and load calculations are performed using Cummins equation. Details of the equation will be provided in the methodology chapter.

The first attempt to model forward speed using Green's functions in the frequency-domain can be attributed to Salvasen et al. (1970) who used the classical strip theory based on the (Korvin-Kroukovsky) theory. The authors applied forward speed corrections by means of encounter frequency and pressure corrections using a uniform flow model. Although the forward speed corrections were originally applied to the strip theory, they are also now widely applied to 3D panel methods.

Evaluation of forward speed influence is the main problem in the solution of Green's functions due to its complex numerical integration process on the waterline sections. Numerical methods need to be implemented to solve BVPs in presence of forward speed and Green's functions need to be satisfied both on the Free-Surface Boundary Condition (FSBC) and on the Body Boundary Condition (BBC). Detailed information about the formulation and the comparison of forward speed ship motions problem are provided in methodology chapter. Mainly, forward speed ship motion problems can be solved using Green's functions by two different techniques (Bunnik et al., 2010):

- AFS formulation where BVP is solved with zero speed Green's functions and then forward speed corrections are applied. This method is known as Pulsating Source (PS) method and widely applied in seakeeping programs widely used in the ship and offshore industries.
- EFS formulation where the exact forward speed Green sources are used to solve forward speed BVP. This method is known as Translating-Pulsating Source (TPS) method.

The PS method has a deficiency which fails to satisfy the forward speed FSBC when the oscillating frequency is low and ship speed is high (Inglis and Price, 1981a). The accuracy limit of the strip theory method is also related to this issue. Despite the limits due to the high frequency and low forward speed, strip theory can provide accurate results for the low frequency range. The main reason for this is that in low frequencies Froude-Krylov and restoring forces are more dominant compared to the radiation and diffraction components. In mathematical modeling, TPS method has more accurate formulation in handling the forward speed effects. However, forward speed boundary conditions are hard to satisfy and are computationally expensive. Due to the high oscillatory nature of the Green's functions near to the free surface, small step sizes are needed in the numerical integration which results in a high computational time (Ba and Guilbaud, 1995). The main difficulty associated with the numerical derivation of the Green’s function is its first and second derivatives and the difficulty in the integration process of the waterline sections. Due to the easier evaluation process of zero-speed Green’s function most of the commercial seakeeping codes use the PS method.

Chang (1977) initiated the first successful application of the TPS method on a Series 60 hull form using 3D panels and observed a better agreement with the experimental data compared to the PS method, except the roll and pitch damping coefficients. The author commented that in order to improve the pitch damping coefficients steady flow effect should be included in the numerical calculations.

Inglis and Price (1981e) used the TPS method to predict hydrodynamic coefficients of a Series 60 hull form advancing with a constant forward speed using a 3D panel method. The authors found better agreement with the experimental data compared to the PS method, but the method over-predicted the pressures around the stern area of the ship due to the lack of viscous forces and artificial stern wave damping. The deficiencies in the heave coefficients were smaller compared to the pitch coefficients when compared with the experimental data. The speed effect was diversely affected by the accuracy of the hydrodynamic coefficients compared to the experiments. It was also noted that inclusion of steady wave effects in the BVP increases the accuracy of the hydrodynamic coefficients; however it is computationally very expensive.

Guevel and Bougis (1982) worked on the TPS method to solve forward speed diffraction-radiation problems using Green’s functions with 3D flat panels. They assessed the added mass and damping coefficients at forward speed using source and doublet distributions on a DNV barge and a Series 60 hull form at low forward speeds. Their results were in good agreement with the results of Chang (1977) in all coefficients except the pitch damping coefficients.

Wu and Taylor (1989) applied quadratic iso-parametric boundary elements to model the ship geometry instead of constant panel elements. Iso-parametric elements provide higher degree of accuracy when finding the fluid velocities near to the hull. Authors applied Galerkin methods to satisfy the BBC in order to overcome the difficulty of source and field points' proximity to the free-surface. In the forward speed steady-unsteady flow interaction problem, evaluation of second order steady potential derivatives is very difficult. The authors overcame the problem using Galerkin method which reduced the second order steady potential derivatives to first order derivatives.

Wu and Taylor (1990) studied on the PS method to calculate hydrodynamic forces on a body oscillating and translating with low forward speed using the perturbation series in terms of forward speed. Provided that the second-order terms in the forward speed are neglected, the hydrodynamic solution can be done with zero speed Green functions. Forward speed correction can be performed using perturbation series of the potential in terms of forward speed. The authors also noted that, linear theory did not satisfy the reverse flow relationship due to the 'line integral effect'. They managed to satisfy the reverse flow relationship by applying coupling effects of the steady and unsteady potentials in the FSBC regardless of whether the body is slender or not. However, forward speed effects were only discussed for a floating circular cylinder and the methodology was not applied on a complex geometry.

Delhommeau and Alessandrini (1991) studied the influence of different approximations in the FSBC in the calculation of second order forces and motion responses. Three different approximation methods were tested on a DNV barge namely exact FSBC, first order FSBC and the zero speed FSBC. The authors commented that three approximations gave similar results due to the low speed, but the exact free-surface case showed singularity at a critical Strouhal number of $\tau=0.25$. They also commented that meshing of sharp edges affects the second order forces significantly.

Iwashita and Ohkusu (1992) presented an efficient algorithm using the TPS method to solve Green's functions and its derivatives at forward speed. They used the single integral formulation of Bessho (1977) which performed the integrations along a path in the complex plane. The development was in the selection of the right path with the steepest descent method in order to perform integration in a straightforward manner and to control the accuracy of the results. The application of the scheme was performed on a submerged slender spheroid by taking into account the m_j terms (gradients of steady velocities in normal direction) contribution on the hydrodynamic coefficients and wave induced forces. Results indicated that hydrodynamic coefficients are affected moderately in the head seas condition while the forward speed effects were found to be more significant in the following seas condition. Unfortunately, the numerical study was only performed for a submerged spheroid and was not applied to surface piercing complex geometries.

Papanikolaou and Schellin (1992) applied the PS method in order to evaluate the motions and wave induced loads on S-175 ship using 3D flat panels. They used a uniform flow model to implement in the Body Boundary Conditions (BBC) and disregarded the higher order terms in the steady-flow velocity and in the total velocity potentials. Radiation potentials were described in terms of speed independent part of the velocity potential, which allowed the forward speed effects to be modeled with the zero-speed Green's functions with forward speed corrections. In their results, motion responses agreed better than the wave induced loads responses compared to the experimental results. They noted that the heave Response Amplitude Operator (RAO) was predicted higher than the experimental results and the reason was attributed to the lack of heave viscous damping. At the midship section, vertical shear forces were over-predicted while the vertical bending moments were under-predicted compared to the experiments.

Ba and Guilbaud (1995) worked on the integration of the unsteady Green's functions and used Kelvin singularities to achieve fast and accurate results. Their method was not dependent on the frequency and speed parameters. A method of resolution of differential equations was applied to calculate integral parts of the Green's functions. In order to decrease the computational time, fourth order polynomials were used to interpolate the integrands. They managed to calculate the first and second derivations of Green's function with small errors in a short computational time.

Boin et al. (2003) used formulation of a simple integral in the Fourier plane instead of double integrals in the complex plane. They used the formulation originally developed by Guevel and Bougis (1982) and then modified by Ba and Guilbaud (1995) and calculated the lifting effects of the hulls related to the integration of second derivatives of the Green function. The authors ranked the integrations of Green function in detail by their computational difficulty evels. They also demonstrated that direct integration of Green functions on the waterline decreased the difficulty of the numerical calculations compared to the direct derivation of Green functions. Despite all numerical advances with the method, it still incurs a high computational cost.

Chapchap et al. (2011) compared the TPS and PS method using 3D panels on S-175 containership for a high forward speed case (Fn=0.275). The authors reported that the heave RAO's demonstrated good agreement between both of the methods. However, the TPS method provided larger responses in the pitch RAO's around the resonance area compared to the PS method. The main reason for the discrepancy between the two methods originated from the pitch damping coefficient B_{55}. In the TPS method, around the resonance area, the pitch damping coefficient B_{55} was predicted to be much lower than with the PS method. The authors noted that in the TPS method the steady-forward speed influence was large in hydrodynamic coefficients and the BBC needs a further investigation due to their complexity.

2.2.1 Steady Flow and Unsteady Flow Interaction

In the frequency-domain analysis it is a complicated task to take into account the interaction of steady waves originating from the ship advancing in still water and the unsteady waves generated by the oscillatory motion of the body advancing in waves. The formulation of unsteady flow BBC including the m_j terms was first introduced by Newman (1979). The major difficulty in numerical solution of steady-unsteady flow interaction is due to the complexity of the second derivatives involved in the steady potential in m_j terms (Kim and Shin, 2007). This interaction effect show itself in the derivation of FSBC and BBC and makes the problem difficult to solve (Inglis and Price, 1981a). Due to the complexity of the problem generally researchers used free-stream flow in order to simplify the m_j terms contribution. Hirdaris et al. (2014) summarized the three levels of flow models in steady wave and unsteady wave interactions as:

- The Neumann-Kelvin (N-K) flow where the interaction between steady and unsteady flow effects are ignored and flow is approximated by a uniform flow of velocity equal to ship speed.
- The Double-body (D-B) flow where the flow around the body mirrored about the mean free surface. Interactions between the steady and unsteady flows manifest themselves in the boundary conditions.
- Steady-wave flow is the most advanced solution where the steady flow potential is obtained from the BVP solution of a ship advancing in still water. The solution of the steady wave problem forms the unsteady wave radiation boundary conditions.

In the present thesis, the PRECAL code is used to solve the BVP using N-K and D-B flow methods. A comparison of both flow models will be examined in detail in the following chapters. In non-linear motions and loads calculations uniform flow model is used and steady-unsteady wave interactions are neglected due to the computational cost. In order to assess the effects of steady-unsteady flow interaction, previous works are reviewed and discussed in the following section.

Inglis and Price (1981a) assessed the effects of steady wave and unsteady wave interaction using translating and pulsating sources with 3D panels on an ellipsoid advancing with constant forward speed in waves. In order to simplify the BVP solution, the steady wave contribution in the FSBC is neglected, while it is retained in the BBC. They showed that the steady flow effect changes the heave and sway added mass coefficients to a large extent especially at low frequencies and at high frequencies the discrepancies are decreasing. The main reason for the discrepancies between the low and high frequencies is due to the constant contribution of the m_j

terms in the BBC over the frequency range, which becomes relatively small at high frequencies (Kim and Shin, 2007).

Zhao and Faltinsen (1990) studied on the elimination of the problems associated with the m_j terms derivation on objects with sharp corners. In their study, steady flow interaction with the BBC and FSBC were taken into account, assuming the wave slopes and Froude number are small. It was concluded that using direct pressure integration can cause large errors in prediction of mean wave forces on bodies with sharp corners due to the m_j terms originating from the BBC.

Wu (1991) proposed a different scheme for the solution of wave-current-body interaction problems. In this scheme, provided that the first order derivatives of the steady potential are calculated accurately with numerical methods, m_j-terms can be treated as that of Dirichlet type. The method was applied to derive m_j-terms on a circular cylinder and elliptical cylinder in an unbounded fluid domain and the error was estimated less than 2% compared to the analytical solutions calculated by Wu and Taylor (1988).

Chen and Malenica (1998) studied the effect of steady flows on wave radiation and diffraction at low forward speeds. A decomposition method was applied to time-dependent velocity potential into linear and interaction components in order to assess the effect of steady wave and unsteady wave interactions. For the sake of simplicity, the linear components satisfied the linear FSBC while the interaction component was retained to find out the effects of steady flow and linear time harmonic potential components. Both of the velocity potentials were solved using Green source formulation provided in Noblesse and Chen (1995). Interaction effects were found to be important in the evaluation of first and second order forces and coupled radiation coefficients. The authors also commented that the decomposition method is more advantageous to the perturbation expansion due to its consistency in the far field unlike the secular terms left unbounded in the perturbation expansion. Furthermore, it was found that the decomposition method can be applied to large size bodies removing the necessity of applying the slender body assumption.

Iwashita and Ito (1998) studied the influence of steady flow on a blunt VLCC ship and found that the steady flow influence in the FSBC is more significant than the BBC around the bow region of the ship.

Fang (2000) accounted for the steady wave effect in the calculation of hydrodynamic forces and moments. However he adopted the free-stream flow approach in the derivation of the m_j terms while neglecting the second order terms. The author solved the BVP using zero-speed Green functions and applied forward speed corrections on the velocity potential. Results were provided for the Wigley hull and a Series 60 hull form comparing the steady flow influence on ship motions. It was found that steady flow effects have large influence on the motion modes, except the heave mode, when the ship has asymmetrical fore-aft shape.

Kim and Shin (2007) presented work about steady wave contributions in the unsteady ship motions using three different steady flow models namely free stream flow, D-B flow and steady-wave flow. The TPS method was applied to solve BVP using 3D panels with Green source formulation. In order to assess the forward speed effects completely, steady sinkage and trim calculations were also included in the analysis. Verifying the results of (Inglis and Price, 1981a), they found that the steady flow affects the heave and pitch added mass and damping coefficients in large extents especially in the low frequency range. Moreover, they also showed the effect of steady flow effects in the heave and pitch motion responses. In heave and pitch motion responses, D-B flow and steady-wave flow models provided a better agreement to the experimental data especially in the resonant region compared to the free-stream flow model which was overestimated. In heave motion response the discrepancy between the free-stream flow and the D-B flow was around 20% and the discrepancy between the D-B flow and steady-wave flow was around 5% while in pitch motion response the difference between the free-stream flow and the D-B flow and between the D-B flow and steady-wave flow was found around 10% and 5% respectively. They also concluded that, for moderate speeds and for simple geometries steady sinkage and trim effect were not significant.

Zhang et al. (2010) compared the effects of forward speed wave-body interactions on the hydrodynamic coefficients using D-B linearization in the FSBC and using Mixed Euler-Lagrange (MEL) time stepping technique. Wigley hull and Series 60 hull results were compared with experiments and other numerical solutions using N-K and D-B flow method. In their conclusion, they stated that generally the D-B method provided better results than the N-K methods compared with the experiments. The significant contribution of the D-B flow method was in the cross-coupling hydrodynamic coefficients and diagonal hydrodynamic coefficients such as A_{55} and B_{55}. In order to understand the main reason for the variation in the hydrodynamic coefficients, the authors compared the D-B flow m_j-terms results with linearized FSBC and with the MEL-D-B method. The results showed that in the D-B flow model m_j-terms interaction affected the cross-coupling added mass (A_{35} and A_{53}) and diagonal coefficients (A_{55} and B_{55}) more significantly while the contribution of the additional terms in the FSBC were contributing less than 10% to the improvement in the prediction of A_{35}, A_{53}, A_{55} and B_{55}. However, it was found that, damping coefficient B_{53} was affected in the same order by the D-B m_j-terms and by the additional terms in the FSBC. The authors also commented that heave and pitch RAO's are over-estimated using the N-K flow methods compared to the other numerical methods and experiments.

2.3 Nonlinear Wave-Rigid Body Interaction

In the previous section of the study all formulations and methodologies were described and reviewed for linear methods in which the wave amplitudes were assumed to be small in comparison with the ship dimensions. In linear methods, ship motions and load responses are linearly proportional to the incident wave amplitude. In order to assess non-linear responses of the ships, one needs to use the time-domain approach to take into account the effects of large amplitude incident waves. When the small amplitude wave assumption is violated, the frequency domain approach is no longer valid since the frequency domain calculations are justified only if the body motions are strictly sinusoidal in time.

Time domain simulation methods can be separated into two approaches namely the impulse-response function (IRF) method and direct time-domain integration method. Both of these methods may have advantages or disadvantages for a particular problem. In the IRF method is a fast and reliable approach for modelling non-linear ship-wave interactions. In IRF method, fluid reaction forces are calculated using convolution integrals formulated by Cummins (1962). In order to calculate the convolution term in the radiation forces, retardation forces need to be calculated from the frequency-domain hydrodynamic coefficients. After the accurate calculation of retardation forces, derivation of motions and loads are very straightforward. In direct time-domain methods, fluid effects are calculated with transient wave Green functions and motion equations are solved at each time step. The forward speed case is easier to take into account in the time-domain method compared to the frequency domain method. However, the computational expense of the direct time domain methods is very high due to the need for small time steps and generally simulations need to be performed on a workstation or a super-computer.

Time-domain BVP can be solved using three different source formulations (Shin et al., 2003) namely: transient Green sources, Rankine sources and mixed-source formulations. In transient Green source formulation, sources are only distributed on the wetted part of the hull, and so FSBC and radiation conditions are automatically satisfied at the far field. However, difficulties arise with non-wall-sided hull forms due to the highly oscillatory behaviour of Green functions near to the free surface. In the Rankine source formulation, sources are distributed on the wetted part of the hull and also on a portion of the free-surface. This method provides accurate results for non-wall-sided hull forms. However, in order to satisfy the radiation condition at the far field a damping beach needs to be applied to the numerical solutions. In order to overcome the drawbacks of both methods, the mixed-source formulation was developed by Lin et al. (1999). In mixed-source formulation fluid domain is divided into two regions where the near field condition is satisfied using Rankine sources and far field radiation condition is satisfied using Green sources. Although the mixed-source formulation provides accurate motion and load predictions, its implementation is difficult and computationally expensive.

The summary of the advantages and disadvantages of the time-domain source methods was provided in ITTC (2011) and listed in Table 2.1 as follows:

Table 2.1: Comparison of time-domain approaches (ITTC, 2011)

Numerical Method	Advantages	Disadvantages
Transient Green Source	Panel distribution on only body surface Radiation is satisfied at far field	Numerical instabilities with non-wall-sided hulls
Rankine Source	Fairly robust for non-wall sided hulls	Need for more panels, panel distribution on hull geometry and on the free surface Need for damping beach at far field.
Mixed-Source	Takes advantage of combined method Accurate results	Long computational time Very hard to implement into non-linear motion calculations

In order to solve nonlinear BVP in large amplitude waves, one needs to satisfy the nonlinear FSBC and BBC at each time step in time-domain motion simulations (Kim et al., 2011). The analytic or numerical evaluation of the FSBC nonlinearity is a hard task and the accuracy might not be very satisfactory. However, numerical application of the BBC nonlinearity is relatively simpler than the FSBC nonlinearity to evaluate. In this study, nonlinear seakeeping methods are reviewed and commented by the taxonomy given by ISSC (2009). In ISSC 2009 nonlinear seakeeping methods were classified into six different levels with respect to their nonlinearity assumptions implemented in the numerical simulations from the linear methods to the fully nonlinear methods as follows:

- Level 1 (Linear)
- Level 2 (Froude-Krylov Nonlinear)
- Level 3 (Body Nonlinear)
- Level 4 (Body Exact/Weak Scatter)

} Eulerian Method

- Level 5 (Smooth Waves) } Mixed Eulerian-Lagrangian (MEL) Method
- Level 6 (Fully Nonlinear) } Reynolds Averaged Navier-Stokes (RANS) Method

The first four levels of nonlinear methods use an Eulerian approach to model the fluid actions. Strictly, in the Eulerian methods scattered waves are assumed to be small compared to the incident waves and steady waves. In the “Smooth Waves” method, scattered waves are no longer assumed to be small and the approach is valid until the wave breaking condition is reached. The MEL method belongs to this level of nonlinearity where the scattered waves are included in the BVP solutions at each time step. The main methodology implemented in the MEL method is the solution of linear BVP performed via Eulerian equations while the time integration of the nonlinear FSBC is performed with Lagrangian equations at each time step during the simulations (ISSC, 2012). In this method accuracy is highly dependent on the stability of free-surface time-stepping integrals which increase the computation time. Due to the complexity of the method it could not applied to ship-like geometries

The fully nonlinear method was developed in order to find an accurate solution for the breaking wave and other complex fluid actions such as spray and the real simulation of water on deck problems. In this method the fluid actions are modelled using Reynolds Averaged Navier-Stokes (RANS) equations with Smoothed Particle Hydrodynamics (SPH), the Moving Particle Semi-implicit (MPS) or the Constrained Interpolation Profile (CIP) methods. In this nonlinearity level fluid viscosity is taken into account in the numerical simulations. This method stands as the most advanced one in the literature regarding the complexity that it implemented in the solution of BVP. However, the method incurs a huge computational expense and in some problems it can take up to one month to find a proper solution. Currently, this method is under development and needs further research to understand its efficiency and performance.

In this section, the emphasis is given to the nonlinear methods using Eulerian formulation and the critical review is conducted for the group of three nonlinearity levels, namely Froude-Krylov nonlinear, body nonlinear and body exact (weak-scatter) methods. The time-domain BVP approach is grouped into three different source formulations in Table 2.2 and Table 2.3, in order to maintain the taxonomy in the methodologies. The time-domain solution approach is classified as an IRF method and a direct time-domain method in order to describe them in a correct theoretical manner. Moreover, the main emphasis is given to 3D panel methods due to the content of present thesis.

2.3.1 Froude-Krylov Nonlinear Methods (Level 2)

In this nonlinearity approximation, Froude-Krylov (F-K) and restoring forces are calculated with respect to the exact wetted area of the ship at each time step. However, the force components which originate from the perturbation potential (radiation and diffraction) are kept as linear and calculated with respect to the mean wetted area of the ship when it is in a static position under the mean water level. In reality, the instantaneous wetted hull includes the influence of the scattered wave field but the effect of this influence is equal to the third order and is ignored in the numerical calculations in this method.

The F-K nonlinear approach provides better accuracy in motion and load estimations than the linear time-domain approach when compared to the experimental results in large amplitude waves because of its capable of representing the nonlinear physical phenomenon more accurately. F-K nonlinear methods are capable to represent the most dominant nonlinearities in the motion and load responses, especially in long waves due to the fact that a large portion of the hydrodynamic forces are originating from F-K and restoring forces. In this section, the previous studies which made important contribution to the nonlinear seakeeping theory using the F-K nonlinear approach are reviewed and discussed on the approach implemented in simulations using the IRF or the direct time-domain approach.

Table 2.2: Classification of time-domain seakeeping methods in the literature I

Classification of time-domain seakeeping methods in the literature I

Boundary Value Problem Approach	**Discretization Method**	**Time Domain**		**Levels of Body Nonlinear Computation**				**Wave Amplitude**
	2D/3D	***IRF***	***Direct***	***Level 1***	***Level 2***	***Level3***	***Level 4***	***Small/Large***
Green Source Formulation				***Linear***	***F-K Non-linear***	***Body Non-linear***	***Body Exact***	
Liapis and Beck (1985)	3D		✓	✓				Small
King (1987)	3D		✓	✓				Small
Lin and Yue (1991)	3D		✓	✓	✓	✓		Large
Lin et al. (1994)	3D		✓	✓	✓	✓	✓	Large
Bingham et.al (1994)	3D		✓	✓				Small
Huang and Hsiung (1997)	3D	✓		✓	✓			Large
Zhu and Katory (1998)	3D	✓		✓	✓			Small
Fonseca and Soares (1998)	2D	✓		✓	✓			Large
Cong et al. (1998)	3D			✓	✓			Large
Ando (1999)	2D		✓	✓	✓		✓	Large
Sen (2002)	3D		✓	✓	✓			Large
Singh and Sen (2007a)	3D		✓	✓	✓	✓	✓	Large
Singh and Sen (2007e)	3D		✓	✓	✓	✓	✓	Large
Zhang and Beck (2007)	2D		✓	✓	✓	✓	✓	Large
Mikami et.al (2008)	2D		✓	✓	✓	✓	✓	Large
Tuitman (2009)	3D	✓		✓	✓			Large
Bandyk and Beck(2009)	2D		✓	✓			✓	Large
Rajendran et al. (2011)	2D	✓		✓	✓			Large
Kukkanen and Matusiak (2014)	3D		✓	✓	✓	✓		Large
Hizir (2015) (Present Thesis)	**3D**	**✓**		**✓**	**✓**	**✓**		**Large**

Table 2.3: Classification of time-domain seakeeping methods in the literature II

Classification of time-domain seakeeping methods in the literature

oundary Value Problem Approach	**Discretization Method**	**Time Domain**		**Levels of Nonlinear Computation**				**Wave Amplitude**
	2D/3D	***IRF***	***Direct***	***Level 1***	***Level 2***	***Level3***	***Level 4***	***Small/Large***
Rankine Source Formulation				***Linear***	***F-K Non-linear***	***Body Non-linear***	***Body Exact***	
Pawlowski and Bass (1991)	3D		✓	✓			✓	Large
Kring et al. (1997)	3D		✓	✓	✓		✓	Large
Kim et.al(1997)	3D		✓	✓				Small
Huang and Sclavounos (1998)	3D		✓	✓	✓		✓	Large
Bruzzone and Grasso (2007)	3D		✓	✓	✓			Large
Bruzzone et al. (2011)	3D		✓	✓	✓			Large
Song et al. (2011)	3D		✓	✓	✓			Large
Kim et al. (2011)	3D		✓	✓	✓		✓	Large

Boundary Value Problem Approach	**Discretization Method**	**Time Domain**		**Levels of Nonlinear Computation**				**Wave Amplitude**
	2D/3D	***IRF***	***Direct***	***Level 1***	***Level 2***	***Level3***	***Level 4***	***Small/Large***
Mixed-SourceFormulation				***Linear***	***F-K Non-linear***	***Body Non-linear***	***Body Exact***	
Lin et al. (1999)	3D		✓	✓	✓	✓	✓	Large
Weems et al. (2000)	3D		✓	✓	✓	✓	✓	Large
Shin et al. (2003)	3D		✓	✓	✓	✓	✓	Large
Liu and Papanikolaou (2012)	3D		✓	✓	✓	✓		Large

Huang and Hsiung (1997) studied shallow water on deck problems on fishing vessels. In time-domain nonlinear motion simulations, the F-K nonlinear method was used to solve ship accelerations and water on deck effects using transient Green sources with 3D flat panels. The authors solved the sloshing problem on the deck using the flux-difference splitting method (Huang and Hsiung, 1994). In this method water particle velocity and the water depth on the deck were calculated using backwards and forwards finite difference formulations. In order to solve motion responses Cummins equation was used while the hydrodynamic coefficients were derived by direct-time domain simulation method. In the results, the authors observed a bore when the roll excitation frequency is close to the roll resonance frequency. That phenomenon was described as the sloshing on the deck around the resonance frequency magnified the roll motion amplitude and also caused a shift in the roll resonance frequency. Despite the inclusion of the maneuvering forces in the analysis, their effects were not described in the paper.

Kring et al. (1997) studied the nonlinear ship motions and loads by using Rankine sources distributed on the hull and on the free surface. Results were provided for the Series 60 hull and Snowdrift hull in head seas for incident wave amplitudes up to the one percent of the ship length. Theoretical formulations of the F-K nonlinear and the Weak Scatter methods were provided in detail. The authors noted that it is crucial to include m-terms in the linear solution. It was also mentioned that there is no need to use m-terms in the Weak Scatter method because the BBC is satisfied on the exact wetted area of the ship at an instantaneous position over the time simulation. The Weak Scatter method was compared with the linear and experimental motion results for the Series 60 hull. Due to the wall-sided geometry of the Series 60 hull around the design water line, all results were found in a good agreement with each other while the Weak Scatter method slightly overestimated the motions compared to the experimental results and the linear motion predictions. Nonlinear motion and load simulations were carried out for the Snowdrift hull using the F-K nonlinear method. It was observed that nonlinear behaviors in motion and load estimations were significant. The F-K nonlinear method provided better results than the linear method compared to the experimental results. However, they showed a significant reduction in motion amplitudes compared to the linear method estimations. In vertical load estimations nonlinearities were found to be much greater than the nonlinearity observed in the vertical motion responses. Asymmetry in the sagging and hogging bending moments was observed while the F-K nonlinear method predicted closer values to the experimental data compared to the linear responses. Unfortunately, the load estimations were not included for the Weak Scatter method in the numerical calculations.

Fonseca and Soares (1998) studied the F-K nonlinear approach in a time-domain method based on strip theory using the IRF formulation. In their study, radiation and diffraction forces were assumed as linear and solved using linear boundary conditions in the frequency-domain. Frequency-domain hydrodynamic forces were calculated using multi-parameter conformal mapping on 2D strips. Free-surface oscillation in the time-domain was modeled using convolution integrals in terms of impulse-response functions. The complex amplitude of diffraction forces was assumed as harmonic during the time-domain simulations. Simulations of vertical motions and loads were carried out for the S-175 container ship at Fn=0.25 in regular waves in head seas and compared with the linear results. Asymmetric response characteristics were assessed in the motion and load responses, where non-linear motion amplitudes were found to be smaller than the linear ones. In the vertical loads at the midship section, the magnitude of sagging moments predicted was larger than the magnitude of hogging moments and linear bending moment estimations. Nonlinear behavior was clearly identified in motion and load simulations where the ship was found to be emerging more in heave motion and submerging the bow more in pitch motion. In reality, due to the outer flare of the bow section of the ship geometry the bow should be emerged more than submerged in pitch motions. The reason for that is the lack of pitch damping around the bow region at the resonant period which needs to be calculated accurately.

Cong et al. (1998) studied the motions and loads on a frigate advancing with a low speed at Fn=0.05 in regular head seas by discretizing the ship using 3D panels and solving the BVP using a Green source distribution. They used the direct time-domain approach and solved the radiation and diffraction forces in the time domain using the Fredholm integral equations of the first kind. The authors included nonlinear F-K forces, nonlinear restoring forces, roll damping forces and maneuvering forces in the simulations while keeping the radiation and diffraction forces linear. The results were compared with the conducted experiments. In the results, motion responses agreed well with the experimental results however pressures near the bow, and VSF and VBM estimations at midship section showed significant discrepancies compared to the experimental data. The main reason for the pressure difference around the bow region was attributed to the nonlinearity of flow around the ship's bow, which was neglected in their study.

Sen (2002) studied 3D ship motions with forward speed using a transient Green source distribution in regular and irregular seas. Nonlinear large amplitude time-domain computations were presented for the Wigley hull and Series 60 hull forms for $Fn \geq 0.3$ and compared with the linear motion results. He modeled the fully nonlinear incident wave using Fourier approximation which was proposed by Rienecker and Fenton (1981). In the Wigley hull results, significant nonlinearities in the motion responses were observed. The author noted that in longer waves nonlinearities were increasing while in short waves nonlinearities were not so significant. In a fast forward speed condition at $Fn=0.5$ it was noted that the linear calculations showed a considerable steady sinkage and trim while the nonlinear simulations did not show the same trend. It was observed that in large amplitude motion responses when the wave steepness increased, the peak value in heave response was reduced. In contrast, the peak values of pitch motion response increased with the increasing wave steepness in long waves. The main reason is the lack of damping forces at that encounter frequency. The Series 60 hull results were not accurate in nonlinear calculations compared to the linear responses due to its complex hull geometry compared to the Wigley hull.

Fonseca and Soares (2005) modified their former approach to assess vertical motion and load calculations for the S-175 container ship in large amplitude waves by adding the steady sinkage and trim influence, identification of the second and third harmonics, influence of viscous forces and water on deck effects on the vertical motion and load estimations. Viscous forces were calculated in the time-domain using the method proposed by Thwaites (1960) using the cross-flow drag coefficient, viscous lift coefficient , the vertical relative velocity, the ship speed and the pitch angle on 2D strips. The authors noted the importance of the viscous forces on rectangular cross sections which had more effect than the triangular sections. When the steady sinkage and trim was included in the calculations, the results showed significant reduction in the heave responses which became closer to the experimental data while the difference in the pitch response was found to be small. In the motion responses, in contrast to their previous study, the ship's bow tended to emerge more than it submerged which was also validated with the conducted experiments. In vertical load estimations, steady sinkage reduced the amplitudes of the VSF around the resonant region while, on the contrary, increased the amplitudes of the VBM. It was noted that at the midship section the 2nd and 3rd harmonics of the VSF estimations should not be disregarded due to their small importance compared to 1st harmonics. The influence of higher order harmonics at the midship section was more significant in the VBM than the VSF calculations and the authors noted that in order to model the physics of the simulation accurately higher order harmonics needs to be assessed properly. Influence of the green water on deck occurrence was calculated using the momentum method proposed by Buchner (1995). Unfortunately, when the green water effect was included in the calculations the motion and load results are diverted from the experimental results. The main reason for this discrepancy was attributed to the water height on the deck, which is the main component of the momentum equation, overestimated by using only the incident wave elevation. Other wave components could not be implemented to the calculation due to the complexity of the problem.

Bruzzone and Grasso (2007) worked on the motion responses of a fast NPL series catamaran using the 3D Rankine panel method. In their work a hybrid solution approach was used to solve the time-domain radiation forces using the IRF method while diffraction forces were assumed to stay harmonic during the simulation. Numerical calculations were performed to solve motion responses for Fn=0.65 and

Fn=0.67 while the maximum wave steepness was applied as ka=0.07. Comparisons of the motion results were performed with the experiments conducted by Molland et al. (2001). In the results, heave and pitch motion responses were overestimated compared to the experiments at the resonant region whilst pitch response did not show a significant difference compared to the linear prediction. In large amplitude incident waves, asymmetry of the heave and pitch motion responses were significant. The authors also commented that due to the limited number of numerical simulations it is not enough to assess the accuracy of motion responses in large amplitude waves.

Rajendran et al. (2011) studied the effects of abnormal waves on the motions and loads responses for a 117m container ship in irregular head seas. They used a 2D strip theory IRF approach based on the paper of Fonseca and Soares (1998) for the motion and load predictions. The validation and comparison of the results was performed with the conducted experiments. It was noted that in the linear method the sagging peak was underestimated where the hogging peak was overestimated in the VBM calculations. However, in non-linear method two sagging peaks were observed in the VBM time history. The reason for the second peak in the VBM time history can be attributed to the second harmonic in the response signal. However it was noted that the second sagging peak was overestimated with the applied methodology.

Bruzzone et al. (2011) modified their former approach by applying two novelties into their research. They calculated the motion and load responses taking into account the nonlinear F-K forces and nonlinear restoring forces, whilst, keeping the radiation and diffraction forces as linear. They related the frequency and time-domain equations using Cummins approach and solved the nonlinear motion equations in frequency-domain by an iterative process. In that way, they overcame the limited range of damping frequencies in the kernel functions and also avoided the transient part of the responses. They also defined the hull geometry using bi-cubic functions and calculated the instantaneous wetted part of the hull pressures effectively. They applied the methodology to the S-175 containership advancing at Fn=0.25 and compared the motion and load responses with the experiments conducted by Fonseca and Soares (2004). Generally, the heave and pitch motion responses were in good agreement with the experiments except the resonance area where they were over-predicted. That was attributed to the lack of damping forces around the resonance area. The VSF and VBM predictions were overestimated compared to the experimental data around the resonant region which was inherited from the overestimated motion responses. The authors noted the reduction in the VSF and VBM with the increasing wave steepness where the sagging peaks were predicted greater than the hogging ones.

Song et al. (2011) assessed the effects of large amplitude motions and loads using 3D Rankine panel method. Motion and load calculations were performed on a modern 6500 TEU container ship for a range of incident wave angles and wave heights. In order to calculate the torsional moment accurately, mass distribution of the hull was modeled based on the Finite Element (FE) model. In this study the nonlinearity in wave-induced load calculations based on the F-K nonlinear method was emphasized as varying with the wave heading and wave steepness. Numerical calculations were performed for low forward speed due to the limitation of the D-B basis flow assumption. In order to maintain the accuracy in oblique waves, viscous roll damping was implemented as 4% of the critical damping as found in zero speed calculations. The authors noted that, in oblique waves and at low frequencies, spring-damper forces had a significant importance in the motion responses. The VSF estimations at the 1/4L distance from the aft peak and 1/4L distance from fore peak were underestimated compared to the experimental data while the VBM at the midship section was in good agreement with the experiments. The discrepancies in the VSF were attributed to nonlinear computation level because the F-K nonlinear method could not solve the complete nonlinear problem. They also commented that at oblique waves and at large incident wave heights the accuracy of the torsional moment can be increased by tuning the roll damping.

2.3.2 Body Nonlinear Methods (Level 3)

The body nonlinear methods are a modified version of the F-K nonlinear methods where the radiation and diffraction potentials are solved for the wetted part of the hull based on the instantaneous position of the body under the still water level. The calculation of nonlinear F-K and restoring forces is implemented with the same approach as it was in the F-K nonlinear methods. In this method radiation and diffraction potential is solved with respect to the exact BBC which is linearized on the still water level. The method has an elevated computational cost due to the re-panelling of the instantaneous underwater hull under the still water level at each time step. Researchers tried to lower the computational cost by applying interpolation methods on the pre-calculated transient part of the Green functions for different ship positions. In this method, rate of change of the fluid added mass varies during the simulation which makes it possible to calculate slamming effects on the ship. In this section, the previous works which made a contribution to the literature using the level 3 method are reviewed and discussed based on their approaches.

Lin W.M. and Yue (1991) worked on a project named Large Amplitude Motions Programme (LAMP) using the 3D time domain approach based on transient Green sources for the assessment of large amplitude wave loads on ships. Validation of the code was performed with the conducted experiments for a sphere and Wigley hull and were found to be satisfactory. The authors noted that the large amplitude heaving motion increased the added resistance and the steady sinkage and trim. Moreover, nonlinear heave added mass was decreased with the increased heave amplitude. Due to the reduction in the added mass, inertia forces were also reduced and this resulted in a forward shift in the natural frequency. It was also concluded that in irregular waves LAMP had a better accuracy in the calculation of transient effects compared to strip theory.

Fang et al. (1997) developed a quasi-non-linear time domain technique to assess large amplitude motions of catamarans in regular head seas. A database was pre-generated using strip theory with respect to the time varying submerged portion of the ship sections during the simulations. The authors assumed that the transient part of the solution died out at each time step and solved only the steady-state part of the motion equations in the time-domain simulations using Runge-Kutta integration. Therefore, the convolution part which accounts for the free surface oscillations was not included in the calculations. In the comparison part, the linear frequency-domain, quasi-non-linear time-domain and experimental results were compared for the V1 catamaran at zero forward speed and at forward speed. Generally the nonlinear time domain method had a better agreement than the linear method in heave and pitch responses but at the same time they were over-predicted compared to the experimental data around the resonant region. The non-linear time domain method captured the asymmetric features in positive and negative peak of heave and pitch motions, but it was unsuccessful in the prediction of non-linear patterns observed in the experimental results. The reason was attributed to the lack of the transient part in the motion equations. In general, heave and pitch responses were over-predicted around the resonant region due to the lack of damping forces. In nonlinear simulations and the experimental results, around the resonant region it was observed that the peak amplitudes of heave and pitch motions were decreasing with the increase in the wave amplitude. It was also noted that the nonlinearities were increased when the forward speed and wave amplitude increased.

Singh and Sen (2007a) compared four different levels of nonlinearities ranging from the linear method (level 1) to the body exact method (level 4) in order to assess their effects on motion responses. Computations were carried out for the Wigley hull and the S-175 containership at forward speed using transient Green sources applied on 3D flat panels in regular and irregular head seas. The main emphasis of their research was given to the effect of the levels of nonlinearities on the derivative response of the vertical displacement and velocity. They decomposed the relative displacement and relative velocity into rigid body motion (Z_{RB}), disturbance wave elevation (η_D) and incident wave elevation (η_I) components. The influence of the components was assessed with the variation in the nonlinear methods. In the Wigley hull results at Fn=0.2 and $\lambda/L=1.2$ and at a wave slope of ka=0.08, nonlinearities were not significant due to its wall sided geometry and η_D was identified to be negligible compared to η_I and Z_{RB}. The next set of computations was conducted for the same conditions but for a faster speed of Fn=0.5. For that case, significant steady sinkage and trim is predicted in the level 3 and level 4 nonlinear computations in which bow submergence was observed. Next set of computations were conducted for S-175 containership at Fn=0.275 at the wave length of λ/L=1.0 and at a wave slope of ka=0.08 where the difference between the nonlinearities was found to be significant for heave, but not so significant for pitch motions. Level 3 and level 4 computations for heave response showed a reduction of 30% compared to the level 1 and level 2 computations which highlighted the importance of the nonlinear modeling of perturbation potential. However, pitch responses did not change at the same order. The authors compared the level 1 and level 4 calculations with and without the contributions of perturbation wave elevation for the relative motions and velocities. In either case the relative velocities were found to be more significant than the relative motions in simulations. They also noted that the body motions had a larger influence on the calculation of relative displacements and velocities than the η_D and η_I contributions. The authors noted that the accuracy of the numerical calculations did not always arise from level 1 to level 4 in order. They also pointed out that modeling of the problem using just the F-K nonlinear method might be not accurate enough. The authors concluded that the relative velocity has a larger influence in slamming calculations than the deck wetness due to the quadratic relative velocity component which appears in the slamming pressure.

Singh and Sen (2007e) modified their previous work to compare the effects of the level of modeling nonlinearities on the pressures and the vertical bending moments. They worked on a 240m tanker hull and on the S-175 containership in regular head seas using 3D panel method with transient wave Green functions. The main focus of their study was the relative comparison of pressures and vertical loads between four levels of nonlinear computations by assessing their variations with the increasing wave slope. The numerical calculations were performed for the tanker hull at Fn=0.2 and λ/L=1.0 where different modeling of nonlinearities did not change the variation of the VBM amidships significantly with respect to the increasing wave slope. However, in the time-history plot for the VBM amidships the asymmetry in the sagging and hogging was clearly observed, where level 2 calculation predicted the largest peak values among other nonlinearity levels for the sagging response. A double peak was observed in the level 2 calculation and the reason was attributed to the nonlinear hydrostatics. The level 3 calculations predicted the smallest VBM amplitudes among all other levels of computation. The authors compared the variation of pressures at the fore part of the ship with respect to the varying wave slope. The pressure amplitude in the level 2 formulation was predicted to be 25% larger than the one in the level 4 calculation. The next set of calculations was performed for the S-175 hull which has a significant geometric nonlinearity. The numerical calculations were performed for the S-175 hull at Fn=0.275 and λ/L=1.0 where VBM at the midship section showed an increase with the increase of wave slope in all levels of prediction except the stable linear calculation. At the fore section of the hull the positive and negative peak pressures were over-predicted by the level 2 computation where the level 3 method predicted the smallest values. Large discrepancies in the predicted pressure values between the level 1 & 2 and level 3 & 4 methods were attributed to the variation of perturbation potential in the level 3 & 4 calculations. The authors also noted the significant increase in the computational cost with the level 4 calculations which is nearly 20 times more than the level 2 calculations.

Kukkanen and Matusiak (2014) studied the motion and load responses on a 171 m roll-on roll-off passenger (RoPax) ship with the distribution of transient wave Green sources on 3D flat panels. Numerical calculations were compared with the conducted experiments at regular and irregular waves in head seas. The authors satisfied the exact BBC using the same approach as Lin and Yue (1991) and compared the results with the conducted experiments. They used a numerical method to solve the acceleration potential in Bernoulli’s equation. The acceleration potential method provided accurate and stable results for the motion and load responses. In order to lower the computational expense during the simulations, the memory part of transient Green function was interpolated during the simulations. The interpolation of the pre-calculated memory part of the Green function was based on FE formulation. The steady sinkage and steady VSF and VBM estimations were calculated for the

RoPax ship, in still water with varying forward speeds. The authors noted that the vertical loads and steady sinkage were increased with the increase in forward speed. In the body non-linear method heave and pitch motion responses were found to agree well with the experimental data. It was noted that in small amplitude incident wave, steady sinkage had a large contribution in the differences between the peaks of sagging and hogging bending moments. However, in large amplitude waves, the nonlinearities were found to originate from ship motions instead of the contribution of the steady bending moment. The authors also investigated the irregular wave responses at zero forward speed. The heave and pitch responses were estimated to be close to the experimental data. However, in the VSF and VBM calculations the numerical model over-estimated the model test results especially at the sagging position of the ship. The reason was attributed to the longitudinal mass distribution around the bow region.

2.3.3 Body-Exact (Weak-Scatter) Methods (Level 4)

The body-exact (weak-scatter) methods are an advanced version of the body-nonlinear methods where the radiation and diffraction potentials are solved on the exact wetted part of the hull based on the instantaneous position of the ship in a seaway. The body-exact methods are the most advanced methods that can be applied using the Eulerian formulation. In order to satisfy the FSBC, the perturbation potential has to be solved on the re-mapped panels under the mean surface level. Re-mapping of the instantaneous wetted panels under the mean sea level is performed by the subtraction of η_I from any point on the original panels. The difference between the level 3 and level 4 computations is due to the treatment of the free surface condition in the radiation potential. In the level 3 method the exact wetted body under the mean water level is taken into account while in the level 4 method the exact wetted body needs to be re-mapped under the mean water level. This method has a large computational cost due to the re-evaluation of the perturbation potential at each time step during the simulations. In this section, the former studies which made an important contribution to the motion and load responses on a rigid ship using the level 4 formulation are reviewed.

Pawlowski and Bass (1991) were the first researchers to study the weak scatter method. They used transient Green sources on 3D flat panels and compared their numerical results for the Series-60 hull and a trawler. The most important contribution of their work was the identification of the order of scattering waves as being small compared to the incident wave amplitude and ship motions.They noted that in steep waves second order wave forces should not be neglected because the scattering waves are proportional to the second order flow quantities. In order to solve the scattering wave problem, modal potential methods were used. In that method the flow disturbance was defined by modal velocity potentials which were evaluated in the time-domain simulations by using the pre-evaluated response and memory potentials. The authors provided the derivation of the weak scatter method explicitly. In the evaluated results, the Series-60 hull provided good agreement with the experimental data due to its simple geometry. However, for the trawler hull the results show large nonlinearities due to the large flare in the geometry.

Lin et al. (1994) modified their former approach in order to satisfy the perturbation potentials for the instantaneous wetted area under the wave profile. Their approach was based on the transient Green source distribution applied on 3D flat panels. They categorized the LAMP code into 4 levels with respect to discretization of the hull geometries and the levels of nonlinearity used in numerical calculations namely, LAMP-1 (Linear), LAMP-2 (F-K nonlinear), LAMP-3 (2.5D, F-K nonlinear), LAMP-4 (Body exact). All of the codes except the LAMP-3 code were developed based on 3D panels where the LAMP-3 code was based on the 2.5D strip theory and was developed for fast ships. The authors commented that when the wave amplitude is large compared to the ship draft, the accuracy of the level 3 method might be unsatisfactory due to the disturbance potential being modeled for the hull below the undisturbed free surface, especially on ships with transom sterns.Validation of the LAMP-1 code was performed on the Series-60 hull (C_b=0.7) and on the S-175 containership. The LAMP-1 code agreed well with the experiments in motion responses on the Series-60 hull. They also compared the LAMP-4 and LAMP-1 for the VBM responses at the midship section.The results were found to be close to each other while LAMP-4 showed an increase in the sagging bending moment at large amplitude waves. For the S-175 ship, they compared the numerical results of LAMP-2 and LAMP-4 codes with the experiments conducted by O'Dea et al. (1992) and the motion results showed the same trend as was observed in experiments whereas the heave motions were over-predicted in the LAMP-2 code. The reason for that was the implementation of ‘m-terms’ in the BBC where the uniform flow formulation was used. In the LAMP-4, the BBC was satisfied at the exact wetted portion of the hull so the m-terms were automatically calculated. However, pitch responses were estimated lower than the experimental values. In the VBM estimations at midship section, LAMP-4 predicted the sagging moment to be larger than the LAMP-1 approach and the hogging moment smaller than LAMP-1. Experimental data for the VBM estimation were not available to assess which method was more accurate.

Zhu and Katory (1998) studied the wave loading and motion responses for a catamaran advancing at a constant speed in oblique waves. They used the 3D transient Green source apporach to model the hydrodynamics of the ship in time-domain simulations. A total scattering potential was used to model the combined effect of radiation and diffraction forces which were satisfied at the instantaneous wetted area of the ship under waves. The numerical results were compared with the conducted experiments in small amplitude oblique waves. In general, vertical motions were found to be in good agreement with the experimental results. However, there was a large discrepancy in the transverse motions of the ship due to the lack of viscous damping forces and the lack of rudder forces. The authors could not investigate the efficiency of the code in large amplitude waves due to the lack of experimental data.

Huang and Sclavounos (1998) studied the weak-scatter method using a Rankine source distribution on 3D flat panels. They compared the linear time-domain method, F-K nonlinear method and the weak-scatter method with the conducted experimental data. The authors noted that there is no need to use m-terms in the weak-scatter method due to the automatically satisfied BBCs. They modified the Rankine source linear time-domain Ship Wave ANalysis (SWAN) code (Nakos and Sclavounos,

1991) for non-linear simulations in order to investigate the large amplitude motions in the seaway. They strictly reminded the reader that in this method the disturbances originating from the ship motions were small compared to the incoming waves and ship motions. In order to model the damping beach, a Newtonian type cooling term was implemented to the kinematic FSBC to damp out the waves of less than about twice the length of the numerical beach. They compared the heave and pitch reponses of the F-K nonlinear method, referred to as a quasi-non-linear method, with the linear methods on the Snow-Drift container ship and investigated the accuracy of the F-K nonlinear method against the linear method compared to the experiments. The discrepancies between the methods were mainly due to the nonlinear F-K and nonlinear restoring forces arising from their dominant behaviour over other remaining hydrodynamic forces. They compared the diagonal added mass and damping coefficients for the Series-60 hull with the weak scatterer and the linear methods and the experiments, but they did not observe significant differences in the values due to the wall-sided geometry. In motion responses for the Snow-Drift and S-175 hull weak-scatter method agreed well with the experimental data and showed a large difference between the level 2 and level 1 calculations especially in the pitch responses. This is due to fact that the nonlinear effects on the ship ends were more significant in pitch than heave motion. They concluded that the level 4 calculations vastly improved the results over the level 2 and level 1 methods in comparison with the experiments and the effect of the nonlinear perturbation forces were found to be large but not more than the influence of nonlinear F-K and restoring forces.

Ando (1999) studied the effects of large amplitude motion and load responses on a Canadian Patrol Frigate (CPF) using strip theory in time-domain and in regular head seas. Sectional added mass and damping coefficients were calculated with respect to the instantaneous draft of the section during the simulations. In order to derive sectional hydrodynamic coefficients, they made an approximation and used the ratio of instantaneous wetted sectional area to the wetted sectional beam. The motion equations were solved using the momentum equation on the body-fixed axis in order to take into account large pitch rotations. The numerical results of the CPF hull was compared with those from the frequency-domain code SHIPMO7 (McTaggart, 1996) and the conducted experiments at Fn=0.12, λ/L=1.01 and at Fn=0.20, λ/L=0.89. For the low speed calculations, nonlinear method agreed well with the experimental data , but when the speed increased, there was a large discrepancy at large amplitude waves in the heave motion. The reason for this was attributed to the lack of damping and green water on deck problems. Heave motion was over predicted for a wave steepness higher than $H/\lambda > 0.04$ and showed instability. The VSF at the station $L_{pp}/4$ from the forward perpendicular and the VBM at the the midship section were in a good agreement with the experiments. In all results, generally, the SHIPMO7 code over-predicted the motion and load responses.

Lin et al. (1999) studied the mixed-source formulation method for the estimation of time domain ship motion and load estimations in large amplitude waves. They used the advantage of the Rankine source method at the inner domain due to its better stability than the Green sources for geometries which have large flares. In the mixed-source formulation Green sources are only distributed on the fixed matching surface which removes the necessity of re-evaluation of the transient Green function while the underwater part of the geometry is changing in the numerical simulations. The authors noted that the mixed formulation was 40 times faster than the original transient Green source formulation where re-evaluation of the convolution integral is very time consuming. They implemented the mixed-source formulation into the LAMP system and compared the motion and load results with the original LAMP code and the conducted experiments. The navy ship AEGIS (CG-47) was used to assess the accuracy of their approach in large amplitude waves. In the LAMP-1 method the agreement between the the motion and experimental results were good but it under-predicted the sagging moment around the bow region. However, LAMP-2 and LAMP-4 agreed well with the motion and load responses even the frequency and the amplitude of the whipping response agreed well with the experiemental data. The authors concluded that the hydrostatic and the incident loads dominated the vertical load estimations in large amplitude simulations.

Weems et al. (2000) modified their former study and implemented the 2nd order FSBC condition on a portion of the free-surface using mixed-source formulation. In order to maintain the accuracy of the FSBC a matching surface was placed further away from the body and that caused more computational time. The authors found good agreement between the motion and load responses and the experimental data, but the influence of the second order FSBC condition was not found to be significant.

Kim et al. (2011) developed a code named Wave-Induced loads and SHip motion (WISH) in order to assess nonlinear behaviour of motion and load responses in large amplitude waves. The WISH code was based on Rankine sources and solved hydrodynamic problems in the time-domain. The code has three different modules inside it corresponding to the level of nonlineraties implemented in the BVP solutions. They are named as WISH-1 (linear method), WISH-2 (F-K nonlinear method) and WISH-4 (Weak Scatter method) where the level of nonlinearities were increasing in order. The numerical results were compared with the experiments performed by O'Dea et al. (1992). In general, the weak-scatter and weakly-nonlinear methods followed the trends of the experiments. They also noted that weak-scatter did not always provide the best results. In large amplitude wave simulations at Fn=0.20 weakly-nonlinear method had closer results than the weak-scatter method compared to the experimental data. They also concluded that Rankine panels methods can model the most important nonlinearities even the strong memory effects and are more advantageous compared to the costly CFD methods in large amplitude motion simulations.

Liu and Papanikolaou (2012) studied the mixed-source formulation in order to assess nonlinear motion and load behaviours on floating structures. In small amplitude numerical solutions heave response was over-predicted due to the influence of m_j-term contribution. In large amplitude waves heave motion response got closer to the experimental data. A shift was observed around the resonant region in heave and pitch motions which was attributed to the uniform steady-flow approximation which was implemented in the m_j-term calculations. In general, the authors found close results compared to the experiments and the responses were followed the experimental trends.

2.4 Rigid and Elastic Ship Experimental Studies

Experimental measurements play an important role in the validation of numerical motion and load predictions and in the investigation of physical phenomenon in large amplitude waves. In this section, due to the content of the thesis, conducted experimental studies on the S-175 containership are reviewed and important factors are highlighted in detail.

Watanabe et al. (1989) studied the vertical loads and the deck wetness problem on the S-175 containership with the original and modified hull with an increase in the bow flare above the waterline. Both of the models were made with synthetic resin and foam urethane to simulate elastic motion of the hull in a seaway. Model tests were performed at Fn=0.25 for regular and irregular head seas on a self-propelled model. In the results part the original and modified hull models were named as O-model and M-model respectively. In the pitch motion responses, flare of the hull did not change the responses to a very great extent compared to the original hull. The vertical accelerations at the Fore Peak (FP) of the O-model were estimated higher than the M-model. The relative accelerations at the FP varied significantly due to the flare of the hull. The reason for the difference was attributed to the wave deformation caused by the flare form since there was not any significant difference observed in the pitch motions. They also measured the pressures at the FP on the deck and the impact pressure at the bottom centerline of the 9 ½ section. The M-model showed higher pressure at the stem and lower pressure on the deck due to the flare angle. In the forward section bending moment measurements, the M-model experienced more nonlinear behavior than the O-model and sagging moments amidships was measured to be larger than the hogging moments. The M-model experienced larger 2nd order harmonics compared to the O-model due to the nonlinear interaction of the hull bow flare with the wave elevation. The results gave an important insight into the effect of the bow flares, but the authors did not provide sufficient experimental data to investigate the influence of the wave steepness on the motion and vertical load responses.

O'Dea et al. (1992) were the first authors to investigate the first order vertical motion amplitudes and phase angles with varying wave slopes. The authors also conducted experiments in order to investigate the effects of the second and third order motion and acceleration harmonics in large amplitude waves. Experiments were conducted for the towed S-175 container model in regular and irregular head seas with two forward speed cases at Fn=0.20 and Fn=0.275 around the resonance frequency ranges. The model was assumed to be rigid in all conducted experimental tests. They used 3rd order Stokes waves approximation in order to model the incoming wave field. In the heave and pitch responses, the variation of motion response amplitudes with respect to the wave steepness was given by the ratio of the first order response to the first order wave amplitude. Heave and pitch motion response amplitudes increased with the increase in the forward speed. In contrast, the motion response amplitudes decreased with the increasing wave steepness. The heave response showed higher decrease compared to the pitch responses with the increase in the wave steepness. The authors, who investigated the second and third order harmonics, found that their magnitude is only %2-3 of the first harmonics. They also noted that the bow accelerations experienced second and third order harmonics more significantly than the motion responses. The reason this is that the accelerations are the second derivatives of the displacements where the displacement harmonics are multiplied with ω^2, $4\omega^4$ and $9\omega^2$ for the first, second and third harmonics respectively. They noted that the second and third harmonics of the vertical acceleration at the bow were by 20% and 8% larger than the first harmonics respectively.

Fonseca and Soares (2004) conducted the most categorized and detailed experiment in large amplitude motions in order to investigate the ship motion and load responses. Experimental analysis of the S-175 containership was conducted at a forward speed Fn=0.25 in head regular waves. A towing carriage was used to conduct the experiments and the ship was assumed to be a rigid body. They investigated the impact of wave steepness on the motion responses, higher harmonic amplitudes with respect to the wave steepness, the VSF and VBM estimations with respect to the wave steepness and the influence of steady structural loads. In order to investigate the nonlinear characteristics of vertical responses, the experiments were conducted for a wide range of wavelengths from $0.4L_{pp}$ to $2.8L_{pp}$ in various wave amplitudes. In order to investigate the influence of wave steepness in large amplitude waves, tests were performed at three wavelengths around the resonant area corresponding to the wavelengths $\lambda/L=1.0$, $\lambda/L=1.2$ and $\lambda/L=1.4$. Still water towing tests were performed in order to investigate the influence of steady sinkage, trim and steady wave loads. It was noted that in small wave amplitudes the asymmetry in the vertical loads originated from the steady vertical loads while in large amplitude waves the asymmetry was dominated by the unsteady motions. The authors noted that the steady results should not be neglected in the motion and load responses. In heave and pitch response functions, with the increase of the wave steepness vertical motion responses were reduced around the resonance frequency. In the case of phase angles, heave phase angles increased by a small amount with the increasing wave slope but the pitch angles showed an opposite trend. In motion responses, higher order harmonics were found to be of a small order compared to the first harmonics. In nonlinear responses ships tended to emerge in heave motion and tended to raise their bow more in pitch motion. In the vertical load responses, nonlinear behavior was observed to be more significant than the motion responses. They observed an asymmetry in the VSF responses especially in large amplitude waves and the reason for that was due to the ship bow flare which was prone to nonlinear impulsive forces. The magnitude of positive peaks (sagging) was found to be larger than the negative (hogging) peaks at station 15 (1/4 L_{pp} from FP). The VBM responses were investigated at the midship section and at station 15. At the midship section the magnitude of the VBM was larger than at station 15. However, at the midship section, increasing wave steepness did not change the trend of the VBM which showed nearly a linear trend. At station 15, nonlinearities in the VBM were more significant where with the increasing wave slope the VBM was increased nearly four times compared to the magnitude in the small wave slopes. The second harmonics of the VBM at station 15 was also more significant than the second harmonics observed at midship section.

In the next sections of this thesis, the validation of the numerical results in small and large amplitude waves will be performed using the experimental results obtained from the study of Fonseca and Soares (2004) due to the provided comprehensive data source. Effects of wave steepness on the motion and load responses in large amplitude waves will be investigated and compared with the experimental data in detail.

Present thesis provides the comprehensive effects of large amplitude waves in motion and load responses taking into account the forward speed. Formerly, researchers solved large amplitude ship responses using IRF formulation up to the level 2 nonlinearity. Current study is the development over the IRF formulation and calculates the nonlinear ship responses using body nonlinear (level 3) approach and fills the gap in the literature providing the insight of the importance of nonlinear radiation and diffraction forces during the nonlinear simulations.

Chapter 3

Theoretical Background for Motions and Loads

3.1 Coordinate Systems

In order to evaluate the motions of a vessel in large amplitude waves three coordinate systems are defined; namely the inertial Earth-fixed frame ($X_eY_eZ_e$), the inertial hydrodynamic frame ($X_hY_hZ_h$) and the non-inertial body-fixed frame ($X_bY_bZ_b$). In linear theory, the body oscillates with small motion amplitudes compared to its dimensions where the hydrodynamic forces are solved in an inertial hydrodynamic reference frame that travels with a constant speed and heading on the course of the ship. In large amplitude waves, in order to evaluate the actual position of the ship, different reference systems need to be introduced. Transformations between the coordinate systems are applied to describe forces and moments in different reference frames.

In the large amplitude motion simulations three right-handed coordinate systems exist and are illustrated in Figure 3.1. A summary of the coordinate system properties can be given as:

- **$X_eY_eZ_e$:** the inertial earth-fixed frame (e-frame). The frame has zero speed. The Z_e axis points vertically upwards and the X_e axis points towards the initial (constant) heading of the vessel. The frame origin is located on the calm water plane.
- **$X_hY_hZ_h$**: the inertial hydrodynamic frame (h-frame). The frame origin translates with a constant velocity and constant heading as the ship advances and lies on the undisturbed free surface. The Z_h axis points vertically upwards and passes through the Centre of Gravity (COG of

the ship and the X_h axis points in the direction in which the ship is heading.

- **$X_bY_bZ_b$**: the non-inertial body-fixed frame (b-frame). The Z_b axis points vertically upwards at the initial time of the analysis while the X_b axis points towards the bow of the ship. In order to simplify the motion equations, the COG is selected as the reference point where the frame rotates and accelerates with respect to the $X_hY_hZ_h$ frame on the ship's course.

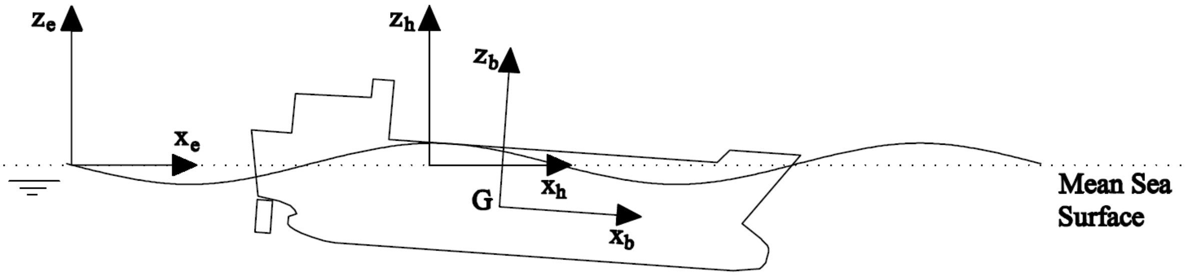

Figure 3.1: Coordinate systems

The motion equations are described in the $X_hY_hZ_h$ frame within the LARes code. The inertia matrix of the ship can be assumed to be constant in time if the ship has small motion amplitudes. In large amplitude vertical motions the pitch angle is usually smaller than 8-10 degrees. Therefore, forces and moments can be represented on the $X_hY_hZ_h$ axis and the equations can be solved using the same system unless the pitch angle is more than 8-10 degrees (Fonseca and Soares, 1998). However, in large amplitude motions, the accurate way of solving the non-linear motion equations is first to solve the ship accelerations on a body fixed frame, then transform them to an inertial frame and integrate by means of Runge-Kutta (R-K) equations. Ship accelerations must be integrated in an inertial frame in order to eliminate the artificial Coriolis and centripetal forces occur in a body-fixed frame. This approach is valid for any arbitrary large motions due to the fact that the mass and the inertia matrix remains constant in time only on the body-fixed axis (Sen, 2002). In the PRETTI code (Van't Veer et al., 2009), all forces calculated in the hydrodynamic frame are translated and rotated to the body-fixed axis in order to solve the resultant accelerations. After the derivation of the accelerations in the body fixed reference frame, transformations are applied and they are integrated to derive the instantaneous velocity and displacement of the ship with respect to the Earth-fixed frame.

Transformations between different reference frames are performed using Euler angles. Euler angles require a fixed order of rotation in which yaw-pitch-roll rotations are adopted in the following formulas. The rotation matrix **T** is used to relate the translational coordinates of the body with respect to the body-fixed frame to the hydrodynamic frame. The **T** matrix has orthogonality, therefore; the inverse of the **T** matrix is equal to the transpose of it. The $\mathbf{T}_\theta$ matrix relates the rotational velocities between the body-fixed frame and the hydrodynamic frame**.** The $\mathbf{T}_\theta$ matrix does not have ortogonality, therefore; the inverse of the matrix does not equal the transpose of itself. Body-fixed axis coordinates and velocities are described in the hydrodynamic frame axis with the following relations (Fossen, 1994) :

$$\overrightarrow{r_e} = T_e^b . \overrightarrow{r_b} \quad \overrightarrow{\dot{\theta}} = T_\theta \vec{\omega} \tag{3.1}$$

$$T = \begin{bmatrix} cos\varphi cos\theta & -sin\varphi cos\phi + cos\varphi sin\theta sin\phi & sin\varphi sin\phi + cos\varphi sin\theta cos\phi \\ sin\varphi cos\theta & cos\varphi cos\phi + sin\varphi sin\theta sin\phi & -cos\varphi sin\phi + sin\varphi sin\theta cos\phi \\ -sin\theta & cos\theta sin\phi & cos\theta cos\phi \end{bmatrix} \tag{3.2}$$

$$T_\theta = \begin{bmatrix} 1 & sin\phi tan\theta & cos\phi tan\theta \\ 0 & cos\phi & -sin\phi \\ 0 & sin\phi/cos\theta & cos\phi/cos\theta \end{bmatrix} \tag{3.3}$$

where the ϕ, θ and φ denote roll, pitch and yaw angles respectively with respect to the hydrodynamic frame. The $\overrightarrow{r_b}$ and $\vec{\omega}$ stand for the displacement and rotational velocity vectors in the body-fixed frame while $\overrightarrow{r_e}$ stands for the displacement vector in the hydrodynamic frame axis.

3.2 General Description of the Frequency-Domain Boundary Value Problem

This section describes the derivation of hydrodynamic forces and coefficients in the frequency domain simulations in detail. In the current study, the approach for solving time domain motion responses is dependent on the frequency domain linear hydrodynamic forces and coefficients which are evaluated using the PRECAL software in 6 degrees of freedom (DOF). In potential flow theory, the fluid properties are determined as incompressible, inviscid and the flow is assumed to be irrotational. Moreover, in the frequency domain simulations the motions are assumed to be harmonic and small compared to the ship dimensions. In these conditions the time-dependent total velocity potential can be expressed in the following form (Van't Veer, 2009):

$$\Phi_T(x,y,z;t) = U[\overline{\phi}_s(x,y,z) - x] + \phi_u(x,y,z)e^{-i\omega_e t} \tag{3.4}$$

where, $U[\overline{\phi}_s(x,y,z) - x]$ is the time-independent total steady wave potential due to the ship resistance problem, $\overline{\phi}_s$ is the steady perturbation potential due to the presence of the ship in the wave field, ϕ_u is the complex amplitude of the unsteady motion of the ship and the ω_e is the encounter frequency. In linear theory, the complex amplitude of the unsteady potential is decomposed into three components:

$$\phi_u(x,y,z) = \phi_I(x,y,z) + \phi_D(x,y,z) + \sum_{j=1}^{6} \xi_j \phi_j \qquad \text{j=1,2,….6} \tag{3.5}$$

where ϕ_I, ϕ_D and ϕ_j are the potentials corresponding to the incident wave, diffraction and radiation potentials due to the j$^{\text{th}}$ mode of the unit amplitude ship oscillation in six degrees of freedom where j=1,2,….6 refer to surge, sway, heave, roll, pitch and yaw respectively. The incident wave potential and the incident wave elevation (ζ) are given as:

$$\phi_I(x,y,z)e^{-i\omega_e t} = \frac{-ig\zeta_a}{\omega_0} e^{k_0 z} e^{i(k_0 x cos\beta + k_0 y sin\beta)} e^{-i\omega_e t}$$

$$\zeta = \zeta_a e^{i(k_0 x cos\beta + k_0 y sin\beta - \omega_e t)} \tag{3.6}$$

where ζ_a is the incident wave amplitude, ω_0 is the incident wave frequency, $k_0 = (\omega_0^2/g)$ is the wave number in infinite depth seas and $\omega_e = \omega_0 - kU\cos\beta$ is the encounter frequency of the ship in the moving reference frame with a constant forward speed of U, g is the gravitational acceleration and β is the wave angle.

In order to solve the Boundary Value Problem (BVP), the total velocity potential and its components need to be satisfied for the boundary conditions in the fluid domain, in the Free-Surface Boundary Condition (FSBC) and in the Body Boundary Condition (BBC) as follows:

a. Laplace equation

$$\nabla^2 \Phi_T = 0 \qquad \text{in the fluid domain} \tag{3.7}$$

b. Linearized FSBC

$$\begin{aligned} &U^2 \frac{\partial^2}{\partial x^2}\overline{\phi}_s + g\frac{\partial}{\partial z}\overline{\phi}_s = 0 \\ &\left(i\omega_e + U\frac{\partial}{\partial x}\right)^2 \phi_u + g\frac{\partial}{\partial z}\phi_u = 0 \end{aligned} \qquad \text{on z=0} \tag{3.8}$$

c. Linearized BBC

$$\begin{aligned} &\frac{\partial}{\partial n}(\overline{\phi}_s - x) = 0 \\ &\frac{\partial}{\partial n}(\phi_I - \phi_D) = 0 \\ &\frac{\partial}{\partial n}\phi_j = -i\omega_e n_j + Um_j \end{aligned} \qquad \begin{aligned} &\text{on the mean hull surface} \\ &\text{j=1,2,....6} \end{aligned} \tag{3.9}$$

In the BVP problem the Laplace equation maintains the continuity in the fluid domain whilst the second equation of the linearized FSBC satisfies the fluid velocity equivalence between the unsteady wave and the free surface itself and equates the wave pressure to the zero ambient pressure. The unsteady velocity potential satisfying the FSBC is that of a translating and pulsating source and when the forward speed U is zero it reduces to the speed independent pulsating source. The second equation of the linearized BBC corresponds to the diffracted incident waves due to presence of the ship and the condition is satisfied with the impermeability condition of the fluid inside the hull boundary. The third equation of the BBC corresponds to the linearized radiation condition on the hull boundary. Besides the above boundary conditions, the unsteady potential needs to satisfy the radiation condition at infinity and the rigid wall condition at the sea bottom. In the radiation condition of the BBC, $(n_1, n_2, n_3) = \vec{n}$ denotes the outward unit normal vector and $(n_4, n_5, n_6) = \vec{r} \times \vec{n}$ denotes the moment of the unit normal vector with respect to the origin of the reference frame. The m-terms (Ogilvie and Tuck, 1969) are defined as the gradients of steady velocities in the normal directions which are given as:

$$
\begin{aligned}
(m_1, m_2, m_3) &= -(\vec{n} \cdot \nabla)\nabla(\bar{\phi}_s - x) \\
(m_4, m_5, m_6) &= -(\vec{n} \cdot \nabla)[\vec{r} \times \nabla(\bar{\phi}_s - x)]
\end{aligned}
\tag{3.10}
$$

The derivation of the m-terms in the BBC includes complex second order derivatives therefore in many seakeeping codes the steady wave flow pattern caused by the advancing ship is neglected via the slender ship assumption. The steady flow perturbation potential $\bar{\phi}_s$ is taken to be zero in the uniform base flow approach. In PRECAL, by default the uniform base flow is used however, the Double Body (D-B) flow approach can be used as well. In the D-B flow approach the flow around the vessel is reflected with respect to the calm free surface level. Diagrams showing the uniform base flow and the D-B flow approaches are presented below in Figure 3.2:

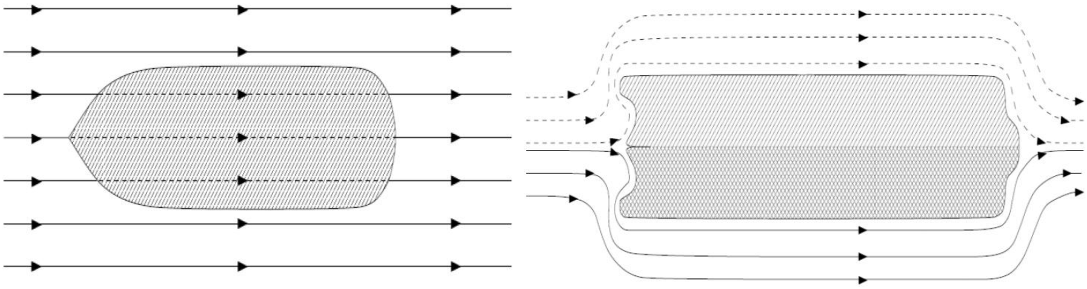

Figure 3.2: Uniform base flow (left) and D-B flow (right) (Bunnik, 1999)

The total steady flow potential is approximated to be -Ux when the uniform base flow model is used and the m-terms are reduced to:

$$
\begin{aligned}
(m_1, m_2, m_3) &= -(\vec{n} \cdot \nabla)\nabla(U, 0,0) = (0,0,0) \\
(m_4, m_5, m_6) &= -(\vec{n} \cdot \nabla)[\vec{r} \times \nabla(U, 0,0)] = (0, -\mathrm{U}n_3, \mathrm{U}n_2)
\end{aligned}
\tag{3.11}
$$

The D-B approach provides a more realistic approach for modelling the steady wave potential. In the D-B flow approach $\bar{\phi}_s$ satisfies the FSBC and BBC condition via

Equation (3.12) in which the first equation satisfies the zero normal velocity condition on the free surface and the second one satisfies the impermeability condition on the body surface. Unlike the uniform base flow approach, the D-B flow approach has a no-flux condition which is satisfied on the ship hull, but due to the absence of the free surface, waves are not generated (Bunnik, 1999).

$$\begin{aligned} &\frac{\partial}{\partial n}(\bar{\Phi}_s)=0 &&\text{On the mean hull surface} \\ &\frac{\partial}{\partial n}(-Ux-\bar{\Phi}_s)=0 &&z=0 \end{aligned} \tag{3.12}$$

On the contrary, the D-B flow is only valid for low forward speeds and, at high forward speeds one needs to solve the steady perturbation potential first and then use the generated steady wave field in the BBC for the solution of the unsteady motion problem. The uniform base flow and D-B flow approaches are compared with the experiments in Figure 3.3 for the S-175 containership at Fn=0.25 using the Approximate Forward Speed (AFS) method in PRECAL software. The results are found as expected in that the D-B flow approach calculated higher values than the uniform base flow approach due to the high forward speed effect. Previously, it was mentioned that for fast ships the steady perturbation potential needs to be solved for the resistance problem otherwise the errors in the motion responses increase. The reason for this is that the m-terms are in linear proportion with the forward speed. Therefore, the error in the motion responses due to the m-terms contribution is high in blunt and/or fast ships and the steady perturbation potential needs to be solved in order to investigate the steady-unsteady wave interaction on the ship's course.

Following the solution of the linear BVP and the evaluation of all potential components, the total hydrodynamic pressure on the body surface can be evaluated using Bernoulli's equation which is defined as

$$P=-\rho\left(\frac{\partial\Phi_T}{\partial t}+\frac{1}{2}|\nabla\Phi_T|^2+gz\right) \tag{3.13}$$

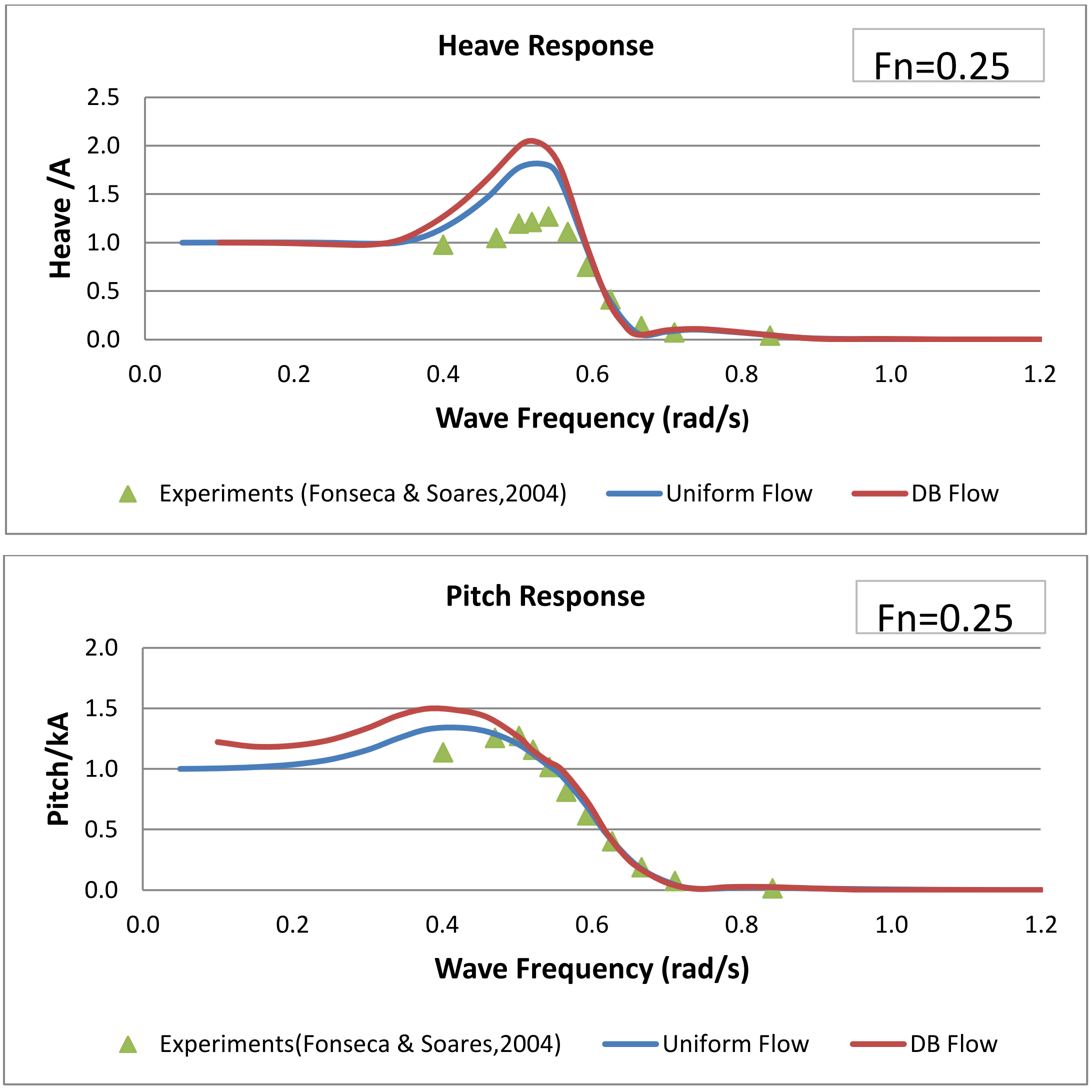

Figure 3.3: Uniform base flow (top) and D-B flow (bottom) comparison for heave and pitch responses at Fn=0.25

When the total velocity potential is inserted into the hydrodynamic pressure equation it leads to

$$P = -\rho\left\{[-i\omega_e\phi_u + U\nabla(\overline{\phi}_s - \mathrm{x})\cdot\nabla\phi_u]e^{-i\omega_e t} + \frac{1}{2}\left(\nabla\phi_u e^{-i\omega_e t}\right)^2 \right. \\ \left. + \frac{1}{2}U^2[\nabla(\overline{\phi}_s - \mathrm{x})]^2 + gz\right\} \tag{3.14}$$

where the last term is associated with the hydrostatic buoyancy force contribution while the squared steady wave component is associated with the wave making resistance and the lift and force components with the time factor $e^{-i\omega_e t}$ correspond to the unsteady force. In order to simplify the problem, higher order terms and the cross products of the steady and unsteady velocity potentials are disregarded and unsteady hydrodynamic pressure is reduced to:

$$P = -\rho\left\{-i\omega_e - U\frac{\partial}{\partial x}\right\}\phi_u e^{-i\omega_e t} \tag{3.15}$$

The total oscillatory hydrodynamic force and moment amplitudes in the jth direction are derived by the integration of the oscillatory pressure on the hull surface, ignoring the time factor $e^{-i\omega_e t}$:

$$F_j = -\iint_S P n_j dS = -\rho\iint_S \left\{i\omega_e + U\frac{\partial}{\partial x}\right\}\phi_u n_j dS \qquad \text{j=1,2,….6} \tag{3.16}$$

In order to express the total oscillatory force in terms of the speed independent force components, Stoke's theorem is applied to the second term in the integrand of the above equation and the total oscillatory force is expressed as:

$$\iint_S U\frac{\partial\phi_u}{\partial x} n_j dS = U\iint_S m_j\phi_u dS - U\int_{C_o} \phi_u dl \times \nabla(\bar{\phi}_s - x)$$

$$\text{j=1,2,….6} \tag{3.17}$$

$$F_j = -\rho\iint_S \left(i\omega_e n_j + U m_j\right)\phi_u dS + \rho U\int_{C_o} \phi_u dl \times \nabla(\bar{\phi}_s - x)$$

The second term appearing in the total oscillatory force is the line integration in which C_o is the intersection between the body surface and the mean free surface and S is the mean wetted surface of the ship under the still water line.

The total oscillatory forces and moments consist of the incident wave, diffraction and radiation force components which are derived in Equation (3.18). The added mass and damping coefficients are the real and imaginary components of the motion induced hydrodynamic forces and moments which originate from the radiation forces. The radiation force and moment in the jth direction due to a unit amplitude motion in the kth direction and the resulting added mass and damping coefficients are given in order as:

$$F_{j,I} = -\rho \iint_S \left\{ i\omega_e + U\frac{\partial}{\partial x} \right\} \phi_I n_j dS$$

$$F_{j,D} = -\rho \iint_S \left\{ i\omega_e + U\frac{\partial}{\partial x} \right\} \phi_D n_j dS \qquad \text{j,k=1,2,….6} \qquad (3.18)$$

$$F_{j,R} = -\rho \iint_S \left\{ i\omega_e + U\frac{\partial}{\partial x} \right\} \phi_{R,k} n_j dS = \omega_e^2 A_{jk} + i\omega_e B_{jk}$$

Finally, after the derivation of all force components and hydrodynamic coefficients the system of motion equation is solved using Newton’s equation where:

$$\left[M_{jk}^h + A_{jk}^h(\omega_e)\right] \cdot \ddot{\xi}_k + B^h(\omega_e) \cdot \dot{\xi}_k + C^h \cdot \xi_k = \left(F_j^I(\omega_e) + F_j^D(\omega_e)\right) \Re\left\{e^{-i\omega_e t}\right\} \qquad (3.19)$$

where M^h is the mass and inertia matrix, A^h and B^h are the frequency dependent added mass and damping matrices, C^h is the linear restoring matrix, $\vec{F}^I$ and $\vec{F}^D$ are the frequency dependent incident wave and diffraction force matrices.

As long as the motions are harmonic the total response of the vessel can be described as:

$$\vec{\xi} = \vec{\xi}_a \Re\left\{e^{-i\omega_e t}\right\} \qquad (3.20)$$

where $\vec{\xi}_a$ is the complex response amplitude of the system. In order to describe motion equations in the frequency domain, excitation forces need to be used in the complex amplitudes, and finally the equation of motion is described as:

$$\left\{-\omega_e^2 \left(M_{jk}^h + A_{jk}^h(\omega_e)\right) - i\omega_e B_{jk}^h(\omega_e) + C_{jk}^h\right\} \vec{\xi}_a = \vec{F}_j^I(\omega_e) + \vec{F}_j^D(\omega_e) \qquad (3.21)$$

An important property of the frequency-domain seakeeping calculation is that the system of motion equations is valid only for small and harmonic motions and in order to evaluate large amplitude responses one needs to use time-domain motion equations.

In frequency domain seakeeping calculations so-called irregular frequencies appear at some resonant frequencies. Irregular frequencies cause large fluctuations in the damping coefficients which are affecting the accuracy of the memory functions in a negative way. Smoothness of the damping coefficients is crucial for the accurate derivation of memory functions in time-domain responses. At irregular frequencies the BVP solution either does not have a solution or the solution exists but it is not unique (Lee and Sclavounos, 1989). In order to alleviate the irregular frequencies, the interior free surface of the body is enclosed by panels at the free-surface level and this solution method is called as the “Lid Panel Method”. The mean water plane area panels at the free-surface level and the mean wetted body surface panels are solved with a modified boundary integral equation. The PRECAL code uses a modified version of the ‘Lee & Sclavounos’ (Lee and Sclavounos, 1989) approach in order to solve the BVP. Unfortunately, in PRECAL software, the Lid Panel Method can only be applied using the zero-speed Green source formulation in the BVP solutions.

Another important problem which occurs in frequency domain response calculations is the derivation of the infinite added mass and infinite damping coefficients. Accurate calculation of infinite added mass and damping values is crucial for the time-domain motion and load responses as well as the slamming calculations. It is also possible in PRECAL to solve the BVP for high frequencies due to the removal of irregular frequencies up to a limit, but a very fine mesh distribution has to be used which results in a long computational time. This approach is impractical and also generally impossible due to limited computer resources. The memory requirements increase quadratically with the increase in the number of the hull panels and that has a consequence of needing computer systems with large memories. That means even if the memory of the system is doubled, the maximum encounter frequency which can be accurately calculated will not double and in reality will be much less than this ratio. In the frequency-domain calculations the limit for the maximum encountering frequency is directly related to the characteristic length of the panels. In PRECAL, in order to simulate the wave patterns, there must be at least 5 panels corresponding to the smallest encountering wave length and the relationship between the maximum encountering frequency and the panel length is given as (Van't Veer, 2009):

$$\omega_{e,max} \cong \sqrt{\frac{2\pi g}{5 \cdot panel\ length}} \cong 3.5/\sqrt{panel\ length} \tag{3.22}$$

In PRECAL the infinite added mass is calculated with a modified frequency independent Green's function in which the unsteady wave potential is set to $\phi_u = 0$. In order to solve the BVP for the infinite frequency, the frequency dependency in the FSBC and the BBC is also removed.

The solution of the frequency-domain BVP for a forward speed case is a very daunting task. In frequency-domain forward speed seakeeping calculations, the calculation of the Green's function which satisfies the exact linearized FSBC in Equation (3.8) is numerically difficult due to highly oscillatory derivatives included in the equations. The Green's function satisfying the exact linearized FSBC has two contour integration parts and both of the contours have two singularities which are hard to integrate accurately due to numerical instabilities. In order to take into account the forward speed effects in the solution of BVP, PRECAL utilizes two types of Green sources which satisfy the exact forward speed and simplified forward speed cases. The Exact Forward Speed (EFS) method follows the Green's function derived by Wehausen and Laitone (1960) and applies it to the BVP solutions using the numerical method provided by Ba and Guilbaud (1995). However, the double integrals appearing in the exact FSBC Green's function are time consuming to evaluate in numerical calculations and in general cause numerical instabilities due to the highly oscillatory nature of the imaginary argument of the exponential functions (Ba and Guilbaud, 1995). The deficiencies in using the EFS method are eliminated using the AFS formulation. In this approximate method, the speed term in the FSBC is neglected assuming the frequency of the oscillation is high and the mean forward speed is low. After the elimination of the higher order terms in the Equation (3.8) the simplified FSBC reduces to:

$$-\omega_e{}^2\phi_u + g\frac{\partial}{\partial z}\phi_u = 0 \qquad \text{on z=0} \tag{3.23}$$

This formulation is known as zero speed FSBC which most of the strip theory and 3D panel models use due to its easier evaluation properties compared to the exact

FSBC condition. In the AFS formulation the forward speed influence is accounted for the forward speed correction terms appearing in the hydrodynamic pressure Equation (3.15), in the body boundary conditions and in the contour integration of the hydrodynamic total force calculation in Equation (3.17). The comparison of the heave motion responses and the heave damping coefficients for the S-175 containership is shown in Figure 3.4 and Figure 3.5 respectively. It is clearly observed from the Figure 3.4 that around the resonant region EFS method predicted closer results to the experimental data compared to the AFS method. However, the damping coefficients obtained using the EFS method are very unstable which is caused by numerical instability problems. The damping coefficients obtained from the EFS solution of the BVP cannot be used to derive memory functions because irregular frequencies in the damping coefficients cause fluctuations in memory functions and this result in inaccurate damping forces in time domain simulations.

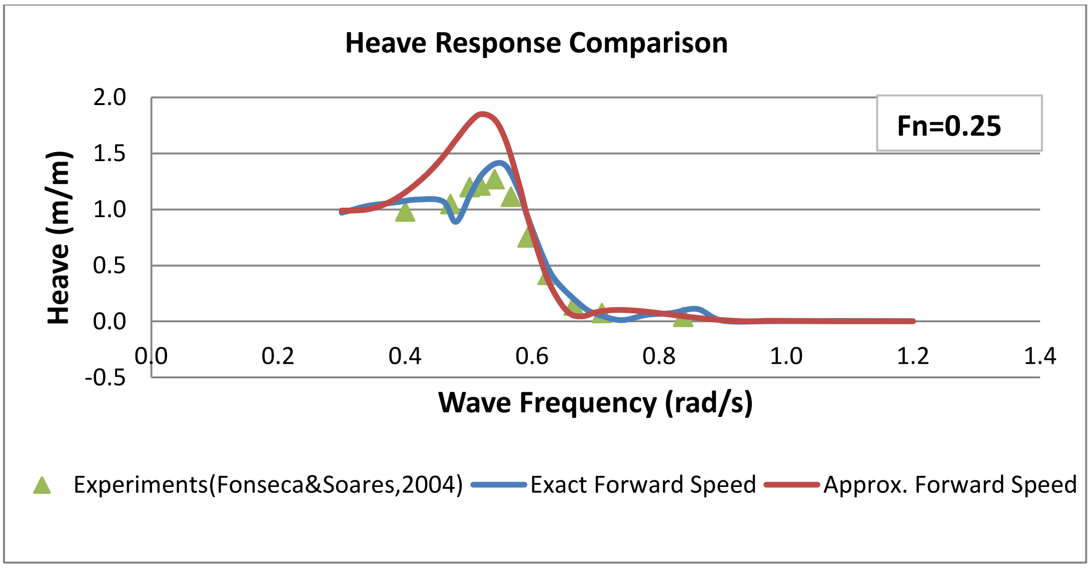

Figure 3.4: Comparison of the heave response for the Exact Forward Speed and Approximate Forward Speed formulations

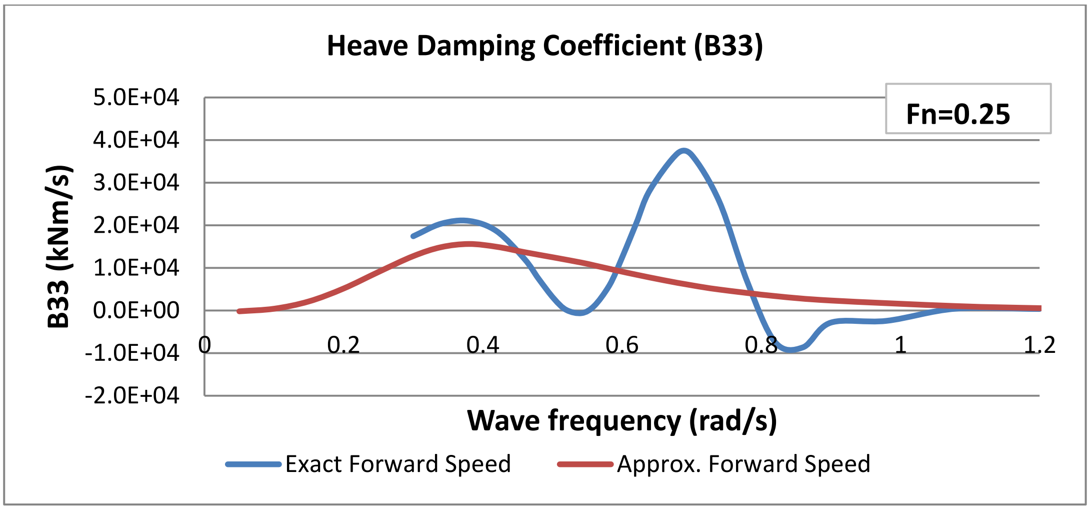

Figure 3.5: Comparison of heave diagonal damping coefficients for the Exact Forward Speed and Approximate Forward Speed formulations

In the next section, the details of the time-domain seakeeping problem will be explained where the hydrodynamic data is pre-calculated using the frequency-domain BVP problem. The numerical stability and the smoothness of the damping curve which is evaluated in the BVP have a crucial importance in time-domain motion calculations. Therefore, in this thesis, in motion and load response calculations the uniform base flow approach is used with the AFS formulation due to the reasons listed below:

- AFS calculations are more stable and take much less time compared to the EFS calculations. In complex non-vertical walled geometries, it is very hard to satisfy the smoothness of the damping curves using the EFS method.
- In PRECAL, the suppression of the irregular frequencies using the “Lid Panel Method” is only available with the zero speed Green’s functions.
- The uniform base flow model is faster than the DB flow model in numerical calculations and for the case of the S-175 container ship, the uniform flow calculations provided closer results than those were obtained from the DB flow approach when compared to the experiments.

3.2.1 Internal Loads in the Frequency Domain Approach

Internal loads at a ship's cross section arise from the difference between the total inertial force and the total hydrodynamic force on the portion of the ship forward of the defined cross section. In order to calculate vertical load responses, sectional mass distribution and the sectional hydrodynamic forces are integrated from the bow position to the defined cross section. In essence, when the ship is divided into parts from the defined cross section, the Vertical Shear Force (VSF) and Vertical Bending Moment (VBM) balance the sum of the forces and moments applied to the ship portion forward of the defined cross section respectively. The VSF and VBM are defined by:

$$V_3 = I_3 - R_3 - D_3 - FK_3 - H_3 \tag{3.24}$$

$$M_5 = I_5 - R_5 - D_5 - FK_5 - H_5 \tag{3.25}$$

where the indices k=3,5 are the forces and moments in heave and pitch motion modes respectively applied to the ship on its course. In Equations (3.24) and (3.25), I_k is the inertial force or moment of the ship's mass distribution forward of the defined cross section while R_k, D_k, FK_k and H_k are the radiation, diffraction, Froude-Krylov (F-K) and restoring forces respectively calculated at the mean position of the ship using the panels forward of the cross section. The sign convention for the vertical loads is defined in the sagging position as positive for the VSF and as negative for the VBM. The sign convention for the vertical loads is illustrated below:

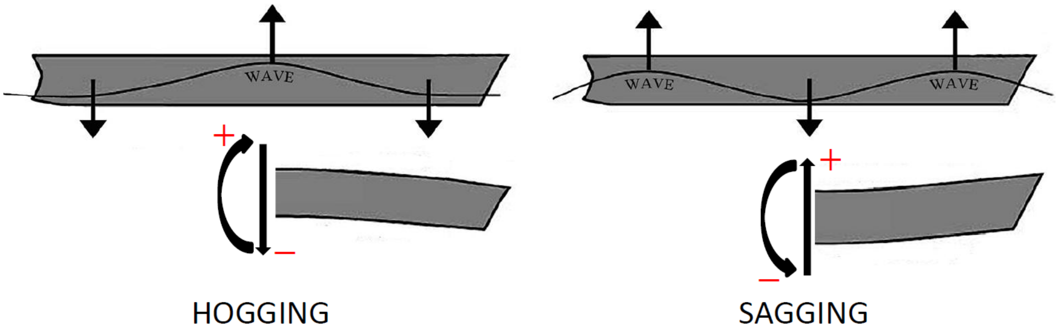

Figure 3.6: Sign convention for the hogging and sagging positions

The inertial forces and moments are calculated by integration of the products of the sectional mass distribution and the global accelerations from the cross section at position x^* to the bow section. The sectional ship inertial forces and moments are given by:

$$I_3^* = \int_{x^*}^{Bow} m(x)(\ddot{\xi}_3 - x\ddot{\xi}_5)\, dx \tag{3.26}$$

$$I_5^* = -\int_{x^*}^{Bow} m(x - x^*)(\ddot{\xi}_3 - x\ddot{\xi}_5)\, dx \tag{3.27}$$

where $m(x)$ is the sectional mass per unit length of the ship. Integrations are performed for the portion of the ship from the cross section x^* to the bow.

The radiation and diffraction components of the hydrodynamic forces and moments are calculated from the global solution of the BVP in the frequency domain analysis. After the evaluation of velocity potential of each panel in the BVP, the panels positioned forward of the defined cross section are integrated in order to derive the sectional radiation and diffraction forces. The formulation of the sectional radiation and diffraction forces is defined using the same formulation in Equation (3.18) for the panels positioned forward of the defined cross section. The sectional radiation and diffraction forces are given by:

$$\begin{aligned} F_{j,D}^* &= -\rho \iint_{S^*} \left\{ i\omega_e + U\frac{\partial}{\partial x} \right\} \phi_D n_j dS \\ F_{j,R}^* &= -\rho \iint_{S^*} \left\{ i\omega_e + U\frac{\partial}{\partial x} \right\} \phi_{R,k} n_j dS = \omega_e^2 A_{jk}^* + i\omega_e B_{jk}^* \end{aligned} \qquad \text{j,k=3\&5} \tag{3.28}$$

where $A_{jk}^*$and $B_{jk}^*$are the sectional added mass and damping coefficients calculated on the sectional ship surface area S^*.

The incident wave forces are derived using the first Equation of (3.18) by the integration of the incident wave pressures for the portion forward of the cross section and are given by:

$$F_{j,I}^{*} = -\rho \iint_{S^{*}} \left\{ i\omega_e + U\frac{\partial}{\partial x} \right\} \phi_I n_j dS \qquad \text{j=3\&5} \qquad (3.29)$$

Finally, the restoring forces are calculated using the restoring matrix for the portion forward of the defined cross section multiplied by the vertical displacements:

$$F_{j,Res}^{*} = C_{jk}^{*} \cdot \xi_k \qquad \text{j,k=3\&5} \qquad (3.30)$$

3.3 General Description of the Time-Domain Method

In the former sections ship motions are assumed to be small compared to the ship dimensions, therefore the seakeeping calculations are valid using the frequency domain approach. In order to model the large amplitude motion and load responses one needs to use the time-domain approach. In the present thesis, time domain vertical motion and load estimations in head seas are calculated in 2 DOF using the rigid body approach and using Cummins (1962) equations. This section explains the methodology of the time-domain motion and load response predictions in detail. The equation of motion is derived using the IRF formulation in two DOF for heave and pitch motion modes. The linear time-domain equation of motion for heave and pitch responses are defined using the Cummins equations for small amplitude responses as shown below:

$$\begin{gathered} \left[M_{jk}^{h} + A_{jk}^{h}(\infty)\right] \cdot \ddot{\xi}_k(t) + B_{jk}^{h}(\infty) \cdot \dot{\xi}_k(t) + \int_0^t K_{jk}^{h}(t-\tau) \cdot \dot{\xi}_k(\tau) d\tau \\ + C_{jk}^{h} \cdot \xi_k(t) = F_j^{I}(t) + F_j^{D}(t) \end{gathered} \qquad \text{j,k=3\&5} \qquad (3.31)$$

where j,k=3&5 subscripts stand for the heave and pitch motion modes respectively. The left side of the equation gives the fluid reaction forces and inertial forces whilst the right hand side of the equation gives the excitation forces in the time domain. In the Equation (3.31), M_{jk}^{h} is the mass and inertia matrix of the ship, ξ_k , $\dot{\xi}_k$ and $\ddot{\xi}_k$ are the time-domain displacement, velocity and acceleration vectors respectively, $A_{jk}^{h}(\infty)$ and $B_{jk}^{h}(\infty)$ are the infinite frequency added mass and damping coefficients, K_{jk}^{h} are the memory functions for related motion modes, C_{jk}^{h} is the constant restoring force matrix, $F_j^I(t)$ and $F_j^D(t)$ are the incident and diffraction forces in the time domain. The superscript h indicates that all hydrodynamic forces are calculated with respect to the hydrodynamic frame in the time-domain simulations. The present thesis focuses on the nonlinear derivation of motion and load responses therefore the linear restoring matrix is not used; instead, restoring forces are calculated by the direct pressure integration method using the exact wetted area of the ship at each time step. Nonlinearity of the diffraction and radiation forces depends on the level of nonlinearity which is implemented in the motion equation.

The seakeeping response in time domain calculations is dependent on the frequency domain hydrodynamic coefficients and diffraction forces. In the present thesis frequency domain hydrodynamic data is calculated using the 3D seakeeping software PRECAL. In the following sections the derivation of hydrodynamic force components in the motion equation are explained and discussed in detail with emphasis put on the level of nonlinearity applied in the hydrodynamic solutions.

3.3.1 Froude-Krylov and Restoring Forces

In seakeeping analysis, the biggest portion of the forces arises from F-K and restoring forces and their importance is proportional to the characteristic wave length. This is especially true for long wave lengths, which are taken to be more than 2 in the wave length to ship length ratio (λ/L_{pp}). Here the F-K and restoring forces are dominant over the radiation and diffraction forces. In non-linear simulations the nonlinear F-K and nonlinear restoring forces are calculated using the instantaneous wetted surface of the hull at each time step. Many different approximations for the evaluation of the F-K pressures can be found in the literature due to the fact that the linear incident wave potential is valid up to the mean free surface level. Indeed, the linear F-K formulation is valid up to the still water level. Fonseca and Soares (1998) and Singh and Sen (2007a) have discussed the four major approaches for the approximate derivation of the non-linear F-K forces above the mean free surface level which are: the hydrostatic approach, the Wheeler stretching (Chakrabarti, 1987), unmodified incident waves formulation and the Fourier approximation method (Rienecker and Fenton, 1981). Unfortunately, there has not been a general consensus on which method provides more accurate results. In the current approximation, the F-K pressure above the mean sea level is taken as a hydrostatic force. A diagram of the total wave pressure distribution in incoming waves is illustrated below:

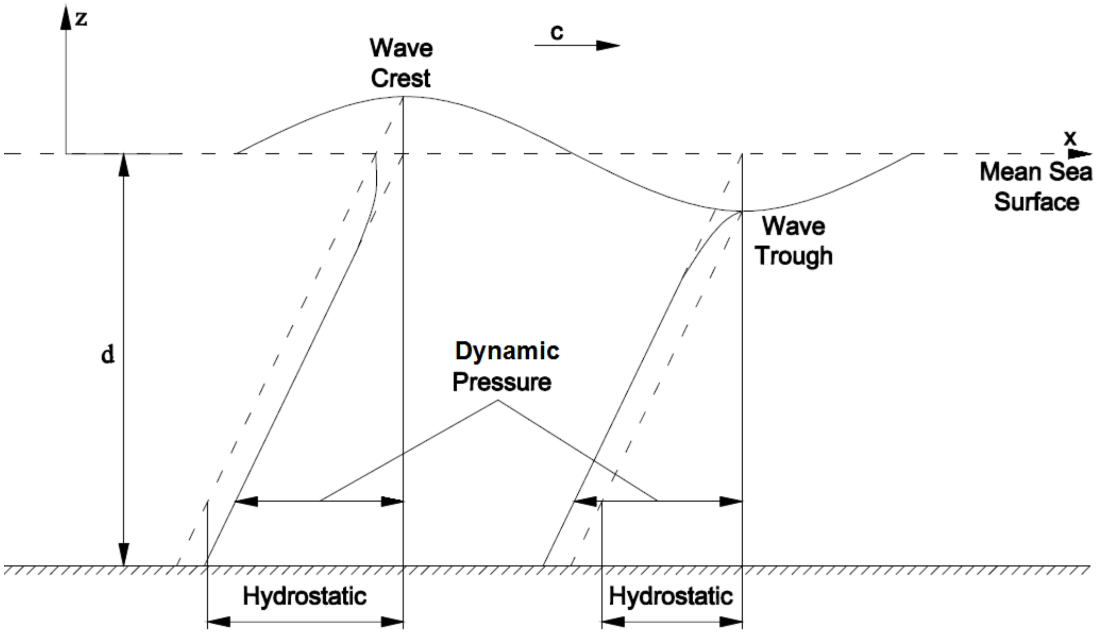

Figure 3.7: Dynamic wave pressure distribution

where c is the wave celerity, d is the depth of the sea. It is clear from the Figure 3.7 that the pressure distribution near to the mean sea level varies for the wave crest and wave trough positions.

In LARes the non-linear incoming wave pressure and non-linear hydrostatic pressure are calculated as (Van't Veer et al., 2009):

$$P_{FK} = \begin{cases} \rho g \zeta_a \left(1 - \frac{z}{\zeta_a}\right) & 0 < z \leq \zeta_a \\ \rho g \zeta_a e^{kz} & z \leq 0 \end{cases} \tag{3.32}$$

$$P_{hydrostatic} = \begin{cases} 0 & 0 < z \leq \zeta_a \\ \rho g z & z \leq 0 \end{cases} \tag{3.33}$$

where ζ_a is the incident wave height, ρ is the water density and g is the gravity acceleration.

The resultant pressure is integrated on the updated instantaneous wetted portion of the surface at each time step and the nonlinear F-K and restoring forces are given by:

$$F_{FK,HS,j} = -\iint_S (P_{FK} + P_{HS}) n_j dS \qquad \text{j=3\&5} \qquad (3.34)$$

3.3.2 Radiation Forces

The time domain radiation forces are represented in terms of impulse-response functions and the infinite added mass and damping coefficients in order to account for the radiating wave forces arise from the non-sinusoidal ship oscillations. The integral represents the transient radiation forces acting on the ship at the current time step which is the convolution of the memory effects related to the free surface oscillations and the time history of the motions. The radiation forces in time domain are defined by Cummins (1962) in terms of impulse-response functions and are given by:

$$\vec{F}_{jk,R}(t) = A^h_{jk}(\infty) \cdot \ddot{\xi}_k(t) + B^h_{jk}(\infty) \cdot \dot{\xi}_k(t) + \int_0^t K^h_{jk}(t-\tau) \cdot \dot{\xi}_k(\tau) d\tau \qquad \text{j,k=3\&5} \qquad (3.35)$$

where $A^h_{jk}(\infty)$ and $B^h_{jk}(\infty)$ are the infinite frequency added mass and damping matrices and K^h_{jk} is the retardation (memory) function which is accounting for the free surface oscillations. In Equation (3.35), the $A^h_{jk}(\infty)$ term depends only on the ship geometry under the still water level while the $B^h_{jk}(\infty)$ term depends on the ship geometry and the forward speed. The frequency dependent part of the radiation forces is contained $K^h_{jk}(t)$ in the term.

In this work, the memory functions are calculated from the damping curves provided by the 3-D linear frequency-domain PRECAL software. Memory functions only depend on the forward speed and the underwater geometry of the ship below the still water level. Retardation functions are calculated using the inverse Fourier transform of the potential damping coefficients obtained from the frequency domain BVP solution at a range of encountering frequencies. Theoretically, the retardation functions need to be integrated from zero to infinite encountering frequency. However, in practice, due to the aforementioned small encountering wave period problems, the highest encountering frequency needs to be defined in advance by using Equation (3.22) for the upper boundary of the integration domain. In order to calculate retardation functions, damping coefficients are preferred since added mass coefficients at very small frequencies are not always smooth (Van't Veer et al., 2009).

The smoothness of the damping curve is crucial for the robustness of the memory functions. Irregularities in the damping curve result in fluctuations in the memory functions and produce inaccurate radiation forces in the time domain motion simulations. In order to prevent this, frequency dependant damping curves are evaluated starting from low frequencies to high frequencies with successive small steps. In general, in forward speed calculations, infinite damping coefficients do not approach zero whilst in zero speed calculations there is generally no need to implement the infinite damping correction in the integrand of the retardation function. The integrand in the convolution integral, which approaches zero as ω_e approaches infinity, corrects the non-zero values of infinite frequencies for the forward speed case. The retardation functions are given by:

$$K_{jk}^{h}(t) = \frac{2}{\pi}\int_{0}^{\infty}\left[B_{jk}^{h}(\omega_e) - B_{jk}^{h}(\infty)\right]\cos(\omega_e \tau)\,d\omega_e \qquad \text{j,k=3\&5} \qquad (3.36)$$

The retardation functions are calculated using the 3 point Simpson integration formulation with 501 interpolated damping coefficient points corresponding to a pre-defined range of encounter frequencies in order to maintain the accuracy of the integration.

A truncation time must be defined to determine the length of the convolution integral. After the truncation time, radiation forces must converge to zero when convoluted with non-zero velocity history because after that time the radiating waves do not influence the pressure on the body surface. The truncation time of the memory forces is applied to be 30 seconds for the performed analyses in the present thesis, which is found to be sufficient time for the radiated waves to die out after the impulses. Radiation forces will apply for only the time span of the memory functions. Diagonal and cross-coupling memory functions for the heave and pitch motion modes (j,k=3&5) for the S-175 ship at a forward speed of Fn=0.275 are illustrated in Figure 3.8. The validation of the memory functions is performed by comparing the results with the PRETTI software (Van't Veer et al., 2009) retardation functions and the results are found to be identical to each other for each mode of memory function.

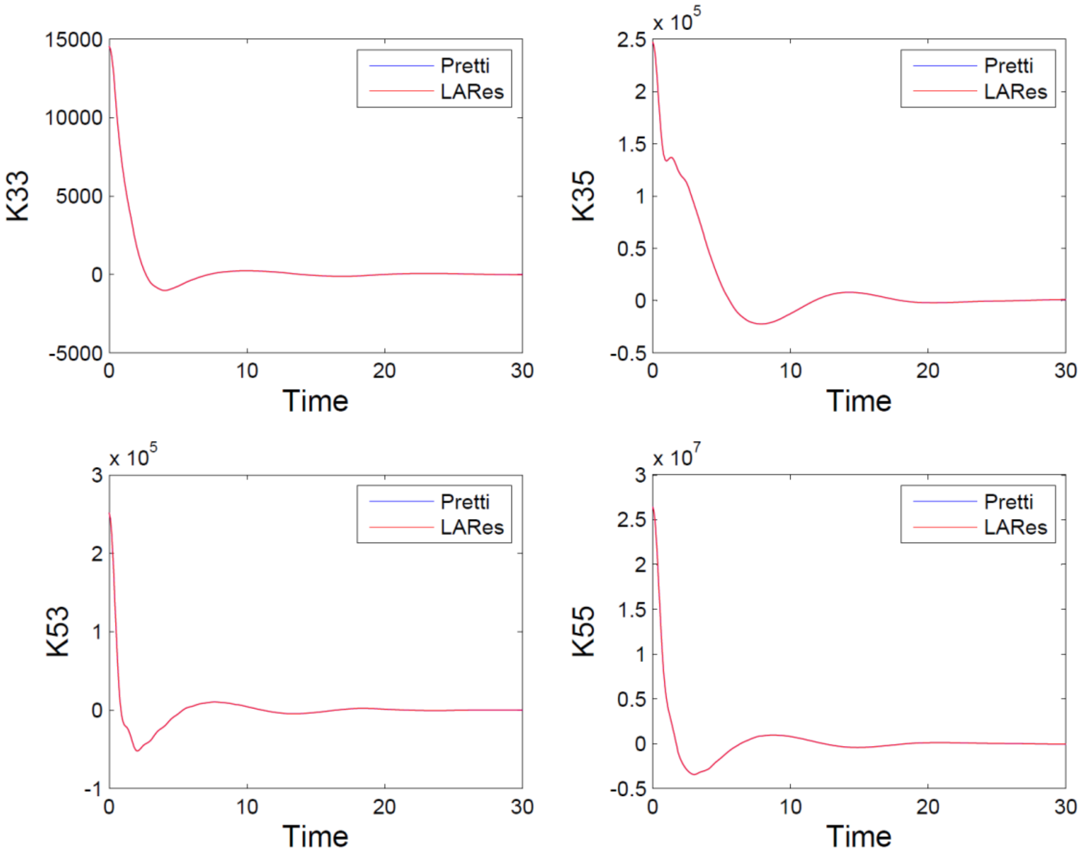

Figure 3.8: Memory functions for S-175 ship at Fn=0.275

Ogilvie (1964) derived the relationship between the frequency domain and time domain radiation problems using the Kramers-Kronig relations (Kotik and Mangulis, 1962). The author applied Fourier transforms to the retardation functions and the time domain radiation forces are related to the frequency domain added mass and damping coefficients given by:

$$B_{jk}^{h}(\omega_e) = B_{jk}^{h}(\infty) + \int_{0}^{\infty} K_{jk}^{h}(\tau)\cos(\omega_e \tau)d\,\tau \tag{3.37}$$

j,k=3&5

$$A_{jk}^{h}(\omega_e) = A_{jk}^{h}(\infty) - \frac{1}{\omega_e}\int_{0}^{\infty} K_{jk}^{h}(\tau)\sin(\omega_e \tau)\,d\tau \tag{3.38}$$

The infinite frequency added mass is frequency independent and is calculated using a modified frequency independent Green's function. It is clear to observe from Equation (3.38) that only infinite frequency added mass needs to be known to generate the whole added mass curve when the retardation functions are derived using the damping coefficients. The infinite frequency added mass value can also be evaluated using the whole added mass curve. The Fourier transform of the retardation functions (invK), time-domain added mass curve and the evaluated infinite added mass curve for the diagonal and cross-coupling heave and pitch motions at a forward speed of Fn=0.275 are illustrated below:

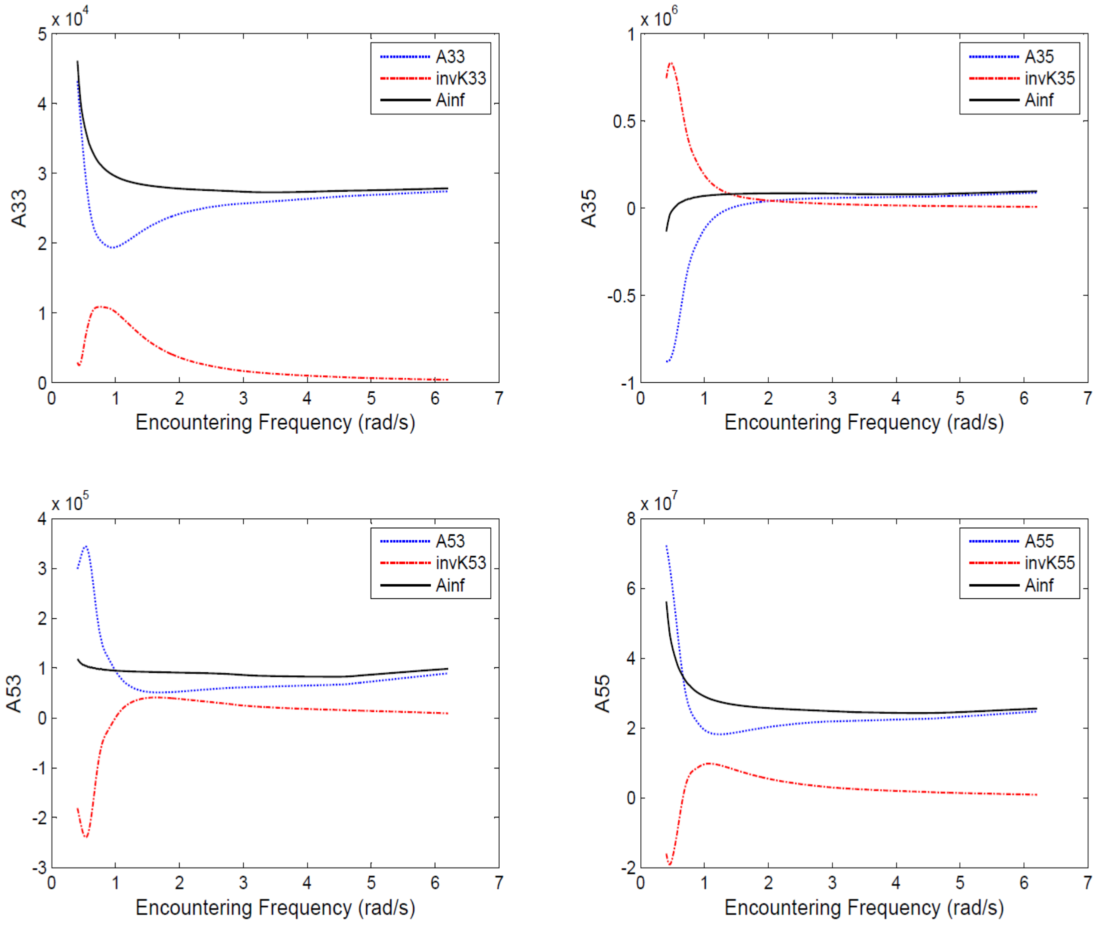

Figure 3.9: Infinite frequency added mass curve for S-175 ship at Fn=0.275

Memory functions are calculated each time in advance and used throughout the duration of the simulations. The nonlinearity level of the computations in the seakeeping analysis affects the utilization of memory functions and the infinite frequency added mass and damping data. In level 2 computations, the memory functions are calculated in advance and the same functions are used during the simulations. However, in level 3 computations, the memory functions and the infinite frequency hydrodynamic coefficients are derived for all pre-defined range of heave and pitch displacements of the ship individually and then interpolated for interim positions during the seakeeping analysis. In both of the nonlinearity levels one needs to calculate updated retardation functions corresponding to the updated forward speed. Further information about the detailed derivation of level 3 retardation functions will be given in the next sections.

3.3.3 Diffraction Forces

Time-domain diffraction forces are calculated using the solution of the linear frequency domain BVP with the second Equation of (3.18). Complex diffraction forces are separated into real and imaginary components to be used in the time-domain calculations. Constant diffraction forces are used during the simulations in which they are extrapolated for the given incident wave amplitude. The resultant diffraction force in time domain analysis for the given incident wave amplitude and for the jth motion mode is equal to:

$$F_{D,j} = \vec{\xi}_a \Re\left\{ \left(F_{D,j}^{Re} + iF_{D,j}^{Im}\right) \cdot e^{-i\omega_e t} \right\} \qquad j=3\&5 \quad (3.39)$$

where $F_{D,j}^{Re}$ and $F_{D,j}^{Im}$ are the real and imaginary components of the complex diffraction forces in the jth mode of the motion mode.

The nonlinearity level of computations in seakeeping analysis affects the utilization of diffraction forces as well. In level 2 computations, the diffraction force amplitude is kept as constant for the given speed and the mean underwater area. However, in level 3 computations, the diffraction forces are derived for all pre-defined heave and pitch displacements of the ship and are interpolated for interim positions during the seakeeping analysis. Further information about the derivation of level 3 diffraction forces will be provided in the next sections.

3.3.4 Internal Loads in the Time-Domain Approach

The time-domain wave induced internal loads are given by the difference between the inertial forces and the sum of the hydrodynamic forces integrated from the bow to position of the cross section and calculated at the each time instant. The time-dependent vertical internal loads (VSF and VBM) are given by:

$$V_3(t) = I_3(t) - FR_3^*(t) - FD_3^*(t) - FK_3^*(t) - H_3^*(t) \tag{3.40}$$

$$M_5(t) = I_5(t) - FR_5^*(t) - FD_5^*(t) - FK_5^*(t) - H_5^*(t) \tag{3.41}$$

where I_k (k=3,5) is the inertial forces or moments of the ship's mass distribution forward of the cross section. In the VSF and VBM formulations FR_k^* and FD_k^* are the time domain radiation and diffraction forces respectively which are calculated with respect to (w.r.t.) the mean sea level, whilst FK_k^* and H_k^* are the time domain F-K and hydrostatic forces respectively which are calculated for the instantaneous wetted portion of the ship at each time step and correspond to the panels forward of the cross section.

In time domain calculations, the inertial forces and moments are calculated using Equations (3.26) and (3.27) by the product of the constant mass distribution and the time dependent sectional accelerations at each time step.

The derivation of the time domain radiation component of the hydrodynamic forces and moments is different from the frequency domain due to the convoluted time history of the radiating waves. The radiation forces for the portion of the ship forward of the cross section are calculated by the convolution of retardation functions with the actual velocity of the ship. The radiation forces corresponding to the ship portion forward of the cross-section are calculated using Equation (3.35) and given by:

$$F^{*}_{jk,R}(t) = A^{*h}_{jk}(\infty) \cdot \ddot{\xi}_k(t) + B^{*h}_{jk}(\infty) \cdot \dot{\xi}_k(t) + \int_0^t K^{*h}_{jk}(t-\tau) \cdot \dot{\xi}_k(\tau) d\tau \qquad \text{j,k=3\&5} \quad (3.42)$$

where $A^{*h}(\infty)$ and $B^{*h}(\infty)$ are the sectional infinite frequency added mass and damping coefficients to and K^{*h} is the sectional retardation function which is accounting for the free surface time history of the radiating waves. The retardation functions are evaluated using the sectional damping coefficients corresponding to the panels positioned forward of the cross section using the second Equation of (3.28) . Sectional retardation functions are calculated from the sectional damping curve provided by the 3D PRECAL Software. The sectional memory functions are given by:

$$K^{*h}_{jk}(t) = \frac{2}{\pi} \int_0^\infty \left[B^{*h}_{jk}(\omega_e) - B^{*h}_{jk}(\infty)\right] \cos(\omega_e \tau) d\omega_e \qquad \text{j,k=3\&5} \quad (3.43)$$

Time-domain sectional diffraction forces are calculated by the solution of the linear frequency domain BVP using the first Equation of (3.28) by the 3D PRECAL software. The derived complex sectional diffraction forces are separated into real and imaginary components and are implemented into the time-domain calculations using Equation (3.44). The resultant sectional diffraction force in time domain analysis for the given incident wave amplitude and for the jth motion mode is equal to:

$$FD^{*}_{j} = \xi_a \Re\left\{ \left(FD^{*Re}_{j} + iFD^{*Im}_{j}\right) \cdot e^{-i\omega_e t} \right\} \qquad \text{j=3\&5} \quad (3.44)$$

where $F^{*Re}_{D,j}$ and $F^{*Im}_{D,j}$ are real and imaginary components of the complex sectional diffraction forces in the jth mode of the motion mode.

The nonlinearity level of the computations affects the utilization of the sectional radiation and diffraction forces as well. In level 2 nonlinearity, sectional retardation functions and diffraction forces are calculated in advance and kept as constant during the simulations. However in level 3 nonlinearity, sectional retardation functions and diffraction forces are calculated in advance for all pre-defined heave and pitch displacements of the ship individually and then interpolated for interim positions during the seakeeping analysis.

The nonlinear sectional F-K and restoring forces are calculated using Equation (3.34) for the instantaneous wetted area of the ship at the time instant. The sectional time-dependent F-K and restoring forces corresponding to the instantaneously wetted area of the ship are derived using Equations (3.32) and (3.33) and given by:

$$F^{*}_{j,FK,HS} = -\iint\limits_{S^{*}} (P^{*}_{FK} + P^{*}_{HS}) n_j dS \qquad \text{j=3\&5} \qquad (3.45)$$

where P^{*}_{FK} and P^{*}_{HS} are the evaluated F-K and hydrostatic pressures for the portion of the ship forward of the cross section at the time instant in the jth mode of the motion mode.

3.4 Summary

In the present thesis, time-domain calculations are dependent on the frequency domain linear hydrodynamic forces and coefficients which are evaluated using the PRECAL software. The formulations of the frequency domain method are provided with a focus on the uniform and D-B flow and the EFS and AFS methods. It is observed that the EFS and AFS methods highly influence the motion responses and damping coefficients. Although the EFS method agreed better with the motion responses, instability in the damping coefficients made it impossible to use them in memory function evaluations. In time-domain method motion and load simulations only the vertical responses are evaluated therefore, only the heave and pitch motion modes are accounted in the equations. Main difference of the time-domain approach arise from the utilization of the impulse-response functions therefore the formulation of the global and sectional time-domain radiation forces are provided in detail. Furthermore, the comparison of the LARes and PRETTI memory functions are found to be identical to each other. Infinite frequency added mass and damping coefficients are also derived using inverse Fourier transform of the evaluated memory functions.

Chapter 4

Numerical Methods

4.1 Development of the Models

In this chapter, the numerical methods applied in the nonlinear motion and load estimations with a focus on the level of nonlinearity models are investigated in detail. The main focus is given to the mathematical modeling of the F-K nonlinear (level 2) and the body nonlinear (level 3) seakeeping prediction methods. The originality of the thesis arises from the utilization of the level 3 nonlinearity formulation with development in the multi-dimensional integration and interpolation processes. In order to maintain the consistency of the thesis in the following sections, the in-house developed LARes tool is sub-grouped under the names LARes L2 and LARes L3 for the level 2 and level 3 approaches respectively. The formulations of the LARes L2 and LARes L3 share some common properties to perform the time domain nonlinear seakeeping simulations. The LARes L2 and LARes L3 tools have 4 common modules while performing nonlinear time domain seakeeping analysis. They can be summarised as follows:

- Data input tool
- 3-D dynamic meshing tool
- Time domain non-linear equation solver
- Post processor

4.2 Data Input Tool

The data input tool is capable of direct import of the discretized ship geometry and 3D panel visualization features. The discretized ship geometry can be imported in a text format using a nodal and facet file consisting of the hull geometry data. The nodal file constitutes the node numbers and nodal coordinates in the hydrodynamic frame axis in x, y and z coordinates whilst, the facet file consists of the nodal coordinate arrangement data in order to generate panels and also each panel's position flag. The position flag determines whether a panel is positioned under the still water level, on the free board or on the deck part of the ship while it is at the initial position. The direct input feature eliminates the restriction on using the PRECAL Auto Mesh Generator (AMG) for discretization and allows the user to import other meshing software outputs. The main responsibility of the data input tool is to import and store the definition of the discretized ship geometry up to the superstructure and also the global mass distribution and the restoring matrix. The sectional mass distribution is used in order to calculate the vertical loads for the portion of the ship forward of the defined cross section. The non-planar panels are re-mapped into planar panels for the hydrodynamic pressure integration. It is important to remember that the restoring matrix is only valid for small amplitude motions therefore it is only used in linear seakeeping analysis in order validate and compare the motion and load responses against the experimental results.

4.3 Dynamic Meshing Tool

Nonlinear ship motion response analysis consists of two important components which need to be performed successively during the simulation at each time step. In brief, the components can be separated as the dynamic panelization and the hydrodynamics solver. It is a known fact that, in non-linear analysis, large portions of the forces acting on the ship arise from the Froude-Krylov (F-K) and the restoring forces therefore they have a crucial importance in the accuracy of the responses calculated. The second component in total hydrodynamic force arises from the radiation and diffraction forces, which also has a significant importance; especially for short wave lengths.

The calculation of the instantaneous wetted portion of the hull surface has always been a challenging subject for the naval engineers due to its complexity and computational cost. In general, there are two approaches widely applied in seakeeping software and they are illustrated in Figure 4.1:

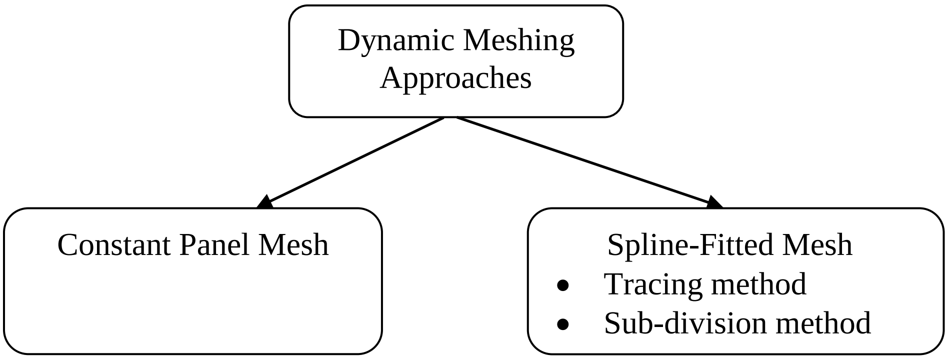

Figure 4.1 : Dynamic meshing approach

In the constant panel mesh method, the geometry and the properties of the panels are calculated at the initial time of the simulation and kept the same for the duration of the simulation. The instantaneous wetted ship surface is evaluated by checking the relative position of the centre point of each panel with respect to the wave elevation at each time step. If the centre point of a panel is under the wave profile it is assumed as wet, otherwise it is assumed as dry and omitted from the calculations at that time step. For complex geometries, the spline-fitted mesh approach is another alternative for evaluating the instantaneous wetted ship surface. This method can be applied with two different approaches: the tracing method and the sub-division method (Ko et al., 2011). The tracing method formulates the topological configuration of intersection via non-linear differential equations. In complex geometries such as bulbous bows, the application of this method can be a problematic task (Ko et al., 2011). In the sub-division method, the parametric domain is divided into rectangular regions using iterative loops until it does not intersect with the wave profile and each region is checked to be sure whether it is under wave profile or not.

The dynamic meshing approaches have both advantages and disadvantages for various kinds of geometries. For ship shaped bodies with large water plane areas, the constant panel mesh method with a fine grid mesh of O(4000-5000) on the whole underwater hull provides enough accuracy for the evaluations of the F-K and restoring force (Singh and Sen, 2007a). However, a coarse grid mesh density of O(300-400) can cause inconsistencies while evaluating the F-K and restoring forces near to the wave profile. In a coarse mesh density, the characteristic area and height of panels are large therefore centre points of the panels can cause fluctuations near to the wave profile during the wet-dry computation for the partly wet panels. Those fluctuations can give rise to spikes at the F-K and restoring forces at particular time steps. The tracing and sub-division methods are the only way to evaluate the F-K and restoring forces in offshore structures with many surface piercing parts like cylinders. Unfortunately, the tracing and sub-division methods are very time consuming and therefore inefficient for ship shaped bodies. Moreover, the tracing method is very hard to implement on complex body shapes and stability in the solution of differential equations can cause problems (Ko et al., 2011). The advantages and disadvantages of the dynamic meshing methods are summarized in Table 4.1 below:

Table 4.1: Advantages & disadvantages of meshing methods

Dynamic Meshing Method	**Advantages**	**Disadvantages**
Constant Panel Mesh	• Accurate for ship-shaped bodies • Accurate wetted panel evaluation with fine mesh grid on hull near the wave profile • Fast and efficient	• Inaccurate wetted panel evaluation with coarse mesh grid on hull near the wave profile • Inaccurate for panels with large heights and can cause spikes in evaluated forces.
Tracing Method	• Accurate for offshore structures • Best accuracy over all methods	• Very hard to implement on complex hull shapes • Inefficient and time consuming
Sub-division Method	• Accurate for offshore structures • The only option for free-surface-piercing parts like cylinders	• Time consuming sub-division iterations.

The LARes L2, LARes L3 and PRETTI software evaluate the non-linear F-K and restoring forces acting on the instantaneous wetted portion of the ship with respect to the wave profile at each time step in the nonlinear motion simulations. LARes utilises the Hess and Smith (1962) method with a single centre point on each panel and checks whether the panel is wet or dry during the simulation time steps. However, the PRETTI software utilizes the 4 point Gauss method in order to integrate pressures. At each time step all Gauss points on each panel are checked to see whether they are under the wave profile or not, and wet points in each panel are taken into the pressure evaluation. Moreover, in the PRETTI software, in order to accelerate the simulations, the maximum possible wave elevation is computed and all possible wet panels are taken into account in the simulations (Van't Veer et al., 2009). In order to eliminate the pressure fluctuations near to the wave profile, LARes L2 and LARes L3 divide the initial panels, which are used in the BVP solution, into four and evaluate the F-K and restoring pressures accurately.

The exact wetted panel properties under the wave profile consist of the area, centre coordinates and normal directions in the x, y and z directions of each panel which are defined in the hydrodynamic axis frame. Panel properties will be used for generation of the hydrodynamic forces and moments applied to the ship during simulation. The complete ship geometry panel discretization for the S-175 ship in LARes is illustrated in Figure 4.2. The length of the panels influence the forward speed results in high extents therefore the maximum panel length is taken to be 1.5 meters.

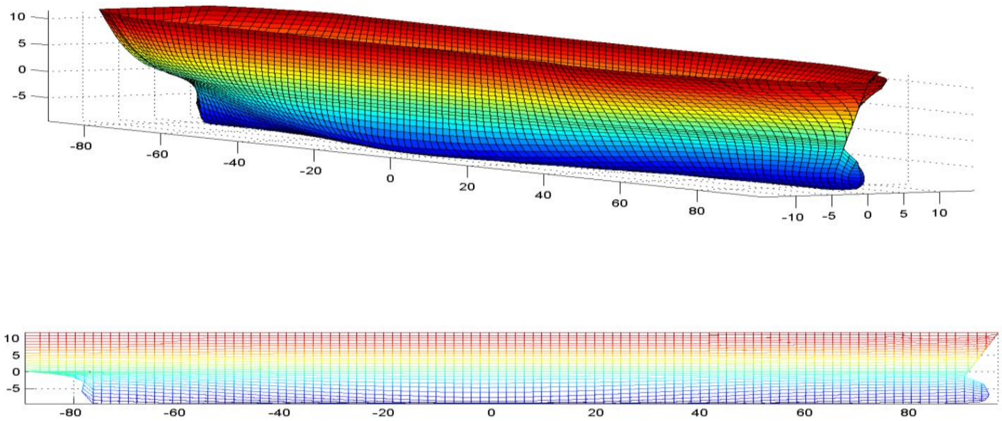

Figure 4.2: LARes discretization of the S-175 ship geometry

The accurate evaluation of wet and dry panels for the force and moment calculations is crucial for ships which are subjected to large amplitude waves. It was mentioned before that the panels close to the instantaneous wave surface cause problems while performing the wet-dry logic test in short waves due to the significant increase in the wave steepness. In Figure 4.3, the S-175 ship in a zero trim condition and at the initial draft position is illustrated while it is subjected to 5 metre incident wave heights. Although the wave steepness is high, with the aid of a high mesh density, LARes performed well in matching the exact wetted area of the ship under the incident waves.

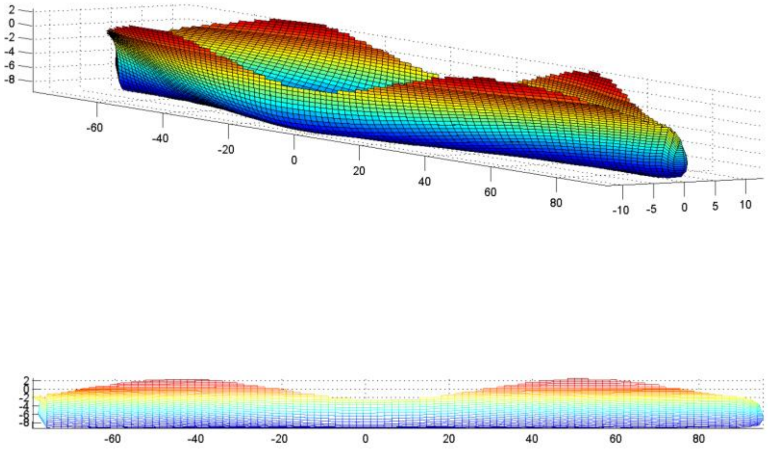

Figure 4.3: LARes S-175 ship geometry under waves in T_θ=0 degrees, H_w=5m

Figure 4.4 shows the examples of dynamic meshing for the cases of +4 (left) and -4 (right) degrees of pitch angle, at initial draft and subjected to 5 metre wave heights with a wavelength to ship length ratio (λ/Lpp) of 0.55. The propeller emergence is observed in the left figure and in the right figure the bow emergence is observed in small pitch angles. The severity of the non-linear behaviours of the ship increases significantly with increasing wave amplitudes. When a ship is subjected to large amplitude waves, it is highly possible that it can experience propeller emergence, slamming and water on deck problems. It must be remembered that, in linear calculations, only the wetted panels under the still water level are taken into account and the instantaneous wave profile is not considered in the simulations.

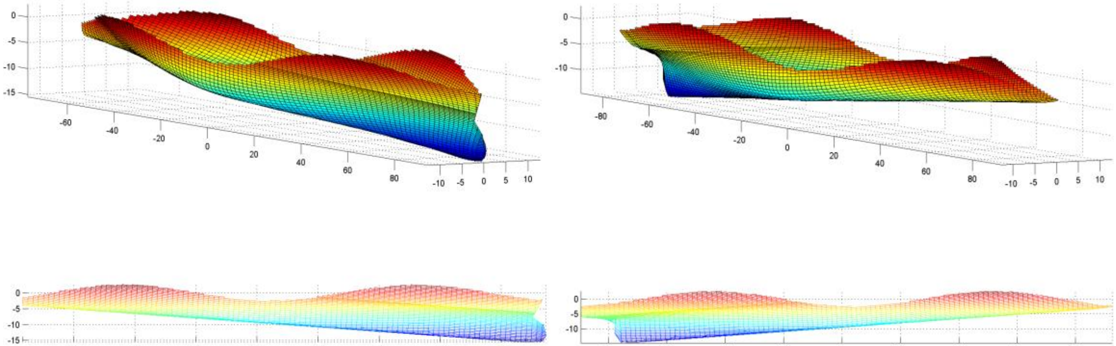

Figure 4.4: LARes S-175 ship geometry under waves in T_θ=4 degrees (left) T_θ=-4 degrees (right), H_w=5m

The dynamic meshing process is the second most time consuming phase of the simulation after the evaluation of the frequency domain hydrodynamic coefficients. The relative position of each panel's centre location needs to be checked with respect to the instant wave profile at each time step which results in elevated computational time. When the mesh distribution on the vessel is very fine in order to maintain the geometric continuity, loops in the dynamic meshing tool take a long time computationally which make the time domain code inefficient. In order to eliminate this drawback, the LARes software utilizes vectorized calculation of the panels. In the vectorized calculation, hull panels are automatically defined in sequential arrays. The main advantage of the vectorized calculation is that it can evaluate all panels on the ship instantly at each time step using the physical memory of the computer without the need to wait for the loops to evaluate the properties of the panels.

The vectorized calculation of the instantaneously wetted properties of the ship panels possesses one of the novelties of the current study. Likewise the looped structure, vectorized algorithm uses the Hess and Smith (1962) method in order to find the wetted panel properties while provides 90% faster solution compared to the conventional looped approach. In order to find the properties of each panel firstly the main diagonal vectors need to be calculated in order to obtain the normal directions of each panel. Then, all corner points need to be defined in the element coordinate system in order to find its exact centroid position and to evaluate the area of each panel. At the end of the calculations each panel's area, centroid coordinates and normal directions in the global ship coordinate system are listed in a matrix. It needs to be mentioned that in non-linear analysis at each time step ship's panel properties need to be calculated for all panels including the upper hull section with respect to the mean sea level. Instead of calculating each panel's properties at each time step after the translation and rotation of the ship, vectorized algorithm defines the nodal points of each panel in a array domain. In general, quadrilateral panels are used in the discretization of the ship geometry therefore nodal points of the panels are divided into four computational domains in sequential arrays. In MATLAB, sequential arrays can be defined in a matrix form and therefore the following mathematical operations can be performed using the element-by-element multiplication of the panel properties matrix. The sequential array domains are defined as:

$$
\begin{aligned}
&Dom\ 1 = [3:4:c-1] \\
&Dom\ 2 = [2:4:c-2] \\
&Dom\ 3 = [1:4:c-3] \\
&Dom\ 4 = [4:4:c]
\end{aligned}
\tag{4.1}
$$

where c is the total number of corner points of panels on the discretized ship geometry. Defined domains are fed into the calculation of the diagonal vector, average centroid position and non-planar panel operations where they are automatically defined in array structures without a need for a looped structure. In order to calculate the normal direction of each panel, diagonal vectors are needed and their definition is shown in the Figure 4.5 below:

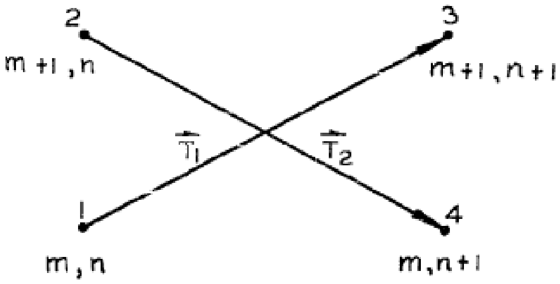

Figure 4.5: The formation of an element (Hess and Smith, 1962)

The x, y, z components of the T1 and T2 diagonal vectors are calculated feeding the sequential array domains into the main nodal input matrix. T1 and T2 vectors are defined as:

$$
\begin{aligned}
&T1x=Inp(Dom1,1)-Inp(Dom3,1) \qquad &&T2x=Inp(Dom4,1)-Inp(Dom2,1) \\
&T1y=Inp(Dom1,2)-Inp(Dom3,2) \qquad &&T2y=Inp(Dom4,2)-Inp(Dom2,2) \\
&T1z=Inp(Dom1,3)-Inp(Dom3,3) \qquad &&T2z=Inp(Dom4,3)-Inp(Dom2,3)
\end{aligned}
\tag{4.2}
$$

where the Inp is the main input matrix constitutes of the x, y, z coordinates of the each panel's corner points with respect to the global coordinate axis. T1 and T2 vectors are calculated for all panels at the same time via calling the row numbers of the main input matrix which is defined in the sequential arrays. This vector operation needs to be performed at each time step for the updated ship position in order to calculate the exact wetted area of the ship under the incident waves. In the conventional looped structure algorithm T1 and T2 vectors need to be calculated for each panel separately therefore it is computationally very costly compared to the efficient vectorized algorithm.

The wet/dry panel evaluation is the key point in the evaluation of the instantaneously wetted hull properties. In order to maintain this hard task, logical structures are utilized with the series expansion. At each time step, firstly the panels under the wave profile are defined and sorted; and secondly the sorted panels are sub-grouped into those under and above the still water level for the F-K and restoring pressure calculations. Instead of using the if-then-else conditions in MATLAB, the logical conditions to sort out wet/dry panels are embedded into the matrix operations therefore each of the logical processes are evaluated simply in one row without the need for loops inside. The matrix operation checks whether the centre of the panel is above or below the wave profile and then marks it either as one or zero corresponding to the wet and dry case respectively and uses flag to identify it. When the wet and dry case flags are input into the same matrix again, it only sorts out the wet ones and omits the dry ones. In this way, only the wet panels are taken into account in the F-K and restoring pressure calculations which increases the efficiency of the code.

4.4 Time Domain Nonlinear Equation Solver

In the time domain non-linear equation solver module, time domain nonlinear force components are processed and executed. All force components are executed with respect to their utilized level of nonlinearity. The equation solver not only provides the motion histories of related degrees of freedom, but also provides the history of non-linear hydrodynamic and inertial force components namely the Froude-Krylov

(F-K), radiation, diffraction and restoring forces, acceleration, inertial forces and the Vertical Shear Force (VSF) and Vertical Bending Moment (VBM) evaluations. Time domain accelerations of the ship are solved in this module and stored for post-processing needs. It is important to point out again that, in LARes L2 and LARes L3 simulations accelerations are solved in the hydrodynamic frame axis and then integrated using the 4th order Runge-Kutta equation to derive the time domain velocity and motion responses.

In order to evaluate the accelerations at each time step, Newton's equation of motion, which is comprised of the linear system of mass, acceleration and forces, needs to be solved. In PRECAL, the motion equations are solved using an iterative process with a Generalized Minimum RESidual (GMRES) method (Saad and Schultz, 1986) which is based on the modified Gram-Schmidt procedure. LARes L2 and LARes L3 use MATLAB sub-routines to solve the linear system of equations. In order to evaluate the linear equation of $M\ddot{x} = F$, MATLAB performs a general triangular factorization using Lower Upper (LU) factorization with partial pivoting. This solution is fast, efficient and reliable for non-symmetric linear systems. It is also possible to utilize the GMRES method in LARes code however it has been found from experience that this is more time consuming than the main procedure.

4.5 Post Processor

The post processor tool activates when the simulation terminates. In the post processor tool, the figures of the time histories of motion responses, non-linear wave excitation, restoring, radiation, diffraction forces and the VSF and VBM responses are sorted and printed for comparison and validation purposes against the experimental results. Formerly it was mentioned that the vertical motion and load responses of ships are highly asymmetric. In order to investigate the asymmetric behaviour of the responses, the maximum and minimum peak points of the time histories in the nonlinear steady-state motion and load responses are also evaluated. A Fast Fourier Transform (FFT) is applied to the LARes L2 and LARes L3 to calculate the first order harmonics and to compare them with the first order responses obtained from the experiments.

4.6 Froude-Krylov Nonlinear (Level 2) Model

The F-K nonlinear model is the initiator of the time-domain non-linear seakeeping analysis. In this level of nonlinearity, the radiation and diffraction forces are kept as linear while the F-K and restoring forces are calculated with respect to the instantaneous position of the wetted hull portion under the wave profile. The radiation forces are calculated using the Cummins's equation based on the PRECAL potential damping coefficients which relate the frequency domain radiation problem to the time domain problem. The complex amplitude of the diffraction forces is directly passed from the 3D Boundary Value Problem (BVP) solution obtained from PRECAL; thereafter the time domain diffraction forces are evaluated using Equation (3.39). At this level of nonlinearity, the memory functions are calculated before the start of simulations using the potential damping coefficients which are evaluated at vessel's initial position. In the time-domain approach the memory functions and the diffraction forces are the function of time, underwater geometry and ship speed variables. Therefore, when the ship speed is modified, memory functions need to be evaluated for the updated speed. The in-house developed software LARes L2 corresponds to this level of nonlinearity and will be used to compare the results with the experiments and with the other levels of nonlinearities.

The LARes L2 software imports the related hydrodynamic data from the 3D PRECAL software; however it is designed to take input from other hydrodynamic solvers as well. The global infinite frequency added mass, damping coefficients curve and the complex diffraction force amplitudes are input from the PRECAL software in order to find the time domain accelerations and the motion responses of the ship. The sectional infinite added mass, damping coefficients and the diffraction force amplitudes corresponding to the portion of the hull forward of the defined cross-section are inputs from the PRECAL as well, in order to evaluate the VSF and VBM responses for the defined cross-section using the acceleration data provided by the global motion solution at that time step. At each time, before the simulations, two sets of memory functions are generated in which the global one is for the motion response analysis and the sectional one is for the vertical load response analysis using Equations (3.36) and (3.43) respectively. The flow chart of the LARes L2 code is illustrated in the Figure 4.6.

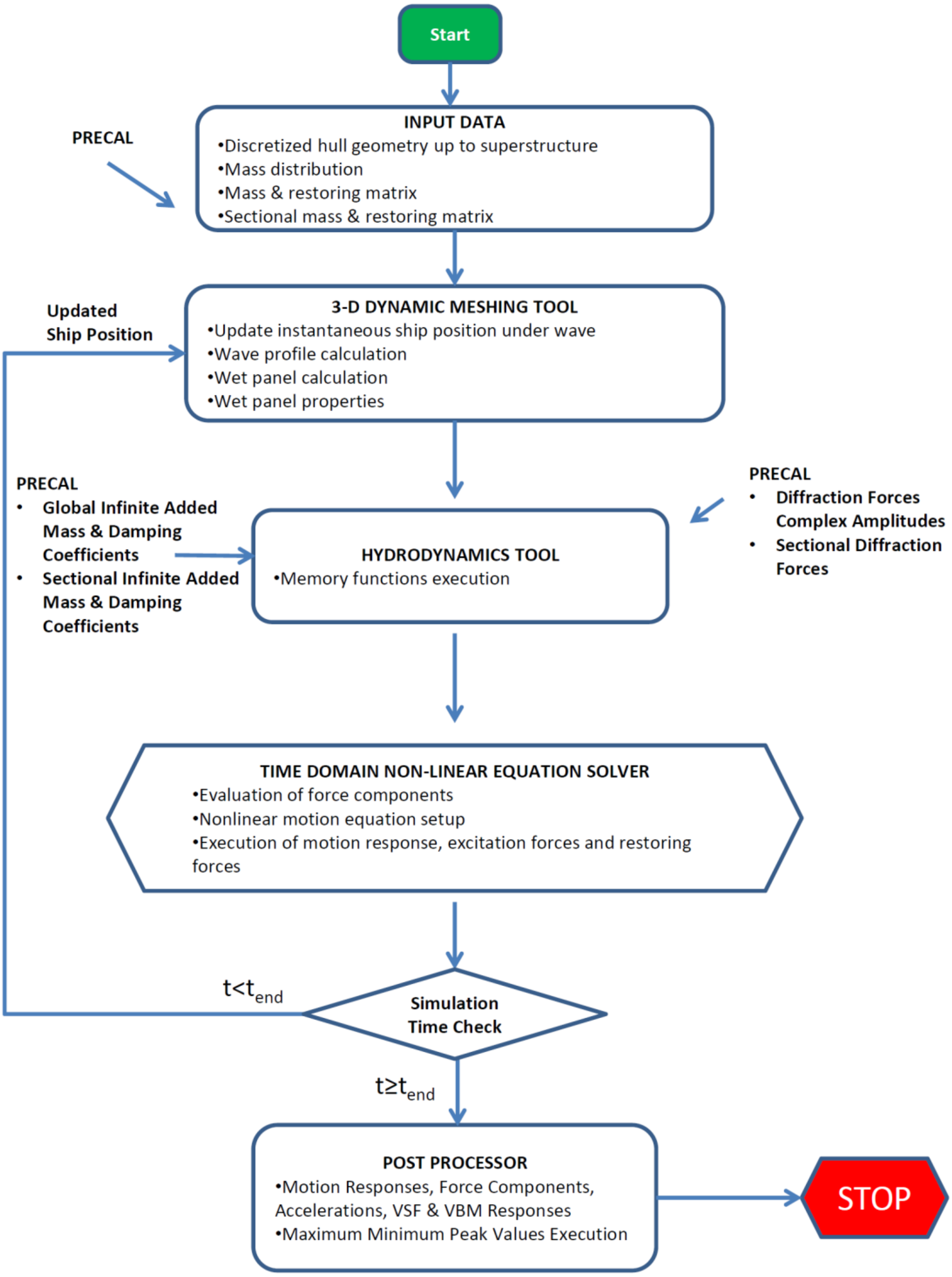

Figure 4.6: LARes L2 flowchart

In LARes L2 at each time step after the evaluation of the accelerations in the time domain solver module, time domain displacements and velocities are calculated by integrating the acceleration using the 4th order Runge-Kutta equations. The updated ship displacements are fed into the meshing tool and the wetted portion of the hull is evaluated for the current time step. In the time domain solver module, the history of body accelerations, velocities, displacements, hydrodynamic force components and the VSF and VBM responses are stored. At each time step the code checks whether the simulation was terminated or not and when the allocated simulation time is finished, all stored motion and force histories are fed into the post-processing module for validation and comparison purposes.

4.7 Body Nonlinear (Level 3) Model

The body nonlinear model is a modification of the F-K nonlinear method which is designed to assess the non-linear effects related to the variation of the radiation and diffraction forces in large amplitude motion simulations. At this level of nonlinearity, the perturbation potential is solved taking into account the varying positions of the vessel under the still water level. Therefore, in this method the rate of change of fluid momentum is not zero unlike the F-K nonlinear method. The incident wave forces and the restoring forces are evaluated with respect to the exact wetted portion of the ship under the wave profile at each time step. The in-house developed software LARes L3 corresponds to this level of nonlinearity and will be used to compare the results with the experiments and the other levels of nonlinearities.

The flowchart of the LARes L3 software is illustrated in detail in Figure 4.7. Mainly, the software is divided into two sections in which the data preparation part is performed only once before the simulations. The second module of the code uses the prepared data and processes it in a repetitive manner until the simulation terminates. Therefore, after the completion of the first section of the code, the complete database is prepared and various cases can be simulated in a short time period. The flowchart of the LARes L3 is more complex than LARes L2 and therefore has an elevated computational cost.

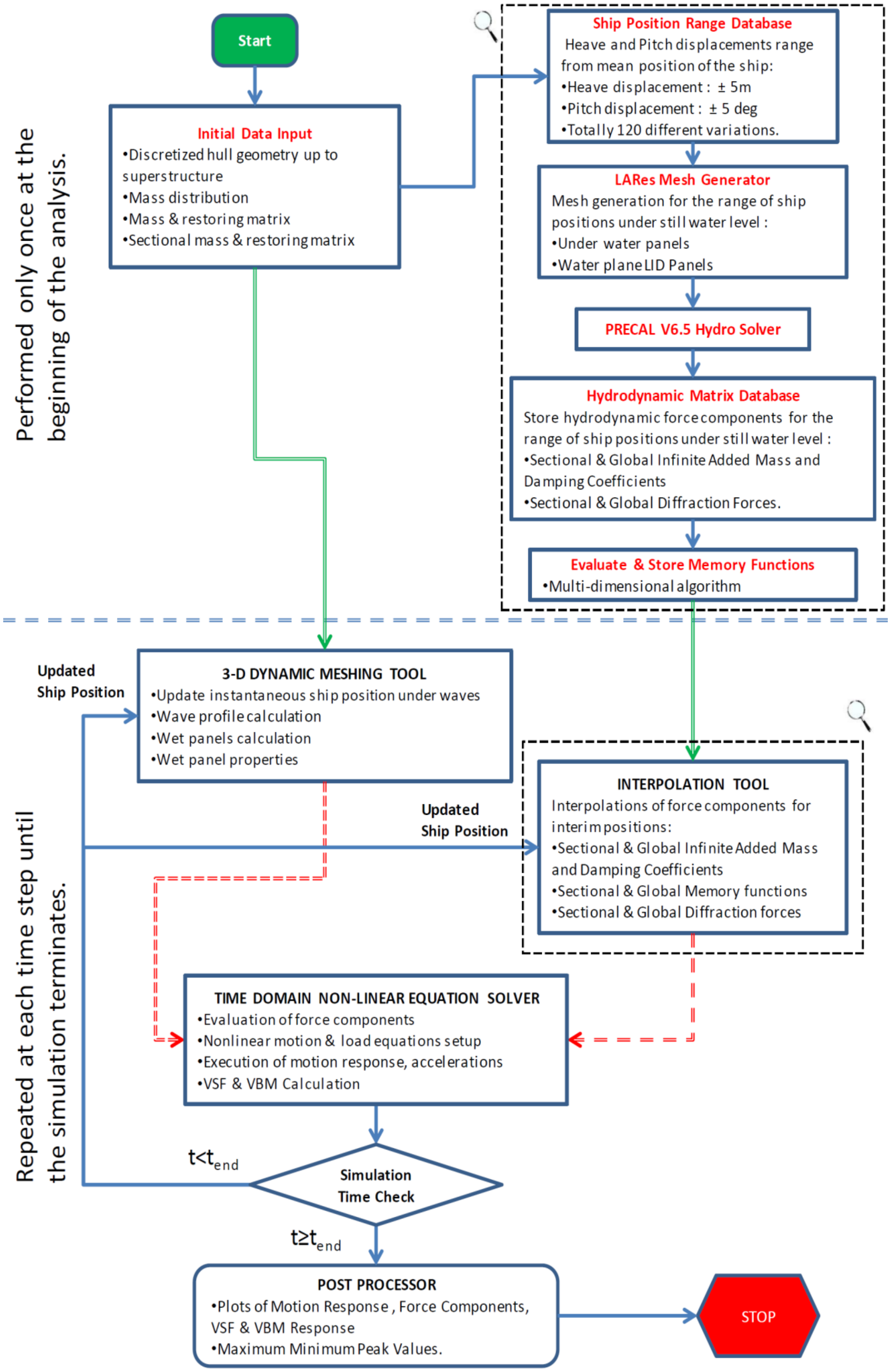

Figure 4.7: LARes L3 flowchart

At the body-nonlinear computation level, a database of pre-calculated global and sectional damping coefficients, diffraction force complex amplitudes and infinite frequency added mass and damping coefficients is generated in PRECAL with respect to a pre-calculated range of instantaneous wetted positions of ship under the still water level. In order to perform this daunting process, a pre-processor called LARes Mesh Generator (LMG) has been developed. In the following sub-section, details of the LMG are explained explicitly.

4.7.1 Mesh Generation

The LMG pre-processor is generated to cut and re-map the ship panels under the still water level after the vessel's translation and rotation. In essence, this process is a simple example of the surface to surface intersection. Although the intersection process seems to be simple, in practice, it is a very time consuming task to perform due to the complexity of the ship hull geometry. The LMG code has been developed in order to eliminate the need to use third party software for the surface to surface intersection process. The LMG code only takes the input of the initial mesh of the ship geometry once and then performs the intersection between the translated and rotated vessel geometry with the mean sea level through a pre-defined translation and rotation range.

The translation and rotation range of the ship is defined in the first module of the LARes L3 software for once. In the current S-175 containership study, the ship position range scans through 120 different variations in which the heave displacement of the ship varies from -5 meters to +5 meters and the pitch displacement varies from -5 degrees to the +5 degrees. It must be remembered that the range of ship positions is not identical for all ships; however for containerships with highly flared geometries, 120 different cases are found to be sufficient to keep the accuracy of the simulation at an acceptable level. In the case of a short range of translations and rotations, it is highly possible to observe jumps in the radiation and diffraction forces in large amplitude seakeeping simulations. In the current analysis, the range of the ship positions includes extreme conditions such as bulb and propeller emergence. It needs to be remembered again that in this level of nonlinearity the

Froude-Krylov and restoring forces are calculated with respect to the actual wetted portion of the vessel under the wave profile. The S-175 ship at a pitch rotation of -4 degrees is shown in the Figure 4.8 with the panels under the still water level and the waterplane area panels.

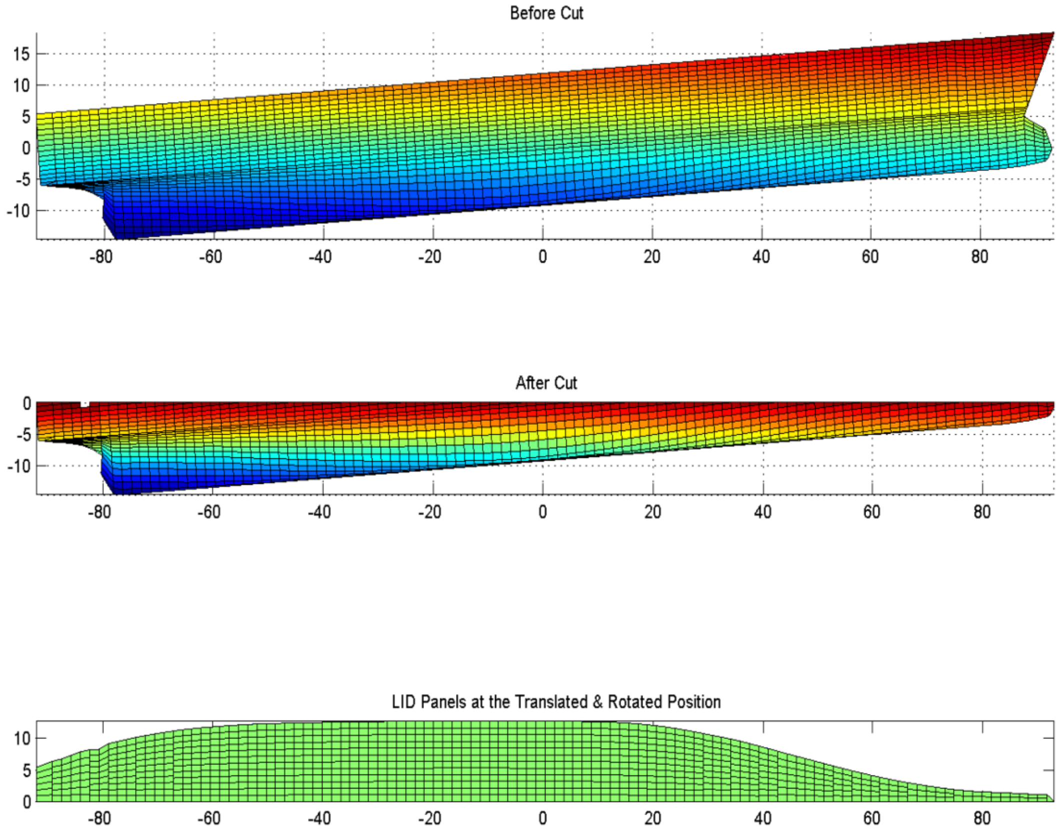

Figure 4.8: Rotated and meshed geometry of S-175 ship at -4 degrees of pitch rotation

After the intersection module, the panels adjacent to the still water level needs to be corrected. Small panels adjacent to the still waterline level cause mathematical singularities in the BVP solution in PRECAL and this result in the software crash. Therefore, small panels close to the still water level need to be re-mapped in order to alleviate the irregular frequencies in the BVP solution. The LMG calculates the properties of each panel during the intersection of the ship hull panels with the still water surface. The panels which have smaller area than the defined area limit are merged with the adjacent below panel and the singularities in the BVP solution are automatically eliminated. The merging process of the panels close to the still water area is illustrated below:

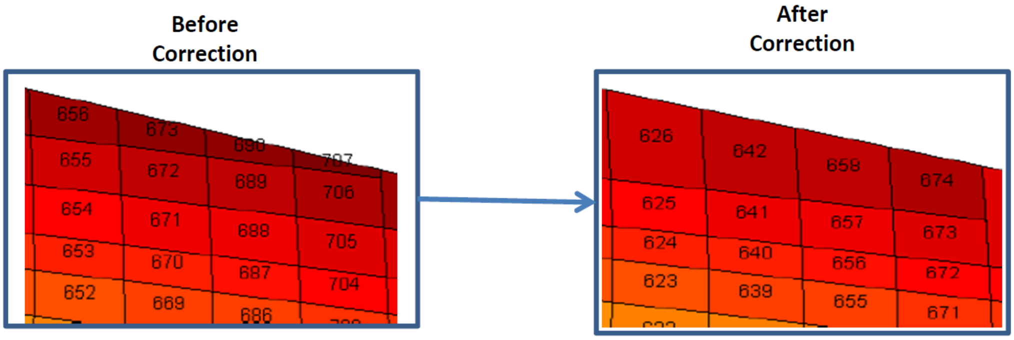

Figure 4.9: Cutted panel correction close to the water surface

The irregular frequencies in the damping curves are eliminated using the “Lid Panel Method” (See Chapter 3) in which the BVP is solved with underwater and waterplane area (LID) panels. The LMG automatically generates water plane LID panels after the intersection process between the updated ship position and the mean sea surface for each position of the ship and generates outputs of the nodal and facet files to be used in the following PRECAL calculations.

The number of distributed LID panes has a crucial importance in the suppression of the irregular frequencies in the BVP. The LID panels can be distributed in a coarse or fine mesh density where both have advantages and disadvantages in BVP solutions. In a coarse mesh distribution the BVP solution is accelerated, but the irregular frequencies might not be suppressed sufficiently. On the other hand, when the fine mesh density is used, it slows down the BVP solution, but in general suppresses all irregular frequencies. In order to suppress the irregular frequencies using the optimum the mesh density, number optimization of the waterplane area panels is performed. The optimum number of panels is calculated to be one panel per each metre of the ship breadth in LARes L3. In the Figure 4.10, the heave and pitch diagonal damping coefficients of the S-175 container ship for the initial position and the -5 degrees of pitch displacement at Fn=0.25 are compared to observe the influence of the LID panels in the BVP solution. It is observed that ship displacements influence the damping curves to a large extent therefore the influence of the position on the memory function evaluations should not be ignored in large amplitude seakeeping simulations and using one LID panel per metre of ship breadth is sufficient to suppress all irregular frequencies.

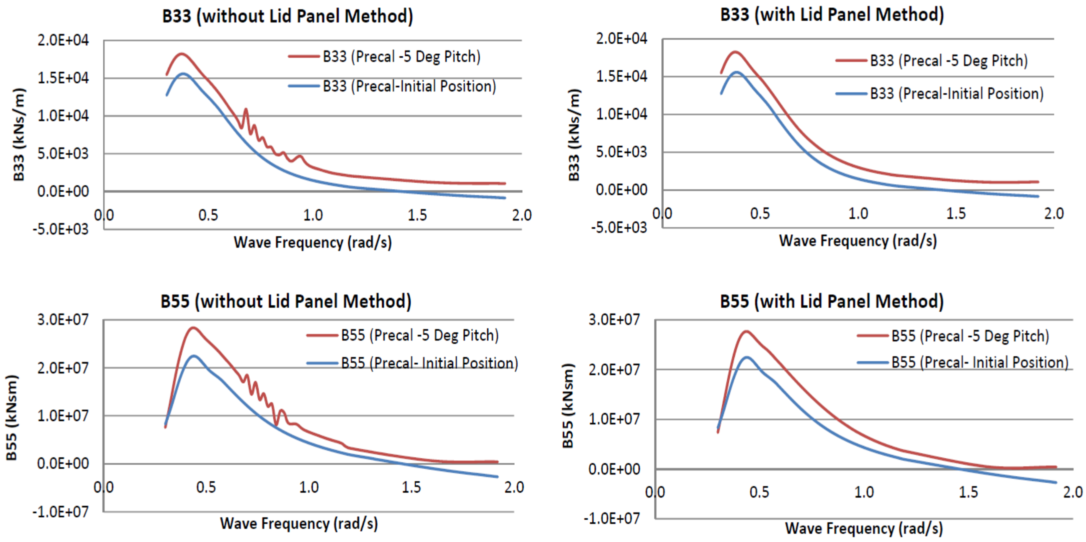

Figure 4.10: Diagonal damping coefficients for S-175 with and without the LID panels at Fn=0.25

The number of the LID panels is related to the translated and rotated position of the ship. In the Figure 4.11, waterplane areas are compared for the cases of -5 degrees and +5 degrees of pitch rotation at the initial draft of the ship and at the initial position of the ship. The change in the waterplane areas affects the restoring matrix in linear solutions and the BVP solution. However, in LARes L3 the linear restoring matrix is not taken into account due to the direct integration of the instantaneous buoyancy forces; instead, the radiation and diffraction force components are taken into account in time domain simulations.

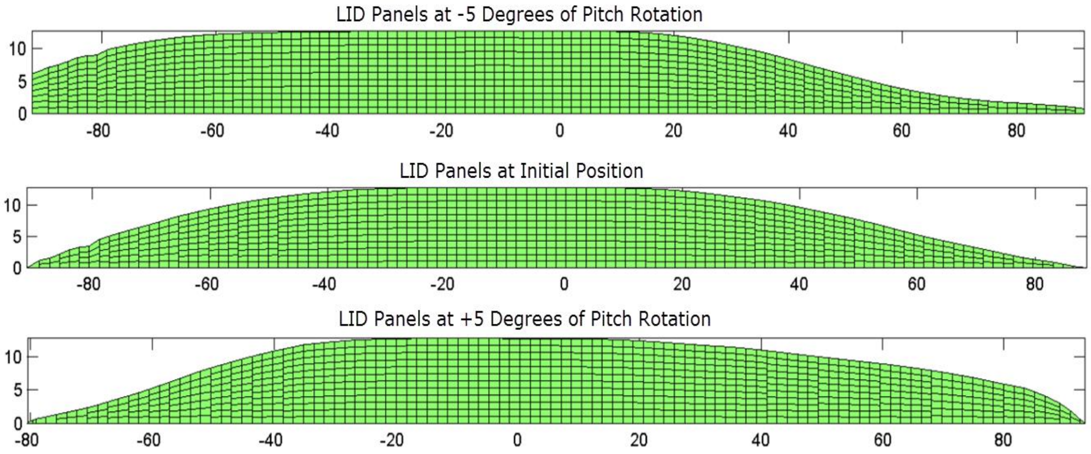

Figure 4.11: LID panels comparison for S-175 ship for various pitch displacements.

4.7.2 Hydrodynamic Matrix Storage

Subsequent to the solution of the BVP in PRECAL, all data related to the radiation and diffraction forces needs to be re-organized in order to accelerate the memory function integrations and subsequently the data interpolation processes. The LARes L3 code is designed to distribute the individual sets of the global and sectional infinite added mass and infinite damping coefficient matrices, damping coefficient curves and complex diffraction force amplitudes into multi-dimensional matrices. The multi-dimensional space algorithm accelerates the integration of the memory functions and the interpolation of the hydrodynamic variables during the simulations. Otherwise, the interpolation of each component in the memory functions, infinite added mass and damping matrices and diffraction force amplitudes would need to be performed one by one and that would result in an elevated computational cost. All of the radiation and diffraction force components have the data sets for 120 different position cases in which all are calculated through the pre-defined frequency range.

4.7.3 Evaluation of Memory Functions

In time-domain seakeeping analysis the evaluation time of the memory functions requires a long computational time. In the present thesis, the time domain equations are solved using the Impulse Response Function (IRF) approach. In the IRF approach, the memory functions need to be evaluated only once before the simulations from the pre-calculated potential damping coefficients and they can be used for various simulation cases. This feature of the IRF approach provides an efficient way to implement transient fluid responses into the time domain seakeeping simulations. In the LARes L3, 120 different position cases are defined to be solved in the BVP which necessitate the derivation of 120 memory functions for each forward speed case. The computational time of the memory functions is directly related to the truncation time. The truncation time and time step in the simulations are defined to be 30 seconds and 0.1 seconds respectively. In order to eliminate the drawback of the computational cost of the memory functions, multi-dimensional space algorithms are utilized in the integration process. In the multi-dimensional integration approach, all position cases are thought of as if they are the composite layers of a cube. The integration process of the memory functions is illustrated in Figure 4.12, which is performed simultaneously using Equation (3.36) for all position cases through the range of potential damping coefficients.

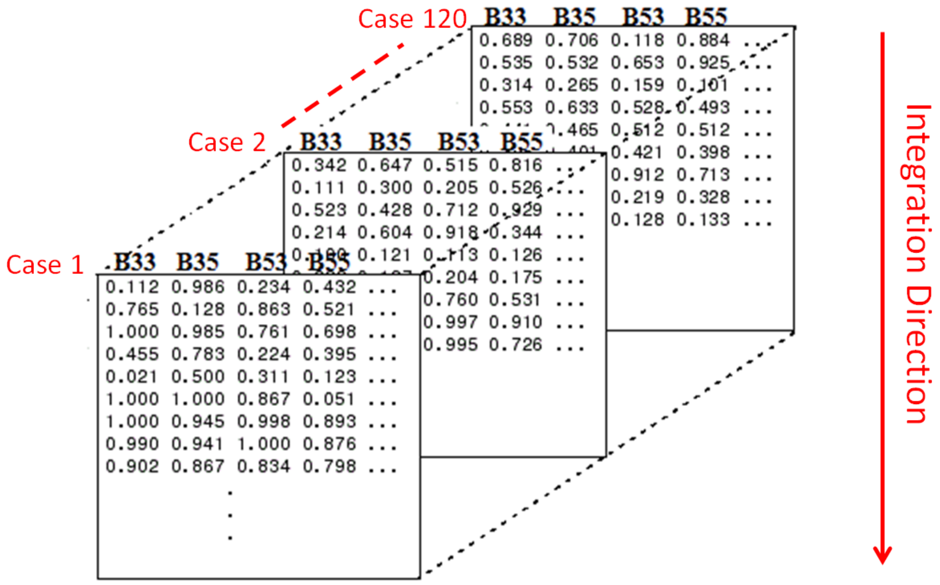

Figure 4.12: Multi-dimensional memory functions integration

4.7.4 Evaluation of Interpolation

Theoretically, at each time step the ship position changes and the BVP needs to be re-calculated with respect to the updated position under the still water level. However, the evaluation of the BVP at each time step increases the computational time and makes the software impractical to run. Hence, in practice, the pre-defined sets of positions are solved in the BVP and then for the interim positions, multi-dimensional interpolation is performed. The multi-dimensional interpolation algorithm is fast compared to the one by one interpolation of all components in the hydrodynamic data sets. All position cases are designed to be the internal layers of a cube. In order to evaluate the hydrodynamic data at an interim position of a ship; the cube is sliced transversely and the mid-layer containing all interpolated data is extracted in one step for the desired position. In the LARes L3 software, global and sectional infinite frequency added mass and damping coefficients, memory functions, and complex diffraction force amplitudes are interpolated through the pre-defined range of database at each time step without extra computational cost.

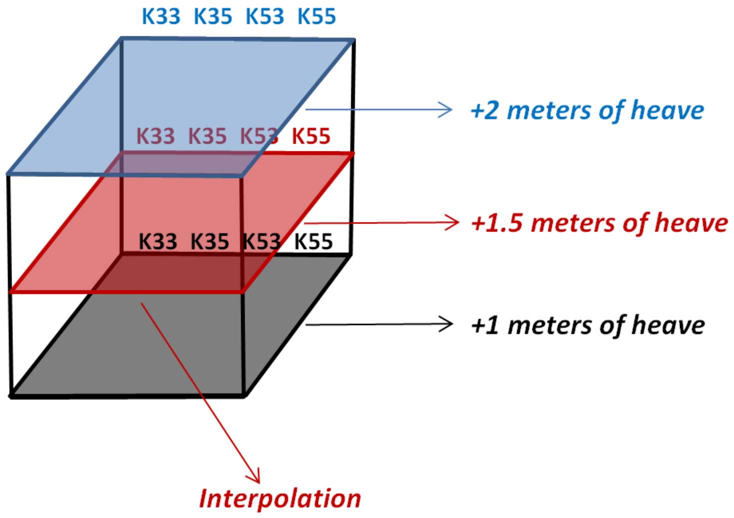

Figure 4.13: Multi-dimensional interpolation of memory functions

The logical interface of the interpolation tool is performed by using the if-then-else structures. In order to evaluate the interim position hydrodynamic forces, all of the cases need to be processed in the logical loops in advance. In LARes L3, the combination of the 120 different position cases is performed in the interpolation tool which satisfies all of the positions. The main subroutine consists of all hydrodynamic date in advance therefore only has the input for exact heave and pitch displacements in order to perform the interpolation.

In heavy weather conditions, ships might experience amplitudes of heave displacement of more than 5 meters and pitch rotation of more than 5 degrees. In such situations, the interpolation module is designed to use the maximum calculated data sets for the positions out of the interpolation range. For most cases, the defined range of ship positions is sufficient to analyze large amplitude motions. Indeed, when the defined range of the interpolation module is exceeded, ships start to experience water on deck incidence and that is not accounted for in the evaluation of the radiation and diffraction forces.

4.8 Summary

The main aim of this chapter is to provide knowledge about the numerical methods applied in the LARes L2 and LARes L3 in detail with a focus on their body nonlinearity levels. The common modules which take part in the LARes L2 and LARes L3 models are explained in detail underlining their importance in the time-domain simulations. The importance of time-dependent meshing process is explained and different meshing approaches are compared to investigate their advantages and disadvantages for floating objects in large amplitude time-domain simulations. Flow charts of the LARes L2 and LARes L3 models are illustrated step by step in order to observe the differences on the applied hydrodynamic forces and to investigate the model differences with respect to the varying body nonlinearity levels. In the body nonlinear (level 3) model, computational domain preparation using the LMG tool is explained with a focus on the inner free surface panels and panel corrections for which are adjacent to the free surface level. Furthermore, in order to store and process hydrodynamic data output from the frequency-domain software PRECAL for different combinations of ship positions; multi-dimensional storage, integration and interpolation tools are explained explicitly. Multi-dimensional integration and interpolation processes increase the computational efficiency to overcome the elevated computational cost in the LARes L3 model.

Chapter 5

Validations

5.1 Introduction

In this chapter, validation of the wave induced ship motion and load estimations are performed. The motion and internal load estimations are compared with the experiments while the hydrodynamic and internal load force components are compared with PRETTI software in order to verify the accuracy of the seakeeping models. In order to achieve this purpose, linear and non-linear time domain seakeeping models are simulated in small amplitude waves and the accuracy of the motion and load equations and its time varying hydrodynamic force components are investigated in detail. In the following section, properties of the seakeeping models which are used to compare the time domain motion and load responses are provided. The LARes model is sub-grouped under the names LARes L1, LARes L2 and LARes L3 for the level 1 (Linear), level 2 (F-K nonlinear) and level 3 (Body nonlinear) approaches respectively.

5.2 Comparison of Time-domain Seakeeping Tools

This section compares different time-domain seakeeping models in detail focusing on their body nonlinearity levels. The comparisons will be used in the next chapters in large amplitude motion and load estimations therefore it has a high importance to reveal the sources of difference in motion and load responses. The details of the formulation of LARes L2 and LARes L3 models were aforementioned in the Chapter 3 and Chapter 4. The aim of this section is to provide the overall comparison of the aforementioned time-domain seakeeping models and to underline the main differences implemented in the numerical methods and in different body nonlinearity levels of hydrodynamic force calculations. In the present thesis, frequency-domain hydrodynamic coefficients are fed to the LARes tool from PRECAL software. PRETTI software is used for the validation purpose in the nonlinear motion and load responses because it uses the PRECAL hydrodynamic forces and coefficients. Table 5.1 provides the comparison of main properties of the LARes L2 and LARes L3 with the PRETTI software below:

Table 5.1: Comparison of time-domain seakeeping tools

Definitions	**PRETTI**	**LARes L2**	**LARes L3**
Source Formulation & Time Domain Equations Solver	3-D Panel Method, Green Source Formulation Cummins's (1962) Time Domain Impulse Response Motion Equations		
Acceleration Solutions Reference Frame	Body Fixed Reference Frame	Earth Fixed Reference Frame	Earth Fixed Reference Frame
Pressure Integration	Gaussian Quadrature	Hess & Smith	Hess & Smith
Body Nonlinearity Level	Level 2	Level 2	**Level 3**
Input of Linear Radiation & Diffraction Forces	3-D Freq. Domain PRECAL	3-D Freq. Domain PRECAL	3-D Freq. Domain PRECAL
Froude- Krylov	Non-linear	Non-linear	Non-linear
Restoring Forces	Non-linear	Non-linear	Non-linear
Radiation Forces	Linear	Linear	**Quasi-Non-linear**
Diffraction Forces	Linear	Linear	**Quasi-Non-linear**
Matrix Inverse Operation	GMRES	LU Decomposition with Partial Pivoting	LU Decomposition with Partial Pivoting

It is clearly observed from the Table 5.1 that in all of the models 3-D panels with Green sources method are used with the IRF time-domain approach. Main differences between the tools arise from the ship acceleration solutions, pressure integration methods, implemented body nonlinearity levels, utilization of the radiation and diffraction forces and matrix inverse operations. It can be clearly observed that the LARes L2 and PRETTI have the same level of body nonlinearity while the LARes L3 has a more advanced formulation compared to the LARes L2 and PRETTI models to evaluate the quasi-non-linear hydrodynamic forces.

Proper evaluation of the instantaneous wetted portion of ship hull is one of the most important factors in the accuracy of the time-domain simulations. In steep waves the panels around the wave elevation level are half dry/wet and this cause problem in the pressure integrations during the simulations. In PRETTI software, four point Gauss integration method is used to integrate the pressures applied on panels. For each panel, each of the Gauss points is checked for the updated ship position with respect to the relative wave elevation and only wetted points are taken into account in the F-K and restoring force evaluations. In PRETTI in order to speed up the simulations, maximum possible wave elevation is computed by the summation of the highest %20 of the wave components without taking into account the phase angles in advance to the simulations and possible dry panels are eliminated from the following time steps (Van't Veer et al., 2009). In LARes L2 and LARes L3 models, in order to maintain the same number of Gauss points with the PRETTI software, original panels which are used in the BVP solution are divided into four sub-panels using the LMG. The subdivision of the panels results in an elevated computational cost in the time-domain solutions and also steady displacement and trim due to the discretization of the volume of the ship under the still water level. In order to alleviate the computational cost, vectorized algorithm is used define the panel properties and at each time-step all panels are checked whether they are wet or dry at the same time. Vectorisation process accelerates the solutions in much extent by cancelling the loops in the hydrodynamic force calculations. The only drawback of the vectorisation process is the need for large amount of computer memory. Nevertheless, the need for the memory for the vectorisation is smaller than it is needed in the BVP solutions.

In PRETTI software the maneuvering reference frames are used therefore accelerations need to be evaluated in 6 DOF at each time step. This means, even a motion mode is suppressed in the simulations, its acceleration component is calculated. For instance, when a ship advances in the head seas, surge acceleration need to be solved to maintain the integrity in the motion equations (Fossen, 1994). In PRETTI software, if a degree of freedom is suppressed, then the acceleration, velocity and displacement corresponding to that motion mode is fixed to zero on the zero speed Earth-fixed frame. However, all degrees of freedom are always taken into account in the solution of the accelerations in the body-fixed frame. The integration of the resultant accelerations is performed using the Earth-fixed frame in order to eliminate the need of the calculation of centripetal and Coriolis forces in the body-fixed reference frame. It was aforementioned in the Chapter 3 that, in large rotational motions, accelerations must be evaluated using the body-fixed reference frame otherwise the inertia matrix cannot be accounted as constant. However, in this thesis, the ship advances in the head seas and the maximum expected pitch rotation angle is less than 8-10 degrees. In small amplitude displacements and rotations inertia matrix of the ship can be assumed as constant in the simulations. Therefore, in LARes L2 and LARes L3 models all accelerations are solved and integrated using the steady advancing hydrodynamic frame.

In the LARes L3 model main difference from aforementioned models arise from the utilization of the hydrodynamic forces with the quasi-non-linear method. In PRETTI and LARes L2 models diffraction forces and memory functions are calculated once before the simulations and used throughout the time-domain simulations. Due to this reason, even in large amplitude waves, there will not be any difference in the diffraction forces in linear and F-K non-linear simulations. In the F-K nonlinear method the integrand in the radiation forces uses the exact nonlinear ship velocities in time domain simulations. Exact ship velocities possess some differences compared to the linear ship velocities especially in large amplitude simulations. In the LARes L3 model, 120 different position cases of diffraction and memory functions are evaluated and stored in the database in order to evaluate the quasi-non-linear radiation and diffraction forces for the container ship advancing in head seas. The influence of the varying diffraction and radiation forces calculated using the quasi-non-linear method will be investigated in the following chapters.

5.3 Main Particulars of S-175 Container Ship

The main particulars of the S-175 container ship and the hull geometry are provided in Figure 5.1 and in Table 5.2 respectively. Structural mass distribution properties of the hull is based on the values provided by Fonseca and Soares (2002).The mass distribution used in the present analysis is illustrated in the Figure 5.2.

Table 5.2: S-175 main particulars

Parameters	Values
L_{pp}	175.0 m
Beam amidships	25.4 m
Draught amidships	9.5 m
Depth amidships	15.4 m
Displacement	24668 tonnes
LCG from the midship	-2.557 m
Pitch radius of gyration	43.75 m
Cb	0.572

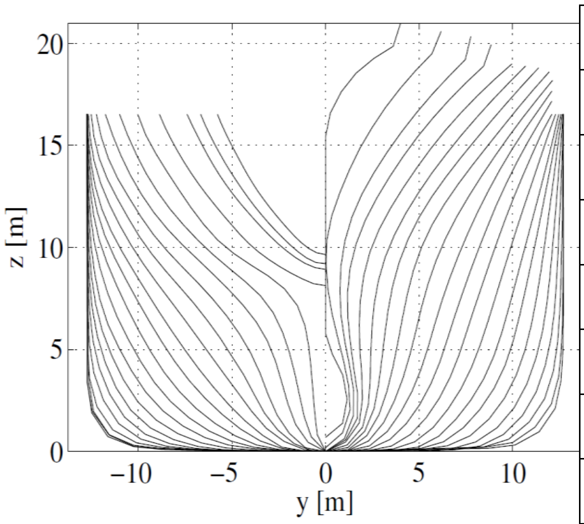

Figure 5.1: S-175 lines plan

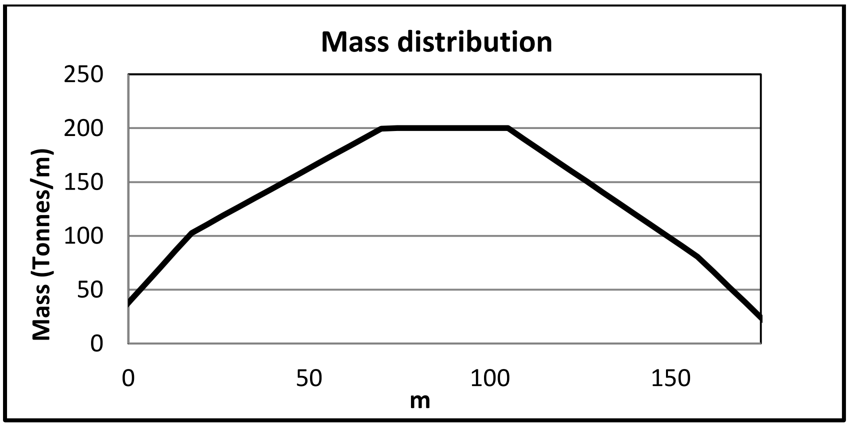

Figure 5.2: S-175 Container ship mass distribution

5.4 Validation of Motion Responses

This section presents the validation of the linear and nonlinear motion responses of a barge and S-175 container ship in small amplitude waves and in head seas with a focus on the body nonlinearity levels. The results of the PRETTI software is used to validate the motion displacements and the global hydrodynamic force components which are calculated in the LARes models. In order to investigate S-175 container ship motions in detail, small amplitude motion results at Fn=0.25 forward speed are compared with the experiments performed by Fonseca and Soares (2004).

5.4.1 Linear Motion Simulation Validations

Linear motion simulation validations are performed in order to verify the setup of motion equations and also the accuracy of the hydrodynamic force components. Time domain hydrodynamic forces are separated into components and compared with the PRETTI hydrodynamic force components in order to build a solid infrastructure for the large amplitude motion and global hydrodynamic force comparisons that will be performed in the next sections. In order to validate LARes L1 results, linear seakeeping analysis of a rectangular barge with main particulars 100 x 20 x 6 m (L, B, T) is performed at zero speed and in head seas and compared with the linear PRETTI results. Heave and pitch Response Amplitude Operators (RAO) are illustrated in Figure 5.3 for the barge at zero forward speed in head seas.

It is clearly seen from the Figure 5.3 that in the LARes L1 and linear PRETTI results heave and pitch RAO's are identical to each other. It was aforementioned that in the linear seakeeping analysis hydrodynamic forces are calculated with respect to the mean wetted surface of the body under the still water level and complex hydrodynamic force amplitudes are fed from the frequency-domain PRECAL software. The results of the frequency domain and time-domain results are nearly the same and small differences are originated from the frequency range of the damping coefficient curves. In the theory, in strictly linear problems, the frequency and time-domain solutions are related by the Fourier transforms therefore they need to be identical. Furthermore, in theory, the computational domain of the damping curves must have a range from zero to the infinite frequency. However, in the current analysis, damping coefficient curves are truncated at the maximum encountering frequency that can be calculated using the Equation (3.22), otherwise at some high frequencies oscillations will occur in the BVP solutions and this will cause fluctuations in the damping coefficients. In order to evaluate accurate memory functions damping coefficients must be smooth. The accuracy of the memory functions are highly dependent on the smoothness of the damping curves.

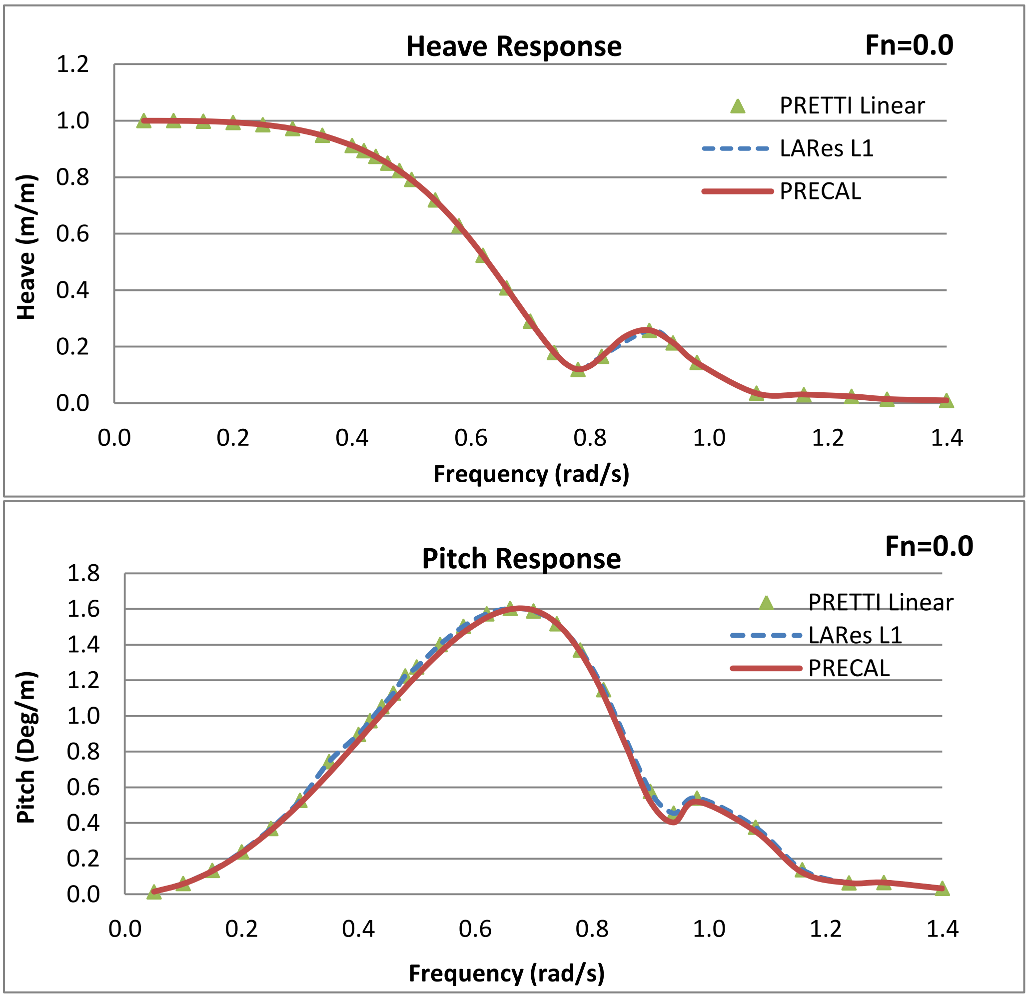

Figure 5.3: Heave and pitch RAO of the barge at Fn=0.0 in head seas

The motion equations are solved using the Newton's equations in time domain simulations and are illustrated below for the barge at zero speed which is subjected to waves at ω=0.3 rad/s and with 1 meters of wave height (H_w):

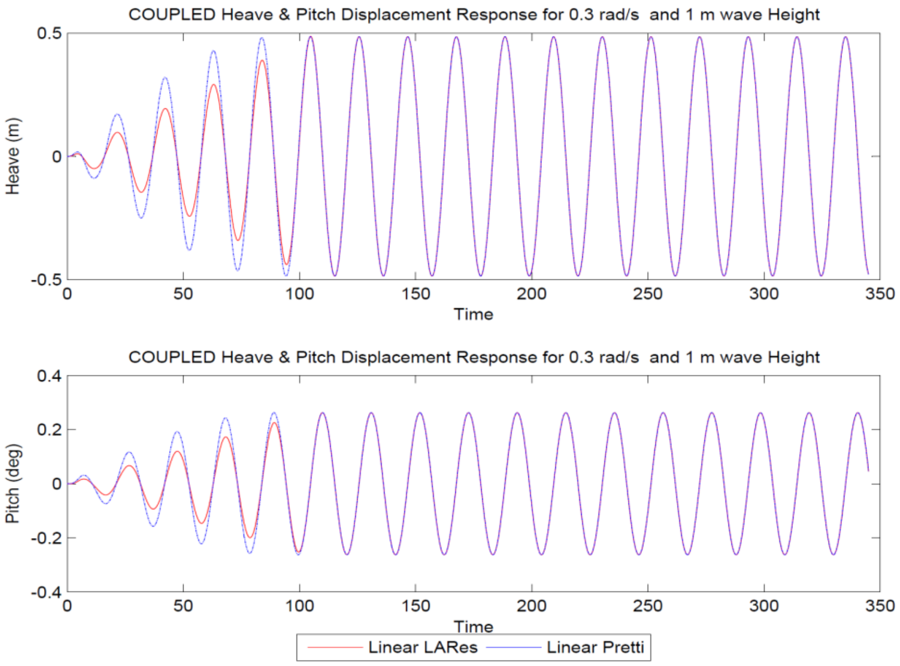

Figure 5.4: Linear motion response of barge at ω=0.3 rad/s at H_w=1m Fn=0.0

It is clearly seen from the motion responses that LARes L1 and linear PRETTI results are identical. The differences at the first parts of the analysis are originated from the preference of the ramp functions. Ramp functions ensure that the wave induced hydrodynamic forces are applied slowly on the structure to avoid large motions at the start. The utilization of ramp functions alleviates the problems which occur at the transient phase of the analysis. PRETTI software uses a sinusoidal ramp function whose length is defined by the user while in LARes linear ramp function is used in the hydrodynamic force evaluations. The formulations of the ramp functions in PRETTI and LARes models are given below:

$$Ramp(t) = sin\frac{\pi t}{2T_{ramp}} \qquad t < T_{ramp} \qquad \text{PRETTI} \qquad (5.1)$$

$$Ramp(t) = \frac{t}{T_{ramp}} \qquad t < T_{ramp} \qquad \text{LARes} \qquad (5.2)$$

The main motion equation constitutes of the mass matrix and the total hydrodynamic forces and moments which are the sum of the hydrodynamic force components. Differences in the hydrodynamic force components cause differences in the motion and load responses therefore their validation is crucial. Linear time domain Froude-Krylov (F-K), restoring, radiation and diffraction forces are compared at zero speed and in head seas with the linear PRETTI results. The comparisons are illustrated in from the Figure 5.5 to Figure 5.8 as shown below:

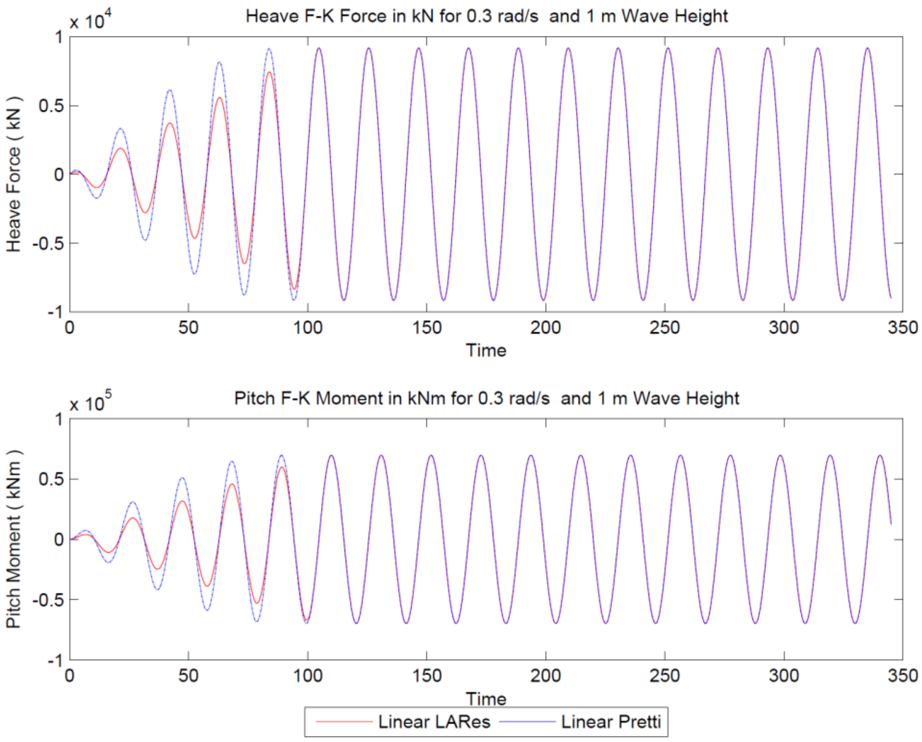

Figure 5.5: Linear F-K forces at ω=0.3 rad/s and Hw=1m at Fn=0.0

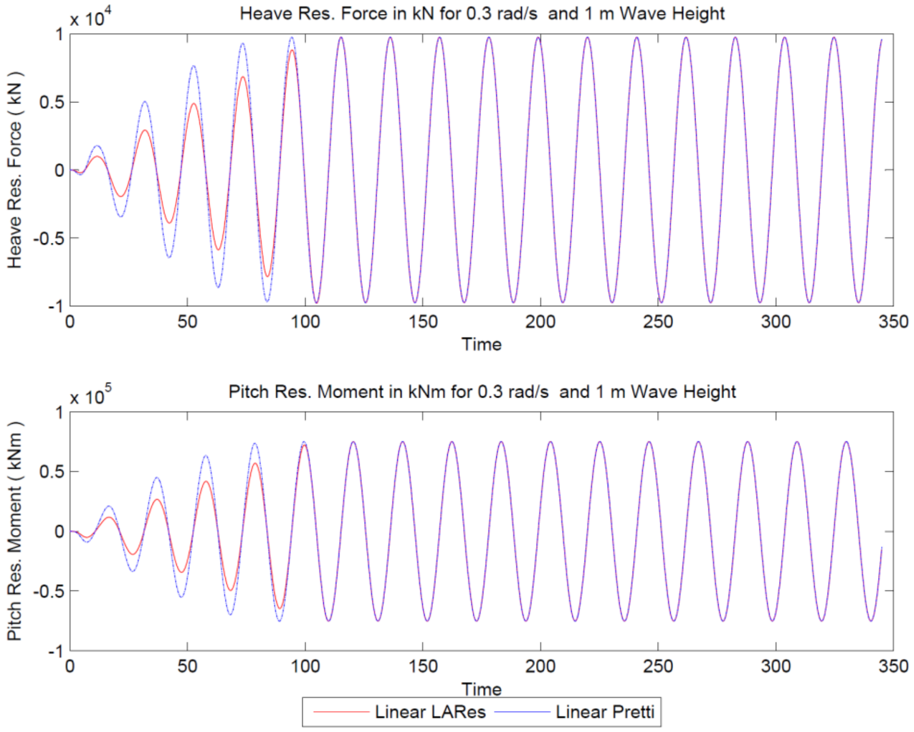

Figure 5.6: Linear restoring of barge forces at ω=0.3 rad/s and H_w=1m at Fn=0.0

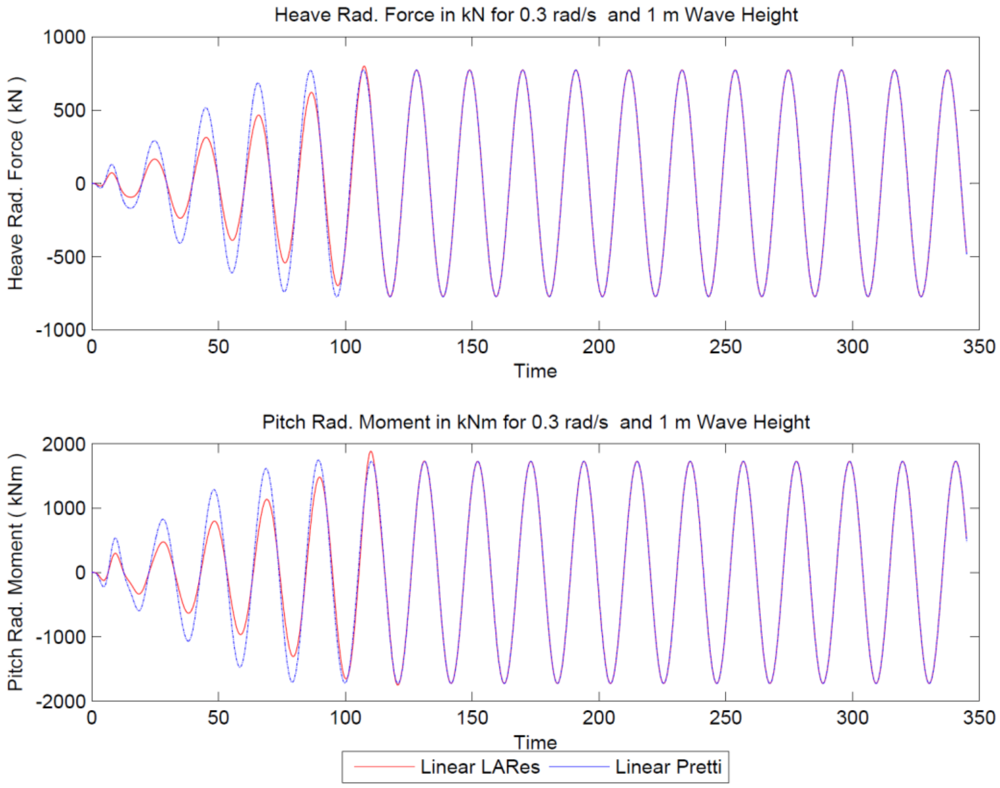

Figure 5.7: Linear radiation forces of barge at ω=0.3 rad/s and H_w=1m at Fn=0.0

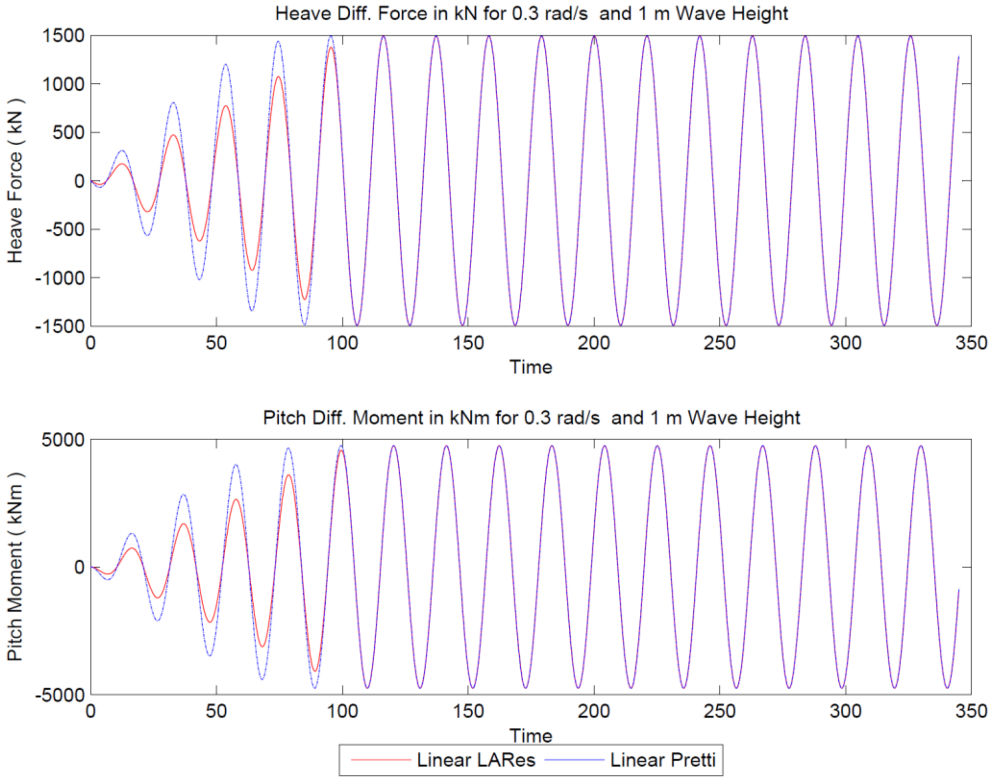

Figure 5.8: Linear diffraction forces of barge at ω=0.3 rad/s, H_w=1m and Fn=0.0

In general, the F-K and restoring forces constitute the biggest portion of the total hydrodynamic forces, especially in long wave lengths. Incident wave forces and restoring forces applied on the barge are illustrated in the Figure 5.5 and Figure 5.6 respectively. It is clearly observed from the figures that the results are identical and this is the validation of the complex force amplitudes and the time factor $e^{-i\omega_e t}$ are applied accurately in the F-K and restoring force evaluations. Otherwise if they were not applied accurately there would have been phase lags between the LARes L1 and linear PRETTI force components. Phase lags results in amplitude differences in the motion responses.

The evaluation of the radiation forces in time domain simulations is crucial in order to apply accurate damping forces. Frequency dependent part of the radiation forces are calculated by the integration of the convolution of the memory functions and the exact velocity history of each motion mode. In order to evaluate the radiation forces accurately, the memory functions and the actual ship velocity components need to be evaluated accurately. In the current analysis, global memory functions are evaluated using the Equation (3.36). Linear radiation forces are compared in the Figure 5.7 and it is observed that the LARes L1 and liner PRETTI radiation forces and moments are identical. This validation possesses a high importance for the future calculations of the nonlinear radiation forces and moments to maintain a solid background for the analyses which will be performed in higher level of body nonlinearities.

The last component of the hydrodynamic force is the diffraction forces and moments which are calculated using the Equation (3.39). Diffraction forces are kept as linear in LARes L1, LARes L2 and in linear and nonlinear versions of PRETTI model. In the evaluation of the time-domain diffraction forces, complex force amplitudes, which are fed from PRECAL software, are multiplied with the time factor $e^{-i\omega_e t}$ and the real part of the force is used in the time-domain equations. In LARes L3 simulations the complex diffraction force amplitudes are calculated in 120 different position cases using the Equation (3.39) and implemented into the time-domain equations while using interpolation functions for interim positions. Therefore, in the LARes L3 the applied diffraction forces are calculated using the quasi-non-linear method. The influence of the different levels of body nonlinearity in the time-domain diffraction forces will be explained in detail in the following chapters. Linear time-domain diffraction forces are compared with the linear PRETTI results in the Figure 5.8 and it is observed that the diffraction forces and moments are identical with the PRETTI model results which maintain the accuracy of the time-domain diffraction forces evaluations in the ship motion simulations.

In the forward speed case, linear motion response analysis of the same rectangular barge is performed at 10 knots (Fn=0.164) in head seas. The frequency domain PRECAL, linear PRETTI and LARes L1 heave and pitch RAO's are compared at Fn=0.164 and the results are shown in Figure 5.9.

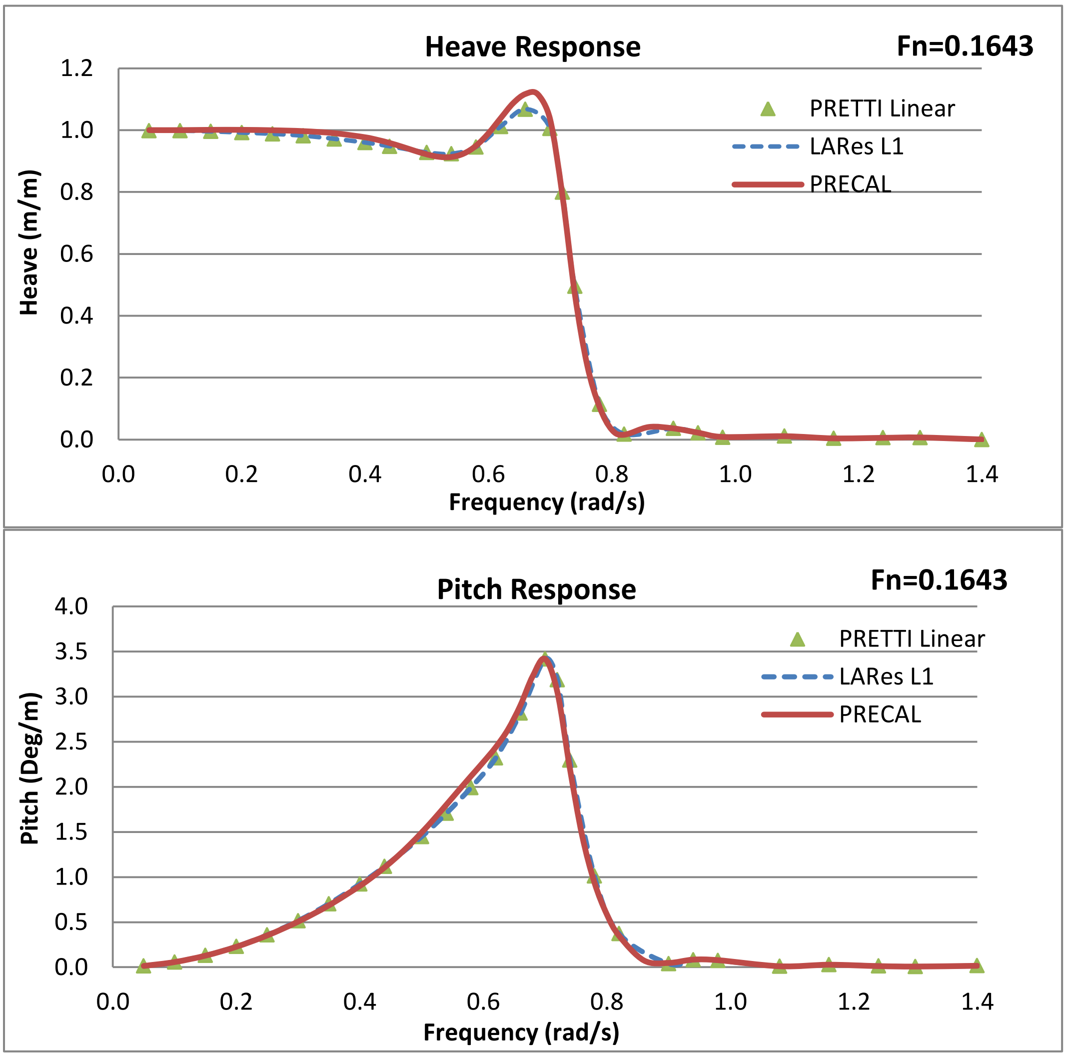

Figure 5.9: Linear heave and pitch RAO of the barge at Fn=0.164 in head seas

It can be clearly observed from the figures that the time-domain linear motion responses are identical in LARes L1 and linear PRETTI results for the forward speed case. At the resonance period time-domain heave responses are slightly under estimated than the PRECAL results due to the large time-domain radiation forces.

In order to validate the linear time-domain responses at a forward speed case, hydrodynamic force components are validated with the linear PRETTI results. Validation of the forward speed hydrodynamic force components verifies the integrity of the force and main motion equations at a forward speed simulation. Linear time-domain motion responses of the barge at ω=0.66 rad/s ($\lambda/L_{pp}\approx1.4$) and in $H_w=1$ and at Fn=0.164 are illustrated below:

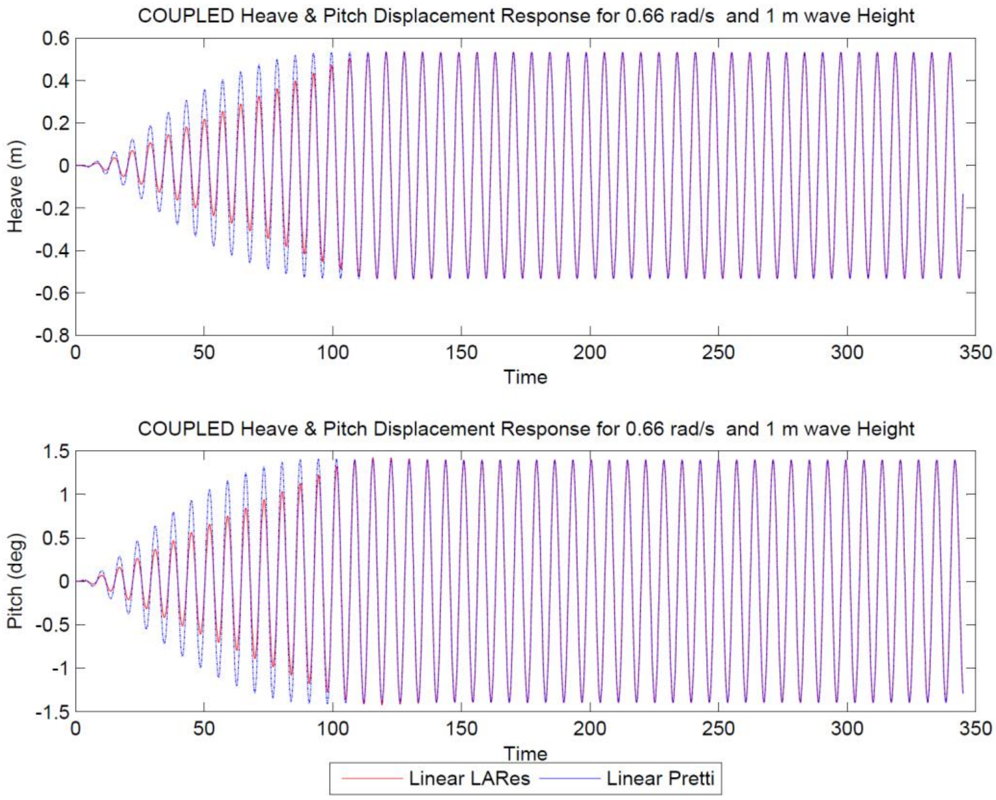

Figure 5.10: Linear motion response of barge at ω=0.66 rad/s, H_w=1m, Fn=0.164

It is clearly seen from the linear motion responses that LARes L1 and linear PRETTI results are identical at a forward speed of Fn=0.164. In order to validate the motion responses, time domain hydrodynamic force components at the same forward speed are investigated. Linear Time domain F-K, restoring, radiation and diffraction force components are compared at Fn=0.164 and in head seas with the linear PRETTI results and, are illustrated from the Figure 5.11to Figure 5.14 as shown below:

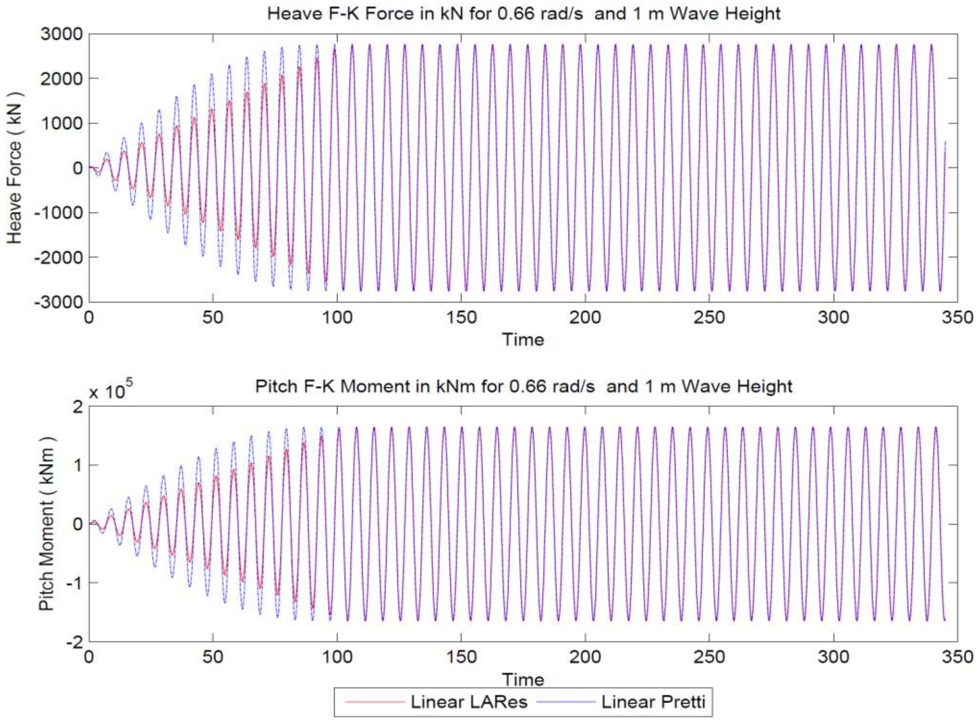

Figure 5.11: Linear F-K forces of barge at ω=0.66 rad/s, Hw=1m, Fn=0.164

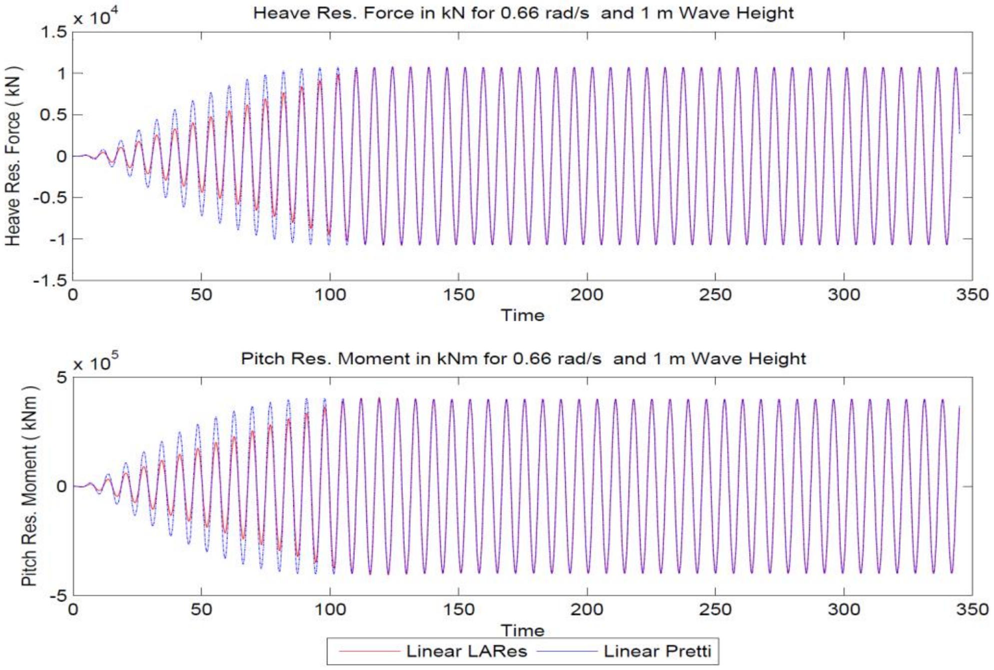

Figure 5.12: Linear restoring forces of barge at ω=0.66 rad/s, H_w=1m, Fn=0.164

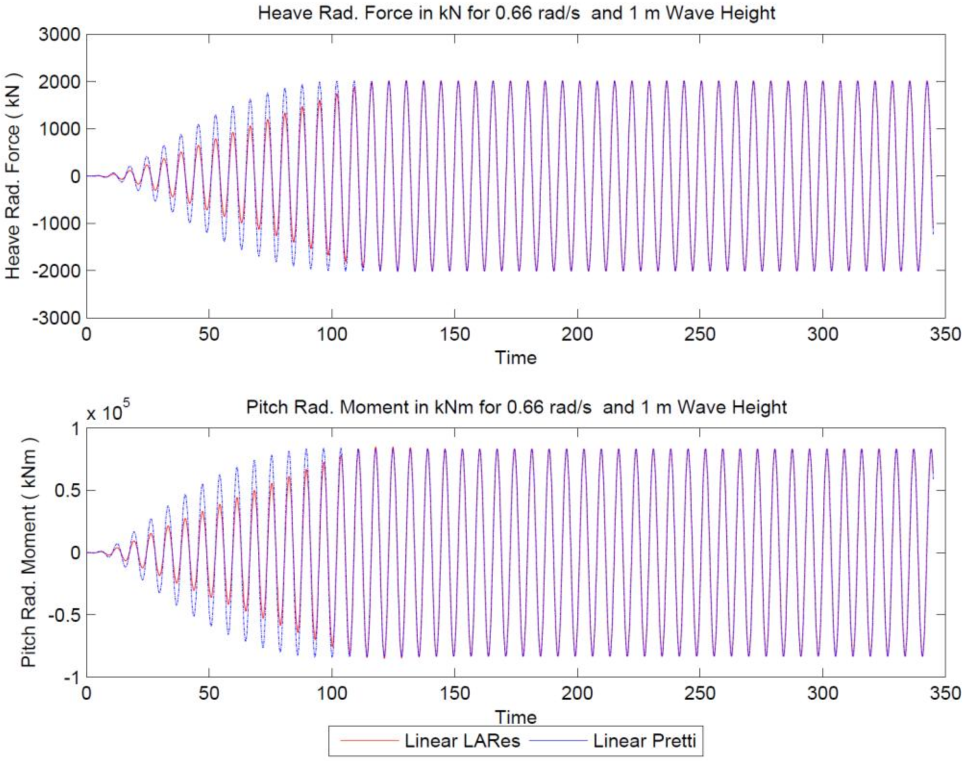

Figure 5.13: Linear radiation forces of barge at ω=0.66 rad/s, H_w=1m, Fn=0.164

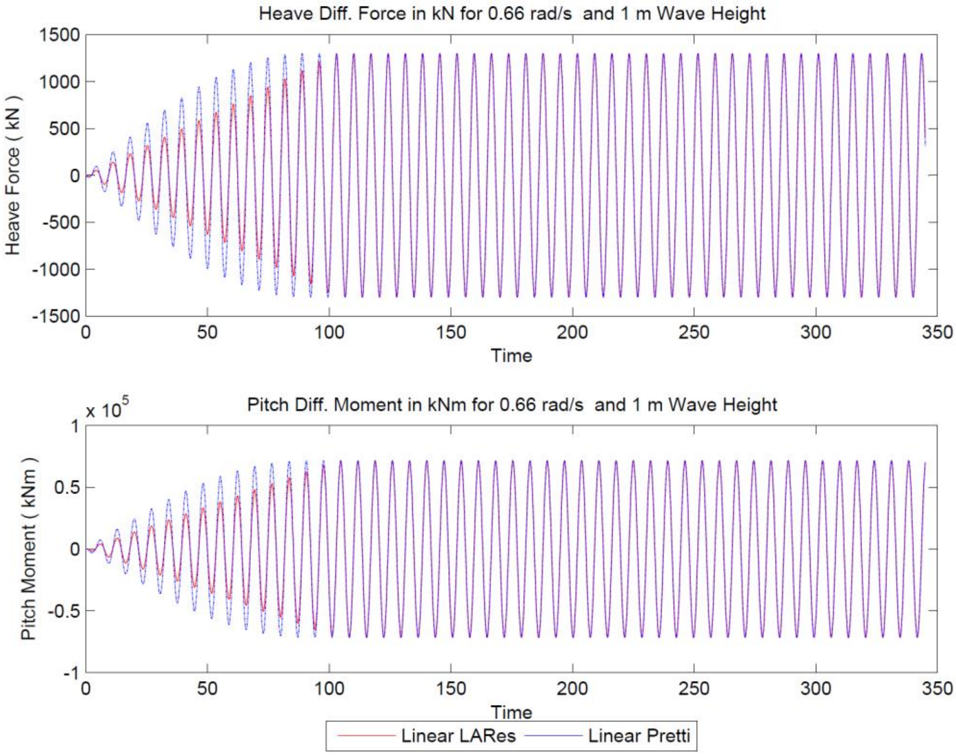

Figure 5.14: Linear diffraction forces of barge at ω=0.66 rad/s, H_w=1m, Fn=0.164

The incident wave forces and restoring forces applied on the barge at Fn=0.164, are shown in Figure 5.11 and Figure 5.12 respectively. It is clearly observed from the figures that the F-K and restoring forces are applied accurately in the forward speed formulation which is the validation of the complex force amplitudes and the complex time factor $e^{-i\omega_e t}$ are applied accurately in the F-K and restoring force evaluations.

The evaluation of the radiation forces in the forward speed time domain simulations needs special care due to the limiting encountering frequency concern which was mentioned in the Equation (3.22). At small encountering wave lengths scattering waves cannot be simulated in the BVP due to the large panel size compared to the wave length. In order to simulate the radiated waves properly, there must be at least 5 panels per encountering wave length. The comparison of the forward speed linear radiation forces are performed at Fn=0.164 with the linear PRETTI software .It is observed from the Figure 5.13 that linear time-domain radiation forces at forward speed case are identical with the PRETTI results. This is the evidence of the accuracy of the memory functions and the velocity histories during the time-domain simulations.

The forward speed diffraction forces and moments are also calculated using the Equation (3.39) with respect to the encountering frequency. Linear time-domain diffraction forces are compared with the linear PRETTI results. It is observed from the Figure 5.14 that the forward speed diffraction forces and moments are identical with the PRETTI results which maintain the accuracy of the diffraction forces evaluations for the linear forward speed linear time-domain simulations.

5.4.2 Nonlinear Motion Simulation Validations

In this section, the computational results of the nonlinear motion responses using the F-K nonlinear (level 2) and body nonlinear (level 3) models are validated with linear and experimental results in small amplitude waves in head seas condition. Level 2 hydrodynamic models are validated using the barge geometry and the differences between the LARes and PRETTI models at zero and forward speed cases are investigated in detail. The LARes level 3 hydrodynamic model is investigated using the S-175 containership at zero and forward speed cases in head seas while and motion responses are compared with the experiments provided in the (ITTC, 2010) at forward speed. In both of the LARes level 2 and level 3 models, hydrodynamic force components are investigated in detail and compared with the PRETTI hydrodynamic force components in order to the find out the origin of the differences in the force components during the simulations. The validation of the F-K and restoring forces, possess a high importance in the level 2 and level 3 computations due to their time dependent integration on the exact wetted area of the ship. The main reason of the selection of the barge geometry is to avoid nonlinear F-K and restoring forces in the time varying pressure integrations during the nonlinear simulations.

In nonlinear simulations restoring and F-K forces applied on the barge are completely linear due to the constant waterplane area and vertical walls around the still water level. The nonlinear heave and pitch response functions of the barge at zero speed, which are calculated using the LARes L1, LARes L2 and nonlinear PRETTI models, are illustrated in the Figure 5.15. It is observed from the figure that nonlinear heave and pitch motion responses are in a good agreement with the linear time domain motion response calculations in small amplitude waves at zero forward speed motion simulations. In small amplitude waves linear and nonlinear results need to be close to each other unless the geometry has a high nonlinearity. Moreover, it is also validated that the LARes L2 and PRETTI nonlinear results are identical in all frequency range at zero speed calculations.

Hydrodynamic force components obtained from the LARes L2 model are compared with the nonlinear PRETTI results in order to validate the force components in small amplitude waves. It was aforementioned that in the level 2 and level 3 formulations the F-K and restoring forces are evaluated with respect to the instantaneous wetted area under the wave profile therefore; the accuracy of these forces possesses high importance in the motion and load estimations. The simulations are performed at zero speed in order to suppress the forward speed effects in the hydrodynamic calculations. Hydrodynamic force components are calculated using the LARes level 2 model and are compared with the nonlinear PRETTI results for the barge around the resonant periods at ω=0.66 rad/s ($\lambda/L_{pp}\approx1.4$) and at H_w=1. This time, the transient part of the simulation is extracted from the simulation time and steady-state part of the hydrodynamic forces are compared and provided in the Figure 5.16 in detail.

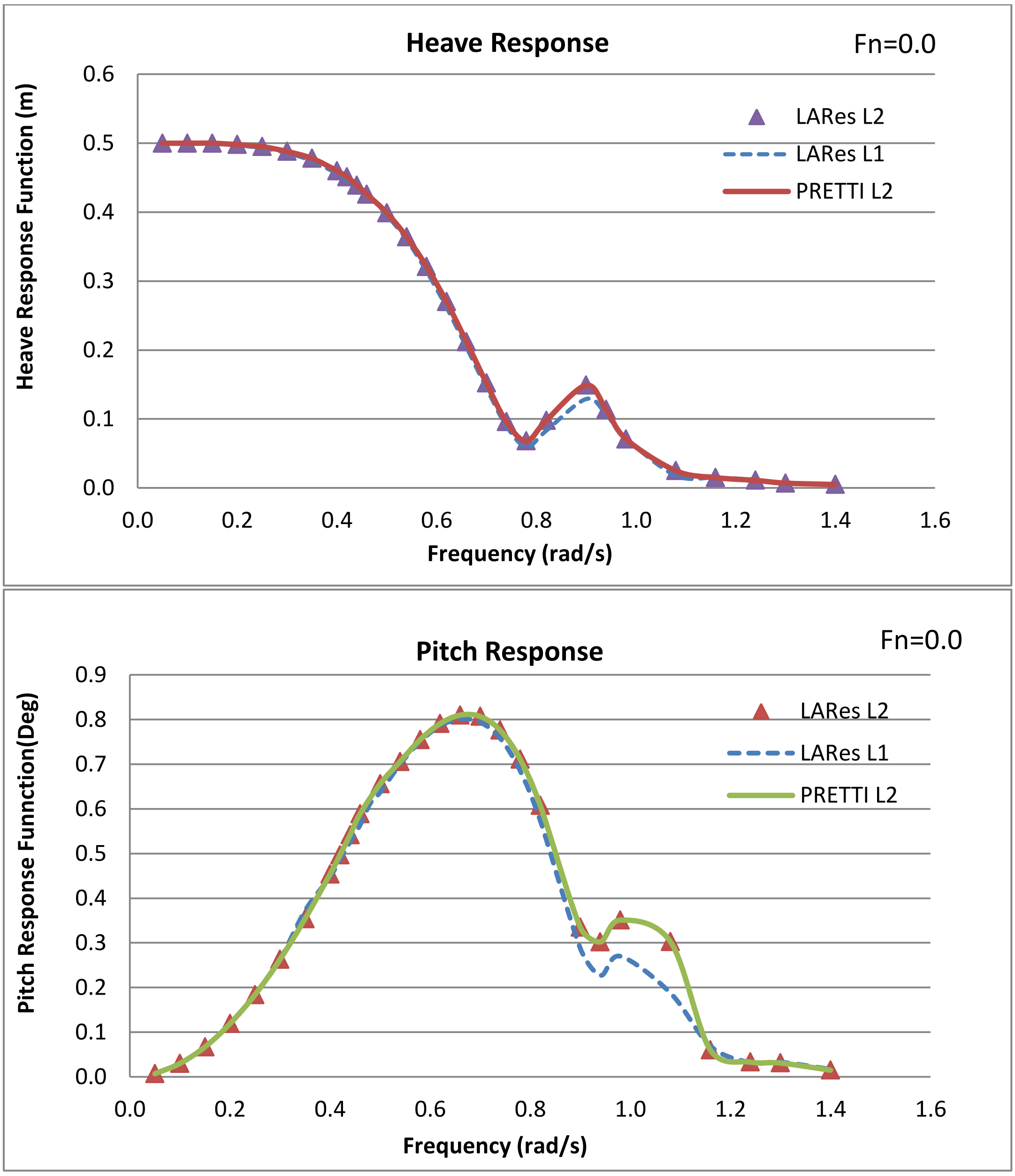

Figure 5.15: Nonlinear heave and pitch response functions of barge at H_w=1m, Fn=0.0

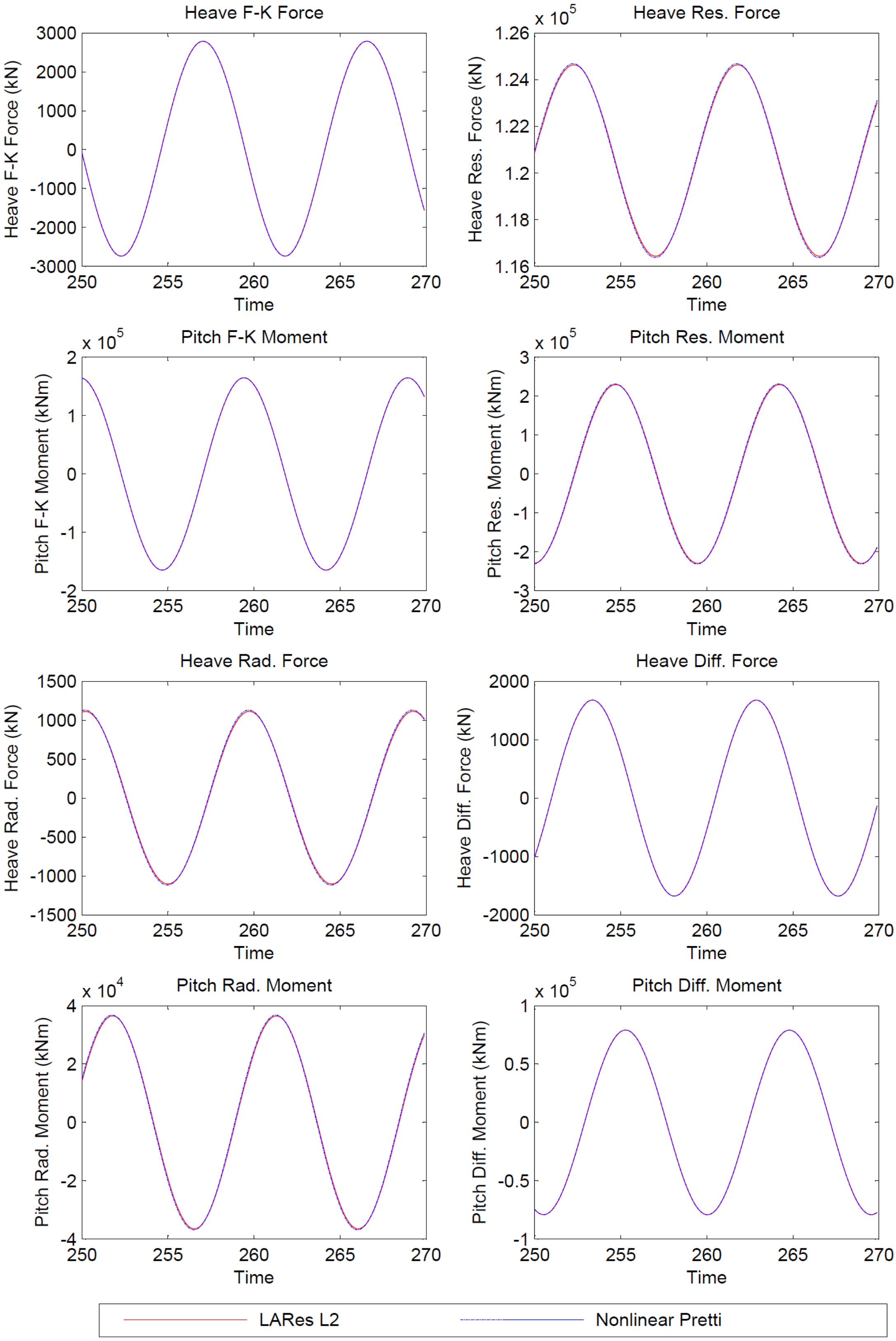

Figure 5.16: Nonlinear hydrodynamic force components of barge at ω=0.66 rad/s, H_w=1m, Fn=0.0

It is clearly observed from the Figure 5.16 that the F-K and restoring forces are identical with the PRETTI results, which is the validation of the pressure integrations on the exact wetted surface is performed accurately. It was aforementioned that, original panels that are used in the BVP solution are divided into four sub-panels in order to maintain the same order of computation level used in the four point Gauss integration in the PRETTI model. The radiation and diffraction forces are found to be identical with the nonlinear PRETTI results at zero speed simulations. In F-K nonlinear simulations radiation and diffraction forces are kept as linear. Diffraction forces are exactly the same as it is calculated in the linear time domain simulations because in the level 2 nonlinearity it is only dependent on the complex diffraction forces which are fed from the 3D PRECAL software. However, the radiation forces are calculated from the convolution integral which convolutes the memory functions with the exact ship velocities. The accuracy of the radiation forces validates the heave and pitch motion velocity vectors and the memory functions corresponding to the motion modes during the time-domain simulations. In non-linear simulations, body velocities show nonlinearity dependent on the encounter frequency and the amplitude of the incident waves. In this sense, radiation forces are partly nonlinear in the level 2 model due to their convolution with the nonlinear ship velocities.

The nonlinear time-domain motion responses at a forward speed case are more complicated due to the surge motion influence in the hydrodynamic force components. In order to investigate the nonlinear motion responses of the rectangular barge, simulations are performed in head seas at Fn=0.164 and the heave and pitch response functions are compared using the LARes L1, LARes L2 and nonlinear PRETTI models in the Figure 5.17. It is clearly observed that, nonlinear models provided different motion responses compared to the linear estimations in which all force are kept as linear. Theoretically, bodies with wall-sided geometries in nonlinear and linear seakeeping models need to provide close results to each other. In order to find identical motion responses kinematic constraints need to be used to control surge responses. The kinematic constraints are automatically taken into account in the physical model tests because vessels are either towed by a carriage or self-propelled system while they advance through the waves.

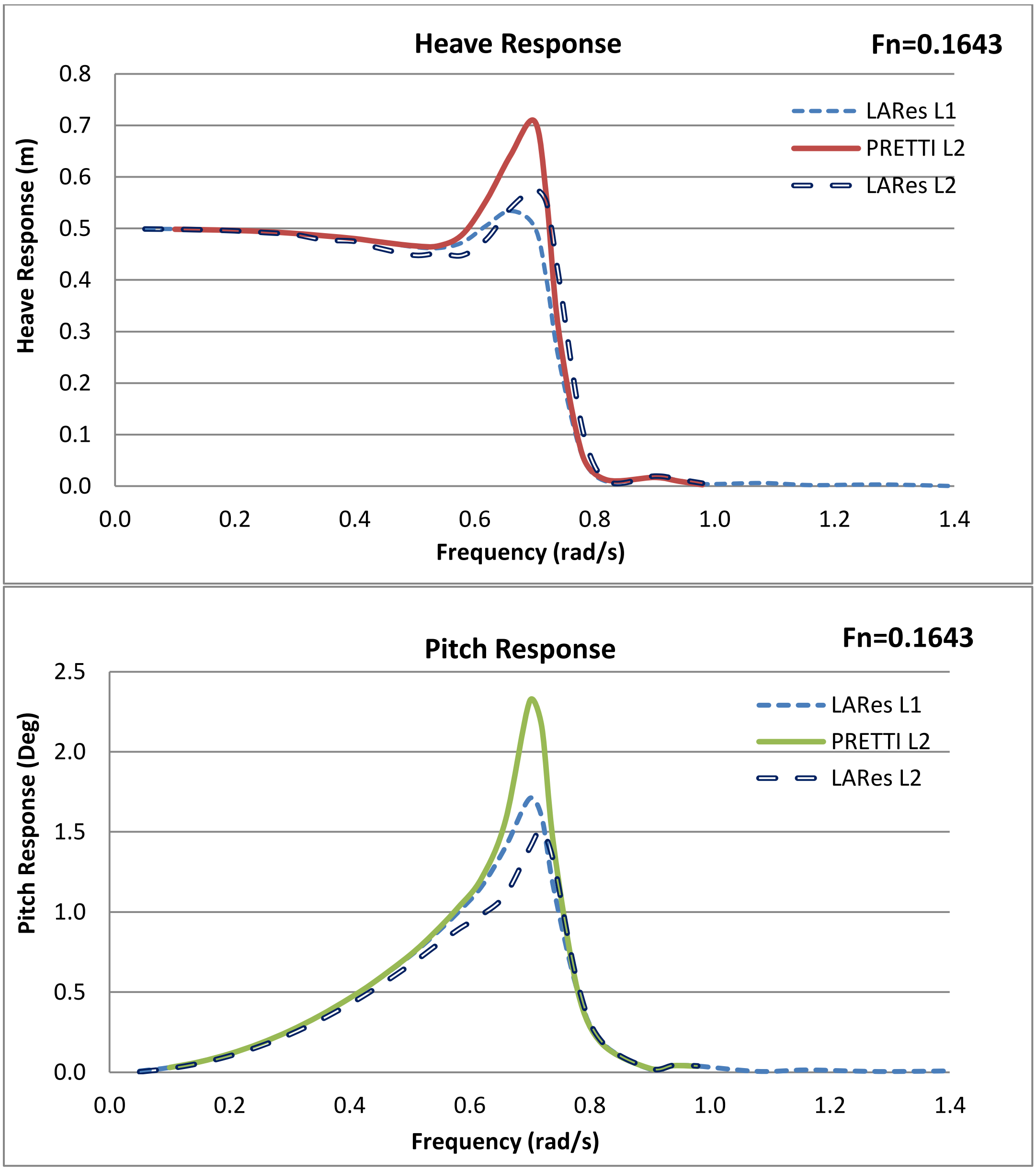

Figure 5.17: Nonlinear heave and pitch response functions of barge at H_w=1m, Fn=0.164

In the current analysis, surge motions have influenced the heave and pitch responses in high extents due to the geometry of the barge. In blunt bodies, such as barge, surge motions affect more compared to the slender bodies due to the vertical normal direction on the body which results in high surge pressures. It was verified before that the LARes L2 and nonlinear PRETTI motion responses are identical at zero speed computations. In that sense, the difference between the linear and nonlinear PRETTI models arise from the surge forces applied in the hydrodynamic force components in forward speed simulations. In order to investigate the effect of the surge motion, LARes L2 motion responses and hydrodynamic force components are compared to the nonlinear PRETTI results near to the resonant area in small amplitude waves. The heave and pitch motion trajectories are extracted from the total simulation time in order to suppress the transient period of the motions and the compared with PRETTI results at ω=0.66 rad/s and at H_w=1 below:

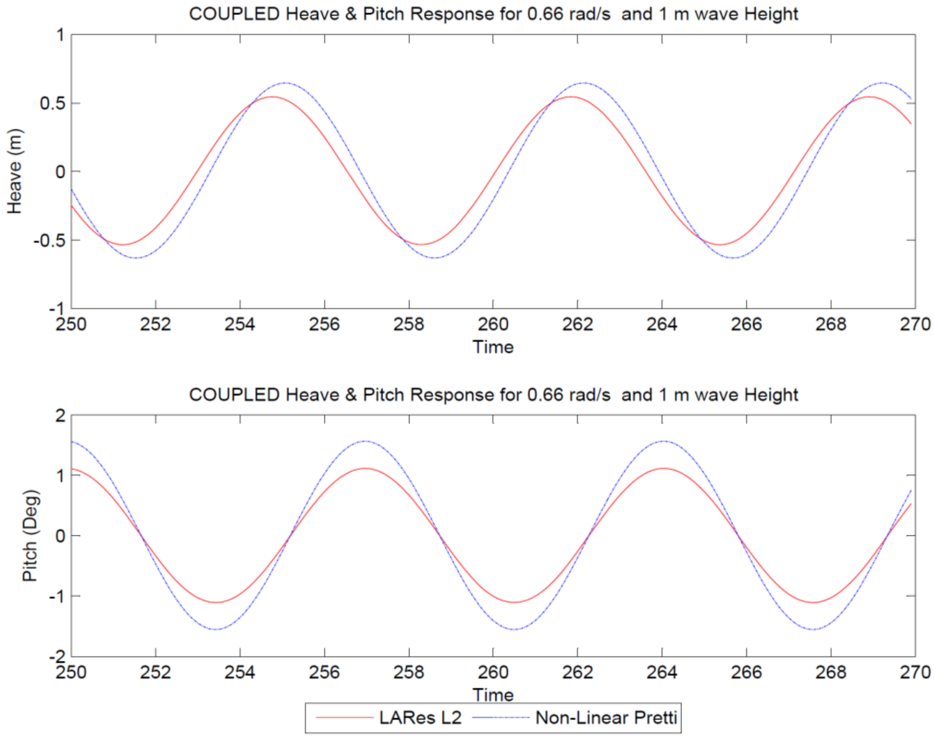

Figure 5.18: Nonlinear motion response of barge at ω=0.66 rad/s, H_w=1m, Fn=0.164

It is clearly observed that LARes L2 and nonlinear PRETTI results have differences in the response amplitude and phase lag in the forward speed simulations. In nonlinear time-domain simulation at forward speed case there are many factors that affect the motion responses. They can be summarized as follows:

- Discretization of the geometry
- Evaluation of hydrodynamic force components
- Frames of reference and degrees of freedom in the simulations.

Firstly, the differences in the motion responses are originated from the discretization of the geometry under the instantaneous wave profile at each time step. The accuracy of the instantaneous wetted portion of the ship is tested and validated at zero speed condition in the Figure 5.16 using the comparison of the nonlinear F-K and restoring forces and, they are observed as identical. Otherwise if they were different, there would have been a computational error in the estimation of the exact wetted portion of the ship geometry during the simulations. Secondly, the evaluation of hydrodynamic force components possesses a high importance in the non-linear time domain simulations. The radiation and diffraction forces are also validated with PRETTI results in the Figure 5.16 at zero speed and they are found to be identical to each other. Thus, the mathematical model of the radiation and diffraction forces is verified at zero forward speed case. Thirdly, the frames of reference and the degree of freedom implemented in the equations affect the solution of accelerations and the resulting ship velocity and displacements. In PRETTI software, body-fixed reference frame is used to solve the accelerations while in LARes models constant or zero speed hydrodynamic frames are used. The differences using these reference frames influence the solution of ship accelerations where in PRETTI six DOF acceleration solution is performed and in LARes models two DOF solution is performed instead.

In order to investigate the contribution of hydrodynamic forces to the motion responses in the nonlinear time-domain solutions, all force components are illustrated in the Figure 5.19. It is observed in the figure that the F-K and diffraction forces and moments are identical to each other which verify the accuracy of the instantaneous wetted area and the mathematical model of diffraction forces respectively.

In the zero forward speed simulation the surge motion influence to the accelerations were small but, in the current forward speed case the surge effect influenced the results at high extents. The differences in the motion responses are originated from the effect of coupled surge forces on the heave and pitch restoring forces and moments in PRETTI which are not taken into account in the LARes models. The lack of surge motions affected the amplitude and phase angle in the heave restoring forces in LARes while in pitch responses it only affected the restoring moment amplitudes. The trend of the radiation forces are following restoring forces because

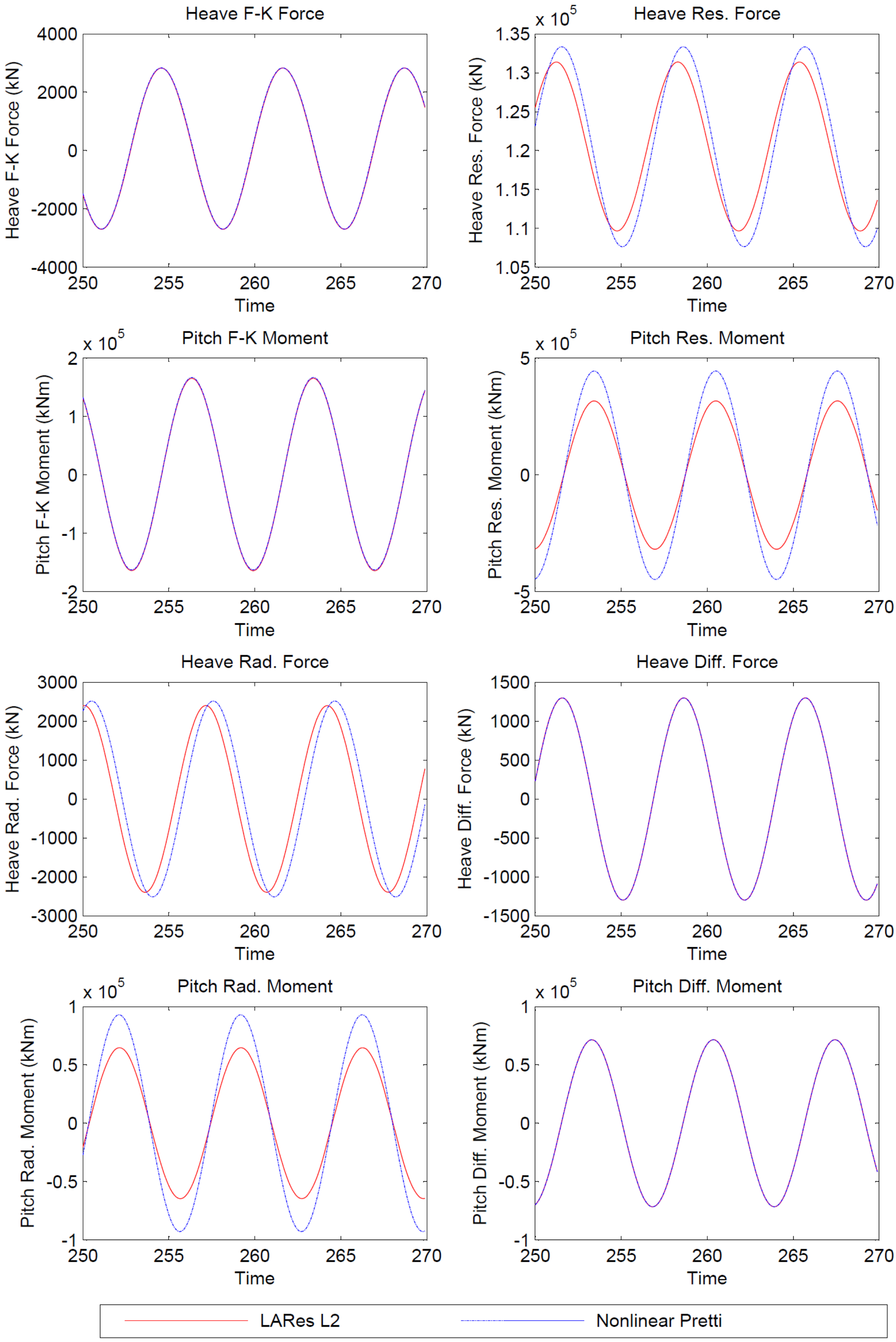

Figure 5.19: Nonlinear hydrodynamic force components of barge at ω=0.66 rad/s, H_w=1m, Fn=0.164

the displacements are integrated from the ship velocity histories which are used in the radiation forces evaluations.

Radiation forces are evaluated from the integration of the convoluted memory functions and the velocity history during the simulations. In PRETTI, 6x6 damping coefficient matrices are used in the memory function calculations; therefore all motion modes influence the radiation forces. However, in LARes only the heave and pitch damping coefficients are used in the evaluation of radiation forces in head seas simulations.

In nonlinear PRETTI software, all force components are taken into account in the ship acceleration solutions and if a motion mode is suppressed then the total forces in the body-fixed system for that DOF is assumed as zero (Van't Veer et al., 2009). However, in PRETTI software even when a DOF is suppressed in the simulations, its contribution in the radiation forces are taken into account and listed in the outputs. Moreover, kinematic forces such as external spring and damping forces are always taken into account in order to maintain the control in the surge motions. In the current barge simulations external spring and damping forces are assumed to be zero in the PRETTI and LARes models. The spring and damping forces are unique for ships and they are purely based on the trial-and-error and experience.

In the current analysis, the differences in the motion responses, which are originated from the preference of the body-fixed and hydrodynamic frame axes in the acceleration solutions, are small due to the small pitch displacements in head seas. Therefore, the mass and inertia matrix in the motion equations are assumed to be constant in LARes models. On the contrary, in PRETTI software, all modes of accelerations need to be calculated in the body-fixed frame axis in order to maintain the integrity of the motion equations (Fossen, 1994).

The validation of the body nonlinear (level 3) model motion responses is performed on the S-175 containership for zero and forward speed conditions. Zero speed heave and pitch motion response comparisons are performed with the numerical computations using the nonlinear PRETTI, LARes L2 and LARes L1 models due to the lack of experiments for this geometry at zero speed. Figure 5.20 illustrates the non-dimensionalized heave and pitch responses, as a function of the non-dimensional wave frequency for the wave slope of H_w/λ=120. Heave and pitch amplitudes are non-dimensionalized by the wave amplitude (ζ_a) and wave steepness ($k\zeta_a$) respectively while H_w represents the wave height, λ the wave length and g the acceleration of gravity in order.

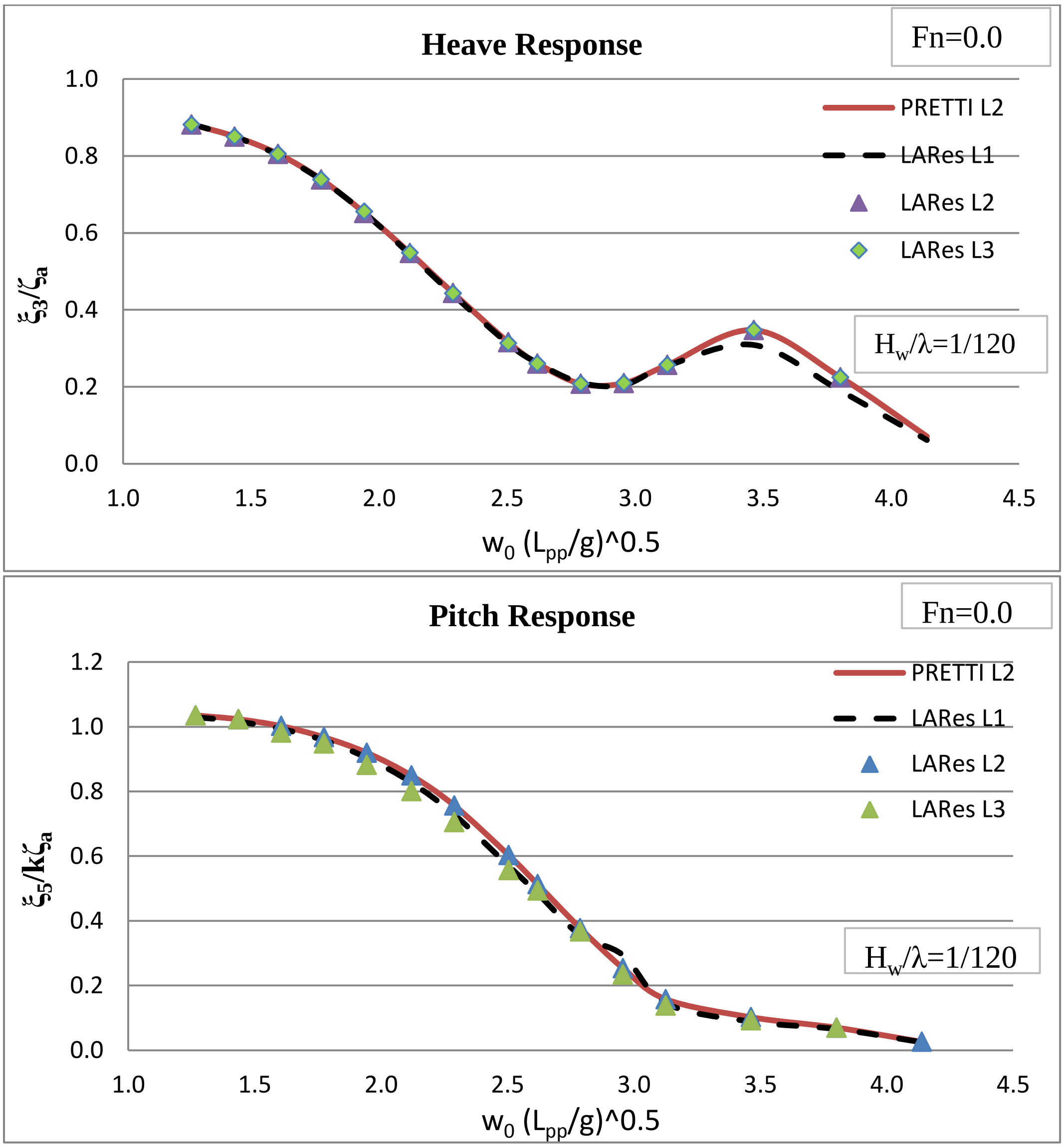

Figure 5.20: Nonlinear heave and pitch response comparison of S-175, Fn=0.0

It is clearly observed from the heave and pitch responses that the LARes level 3 and level 2 models are well agreed with the nonlinear PRETTI model at zero forward speed due to lack of the surge motion influence. In the nonlinear PRETTI model ship motion simulations at zero forward speed, body-fixed surge velocity is very small compared to large the forward speed body-fixed surge velocities. Small surge velocity cross-coupling components which are fed into the coupled terms of the convolution integrals result in small surge radiation forces and therefore they do not affect the motion responses at a large extent. In pitch motion around the resonance peak, LARes level 3 model estimated slightly smaller responses compared to the level 2 model, but the relative difference is small compared to the absolute value of the pitch amplitudes. The trends of the both heave and pitch motion response curves show reasonable correspondence to other models that are investigated.

In order to investigate the variations between the heave and pitch motion responses at zero forward speed, LARes level 3 and level 2 model hydrodynamic force components are compared in detail around the resonant frequency range with a wavelength to ship length ratio of $\lambda/L_{pp}=1.2$ and at a wave steepness of $H_w/\lambda=1/120$ in the Figure 5.21. It is observed from the figure that the nonlinear F-K and restoring forces are identical for the level 3 and level 2 model estimations. However, radiation and diffraction forces have differences in small order. The level 3 model heave and pitch diffraction force amplitudes are nearly identical with the level 2 model but have a slight negative shift. In a similar way, the level 3 model heave radiation force amplitude is the nearly identical to the level 2 model with a slight negative shift. On the other hand, the level 3 model pitch radiation amplitude is slightly higher than the level 2 model which results in higher pitch damping moment. For this reason, around the resonant frequency the level 3 model pitch response amplitudes are slightly smaller compared to the level 2 model results at zero speed simulations.

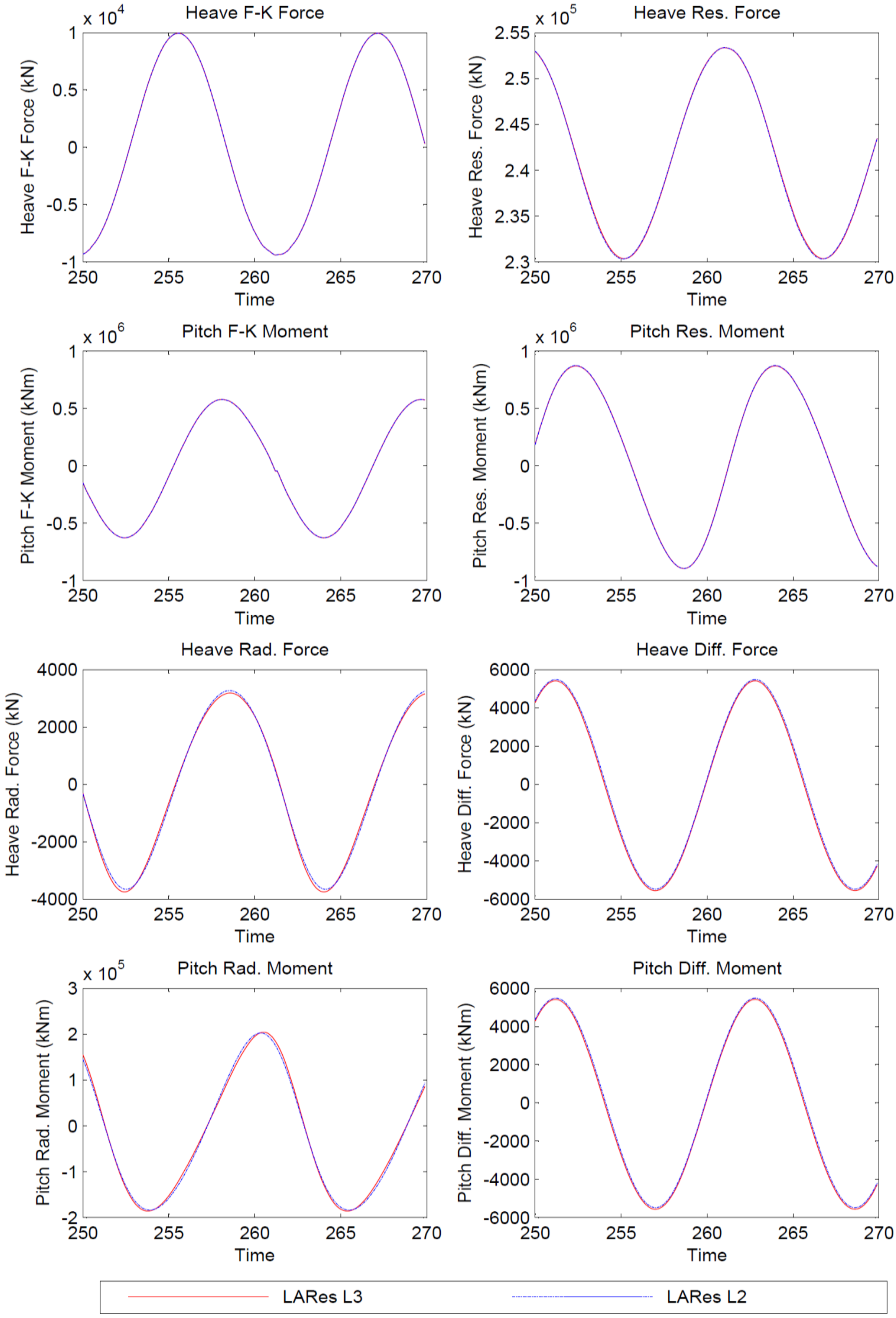

Figure 5.21: LARes level 3 and level 2 hydrodynamic force components of S-175 at λ/L_{pp}=1.2, H_w/λ=1/120, Fn=0.0

In the forward speed case, LARes level 3, level 2 and level 1 models are compared with the nonlinear PRETTI and experimental data obtained by Fonseca and Soares (2004) at Fn=0.25 and at a wave steepness of $H_w/\lambda=1/120$. The heave and pitch responses are illustrated in the Figure 5.22 below:

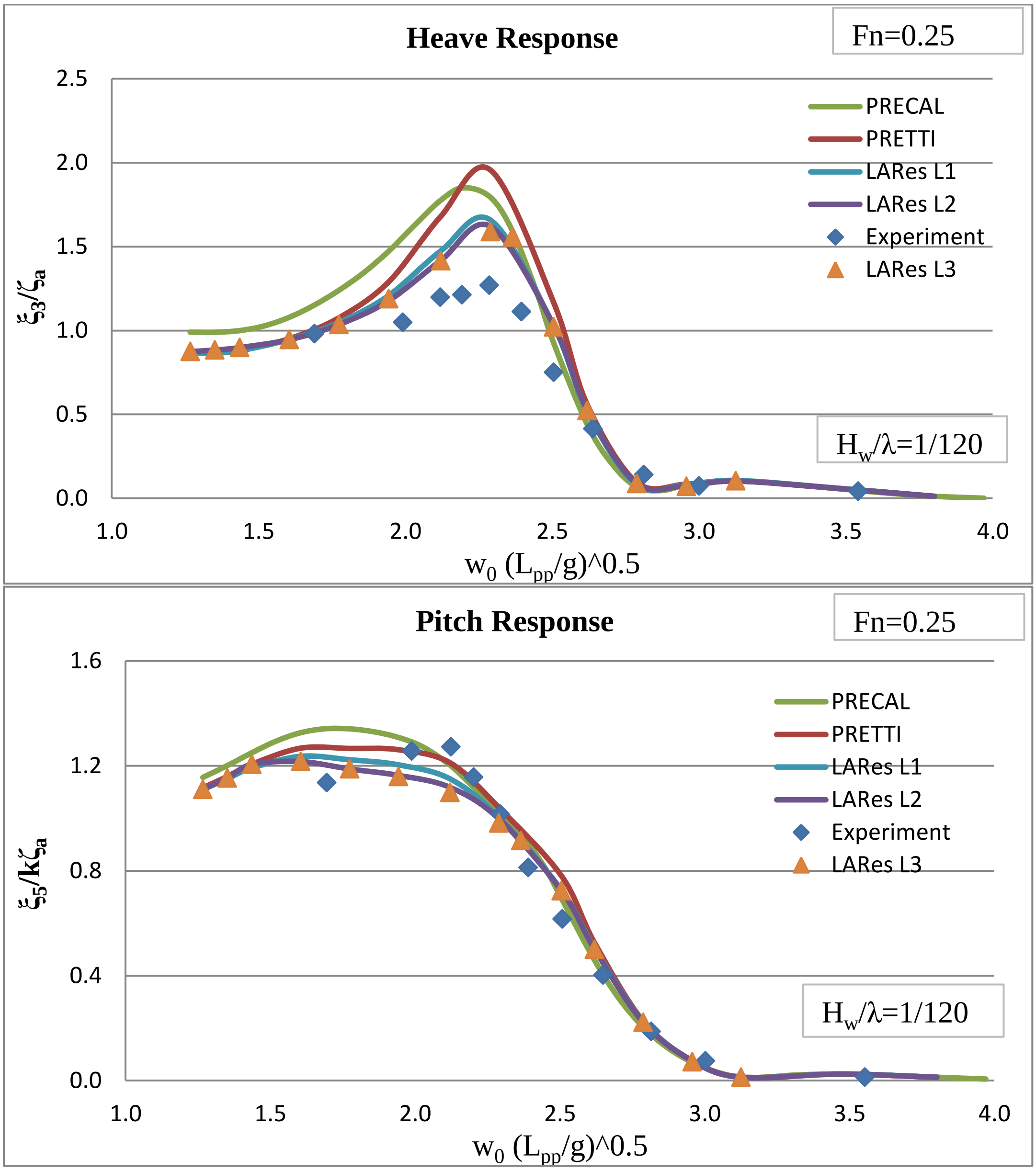

Figure 5.22: Nonlinear heave and pitch response functions of S-175 at Fn=0.25, $H_w/\lambda=1/120$

In the forward speed case, the peak of heave motion has a non-dimensional resonance frequency of 2.3 while the non-dimensional pitch resonance frequency occurs at a slightly smaller frequency. Due to the small amplitude incident waves LARes level3, level 2 and level 1 models heave and pitch responses show reasonable correspondences while around the resonant frequencies level 3 model estimates slightly smaller responses compared to the level 2 model. At smaller and higher frequencies than the resonant frequency region, heave and pitch responses are nearly identical for all LARes models. In order to validate the heave and pitch motion responses LARes level 3 and level 2 response amplitudes are compared with the PRETTI results. The same phenomenon like the zero speed estimations is also valid in this analysis that, especially in heave response function, the LARes level 2 model estimated smaller amplitudes compared to the nonlinear PRETTI heave response function due to the lack of the surge motion influence in the hydrodynamic force components. In particular, in heave motion LARes level 3 and level 2 models have a better agreement with the experimental data compared to the nonlinear PRETTI model. The pitch response has a fair agreement with the nonlinear PRETTI results while around the resonance frequency nonlinear PRETTI results agrees better with the experimental data than the LARes level 3 and level 2 models, however the difference between models are small compared to the difference in heave response functions. However, in the pitch response, for the frequencies smaller and bigger than the resonant frequency, LARes L3 has better agreement than the nonlinear PRETTI results.

In order to investigate the details of variations between the heave and pitch motion responses at the forward speed of Fn=0.25, LARes level 3 and level 2 model hydrodynamic force components are compared around the resonant frequency at frequency of λ/L_{pp}=1.2 and at a wave steepness of H_w/λ=1/120 in the Figure 5.23. Likewise the zero forward speed estimations, nonlinear F-K and restoring forces are nearly identical in level 3 and level 2 model simulations. However, this time, the difference in the radiation and diffraction forces between the level 3 and level 2 models are larger than the zero forward speed solutions. The main reason for that is, at the forward speed of Fn=0.25, maximum peak amplitude of heave and

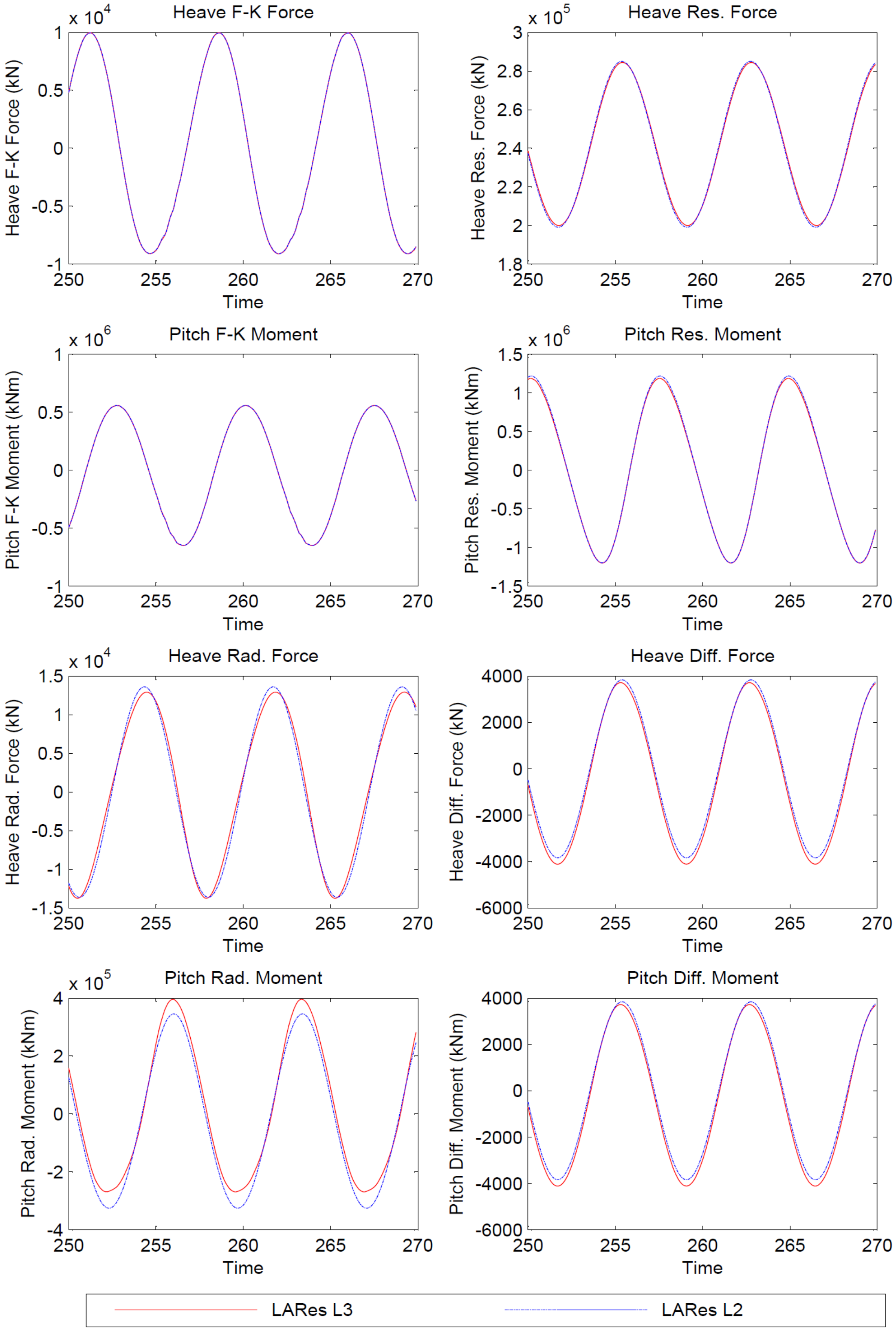

Figure 5.23: LARes level 3 and level 2 hydrodynamic force components of S-175 at λ/L_{pp}=1.2, H_w/λ=1/120, Fn=0.25

pitch motion amplitudes are more than two times larger than the zero speed results.In level 3 model, radiation and diffraction forces are calculated at the instantaneous position of the vessel therefore they differ compared to the mean position estimations calculated in the level 2 model. In general, level 3 radiation moment amplitude is higher than the level 2 model estimations and this result with smaller pitch motion amplitude due to an extra damping moment applied in the simulations. The diffraction forces computed using the level 3 model have a slight shift in the negative direction compared to the level 2 model estimations although they have nearly the same amplitudes. The level 3 model radiation forces have different trend compared to the level 3 diffraction forces. In level 3 model, heave radiation force amplitude is slightly smaller than the level 2 estimations while a relative shift is not observed between the curves. However the pitch radiation moments in the level 3 model have a positive shift compared to the level 2 estimations while the mean amplitude of radiation moments in the level 3 model are slightly higher than the level 2 model estimations.

5.5 Validation of Load Responses

This section presents the validation of the linear and nonlinear internal load responses of a barge and S-175 container ship in small amplitude waves and in head seas with a focus on the body nonlinearity levels. The results of the PRETTI software are used to validate the Vertical Shear Force (VSF) at station 15 (1/4 L_{pp} from FP) and Vertical Bending Moment (VBM) results at the midship section (st 10) of the vessels. Moreover, PRETTI software is used to compare the sectional hydrodynamic force and inertia components with the LARes models. For the S-175 container ship case, experimental internal load results, which are obtained by Fonseca and Soares (2004), are used to compare the results of LARes and PRETTI models at small amplitude waves. Due to the lack of experimental data, internal loads of the barge are only compared with the PRETTI model. In the next figures, VSF and VBM responses are non-dimensionalized by $\rho g B L_{pp} \zeta a$ and $\rho g B L_{pp}^2 \zeta a$ respectively, where ρ is the fluid specific density and B is the ship beam amidships and ζa is the incident wave amplitude.

5.5.1 Linear Load Simulation Validations

Linear internal load validations are performed in order to verify the integrity of internal load equations therefore to verify the balance of the forces and moments acting on the ship portion forward of the defined cross section. Moreover, in the LARes models, sectional hydrodynamic forces and moments are compared with the PRETTI sectional hydrodynamic forces.

Linear VSF and VBM responses of barge are compared at Fn=0.0 using linear LARes and linear PRETTI models in the Figure 5.24 at station 15 and station 10 respectively.

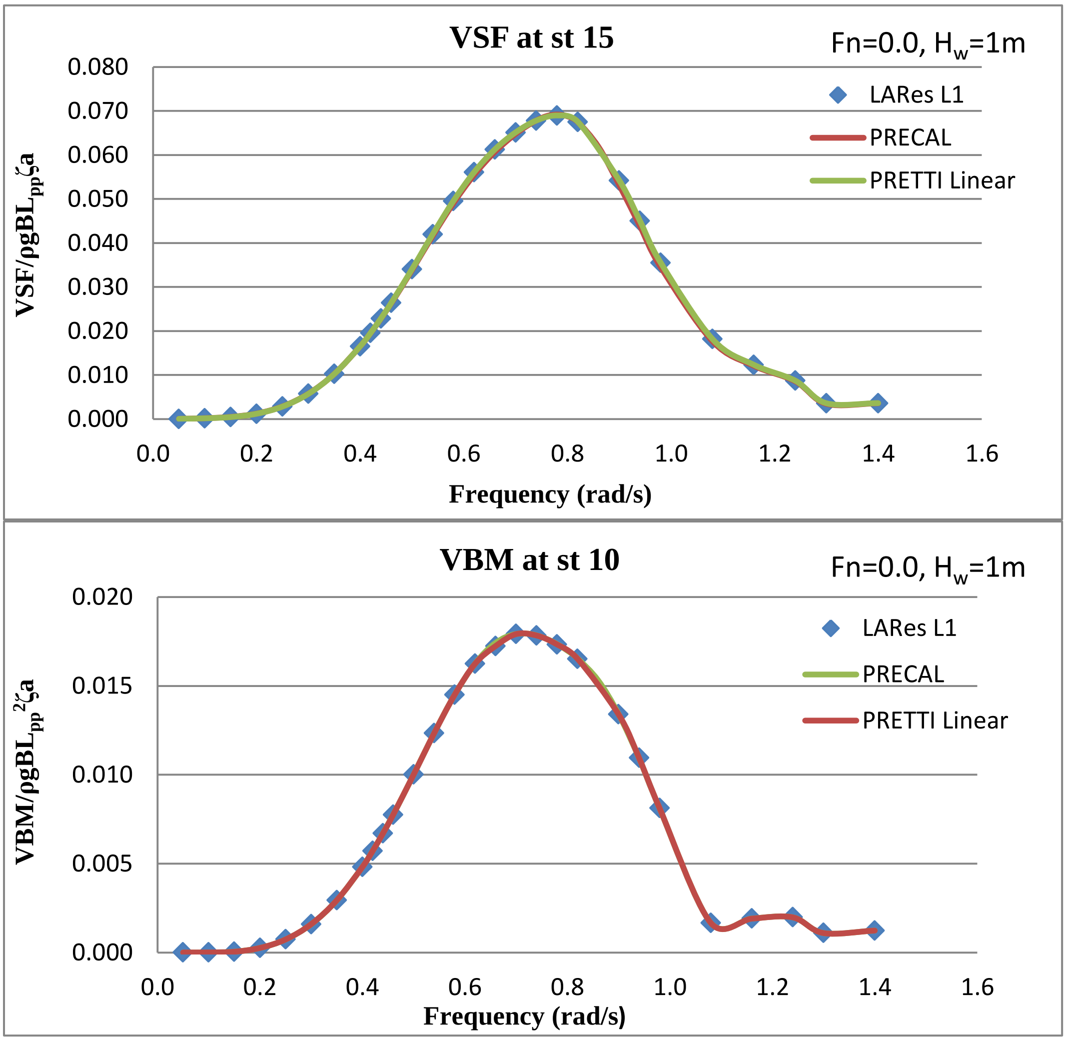

Figure 5.24: Linear VSF (st 15) and VBM (st 10) responses of barge (Fn=0.0, β=180)

It is clearly seen from the Figure 5.24 that, in the LARes L1 and linear PRETTI models VSF (st 15) and VBM (st 10) responses are identical to each other. In the internal load responses, in the linear approach, sectional hydrodynamic forces are calculated with respect to the mean wetted surface of body under the still water level and for the ship portion forward of the defined cross section. The sectional complex hydrodynamic force amplitudes are fed from the frequency-domain PRECAL software for the ship portion forward of the defined cross section. The results of the frequency-domain and time-domain results are identical for the VSF and VBM responses. It is important to mention that for barge geometry due to the uniform load conditions and vertical walls of the ship geometry, at the midship section VSF needs to be zero. In PRECAL software, internal load calculations are performed using the initial panel discretization of the vessel. That means, original panels which are positioned on the cut cross-section are not sub-divided into panels. Therefore, if a panel's center point is positioned on the forward part of the defined cross-section it is taken into account in the sectional hydrodynamic coefficients. The second important point is, in PRECAL, mass distribution of the ship is inputted in mass points therefore it is not continuous. When a mass point is defined directly on the cut cross-section, PRECAL translates it slightly back of the cross-section and do not take into account in the inertial force and moment calculations for the forward part of the cut section. In order to prevent this effect in the barge, at the midship section there is not any mass point defined and remaining mass points are distributed symmetrically on the ship without altering the Centre of Gravity (COG) of the ship. The new mass distribution of the ship is taken into account in the calculation of pitch radius of gyration. It needs to be underlined that, this mass distribution operation is only valid for transversally symmetric structures.

Linear time-domain internal load responses of the barge at ω=0.66 rad/s ($\lambda/L_{pp}\approx1.4$), at H_w=1 meters and at Fn=0.0 are illustrated in the Figure 5.25. It is clearly seen from the VSF (st 15) and VBM (st 10) responses that LARes L1 and linear PRETTI results are identical. The differences at the transient part of the analysis are originated from the preference of the ramp functions.

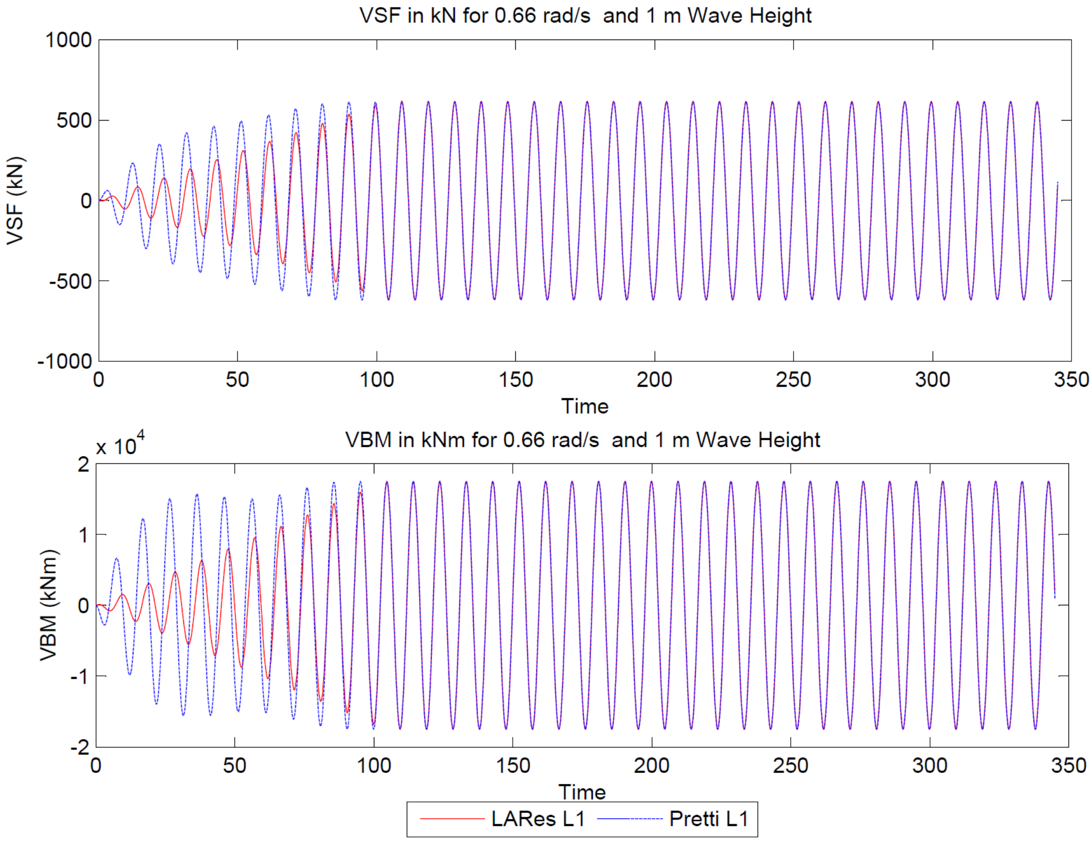

Figure 5.25: Linear VSF (st 15) and VBM (st 10) time history of barge at ω=0.66 rad/s at H_w=1m (Fn=0.0, β=180)

In order to validate the linear time-domain internal load responses at zero forward speed, the sectional hydrodynamic force components are validated with the linear PRETTI results. Validation of the sectional hydrodynamic force components verifies the integrity of the forces and moments applied on the portion of the hull forward of the defined cross-section. Linear time domain sectional F-K, restoring, radiation, diffraction, infinite damping and inertia forces are compared at zero speed and in head seas with the linear PRETTI results for the portion of the ship forward of the defined cross-section. Moreover, in order to verify the VSF and VBM responses, which equal to the difference between the inertia and hydrodynamic forces for the portion of the ship, balance of the hydrodynamic forces are calculated again and illustrated in the sectional total forces and moments graphs. Again, the transient part of the simulation is extracted from the simulation time and steady-state parts of the hydrodynamic forces are compared to each other. The comparisons are illustrated in the Figure 5.26 and Figure 5.27 respectively.

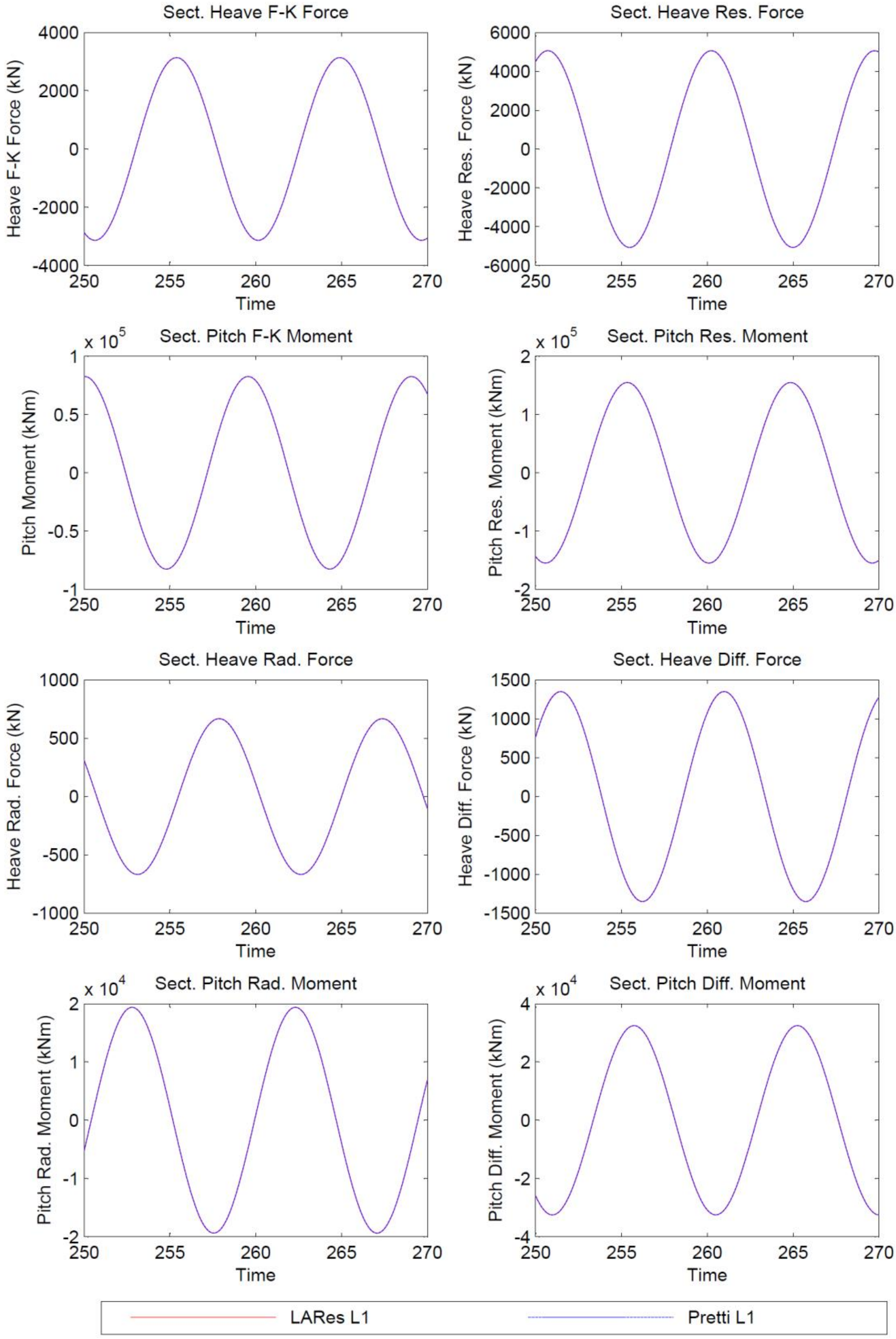

Figure 5.26: Linear sectional hydrodynamic force components comparison of barge forward of the midship section at ω=0.66 rad/s, H_w=1m (Fn=0.0, β=180)

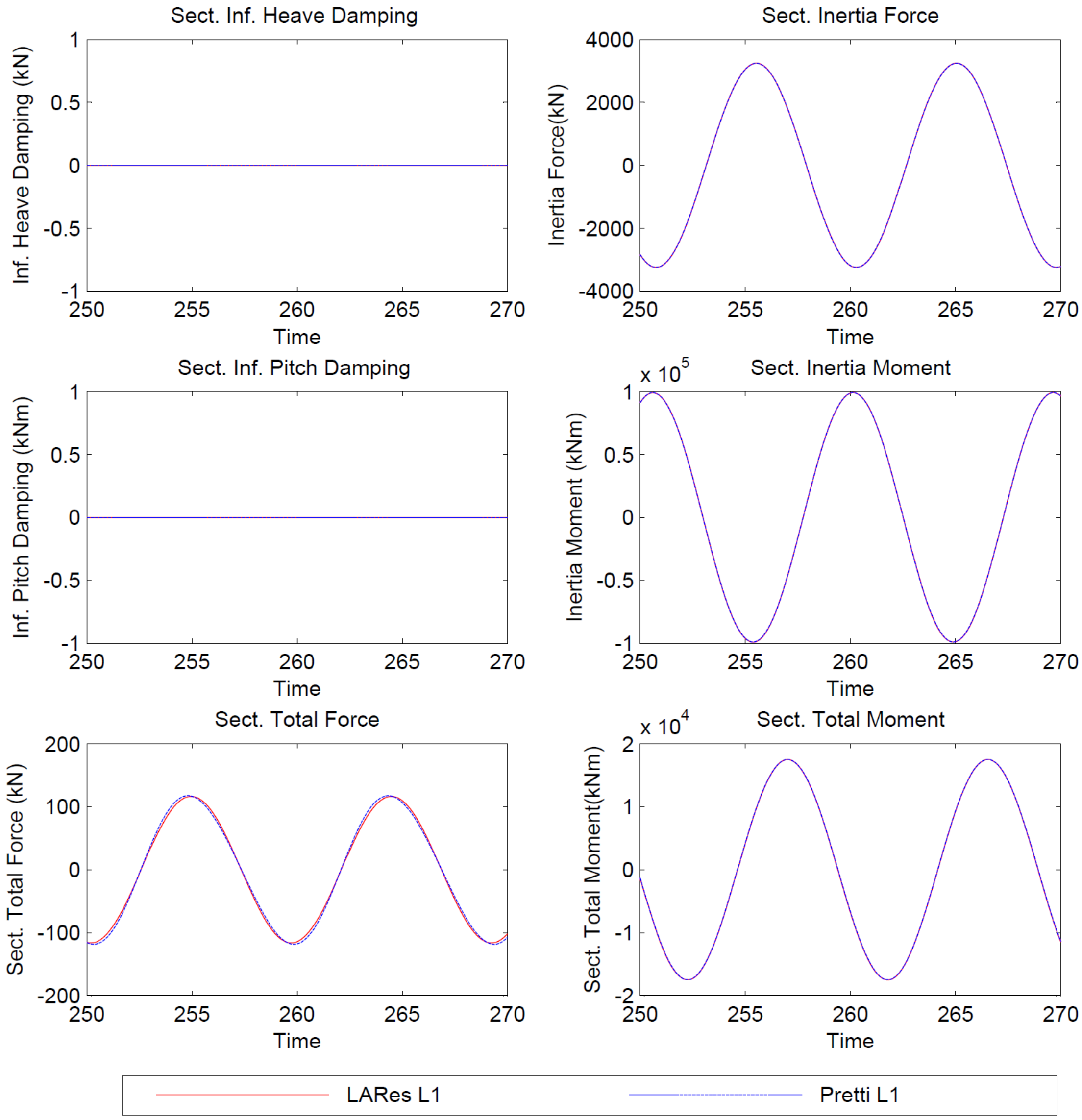

Figure 5.27: Sectional hydrodynamic and inertial force components comparisons of barge forward of the midship section at ω=0.66 rad/s, H_w=1m (Fn=0.0, β=180)

It is clearly observed from the Figure 5.26 that all of the sectional forces are identical with the linear PRETTI results, which is the validation of the sectional force amplitudes and phases that are calculated accurately. In the linear internal load responses, sectional restoring forces are calculated from production of the sectional restoring matrix and the resultant global motion displacements. It needs to be underlined that, sectional radiation forces and diffraction forces are calculated using the sectional damping coefficient curves and sectional complex diffraction force amplitudes respectively which are defined for the portion of the ship forward of the defined cross-section. Moreover, sectional F-K forces are also calculated from the linear complex F-K force amplitudes for the portion of the vessel under the still water level. In the Figure 5.27, sectional infinite damping, inertia forces and sectional total forces are illustrated. It is observed that sectional infinite damping forces are zero for all time history, because, at zero forward speed simulations, infinite damping coefficients approach to zero therefore when they are multiplied with the global velocity vector it results with zero infinite damping force. Sectional inertia forces are found to be identical with the PRETTI results in which they are calculated from the multiplication of the sectional mass distribution and infinite added mass with the resultant global acceleration vector. Sectional total force and moment need to provide the same values with the VSF and VBM results respectively therefore they are used to verify the internal load results.

5.5.2 Nonlinear Load Simulation Validations

In this section, the computational results of the internal load responses using the F-K nonlinear (level 2) are validated at station 10 (amidships) and at station 15 (1/4 L_{pp} backwards from FP) with linear and nonlinear PRETTI results in small amplitude waves in head seas using the barge geometry. The differences in the internal load results between the LARes and PRETTI models at zero forward speed case is investigated in detail. Moreover, body nonlinear (level 3) model is validated for the VSF (st 15) and VBM (st 10) responses using linear and non-linear numerical results and with the available experimental results in small amplitude waves in head seas. The internal loads of the level 3 hydrodynamic model of the LARes is investigated using the S-175 containership at zero and forward speed cases in head seas while the VSF and VBM responses are compared with the experiments provided in the Fonseca and Soares (2004) at Fn=0.25. In both of the LARes level 2 and level 3 models, sectional hydrodynamic force components are investigated in detail and compared to the PRETTI sectional hydrodynamic force components in order to the investigate the origin of the differences in the sectional force components.

Nonlinear VSF (st 15) and VBM (st 10) responses are compared using LARes L2, LARes L1 and PRETTI L2 (nonlinear) models in the Figure 5.28 at zero forward speed.

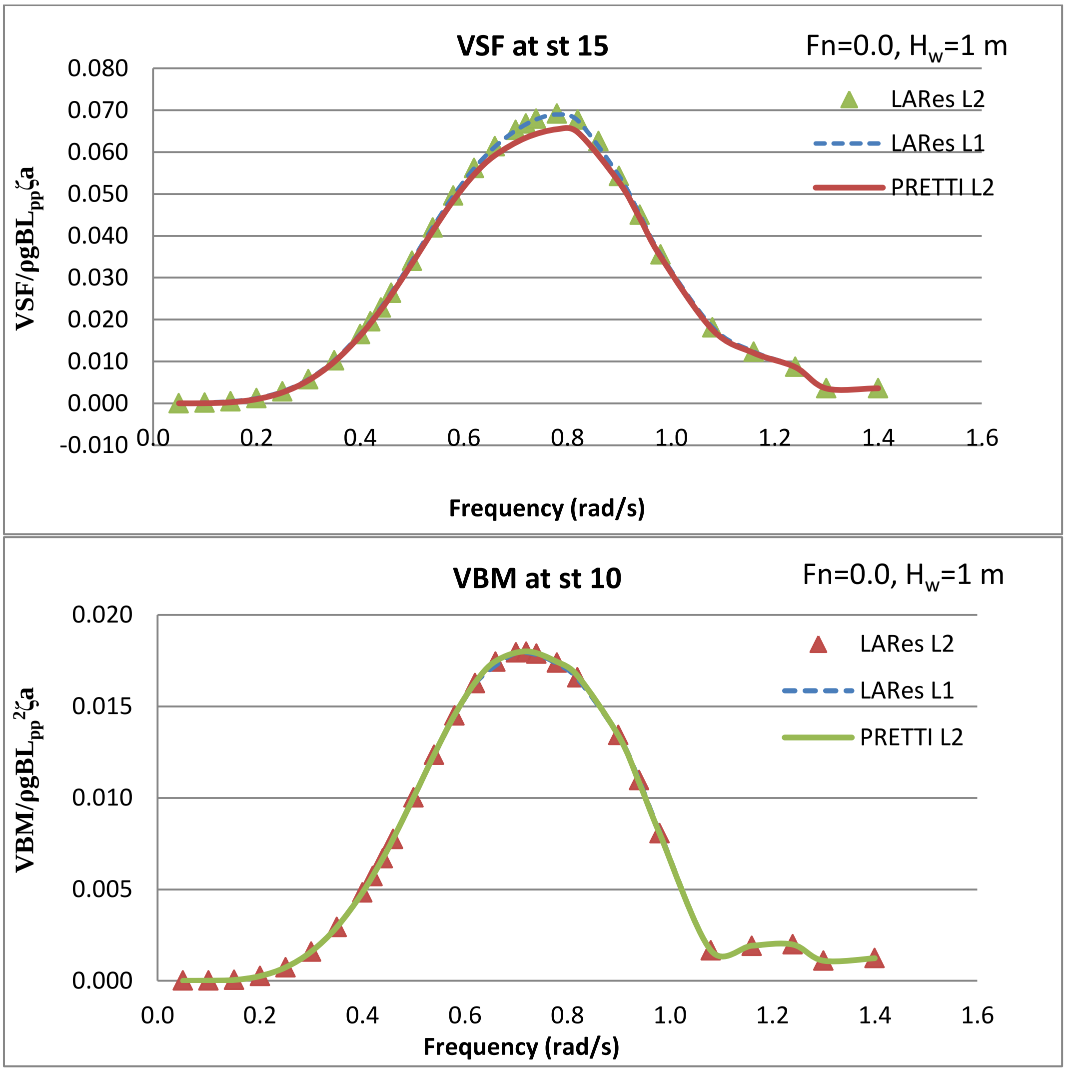

Figure 5.28: Nonlinear VSF (st 15) and VBM (st10) comparison of barge (Fn=0.0, β=180)

It is clearly observed from the Figure 5.28 that in the LARes L2, LARes L1 and nonlinear PRETTI model’s VBM responses are identical to each other amidships. In LARes L2 and L1 models VSF responses at station 15 are slightly over-predicted compared to the PRETTI L2 model. Small differences in the VSF responses are due to the reference frames and integration preferences.

Nonlinear time-domain internal load response histories of the barge at station 10 and 15 at ω=0.66 rad/s ($\lambda/L_{pp}\approx1.4$), at H_w=1m and at Fn=0.0 are illustrated in the Figure 5.29. It is clearly seen from the VSF response at station 15 and VBM response at station 10 that LARes L2 model and PRETTI L2 model results are identical.

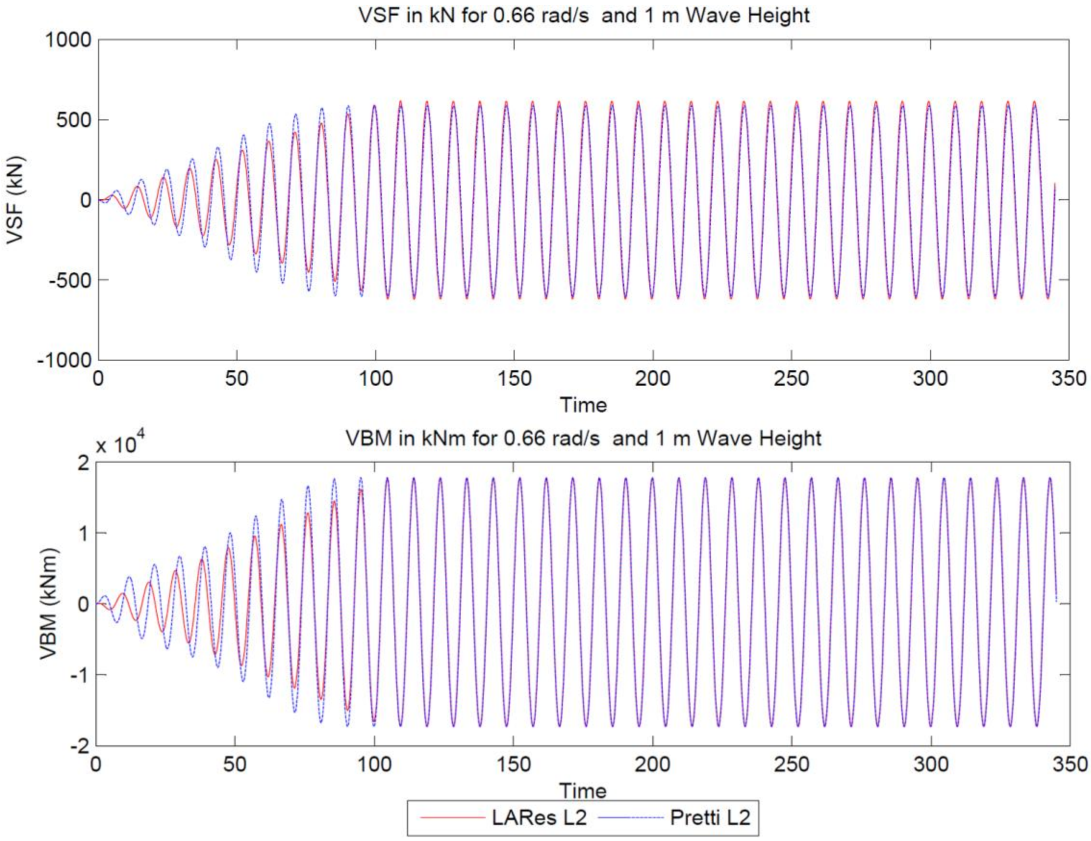

Figure 5.29: Nonlinear VSF (st 15) and VBM (st 10) time history of barge at ω=0.66 rad/s, H_w=1m (Fn=0.0, β=180)

In the internal load responses, in nonlinear approach, sectional F-K and buoyancy forces are calculated at each time step with respect to the exact wetted surface of body under the wave profile for the ship portion forward of the defined cross section. In LARes L2 and PRETTI L2 models, sectional radiation, diffraction and infinite damping forces are calculated with respect to the mean wetted surface of the body under the still water level for the ship portion forward of the defined cross section. The sectional hydrodynamic and inertia forces for the body portion forward of midship section are illustrated in the Figure 5.30 and Figure 5.31 respectively.

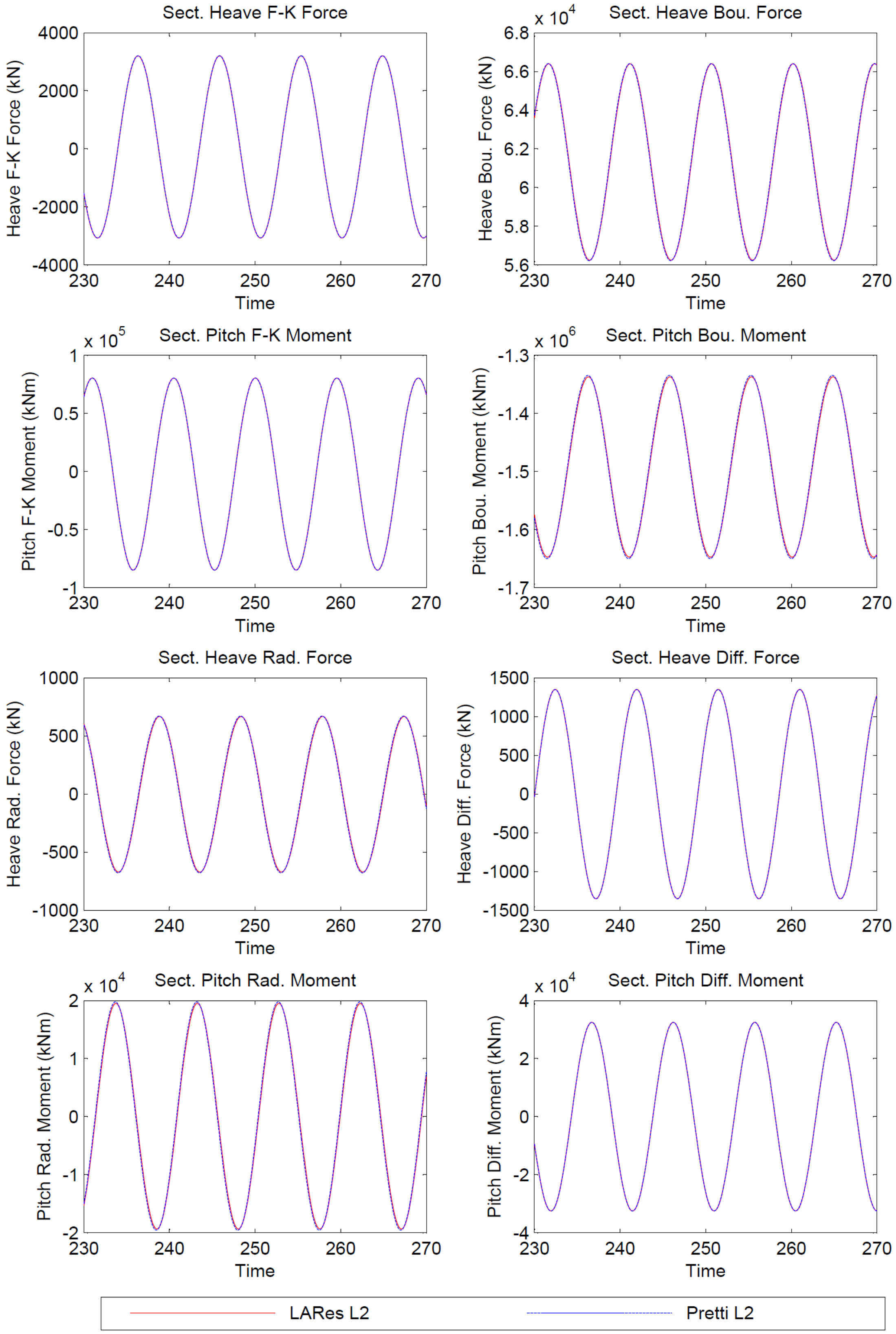

Figure 5.30: Nonlinear sectional hydrodynamic force components comparison of barge forward of midship section at ω=0.66 rad/s, H_w=1m (Fn=0.0, β=180)

It is clearly observed from the Figure 5.30 that all of the sectional forces are identical with the PRETTI L2 model, which is the validation of the accuracy of non-linear time domain hydrodynamic forces. Furthermore, LARes L2 model sectional F-K and buoyancy forces are identical to the PRETTI L2 model which validates the accuracy of exact wetted surface pressure integrations at each time step. In the Figure 5.31, infinite damping, inertia and total forces and moments for the defined section are illustrated. Again, due to the zero forward speed simulation sectional infinite damping forces are calculated to be zero.

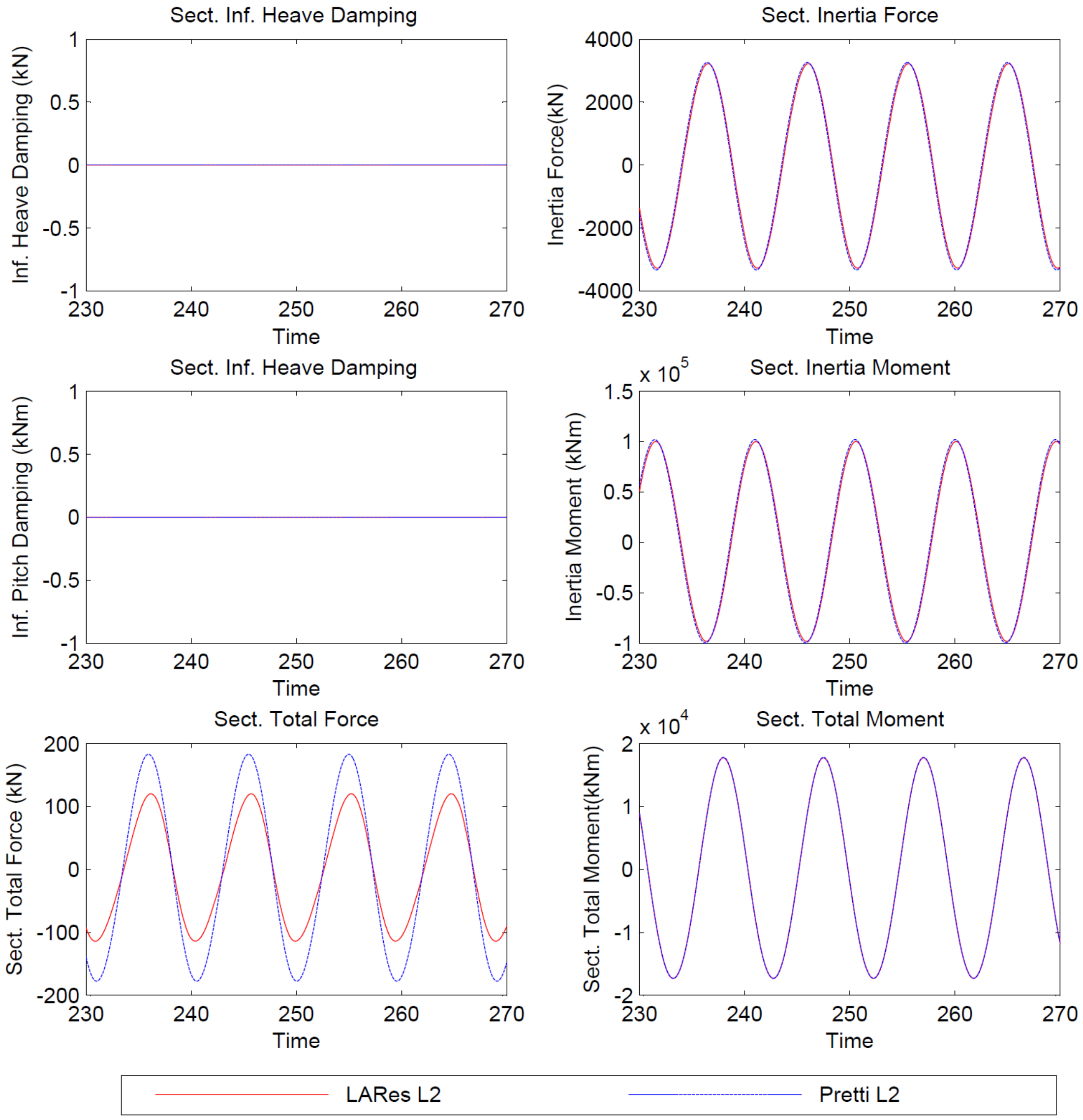

Figure 5.31: Sectional hydrodynamic and inertial force components comparisons of barge forward of midship section at ω=0.66 rad/s, H_w=1m (Fn=0.0, β=180)

Moreover, LARes L2 model and PRETTI L2 model sectional inertia forces are found to be identical to each other which verifies the accuracy of global acceleration vector. The difference in the VSF responses at the midship section can be seen in large scale in the sectional total force diagram in the Figure 5.31. It is observed that the amplitude of the VSF (st 10) response is very small compared to the amplitude of VBM at the midship section. There are small differences in the sectional force components during the time history due to the integration and reference frame preferences and these small differences are summed up and resulted with the difference in the VSF responses.

The validation of the body nonlinear (level 3) model internal load responses is performed on the S-175 containership at zero speed and at Fn=0.25 forward speed case. Zero speed VSF and VBM response comparisons are performed with numerical computations using the nonlinear PRETTI, LARes level 2 and LARes level 1 models. Due to the lack of experiments for this geometry at zero speed case, experimental results cannot be taken into account in the internal load comparisons. Figure 5.32 illustrates the non-dimensionalized VSF (st 15) and VBM (st 10) responses as a function of the non-dimensional wave frequency for the wave slope value of $H_w/\lambda=1/120$ at zero speed. It can be seen clearly that at zero forward speed simulations LARes L2 and L3 models are nearly identical with the PRETTI model's VSF and VBM results. The slight difference in the VSF responses are attributed to the hydrodynamic axis preference and pressure integration on the panels positioned at the forward part of the defined cross-section and also the lack of the surge motion in the LARes L2 and L3 model. Lack of the surge motion influences the body accelerations in which they are observed to be smaller than the PRETTI accelerations. Moreover, in the PRETTI model the sectional hydrodynamic and gravitational forces are integrated in the body-fixed frame axis and the gravitation force components in the hydrodynamic frame axis are rotated to the body-fixed axis coordinate system. It is also observed that in internal loads calculations reference frame axis selection and hydrodynamic pressure integration techniques affect the sensitivity of the results more than it is in the motion responses.

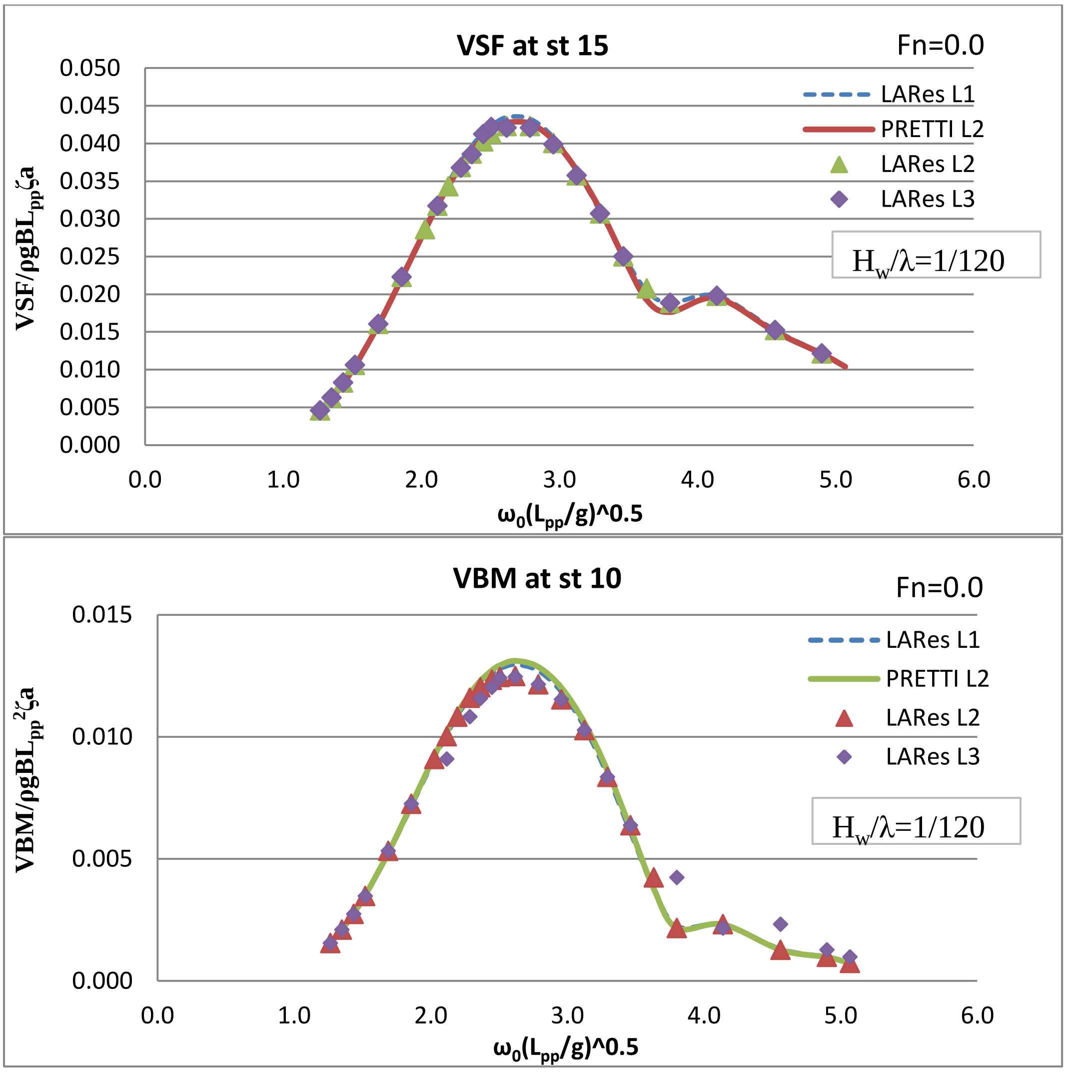

Figure 5.32: Nonlinear VSF (st 15) and VBM (st 10) comparison of S-175 (Fn=0.0, β=180)

The validation of the body nonlinear (level 3) model internal load responses on the S-175 containership at Fn=0.25 forward speed case is illustrated in the Figure 5.33. Forward speed VSF and VBM response comparisons are performed with numerical computations using the nonlinear PRETTI, LARes level 2 and LARes level 1 models and experimental results obtained by Fonseca and Soares (2004). Figure 5.33 illustrates the non-dimensionalized VSF (st 15) and VBM (st 10) responses as a function of the non-dimensional wave frequency for the wave slope value of $H_w/\lambda=1/120$ and at Fn=0.25 forward speed case. The VSF and VBM responses of the numerical models are observed to be close to each other. The differences between the numerical models in the VSF responses are identified to be higher than the VBM responses due to the sensitivity of the VSF responses. Especially, around the midship section VSF responses functions generally approach to small values therefore it is hard to identify their behavior in the numerical and experimental results.

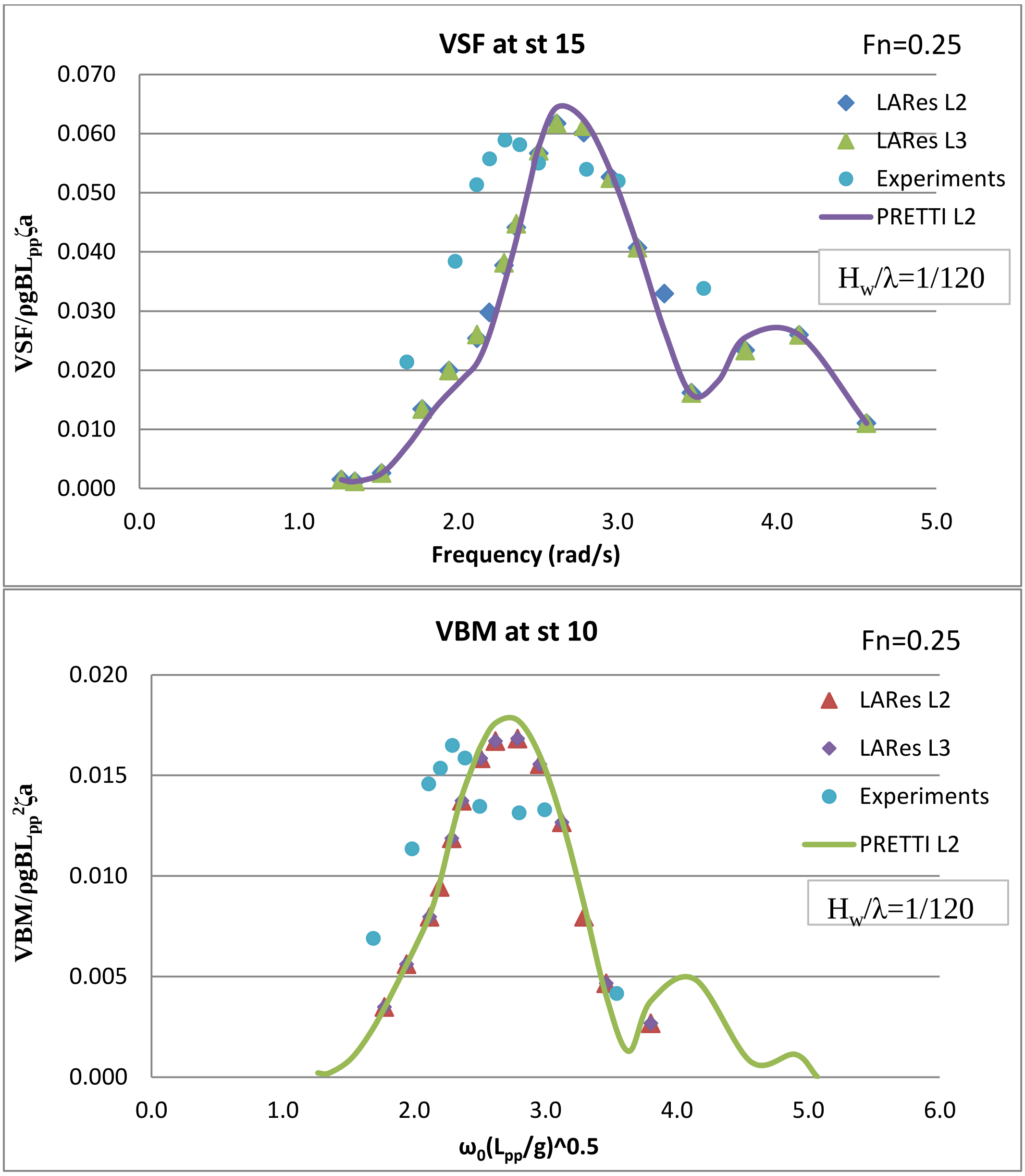

Figure 5.33: Nonlinear VSF (st15) and VBM (st 10) comparison of S-175 (Fn=0.25, β=180)

It is clearly observed there is a frequency shift in the maximum peaks of the experimental and numerical results in VSF and VBM responses. The main reason for that is attributed to the difference in the mass distribution between the numerical and experimental models. Although the numerical models and the experimental model have the same Longitudinal Center of Gravity (LCG) the weight distribution characteristics are different. It is clearly observed that LARes and PRETTI models have the same forward frequency shift compared to the experimental results. LARes models use the same mass distribution data that is provided in the PRETTI model therefore the same shift in the frequency in the maximum peak points are observed. The influence of the weight distribution is also mentioned in the work of Fonseca and Soares (2004) that the VSF and VBM are highly dependent on the longitudinal inertia of the model segment forward of the section. The authors compared their results with the experiments have been performed by Watanabe et al. (1989) and they found that around the resonant frequency the results are 30% smaller than the Watanabe’s experimental results. In the current numerical simulations the weight distribution is taken from the work of Fonseca and Soares (2002) and found to be in a well agreement with the discretized ship geometry. It also needs to be mentioned that the numerical VSF (st 15) and VBM (st 10) responses are slightly larger than the experimental results. The difference between the numerical and experimental results is attributed to the uncertainties in the longitudinal mass distribution and structural properties of the model in the experimental setup.

In order to investigate the details of variations between the VSF and VBM responses responses at the forward speed of Fn=0.25, LARes level 3 and level 2 model sectional hydrodynamic force components and sectional inertia forces are compared around the resonant frequency of λ/L_{pp}=1.4 and at a wave height of H_w=1m in the Figure 5.34 and Figure 5.35 for the body section forward of the midship section. It can be clearly observed that sectional F-K and buoyancy forces are identical to each other in the LARes L3 and L2 models. Moreover, differences in the sectional radiation and diffraction forces are observed between the LARes L3 and L2 models and in the pitch radiation moments there is a slight translation observed in the LARes L3 model compared to the LARes L2 model. In the Figure 5.35 sectional infinite damping forces, inertial forces and sectional total moments are illustrated. It is important to mention that at forward speed cases infinite damping forces and moments are not zero. It is observed that LARes L3 and L2 models are in a well agreement for the sectional forces and moments.

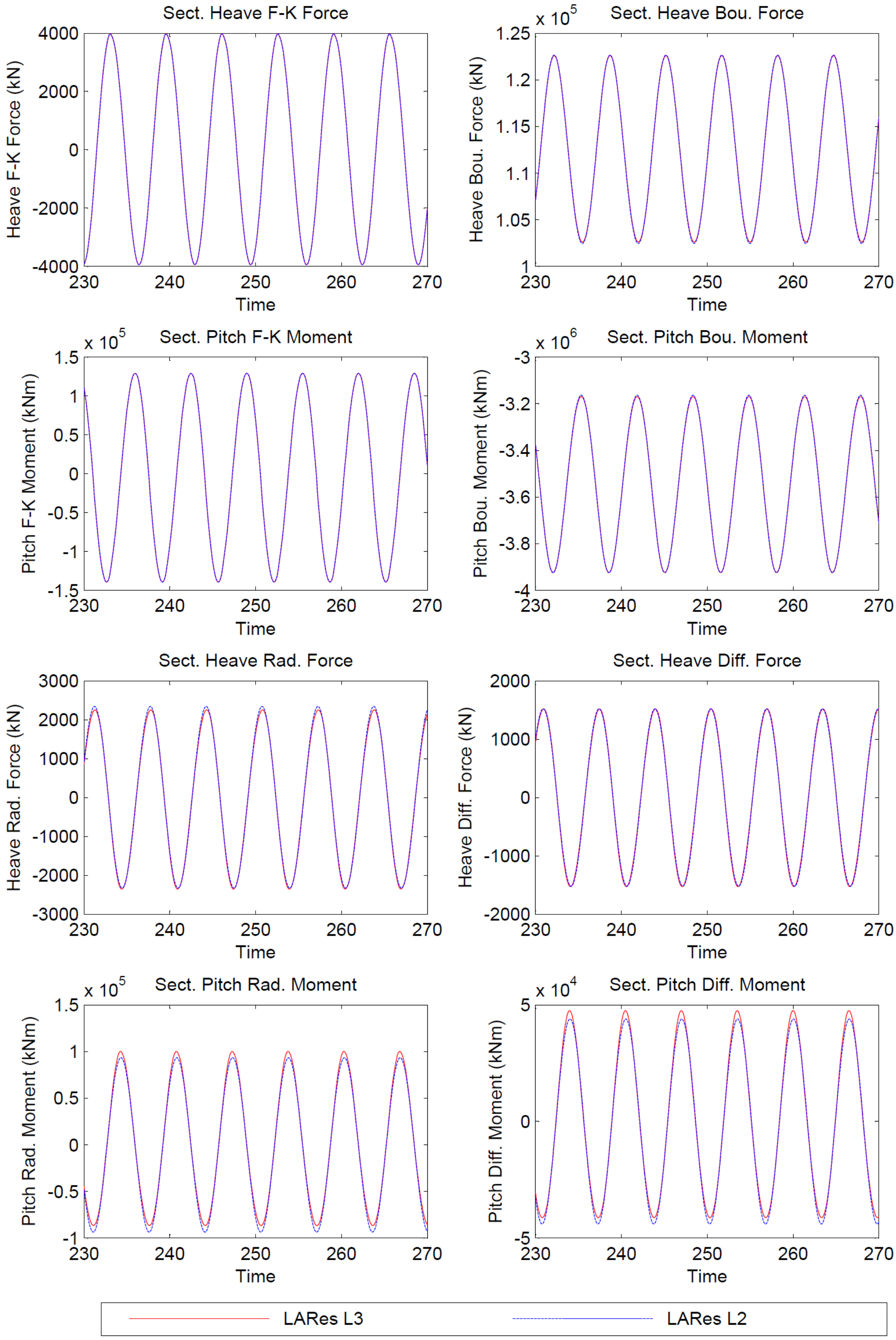

Figure 5.34: Nonlinear sectional hydrodynamic force components comparison of S-175 forward of the midship section at ω=0.5934 rad/s, H_w=1m (Fn=0.25, β=180)

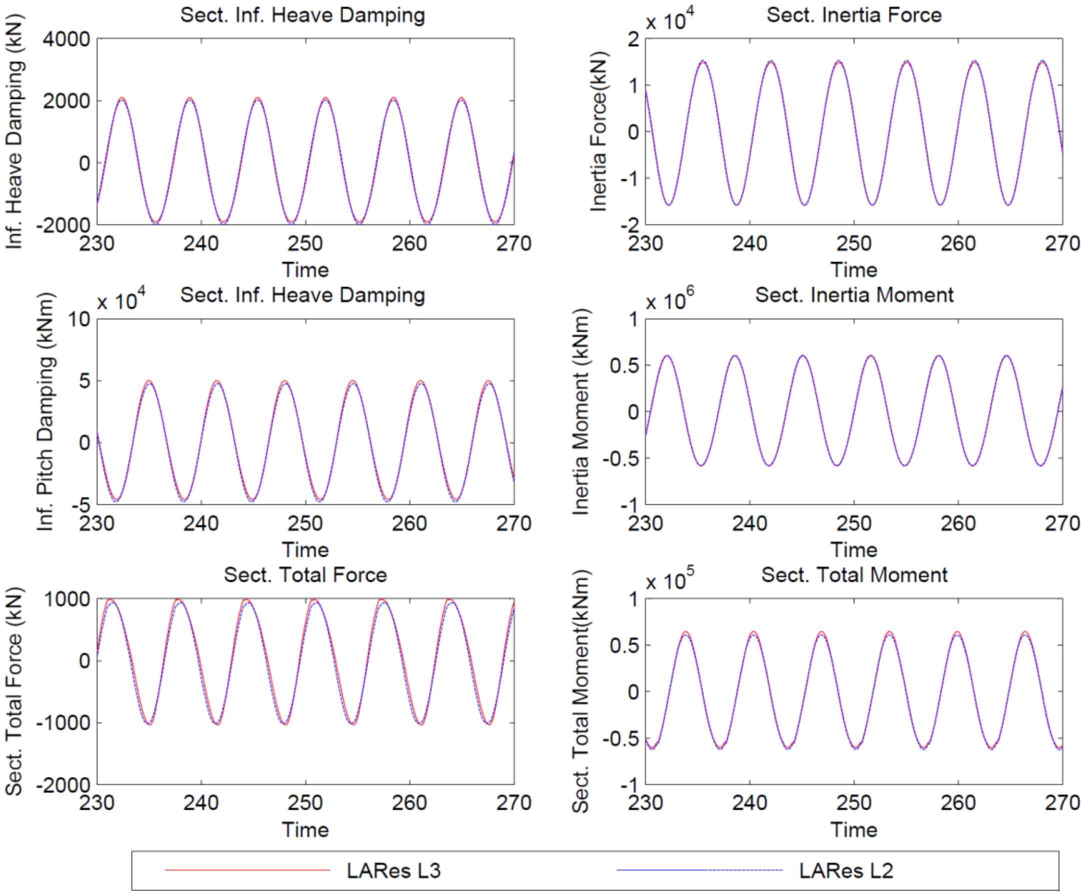

Figure 5.35: Nonlinear sectional hydrodynamic force components comparison of S-175 forward of the midship section at ω=0.5934 rad/s, H_w=1m (Fn=0.25, β=180)

There is a slight difference in the sectional total forces and moments between the LARes L3 and L2 models are observed due to the quasi-non-linear radiation and diffraction forces, but the differences are very small therefore the results are found to be in a well agreement.

5.6 Summary

In this chapter the validation of the linear and nonlinear motion and load responses of a barge and S-175 container ship in small amplitude waves and in head seas with a focus on the body nonlinearity levels is performed. The results of the PRETTI software is used to validate the motion and load responses and the global and sectional hydrodynamic force components which are calculated in the LARes models. In order to investigate S-175 container ship motion and load responses in detail, small amplitude motion and vertical load responses at Fn=0.25 forward speed case are compared with the experiments performed by Fonseca and Soares (2004).

In the barge geometry, LARes L2 and L1 models motion and load results are tested and compared in detail with the PRETTI model linear and nonlinear results. In zero forward speed case either in linear or in nonlinear simulations it has been observed that all global hydrodynamic force components are in a well agreement with the PRETTI results and therefore it validates the accuracy of the system of motion equations. The barge is also tested at 10 knots of forward speed and LARes L2 and L1 models are observed to have smaller peak values around the resonant frequency compared to the PRETTI model. The main reason for that decrease is attributed to the lack of the surge motion influence in LARes models and also the hydrodynamic axis frame selections. It is clearly observed that the differences are not originated from the F-K forces but originated from the smaller restoring forces in the motion equations in the LARes models. The selection of the barge is important due to the wall sided geometry which maintains linear F-K and restoring forces during the time-domain simulations. In the internal loads calculations at station 15 and station 10 LARes L2 and L1 results agreed well with the nonlinear PRETTI model at zero speed case. The VBM responses are found to be identical in the LARes and PRETTI models while the VSF responses is slightly over-estimated in the LARes models compared to the PRETTI model around the resonant frequency. The main reason for this is attributed to the sensitivity of the VSF responses and the pressure integration techniques and also the hydrodynamic axis preferences in the PRETTI and LARes models.

In the S-175 containership geometry, at zero speed case, LARes L3, L2, L1 models motion and load responses are tested and compared in detail with the nonlinear PRETTI results. It has been observed that either in linear or in nonlinear simulations all global hydrodynamic force components are in a well agreement with the PRETTI results and therefore it validates accuracy of the system of motion and loads equations. At the Fn=0.25 forward speed case, the LARes L3, L2 and L1 models heave and pitch responses are compared with the nonlinear PRETTI, linear PRECAL and the experimental results obtained by Fonseca and Soares (2004). LARes model results agreed better with the experimental results, especially for the heave responses, than the PRETTI model due to the lack of the surge motion influence and the pressure integration preferences. In the internal load responses, LARes L3, L2 and L1 results are well agreed with the PRETTI model results. However, the peak values of the VSF (st 15) and VBM (st 10) responses in the numerical models are found to be shifted to higher frequencies when compared to the experiments. The main reason for that is attributed to the difference between the longitudinal mass distribution in the numerical models and the experiments.

Chapter 6

Application of the Methodology on Motion Responses

6.1 Introduction

In this chapter, the effects of nonlinearity level on the motion responses using the developed seakeeping models are investigated and compared in detail. The main aim of the current chapter is to underline the effects of nonlinearity on the ship motion responses, highlight the origin of the differences and to perform benchmark tests of the in-house developed LARes L3 and LARes L2 models by comparing the motion results in large amplitude waves with experimental data. In order to perform comparisons of different seakeeping models, available experimental results are used and the relative performance of the models is investigated focusing on the level of nonlinearity, forward speed, wave length, maximum and minimum motion amplitude peaks. Moreover, quasi-non-linear radiation and diffraction forces and moments are compared with the linear radiation and diffraction forces at large amplitude waves.

6.2 Effect of the nonlinearity level in motion responses

In this section, the effects of the nonlinearity level of modelling on the predicted motions of the S-175 containership in large amplitude waves are investigated. Large amplitude seakeeping analyses are performed using the LARes L3, L2 and nonlinear

PRETTI models compared with the available experimental results. In order to investigate the nonlinear ship motions in detail three different ship speeds (Fn=0.20, 0.25, 0.275), and for each speed case, three different wave lengths (λ/L_{pp}=1.0, 1.2, 1.4) around the resonant frequency have been selected to investigate the motion responses in head seas. Large amplitude ship motion results are compared with the experiments performed by the ITTC (2010) with respect to the increasing wave slope and are given in the form of non-dimensional heave and pitch response amplitudes.

The non-dimensional vertical motion amplitudes at a forward speed of Fn=0.20 (≈16 knots) with three wavelengths around the resonance frequency are illustrated in the graphs from Figure 6.1 to Figure 6.3. The non-dimensional vertical motion amplitudes using PRETTI, LARes L2 and LARes L3 models are compared with the corresponding experimental results. Initially, it appears that the LARes L2 and LARes L3 models agree better with the experimental data compared to the PRETTI results.

In the non-dimensional heave responses at Fn=0.20 and λ/L_{pp}=1.0, the PRETTI results show a constant trend and do not show the reduction of the response amplitudes with the increasing wave slope, while the experiments show a reduction of about 35% around the small wave slopes. In this simulation, the LARes L2 and LARes L3 heave results agree better with the experimental data than the PRETTI results due to the lack of surge motion influence in the system of motion equations. As for the PRETTI model, the LARes L2 model does not show a decrease in heave amplitudes with respect to the increasing wave slope. However, the decrease in the non-dimensional heave response amplitudes is obsolete in the LARes L3 model, which shows the significance of the influence of nonlinear radiation and diffraction forces. In heave responses, the LARes L3 model agrees better than other models with the experiments, whilst the difference between the LARes L3 and LARes L2 results is up to 15% in large amplitude waves. In the non-dimensional pitch amplitudes for the same simulation case, LARes L2 and L3 responses agree better with the experimental data compared to the PRETTI model results. There is an increasing trend in the pitch amplitudes for the LARes L2 and PRETTI models around the wave slope $k\zeta_a$=0.06, which corresponds to H_w≈3.8m, and after this wave height threshold, non-dimensional pitch amplitudes decrease around 10%. The same trend of increase and then decrease in the pitch amplitudes is also observed in the experimental results, but the slope of the variation is smaller than the LARes L2 and PRETTI results. The LARes L3 model, shows the best agreement with the experimental results among other models and the results follow the exact trend of the experimental results while possessing a reduction in the non-dimensional pitch amplitudes of around 15% when compared to the LARes L2 results.

In Figure 6.2 the non-dimensional heave and pitch amplitudes at Fn=0.20 and λ/L_{pp}=1.2, which is the resonance frequency for the heave response, are illustrated. The PRETTI model shows a decreasing trend up to the wave slope $k\zeta_a$=0.08 (H_w≈5m) and then shows a sharp increase with respect to the increase in the wave slope. The increase in the heave response amplitude in the PRETTI model is due to the large amplitude waves which increase the influence of cross-coupling forces arising from large surge displacements and also the high wave slopes which invalidate the small scattering wave assumption. In the LARes L2 model, heave amplitudes decrease up to the threshold and remains constant afterwards and this is due to the lack of surge motion responses. The LARes L3 model non-dimensional heave amplitudes agree better with the experiments compared to the LARes L2 and PRETTI models. The difference in the predicted heave motion amplitudes between the LARes L3 and L2 models is about 10% at high wave slope values. In the non-dimensional pitch amplitudes for the same simulation case, all models show a decrease in the pitch amplitudes with the increasing wave slope. The PRETTI model results are higher than the experimental results however the LARes L2 and L3 models demonstrate good agreement with the experimental data. The difference between the LARes L2 and L3 models increases around a wave slope value of $k\zeta_a$=0.08, but then shows a small reduction. This decrease is due to the large slope of the waves and if large scattering waves are of concern, smooth particle methods or CFD methods should be used instead of potential-based solutions for predicting the motions.

In Figure 6.3 the non-dimensional heave and pitch amplitudes at Fn=0.20 and λ/L_{pp}=1.4, which is the longest wave case for the simulation around the resonance frequency are illustrated. All results show that they agree well with the experimental results however the heave responses are over-predicted. The difference between the models is small for the other wavelengths and results show a constant decrease with the increasing wave slope. At the highest wave slope the difference between the LARes L2 and L3 models is about 5% where the LARes L3 results agree better with the experiments. For the same simulation case, the numerical non-dimensional pitch results show a steep decrease whereas the experimental results show a nearly constant trend with the increasing wave slope. All of the results over -predict the experimental results whilst the PRETTI results have the worst agreement with the experiments compared to the LARes L2 and L3 model estimations. The difference between the pitch amplitudes using the LARes L3 and L2 results at the highest wave slope increases up to 8%.

In Figure 6.4 the non-dimensional heave and pitch amplitudes at Fn=0.25 and λ/L_{pp}=1.0 are illustrated. At first glance, the results appear to be over-predicted when compared to the experiments while the PRETTI and LARes L2 models show a slight increase in non-dimensional heave amplitudes with the increasing wave slope. The experimental results show a constant trend with the increasing wave slope and the results obtained from the LARes L3 model has managed to maintain the same trend compared to the experiments. The difference between the LARes L3 and LARes L2 models increase up to 15% with the increasing wave height while LARes L3 provides the best agreement with the experiments among the other models. For the same simulation case, all of the models over-predict the non-dimensional pitch amplitudes compared to the experimental results. The same trend also occurs in the pitch responses, where the results obtained from the PRETTI and LARes L2 models show an increase with the increasing wave slope. However, the experimental results show a constant trend and the LARes L3 results again maintain the same trend with the experimental results and show the best agreement. The success of the LARes L3 model is due to the evaluation of quasi-non-linear radiation and diffraction forces.

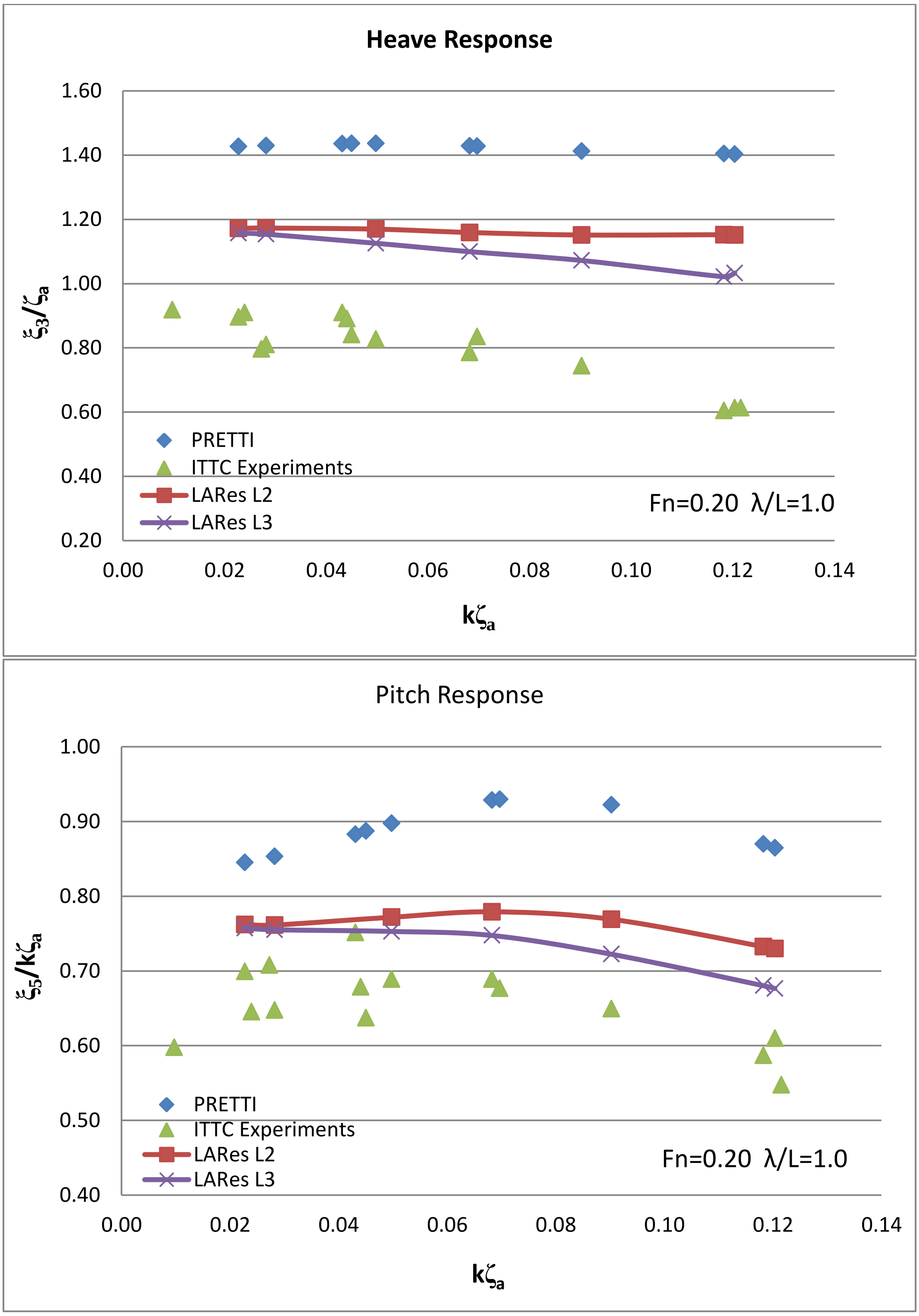

Figure 6.1: Variation of non-dimensional heave and pitch response with the wave steepness (Fn=0.20, λ/L=1.0)

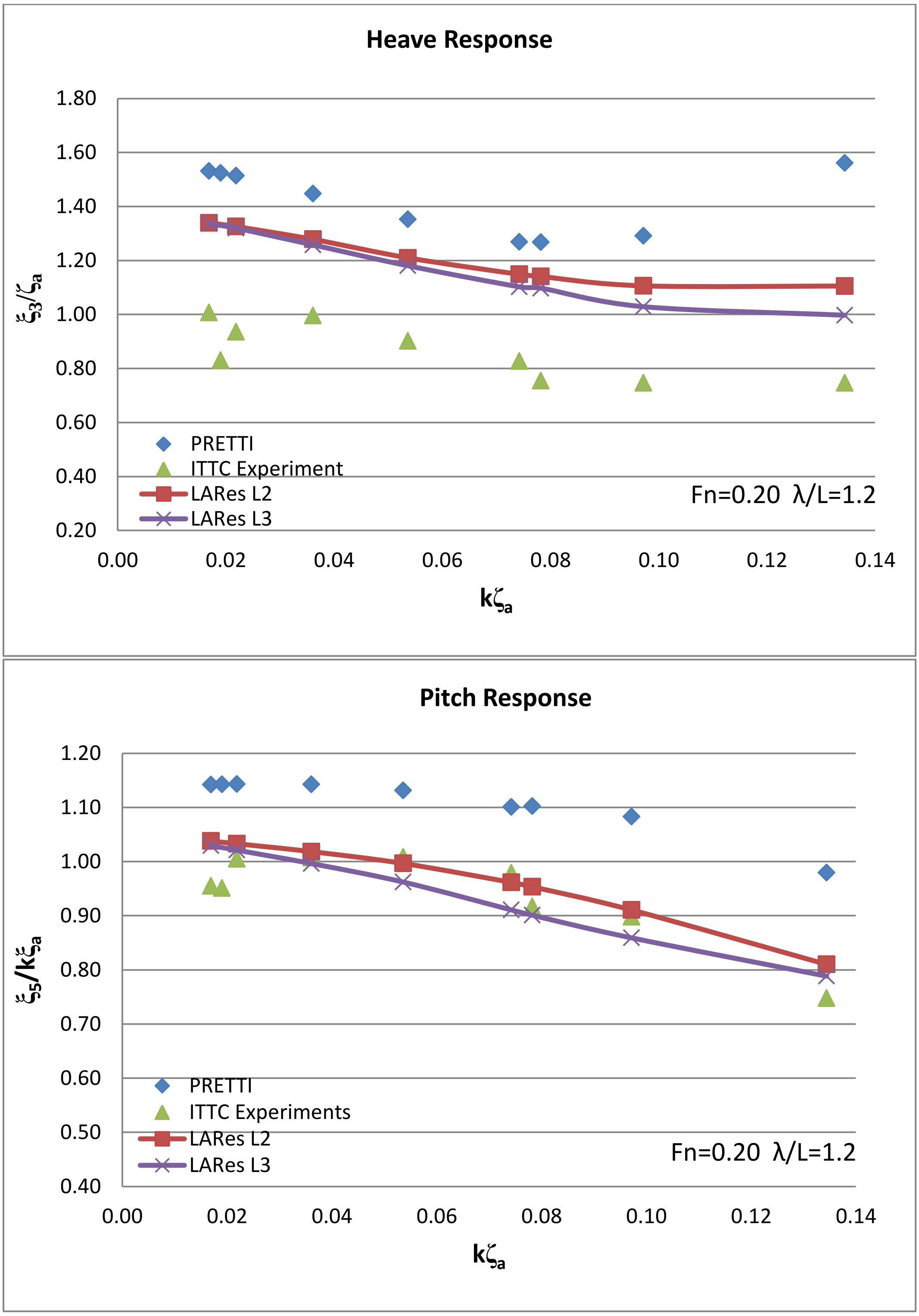

Figure 6.2: Variation of non-dimensional heave and pitch response with the wave steepness (Fn=0.20, λ/L=1.2)

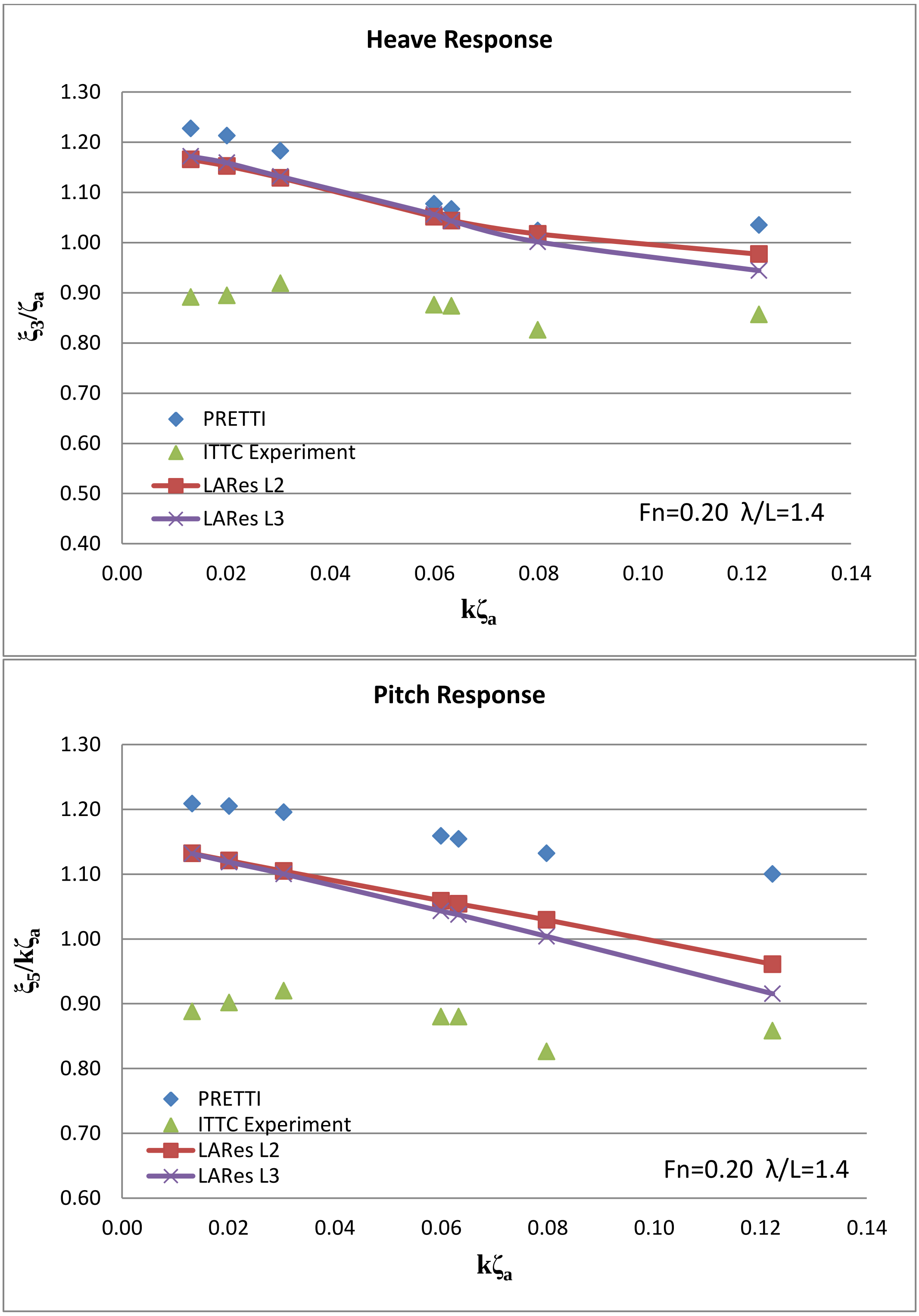

Figure 6.3: Variation of non-dimensional heave and pitch response with the wave steepness (Fn=0.20, λ/L=1.4)

In Figure 6.5 the non-dimensional heave and pitch amplitudes at Fn=0.25 and λ/L_{pp}=1.2 are illustrated. The numerical estimations of all three models over-predict the heave response amplitudes when compared to the experimental results. In the experimental results a decrease in the heave amplitudes is observed with the increasing wave slope. In the PRETTI model, heave amplitudes show a reduction until a wave slope value of $k\zeta_a$=0.08 and then they have a slight increase with the increase in the wave slope. The LARes L2 and L3 model non-dimensional heave amplitudes agree better with the experimental results compared to the PRETTI estimations. They show a decreasing trend of heave amplitudes which follow the same trend as the experimental data. The LARes L3 model provides closer results to the experiments compared to the LARes 2 model due to the quasi-non-linear radiation and diffraction forces being accounted for. The difference in heave amplitudes between the LARes L3 and L2 model are up to 15% with the increasing wave slope. For the same simulation case, the non-dimensional pitch amplitudes are over-predicted by the PRETTI model whist the LARes L2 and L3 models agree well with the experimental results. In the experimental data, there is a slight increase in the pitch amplitudes until the wave slope of $k\zeta_a$=0.06 and then a decrease with the increasing wave slope. The LARes L2 and PRETTI models show the same trend as the experimental results however the LARes L3 model showed a constantly decreasing trend of pitch amplitudes with the increasing wave slope. The difference between the LARes L3 and LARes L2 models non-dimensional pitch responses are observed to be up to 6% dependent on the wave amplitude.

In Figure 6.6 the non-dimensional heave and pitch amplitudes at Fn=0.25 and λ/L_{pp}=1.4 are illustrated. In the heave amplitudes, all models over-predict the experimental results. The experimental results show a decrease with the increasing wave slope while the PRETTI and LARes L2 models show a decrease until the threshold of wave slope $k\zeta_a$=0.08 and then a slight increase with the increase in the wave slope. On the contrary, LARes L3 heave amplitudes provide almost the same results as the LARes L2 model until the wave slope values of $k\zeta_a$=0.06 and when the wave amplitude is increased the LARes L3 model demonstrates better agreement with the experimental results compared to the other models. For the same simulation case in the Figure 6.6, the PRETTI model non-dimensional pitch amplitudes agreed better with the experimental results while the LARes L2 and L3 estimations slightly under estimate the pitch amplitudes. The under-estimation of the pitch amplitudes at high wave slope is about 5% compared to the experiments and this is due to the lack of surge motion influence in the LARes L2 and L3 models, and in the LARes L3 model, it is additionally due to the larger damping forces due to the quasi-non-linear radiation forces. In the pitch amplitudes, experimental data and LARes L2 and L3 models show a slight decrease while the PRETTI model show a constant trend with the increasing wave slope.

In Figure 6.7, the non-dimensional heave and pitch amplitudes at Fn=0.275 and $\lambda/L_{pp}=1.0$ are illustrated. In the heave amplitudes, all models over-predict values compared to the experimental results. The PRETTI and LARes L2 models show an increase in the heave amplitudes with the increase in the wave slope. However, in the PRETTI model the increasing trend is maintained until a wave slope value of $k\zeta_a=0.09$ ($H_w\approx5m$) and then has constant values with the increase in the wave slope, while the LARes L2 model has a constantly increasing trend. The LARes L3 model shows a slightly decreasing trend with the increasing wave slopes. In general, the LARes L3 model has a better agreement with the experiments compared to the other models. The difference in the heave amplitudes between the LARes L3 and L2 is up to 10% at high wave slopes. For the same simulation case, in Figure 6.7, all of the models over-estimate the non-dimensional pitch amplitudes compared to the experimental results. The results obtained from the PRETTI and LARes L2 models have an increasing trend until a wave slope value of $k\zeta_a=0.09$ and then have a constant trend. The LARes L3 model has a decreasing trend of pitch amplitudes which is the same as observed in the experimental results. The LARes L3 model predictions show the best agreement with the experimental data compared to the other models. The difference in the pitch amplitudes between the LARes L3 and L2 models is observed to be up to 8% at the large wave slopes.

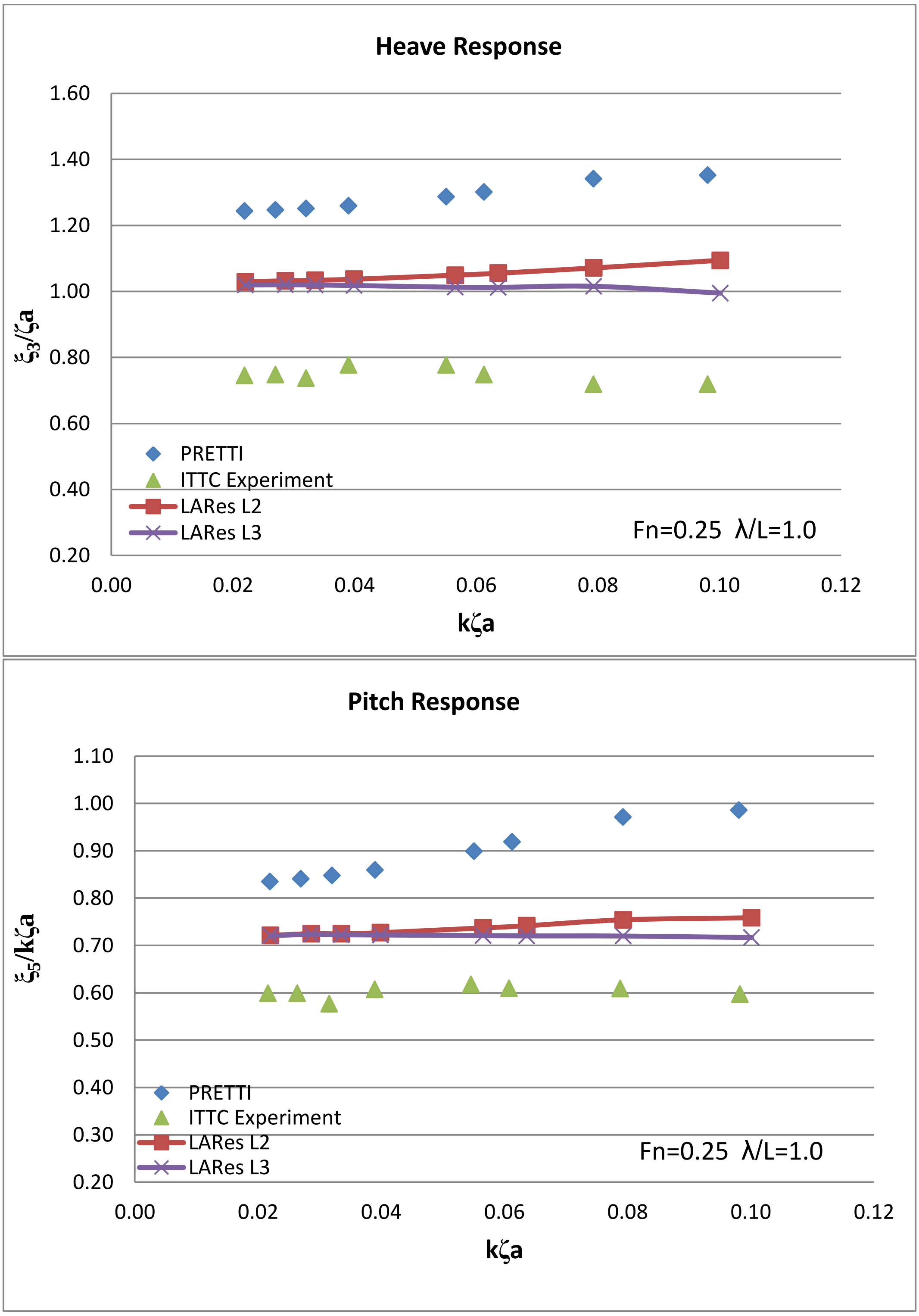

Figure 6.4: Variation of non-dimensional heave and pitch response with the wave steepness (Fn=0.25, λ/L=1.0)

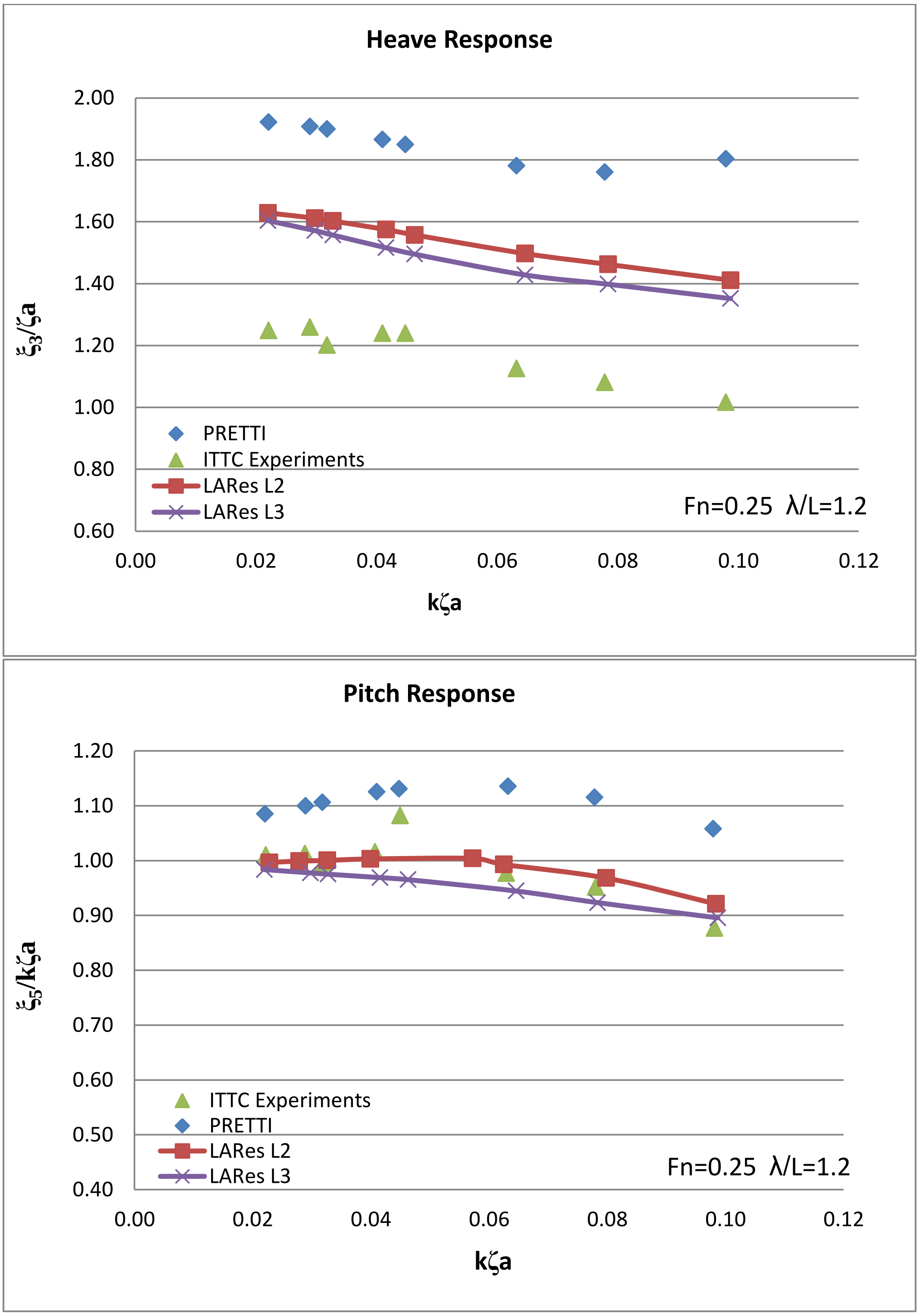

Figure 6.5: Variation of non-dimensional heave and pitch response with the wave steepness (Fn=0.25, λ/L=1.2)

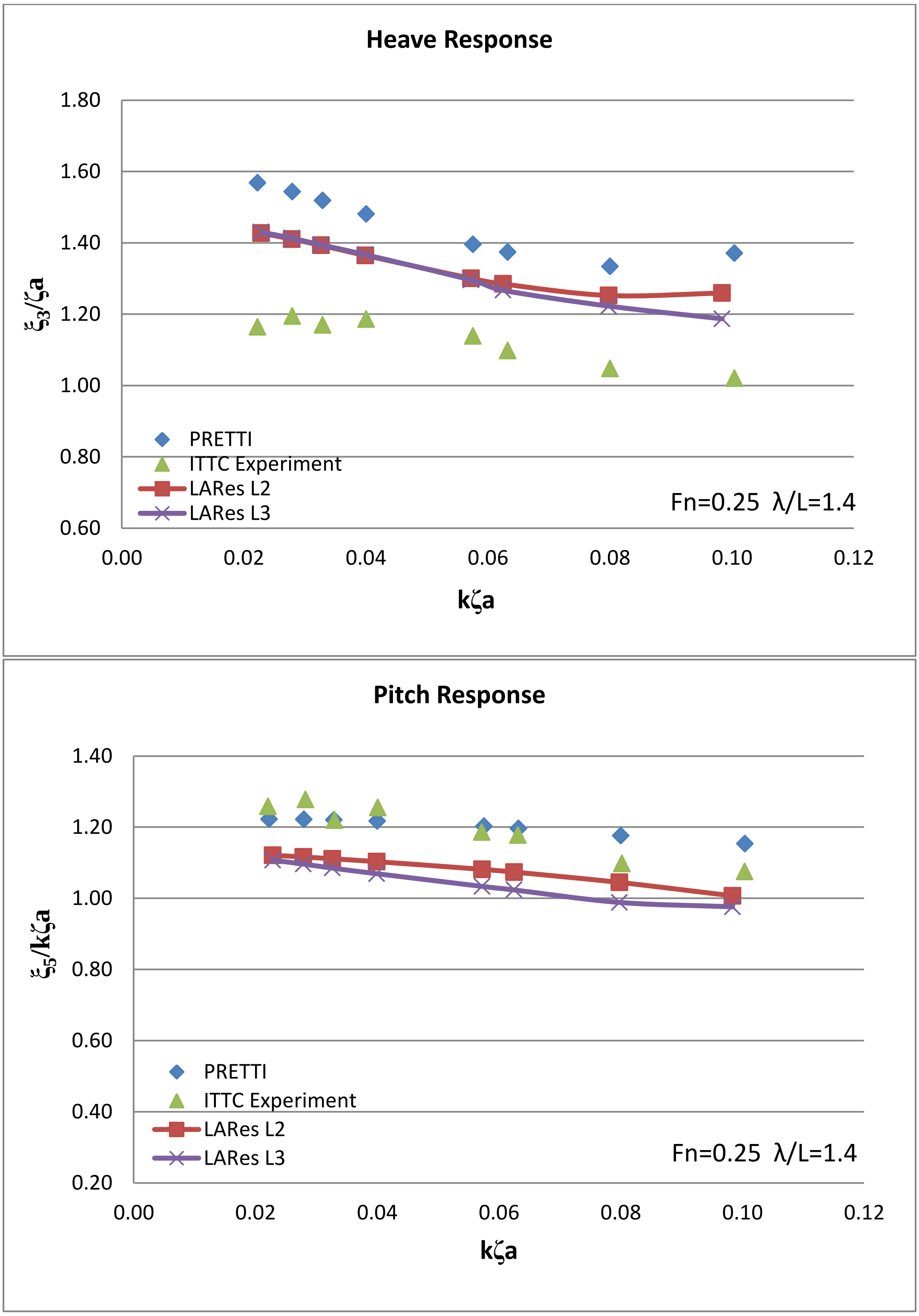

Figure 6.6: Variation of non-dimensional heave and pitch response with the wave steepness (Fn=0.25, λ/L=1.4)

In Figure 6.8 the non-dimensional heave and pitch amplitudes at Fn=0.275 and λ/L_{pp}=1.2 are illustrated. In the non-dimensional heave amplitudes, all models give an over-prediction when compared to the experimental results. In the PRETTI model, non-dimensional heave amplitudes show a slight decrease with the increasing wave slope, however in the LARes L3 and L2 models the slope of the decrease is higher than the PRETTI model and therefore they agree better with the experiments. The LARes L3 model has the best agreement with the experiments. The difference between the LARes L3 and L2 models is in the order of 15%. For the same simulation case, the non-dimensional pitch amplitudes agree well with the experiments. All the numerical models have under-predicted the pitch amplitudes at small wave slopes up to $k\zeta_a$=0.05 ($H_w\approx$4m). However, the results from the PRETTI model over-predicted the pitch amplitudes after this threshold while the LARes L2 and L3 models agreed well with the experiments for wave slopes higher than $k\zeta_a$=0.05.It must be noted that the LARes L3 and L2 model results are nearly identical for pitch responses for this simulation case except the last value of pitch at very large wave slope.

In Figure 6.9 the non-dimensional heave and pitch amplitudes at Fn=0.275 and λ/L_{pp}=1.4 are illustrated. In the non-dimensional heave amplitudes, all models over-predict when compared to the experimental results. The results obtained from the PRETTI and LARes L2 models show a decreasing trend of the heave amplitudes up to the wave slope value of $k\zeta_a$=0.08 ($H_w\approx$6m) and after they have an increasing trend which is the opposite of the trend of the experimental results. The LARes L3 results show a constant decreasing trend therefore agrees the best with the experimental results. At very high wave slopes, the difference in the non-dimensional heave amplitudes between the LARes L3 and L2 estimations is of the order of 20%. For the same simulation case, the non-dimensional pitch amplitudes of all models agree well with the experiments. The non-dimensional pitch amplitudes obtained from PRETTI are under-predicted up to a wave slope value of $k\zeta_a$=0.06 and then slightly over-predicted. The LARes L3 and L2 models show the same decreasing trend as experimental results however they slightly under-predict the nonlinear pitch amplitudes due to the lack of surge motion influence. The difference between the LARes L3 and L2 models is in the order of 5% and this difference originates from the quasi-non-linear radiation forces which apply larger damping forces to the system of motion equations.

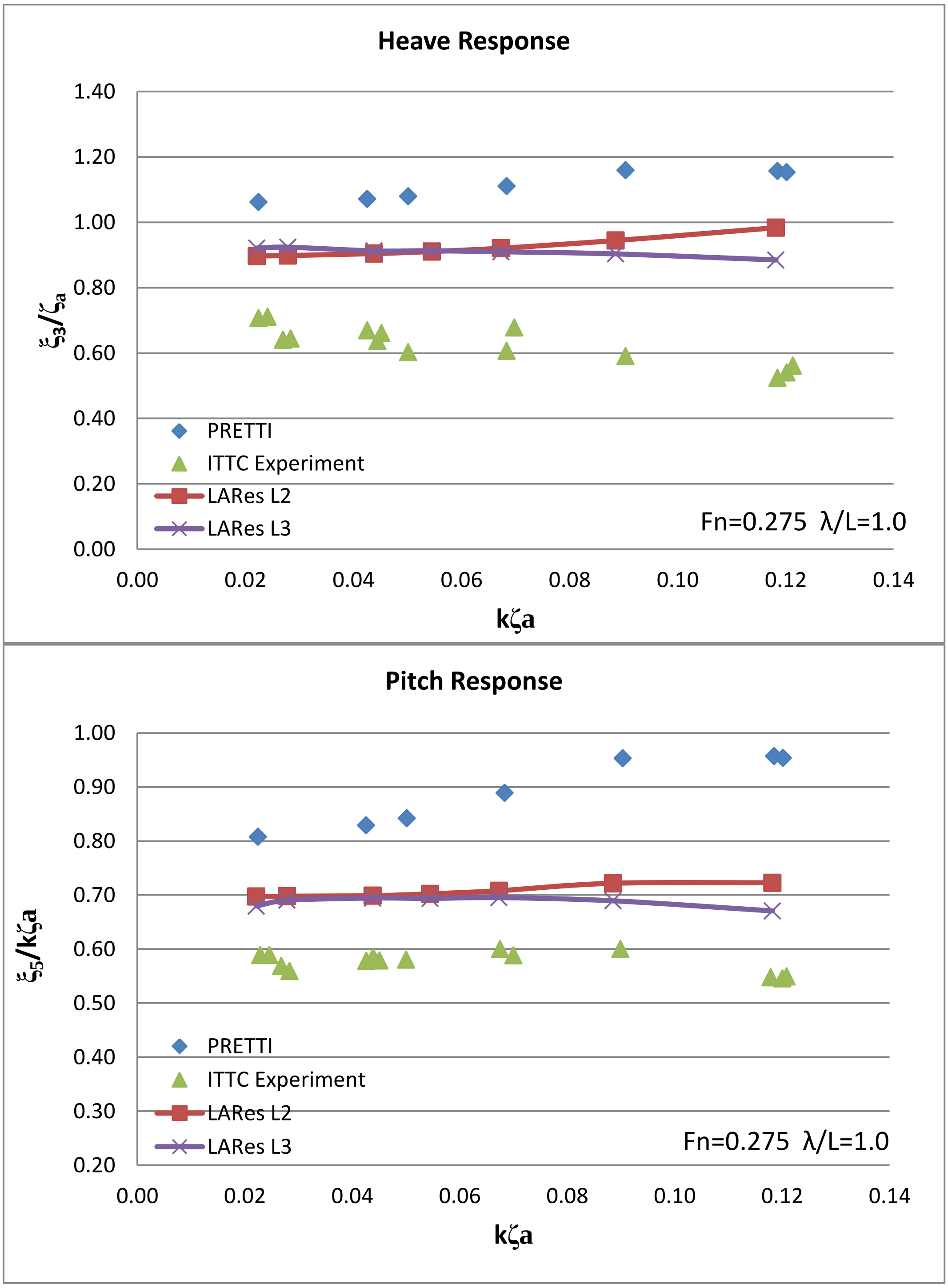

Figure 6.7: Variation of non-dimensional heave and pitch response functions with the wave steepness (Fn=0.275, λ/L=1.0)

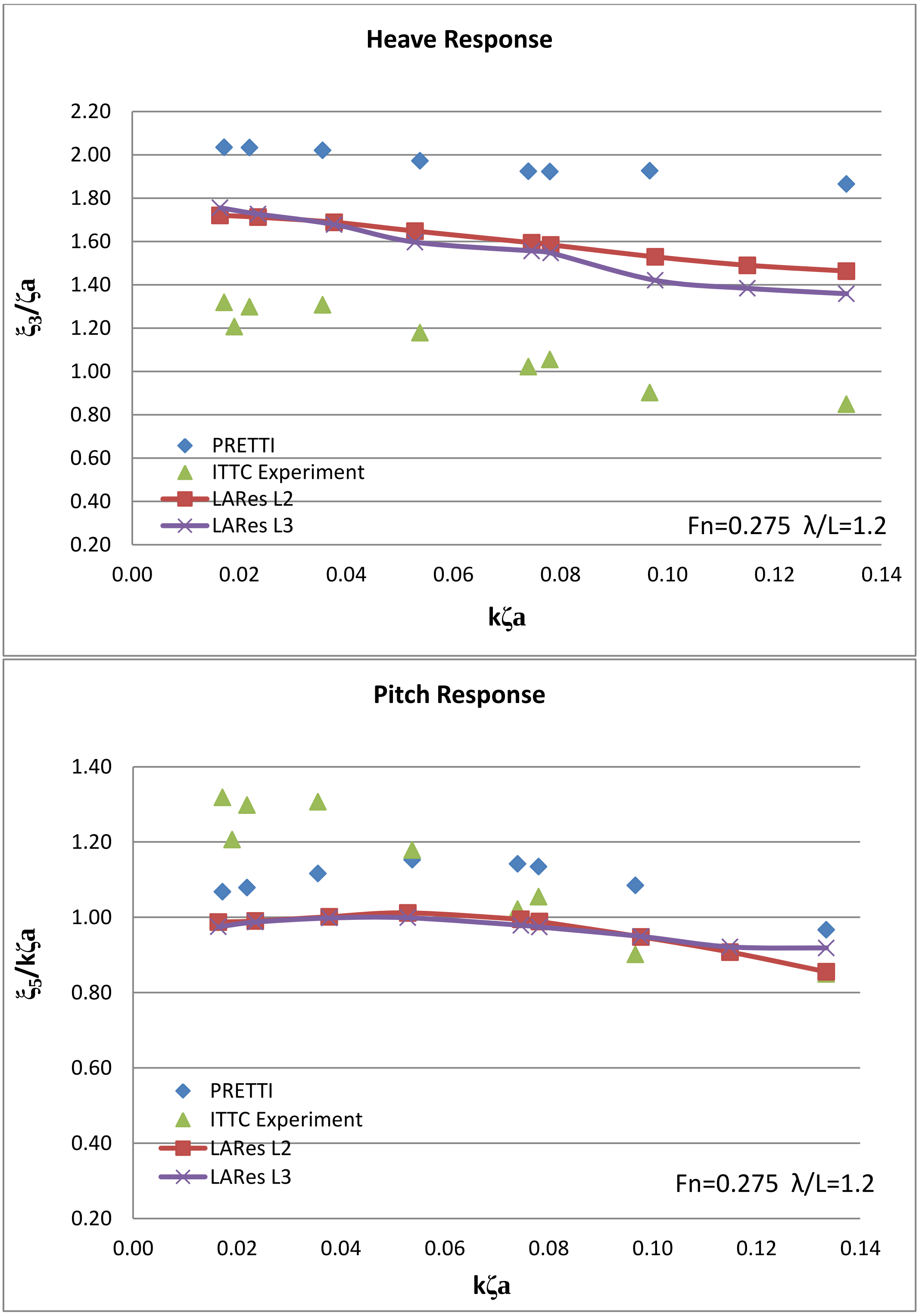

Figure 6.8: Variation of non-dimensional heave and pitch response with the wave steepness (Fn=0.275, λ/L=1.2)

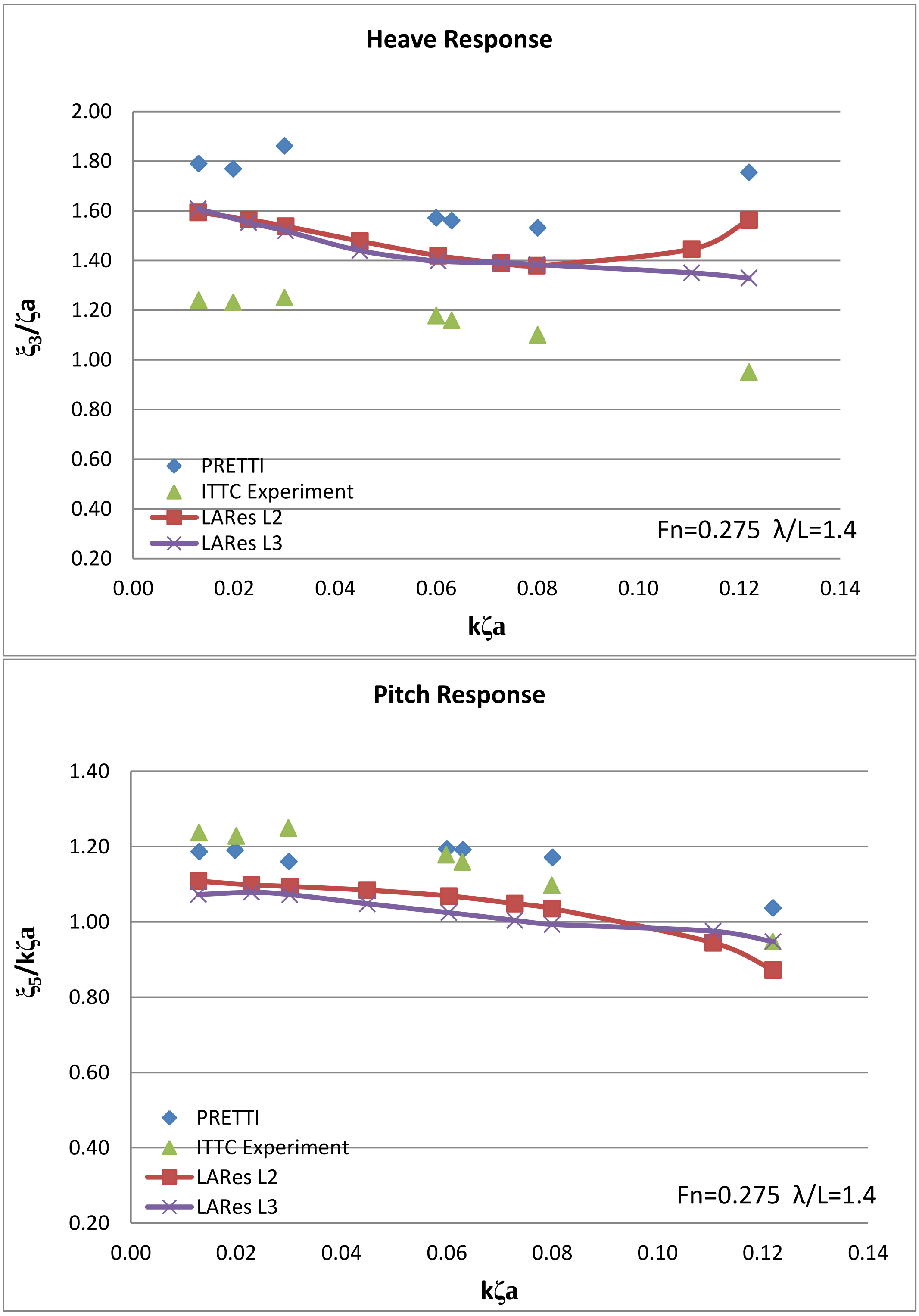

Figure 6.9: Variation of non-dimensional heave and pitch response with the wave steepness (Fn=0.275, λ/L=1.4)

6.3 Influence of the wave length on motion responses

In this section the influence of wave length on ship motion responses are investigated in detail for three forward speed cases (Fn=0.20. 0.25, 0.275) and for each forward speed case, three wave lengths around the resonant frequency are considered. Comparisons of the wave length influence ion the predicted ship motions are illustrated in Figure 6.10, Figure 6.11 and Figure 6.12 for the Fn=0.20, 0.25 and 0.275 cases respectively.

In Figure 6.10 the effects of the variation in the wave lengths around the resonant frequency on the non-dimensional heave and pitch amplitudes at Fn=0.20 are illustrated. In non-dimensional heave responses, in the experimental results an increase in the heave amplitudes is observed at λ/L_{pp}=1.2 and for longer waves than this wave length it is followed by a decrease. Moreover, in all wave lengths when the wave slope is increased a decreasing trend of heave amplitudes is observed. In all of the results at Fn=0.20, the LARes L3 model results agreed the best with the experiments and followed the experimental data trend well. The results obtained from PRETTI and LARes L2 models, show an instant increase around the large wave slope region when λ/L_{pp}=1.2 and 1.4, which can be attributed to the lack of nonlinear radiation and diffraction forces. In the heave responses, as expected, the difference in the heave amplitudes between the LARes L3 and other models is observed to be higher. The reason for this is attributed to the increase in the influence of radiation and diffraction forces in shorter waves whereas in long waves, most of the forces originate from the F-K and restoring forces. Therefore, in shorter waves the influence of the quasi-non-linear radiation and diffraction forces are more pronounced and the difference between results obtained from the LARes L2 and L3 models is observed to be around 15%. In the non-dimensional pitch responses for the same simulation case, an increase in the pitch amplitudes is observed in the experiments around the resonant frequency and this is followed by a decrease at longer wave lengths. In all of the wave length cases, the LARes L3 model agrees the best amongst with the experimental data compared to the other models tested and follows the exact trend as is also observed in the experimental results. At a wave length to ship length ratio of

λ/L_{pp}=1.0, the differences between the LARes L3 and L2 model results observed at the highest level and the order of the reduction in the pitch amplitudes are observed to be around 10%. At the resonant frequency, LARes L2 and L3 agree very well with the experimental results by following the exact trend of the experiments. At the longest wave case (λ/L_{pp}=1.4), all models over-predicted the results, but the LARes L3 model results show the best performance compared to the other models in the agreement with the experimental results. The maximum difference in the pitch amplitudes between the LARes L3 and L2 model is observed to be 10%. Moreover, all of the models showed a high slope of decrease with the increasing wave slope while the experiments show a nearly constant trend in pitch amplitudes.

In Figure 6.11 the effect of the variation of wave lengths on the non-dimensional heave and pitch amplitudes at Fn=0.25 are illustrated. In the heave amplitudes, at the smallest wave length (λ/L_{pp}=1.0) the results show a constant trend, but at λ/L_{pp}=1.2 and 1.4, the heave amplitudes show a decreasing trend with the increase in the wave slope. In the λ/L_{pp}=1.0 simulations, the results obtained from PRETTI and LARes L2 models show a decrease in the high wave slope region while the experiments show a constant trend. The LARes L3 model results follow the experimental data trend well and have the best agreement with the experiments compared to the results obtained from other models. The difference in the predicted heave amplitudes between the LARes L3 and L2 is observed to be 15%. In the λ/L_{pp}=1.2 simulations, heave responses are amplified in all models and in the LARes L3 and L2 models a decreasing trend of heave amplitudes is observed while the PRETTI model shows an increasing trend at large wave slopes, which is opposite to the experiments and other models. At the longest wave case (λ/L_{pp}=1.4), the LARes L3 and L2 results are nearly identical up to a wave slope value of $k\zeta_a$=0.06 and at large wave slopes LARes L3 results agreed better with the experiments. The difference between the LARes L3 and L2 models is observed to be around 10%. For the same forward speed, at λ/L_{pp}=1.0, experimental non-dimensional pitch amplitudes show a constant trend while at λ/L_{pp}=1.2 and 1.4 they show a slight decrease with the increase in the wave slope.

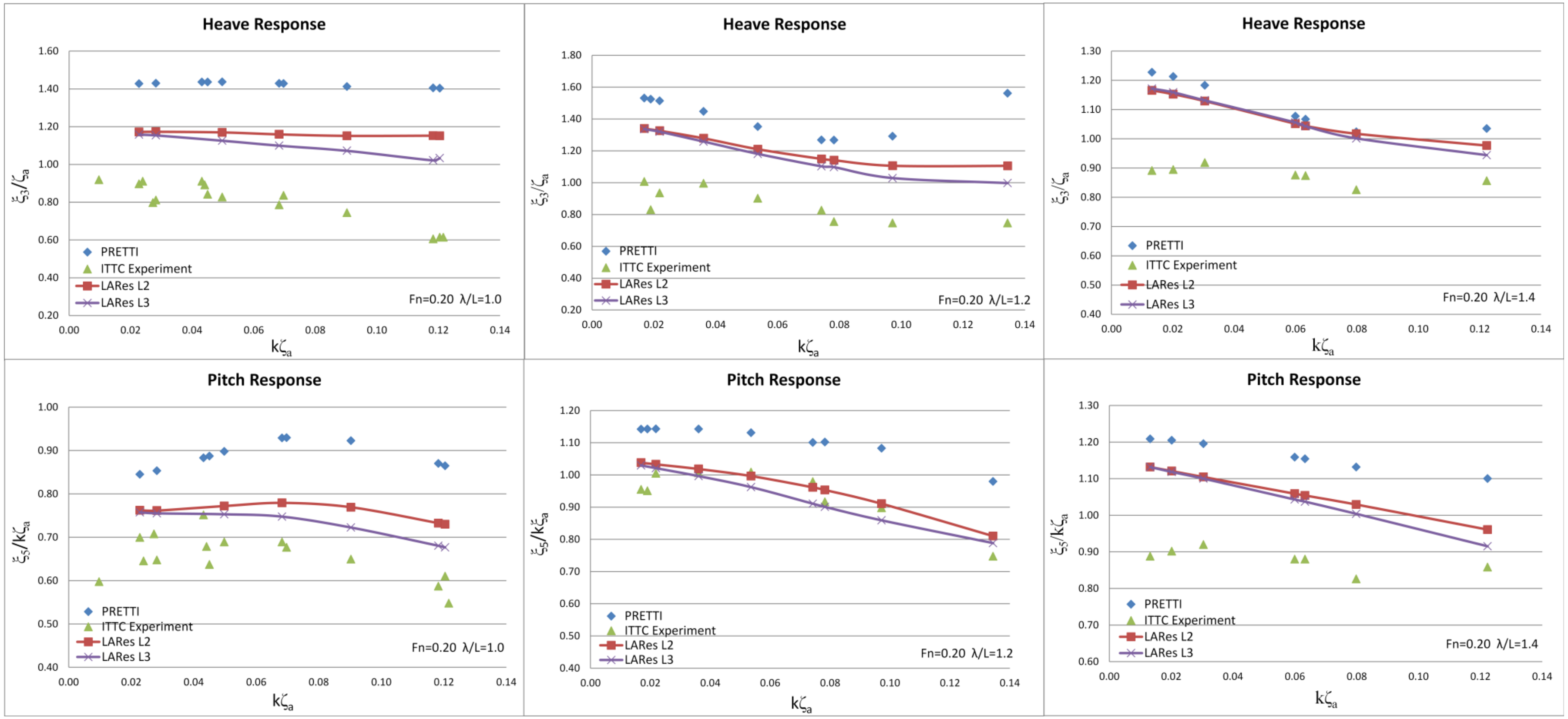

Figure 6.10: Influence of wave length and wave steepness on the non-dimensional heave and pitch responses (Fn=0.20, λ/L=1.0, 1.2, 1.4)

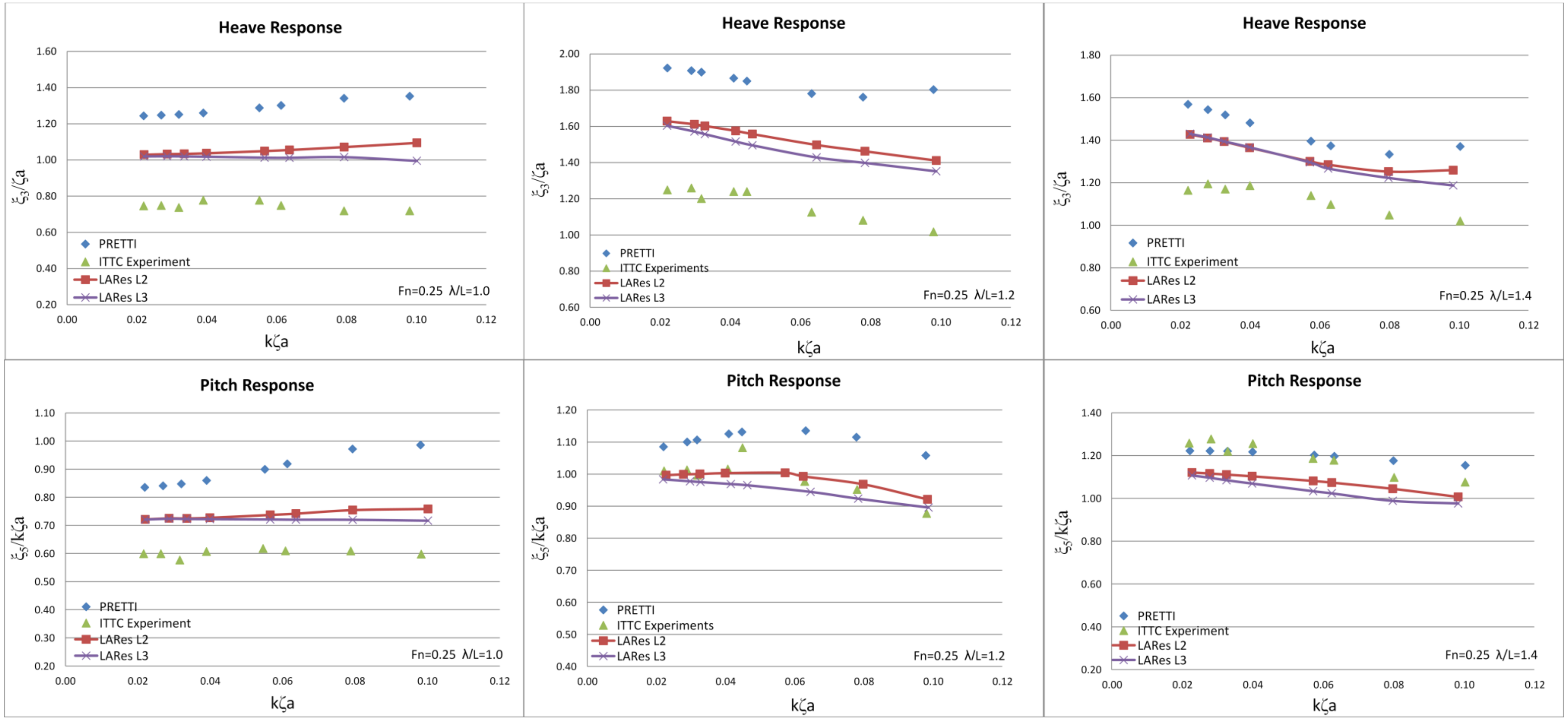

Figure 6.11: Influence of wave length and wave steepness on the non-dimensional heave and pitch responses (Fn=0.25, λ/L=1.0, 1.2, 1.4)

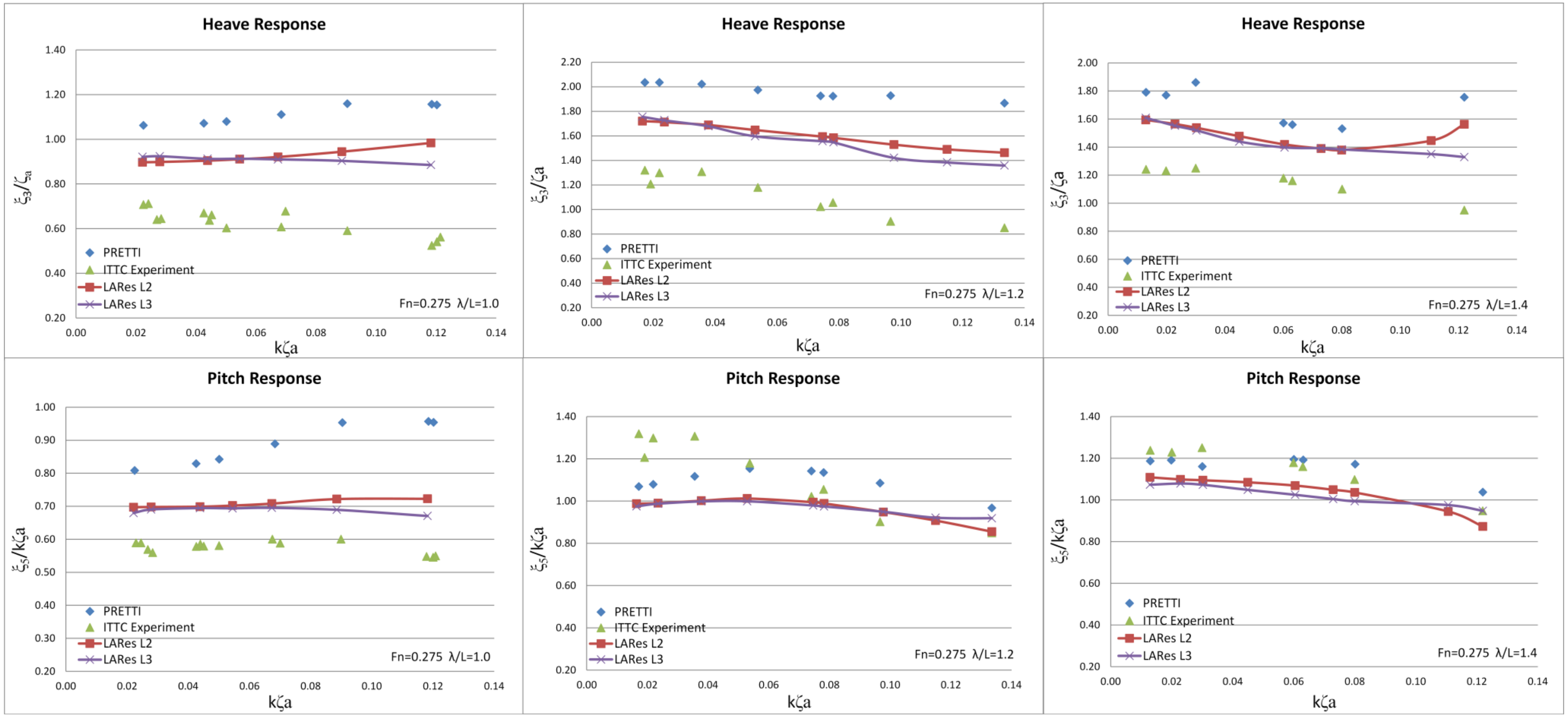

Figure 6.12: Influence of wave length and wave steepness on the non-dimensional heave and pitch responses (Fn=0.275, λ/L=1.0, 1.2, 1.4)

In the PRETTI model non-dimensional pitch amplitudes, except the λ/L_{pp}=1.4 simulation case, over-predict the experimental results. At the smallest wave length case (λ/L_{pp}=1.0), PRETTI and LARes L2 model pitch amplitudes show an increasing trend with the increasing wave slope which is the opposite of the experiments. The LARes L3 model shows a constant trend of pitch amplitudes and agrees well with the experiments. The difference between the LARes L3 and L2 model for this case is found to be 7% at high wave slopes. At the λ/L_{pp}=1.2 case, the LARes L3 and L2 models agree well with the experiments while the LARes L2 model shows a slight increase in pitch amplitudes up to a wave slope value of $k\zeta_a$=0.06 and then shows a decrease. The LARes L3 model show a constant decrease with the increase in the wave slope. At the λ/L_{pp}=1.4 case, the LARes L3 and L2 model results under-predict the pitch amplitudes due to the lack of the surge influence in the system of motion equations. The PRETTI model results agree well with the experimental data and provide the best results for this case.

In Figure 6.12 the effect of the variation in the wave lengths on the non-dimensional heave and pitch amplitudes at Fn=0.275 is illustrated. In the heave amplitudes, experiments show a decreasing trend with the increase in the wave slope. In the λ/L_{pp}=1.0 case, the PRETTI and LARes L2 model results show an increase in the heave amplitude with the increase in the wave slope while the LARes L3 model results show a decrease similar to the experiments and provide the best agreement with the experimental data amongst the models. In the λ/L_{pp}=1.2 case, the results obtained from all models show a decreasing trend with increasing wave slope. The LARes L3 model show the best agreement with the experiments in the heave amplitudes and the difference between the LARes L3 and L2 model is observed to be 10% at high wave slopes. For the λ/L_{pp}=1.4 case, the PRETTI and LARes L2 model heave amplitudes show a decrease up to the wave slope of $k\zeta_a$=0.08 and then an increase. The main reason for the increase at high wave slopes is attributed to the large scattered waves which cannot be calculated with the level 2 models The LARes L3 model provides the best agreement in the heave amplitudes amongst the other models tested by following the decreasing experimental data trend. For the same forward speed case, the non-dimensional pitch amplitudes in the experiments show a constant trend at λ/L_{pp}=1.0 and a decreasing trend for the λ/L_{pp}=1.2 and 1.4 experiments. At the λ/L_{pp}=1.0 case, the PRETTI and LARes L2 models show an increase in the pitch amplitudes up to a wave slope of $k\zeta_a$=0.08 and then remain constant with respect to the increasing wave slope. The LARes L3 model results follow the experimental data well and provide the best agreement compared to the other models. In the λ/L_{pp}=1.2 case, all the numerical models under-predict the pitch amplitudes up to a wave slope of $k\zeta_a$=0.06, but after this threshold the PRETTI model over-predicts the experimental results. The LARes L3 and L2 models show nearly identical curves while they have a good agreement with the experiments in the large wave slope region. In the λ/L_{pp}=1.4 case, PRETTI results show the same trend as with the λ/L_{pp}=1.2 case while LARes L3 and L2 models slightly under-predict the pitch amplitudes compared to the experimental results while still following the same trend as the experiments.

6.4 Influence of speed on motion responses

In this section, the influence of forward speed on large amplitude motions is investigated in detail by keeping the wave length constant and increasing the forward speed of the vessel around the resonant frequency. Comparisons of the forward speed influence on the ship motion responses are illustrated in Figure 6.13, Figure 6.14 and Figure 6.15 for the λ/L_{pp}=1.0, λ/L_{pp}=1.2, λ/L_{pp}=1.4 cases respectively.

In Figure 6.13 the effect of the variation in the forward speed of the non-dimensional heave and pitch amplitudes at λ/L_{pp}=1.0 case is illustrated. The importance of the λ/L_{pp}=1.0 simulation is that this is the shortest wave case around the resonant frequency region and the differences between the LARes L3 and L2 models are observed to be the largest due to the dominance of radiation and diffraction forces. In the current case, the mean amplitude of the experimental heave responses decreases with the increasing forward speed. However, it is hard to draw a general conclusion for the behavior of the heave response trends where at Fn=0.20 and 0.275 there is a reduction of amplitudes while at Fn=0.25, they have a constant trend with the increasing wave steepness. In general, the results obtained from LARes L3 and L2 models agree well with the experiments while the largest difference between the models is observed in the lowest forward speed case. The reason for that is the correction of the forward speed effects in the solution of BVP problems in LARes and PRETTI models. At high forward speed, corrections are of a higher order than slow forward speeds and this lead to the loss of sensitivity in the responses. In the experimental pitch results, mean response amplitudes are observed to be decreasing with the increasing forward speed. The trends of the pitch motion curves decrease at Fn=0.20 but at Fn=0.25 and 0.275 they are observed to have a constant trend. The results obtained from the LARes L3 and L2 models generally agree well with the experimental pitch responses while the largest difference between the models is observed in the lowest forward speed case. The LARes L3 model has the best agreement among the other models and follows the experimental trend very well.

In Figure 6.14 the effect of the variation in the forward speed on the non-dimensional heave and pitch amplitudes at λ/L_{pp}=1.2 case is illustrated. This case is important because it is the closest frequency to the resonant frequency and therefore all responses are amplified when compared to other wave frequencies. In the current case, the mean amplitude of the experimental heave responses increase with the increasing forward speed. Moreover, all the forward speed cases have a downward slope with the increasing wave steepness. The results obtained from the LARes L3 and L2 models follow the experimental result trend line well and the largest difference between the level 3 and level 2 models is observed in the Fn=0.20 case due to the slow forward speed influence on the radiation and diffraction force components. In the experiments the pitch responses show an increase with the increasing forward speed and at all forward speed cases a reduction in the pitch motion amplitudes is observed with the increasing wave steepness. The LARes L3 and L2 models have a good agreement for the Fn=0.20 and 0.25 cases with the experimental results, but at Fn=0.275 the responses are under-predicted around small wave slopes compared to the experiments.

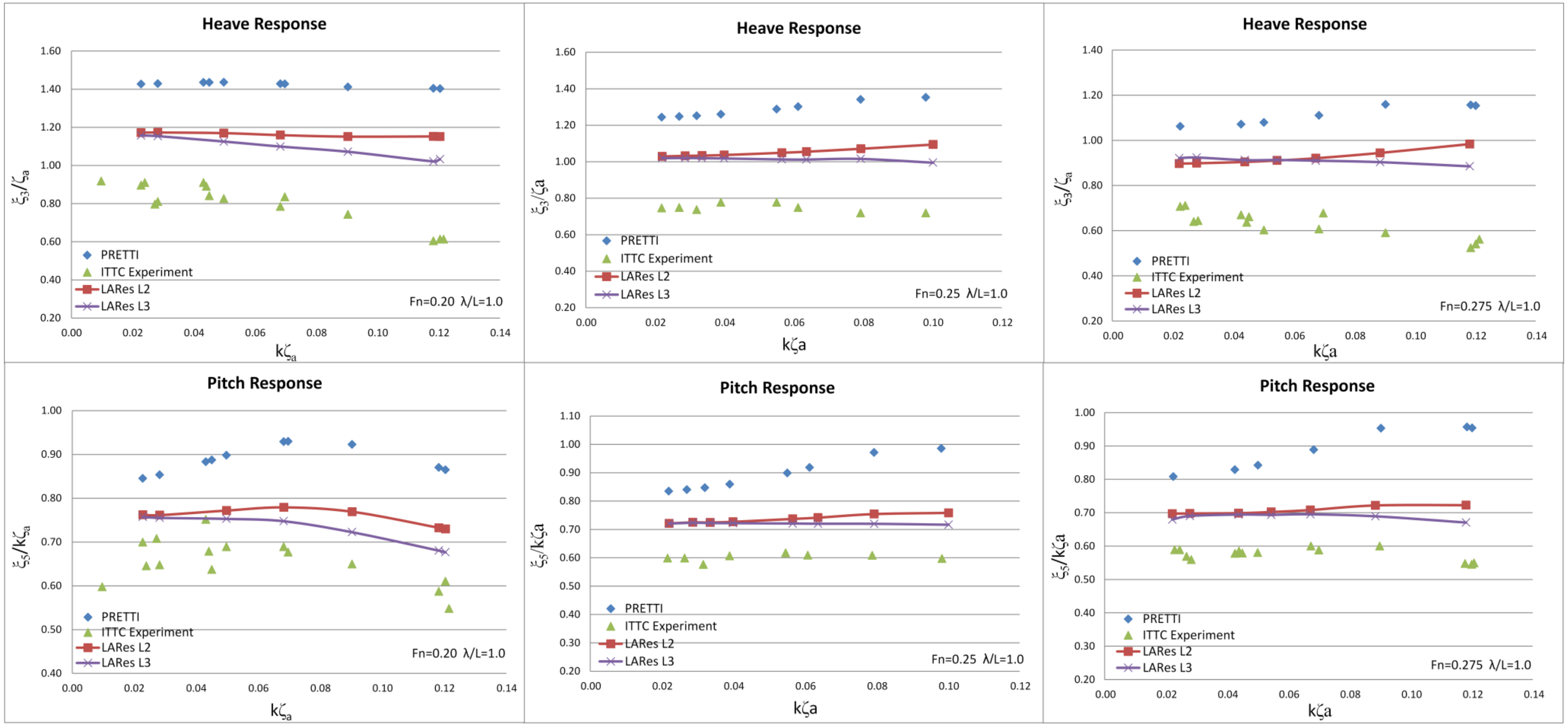

Figure 6.13: Influence of speed and wave steepness on the non-dimensional heave and pitch responses (Fn=0.20, 0.25, 0.275, λ/L=1.0)

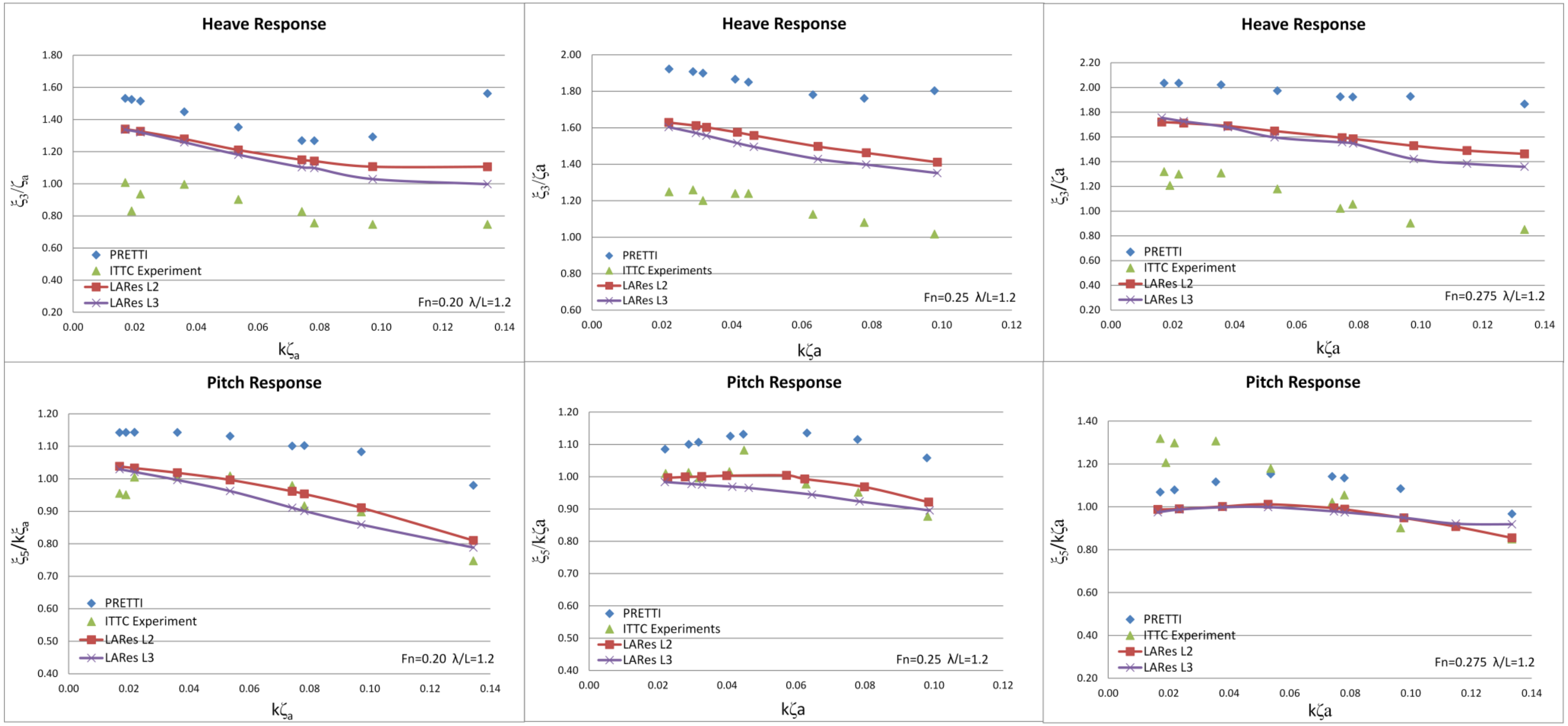

Figure 6.14: Influence of speed and wave steepness on the non-dimensional heave and pitch responses (Fn=0.20, 0.25, 0.275, λ/L=1.2)

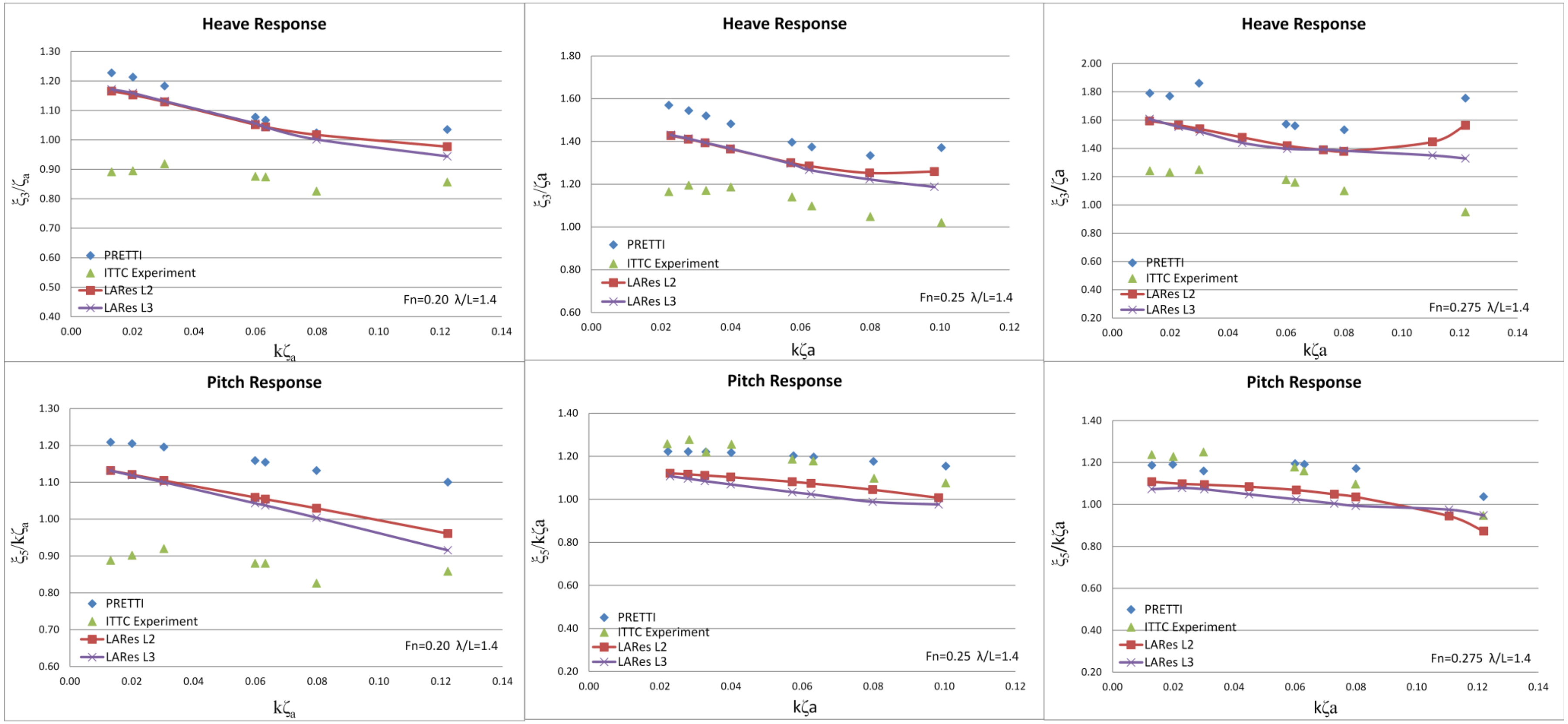

Figure 6.15: Influence of speed and wave steepness on the non-dimensional heave and pitch responses (Fn=0.20, 0.25, 0.275, λ/L=1.4)

In Figure 6.15 the effect of the variation in the forward speed on the non-dimensional heave and pitch amplitudes at λ/L_{pp}=1.4 is illustrated. In the current case, the mean amplitude of the experimental heave responses shows a slight increase with the increasing forward speed. Moreover, all the forward speed cases have a reduction of heave amplitudes with the increasing wave steepness. The LARes L3 model has the best agreement compared to the other models and predicts the trend of the heave responses very well. In the experiments the pitch responses show an increase with the increasing forward speed and at all forward speed cases a reduction on the pitch motion amplitudes is observed with the increasing wave steepness. The LARes L3 and L2 models have a good agreement for the Fn=0.20 and 0.275 cases with the experimental results, but at Fn=0.25 the responses are slightly under-predicted compared to the experiments.

6.5 Nonlinear behavior in motion responses

In this section, the nonlinear behavior in the ship motion responses in large amplitude waves is investigated in detail. It is known from the experiments that, when a ship is subjected to large amplitude waves, motion characteristics violate the linear assumption of symmetrical motion responses and this result in unsymmetrical positive and negative peak values in the motion history. The nonlinear behavior of a ship is identified in the motion responses by the ship emerging more than it submerges in heave motion and in pitch motion the bow submerges more than it emerges. In order to investigate the ship motions in detail all results are compared with the experiments performed by Fonseca and Soares (2004). Due to the lack of experiments detailed in this paper, comparison of the different models are performed only at Fn=0.25 and at λ/L_{pp}=1.2 and 1.4 wave lengths where the λ/L_{pp}=1.2 case results are directly taken from the source and λ/L_{pp}=1.4 case results are derived from other motion response curves.

In Figure 6.16, the results from the positive and negative peak points and mean values of the experiments, PRETTI and LARes L3 models are illustrated in detail for the Fn=0.25 and λ/L_{pp}=1.2 and 1.4 cases. It is clearly seen from the experimental results that, in heave responses, there is a reduction in the positive and negative peaks and a constant trend of mean values with the increasing wave slope. Moreover, in heave responses, mean values of motion have a positive value which means that the ship emerges more than it submerges. This is directly related to the geometric properties of the ship and in container ships the outer flares result in the increase in restoring forces and therefore vessels submerge less.

In the heave motion responses for the λ/L_{pp}=1.2 case, positive peaks in the PRETTI model are over-estimated compared to the positive peaks obtained in the experimental study while the LARes L3 has a better agreement with the experiments. Moreover, positive peaks in the PRETTI model have a constant trend whilst LARes L3 follows the decreasing trend of the experiments. In negative peaks, the results obtained from the LARes L3 and PRETTI models show a reduction of peaks while LARes L3 results have closer results to the experimental data. When the mean values of heave responses are considered, the LARes L3 results show a constant trend and nearly identical results with the experiments while the PRETTI model shows an increasing trend with the increase in the wave slope. In the λ/L_{pp}=1.4 case, the LARes L3 results agree well with the positive peaks of the experimental results and show a decreasing trend while the PRETTI results show a reduction of peak values up to $k\zeta_a$=0.08 and then show an increase with the increasing wave slope. In the negative peaks, the PRETTI and LARes L3 results show a reduction of peaks with the wave steepness while the LARes L3 results show a better agreement with the experiments. In the mean values of heave amplitudes, the PRETTI model shows an increase with the increasing wave steepness whilst the LARes L3 shows identical results with the experimental mean values. In the pitch motion responses, in the λ/L_{pp}=1.2 case, positive peaks in the PRETTI model over-estimated the positive peaks obtained in the experimental study while the LARes L3 model shows results close to the experimental positive peak points. Furthermore, results obtained from both of the models followed the decreasing trend of positive experimental peaks well.

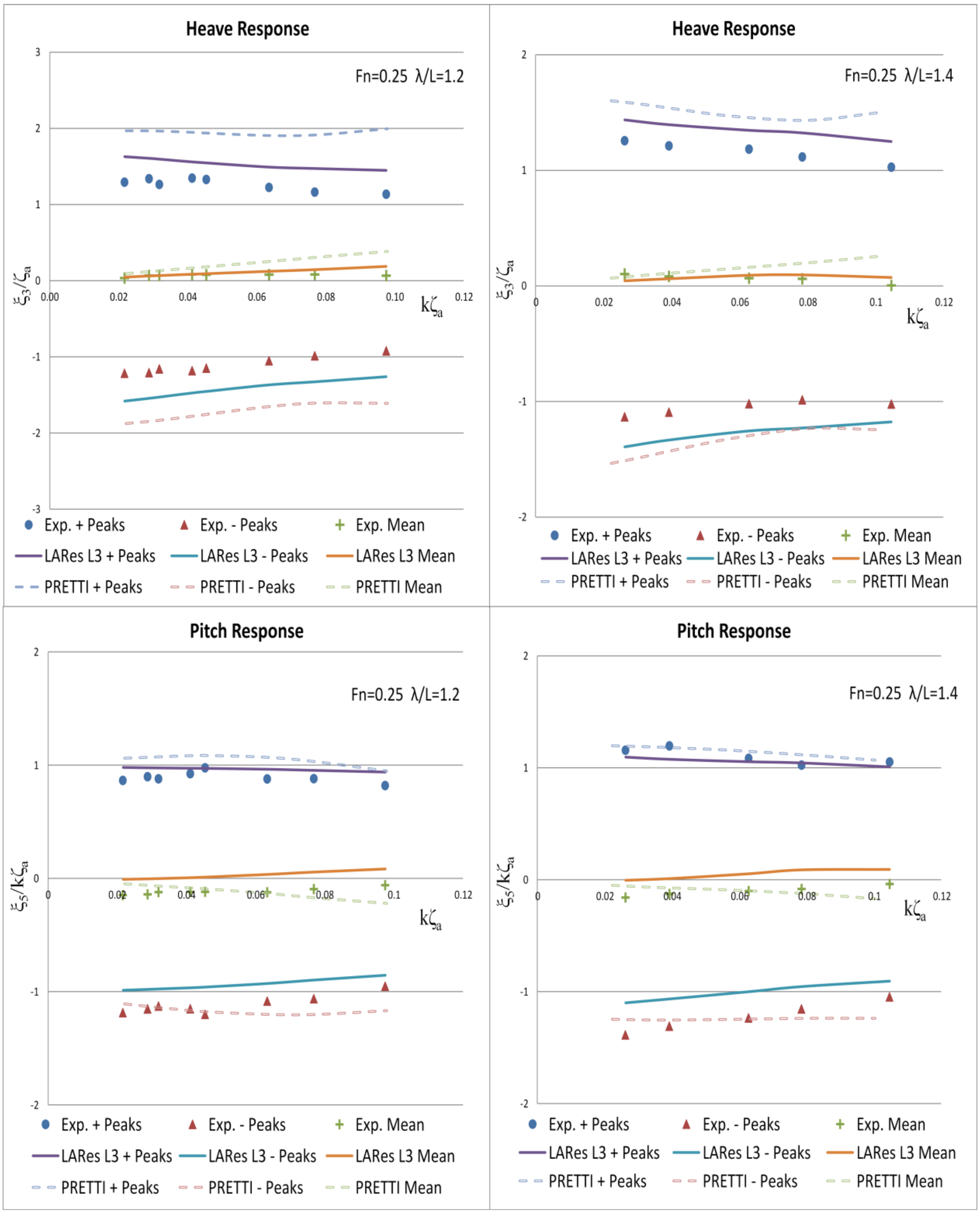

Figure 6.16: Positive, negative and mean values of non-dimensional heave and pitch responses (Fn=0.25, λ/L=1.2, 1.4)

In the λ/L_{pp}=1.2 case, positive peaks obtained from the PRETTI and LARes L3 models agree well with the experiments while the PRETTI model slightly over-estimated the positive peaks in the experiments. In the negative peak responses, LARes L3 results followed the decreasing trend of the negative pitch peaks seen in the experiments with the wave steepness but slightly over-reduced the negative peak points. The PRETTI model has closer negative peak results to the experimental data however the trend of the results does not follow the experiments well. Especially for the λ/L_{pp}=1.2 case, the experiments show reducing negative peaks while the PRETTI model shows a constant trend. The reason for that is attributed to the lack of pitch damping forces and also the surge motion influence in the coupled pitch motion components in the LARes L3 and L2 models. When the mean values of pitch response are considered, the LARes L3 model shows a constant trend up to $k\zeta_a$=0.06 and then an increasing trend with the wave steepness whilst the experiments show a constant trend. The LARes L3 results show that the bow is submerging more due to lack of damping forces while the PRETTI results show that the bow is emerging more. In the experimental data, the bow emerges slightly more in both cases. The difference in the mean values between the LARes L3 and the experimental results is increasing with the increase in the wave steepness due to the influence of large scattered wave effects.

6.6 Nonlinearity in radiation and diffraction forces

In this section, the nonlinearity in radiation and diffraction forces is investigated in detail. It was mentioned in the previous chapters that the LARes L3 model has the capability to calculate the quasi-non-linear radiation and diffraction forces in the system of equations. This property makes the code advantageous over its predecessor, the code based on the LARes L2 model, in large amplitude waves. In the level 2 model seakeeping calculations, it is impossible to take into account nonlinear radiation and diffraction forces. Especially, the diffraction force amplitudes are obtained from the BVP solution and even in large amplitude waves symmetric peaks are observed in the diffraction force time histories. The radiation forces are derived from the convolution of the memory functions with the exact velocity history; therefore the radiation forces show slightly asymmetrical peak behaviors in the radiation force time history during the simulations. This section investigates the differences in the radiation and diffraction forces as obtained from the LARes L3 and L2 models in large amplitude motions and provides a detailed investigation of the nonlinearity patterns observed in the radiation and diffraction forces. An example of the nonlinear behavior in the radiation and diffraction forces is illustrated in Figure 6.17 at Fn=0.25, λ/L=1.2 and at a wave height of 6 metres. The nonlinear patterns can be observed clearly from the figure, especially in the pitch radiation and diffraction moments. In the level 3 model heave radiation force, the mean amplitude of the force is slightly smaller than in the level 2 model while the mean amplitude of the radiation moment is slightly higher than for the level 2 model. In the level 3 model, the mean amplitude of the heave diffraction force is higher than the level 2 model while negative peaks are observed to be higher than the positive ones. The mean amplitude of the pitch diffraction moments is higher in the level 3 model compared to the level 2 model while positive peaks are more pronounced.

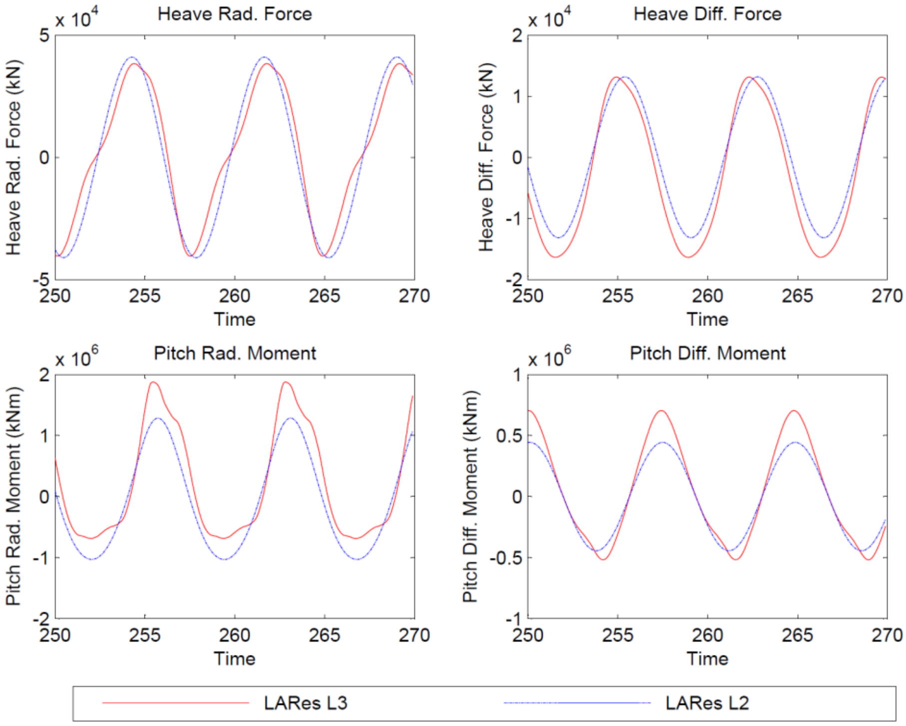

Figure 6.17: Time history of comparison of radiation and diffraction forces and moments (Fn=0.25, λ/L=1.2, H_w=6m)

The variations of heave and pitch radiation and diffraction forces and moments are investigated in detail from Figure 6.18 to Figure 6.21 for the forward speeds of Fn=0.20, 0.25 and for the wave length to ship length ratios of λ/L_{pp}=1.0, 1.2, 1.4. The focus is given to the asymmetric behavior in the time history of the radiation and diffraction forces and moments.

In Figure 6.18 diffraction forces and moments at Fn=0.20 and at λ/L_{pp}=1.0,1.2 and 1.4 are illustrated with respect to the increasing wave amplitude. Unfortunately, there is a lack of experimental data in the radiation and diffraction forces therefore the comparisons are performed only between the LARes L3, LARes L2 and linear results. It can be observed from the first and the second rows of Figure 6.18 that LARes L2 heave and pitch diffraction forces and moments are identical to the linear calculations for all wave lengths and they do not show asymmetric behavior in peak values. The reason for this is that the complex amplitudes are directly fed from the BVP solution. It can be observed from the heave diffraction forces that the LARes L3 model estimates the negative peak values to be larger than the linear peak values. The positive peak values were estimated to be smaller than the linear peaks except in the shortest wave condition. Nonlinearity in the heave diffraction forces increases with the increasing wave amplitude whereas the highest difference in the LARes L3 and L2 is observed at the resonant frequency λ/L_{pp}=1.2 due to the amplified motion responses. The positive peak values of the pitch diffraction moments are estimated to be larger than the linear peak values by the LARes L3 model while the negative diffraction moments are estimated to be larger than the linear peak values except for the λ/L_{pp}=1.0 case. Moreover in the LARes L3 model, in all cases, positive peak values of the diffraction moments are larger than the negative peak values. It is important to state that in all diffraction forces and moments average values of the peaks in the LARes L3 are higher than the average value of the LARes L2 and linear models. Therefore, this results in larger diffraction forces and reduces the motion responses.

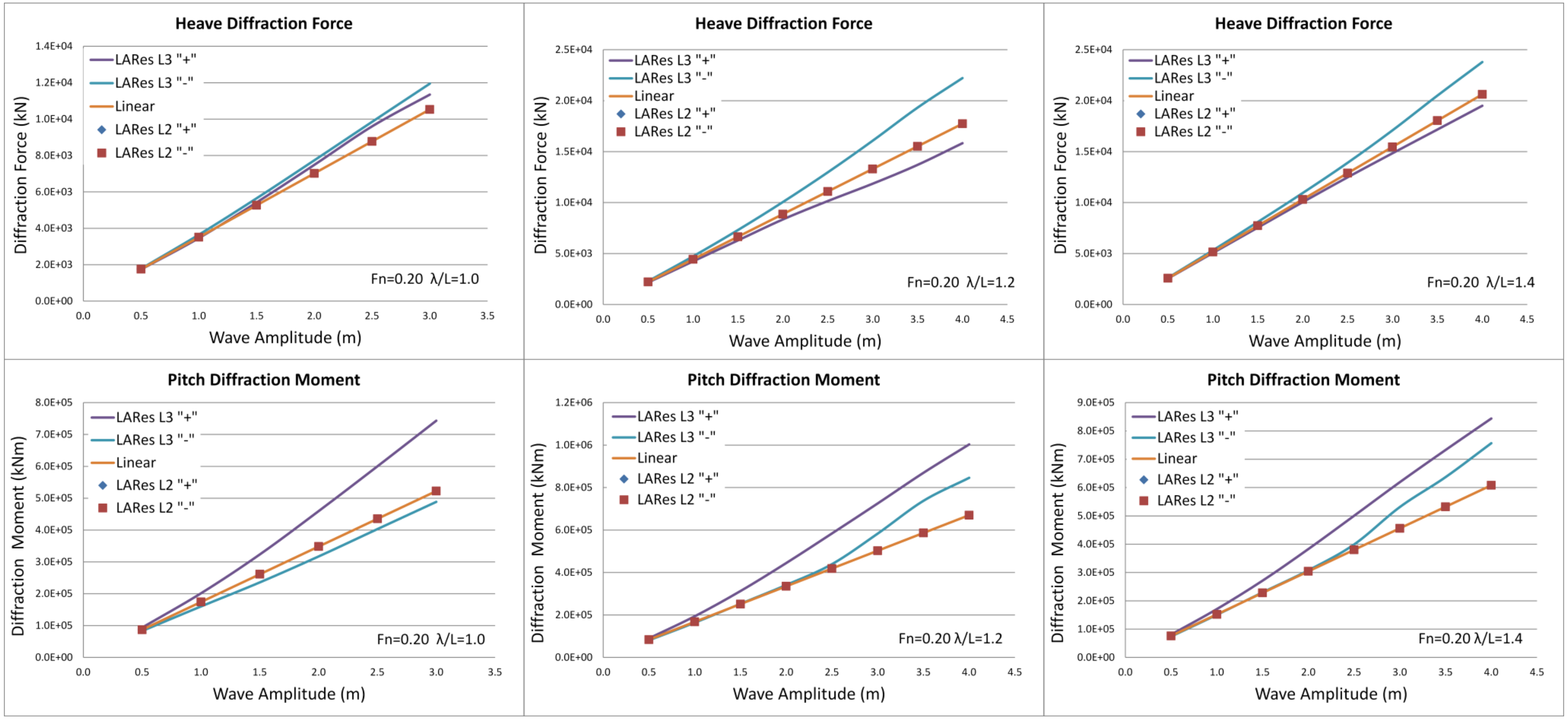

Figure 6.18: Influence of wave length and wave amplitude on the positive and negative peaks of the heave and pitch diffraction forces and moments (Fn=0.20, λ/L=1.0,1.2,1.4)

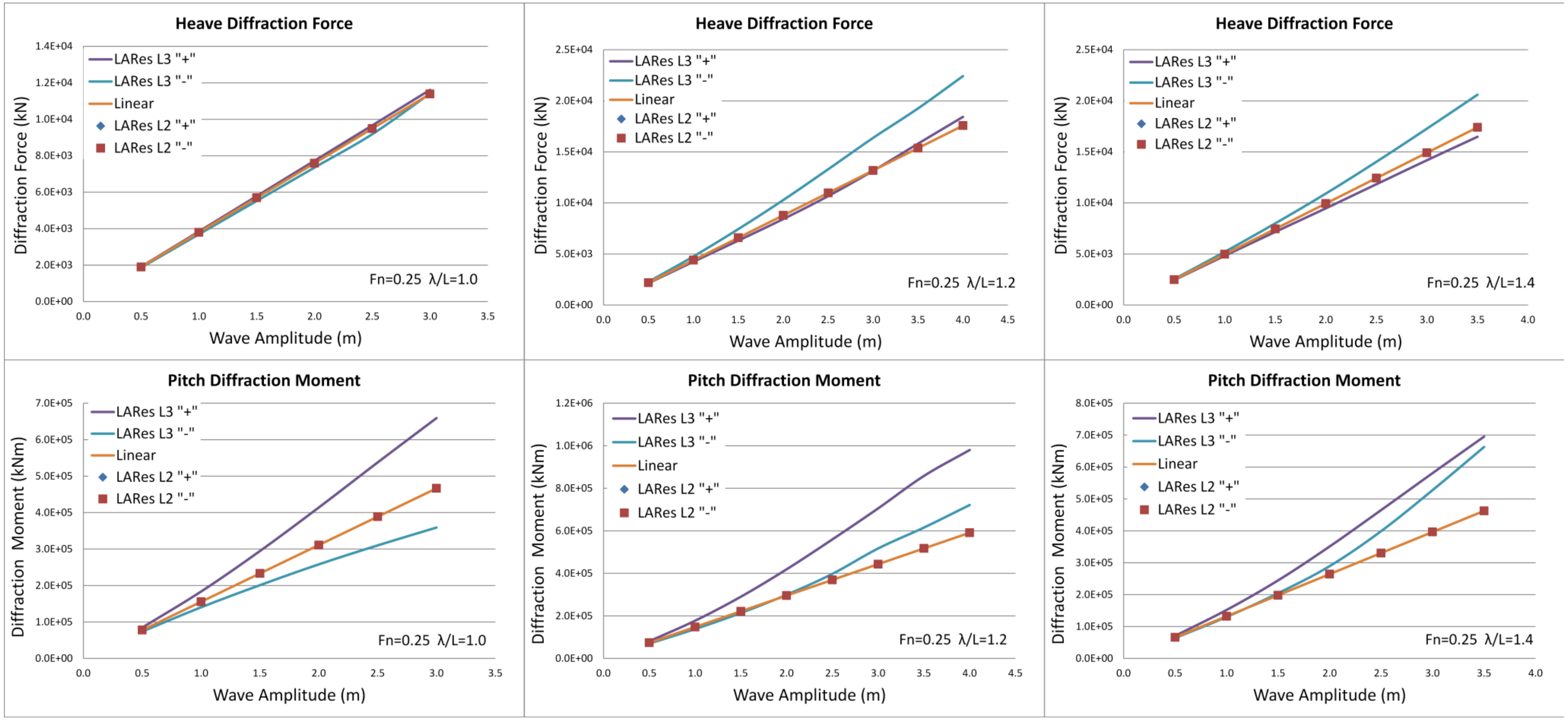

Figure 6.19: Influence of wave length and wave amplitude on the positive and negative peaks of the heave and pitch diffraction forces and moments (Fn=0.25, λ/L=1.0,1.2,1.4)

In Figure 6.19 diffraction forces and moments at Fn=0.25 and at λ/L_{pp}=1.0,1.2 and 1.4 are illustrated with respect to the increasing wave amplitude. It is clearly observed from the first and second rows of Figure 6.19 that LARes L2 heave and pitch radiation forces and moments are identical to the linear calculations for all wave lengths due to the aforementioned reasons. In heave diffraction forces, in general, the LARes L3 model predicts the negative peak values to be larger than the linear peak values except for the λ/L_{pp}=1.0 case. In the heave radiation forces in the shortest wave case, the LARes L3, L2 and linear model peak points show nearly identical values. In the λ/L_{pp}=1.4 case, the LARes L3 model predicts the positive peak values of the heave diffraction forces to be smaller than the linear peak values. Moreover, the average values of the peak points are larger in the LARes L3 model than the LARes L2 model. The positive peak values of the pitch diffraction moments were estimated to be larger than the linear peak values by the LARes L3 model. The negative diffraction moments were estimated to be larger than the linear peak values except in the λ/L_{pp}=1.0 case. The average values of the peak points are observed to be larger in the LARes L3 model than the LARes L2 model.

In Figure 6.20, radiation forces and moments at Fn=0.20 and at λ/L_{pp}=1.0, 1.2 and 1.4 are illustrated with respect to the increasing wave amplitude. It can be observed from the first row of Figure 6.20 that the LARes L2 heave radiation force peak values are smaller than the linear peak values except in the λ/L_{pp}=1.0 case which has identical values compared to the linear peak points. For the λ/L_{pp}=1.2 and 1.4 cases, the negative amplitudes of the radiation forces are observed to be larger than the positive peak values with the increasing wave amplitude which is the sign of slightly nonlinear heave body velocities. The LARes L3 model predicts the positive and negative amplitudes of the radiation force to be smaller than the linear peak points. However, in the λ/L_{pp}=1.4 case the negative amplitudes of the heave radiation forces are observed to be larger than the linear radiation force amplitudes. Moreover, in all wave lengths the negative peaks are observed to be larger than the positive peaks. It is clear to observe that asymmetric behavior in the radiation force amplitudes increases at the resonant frequency and is highly dependent on the wave amplitude.

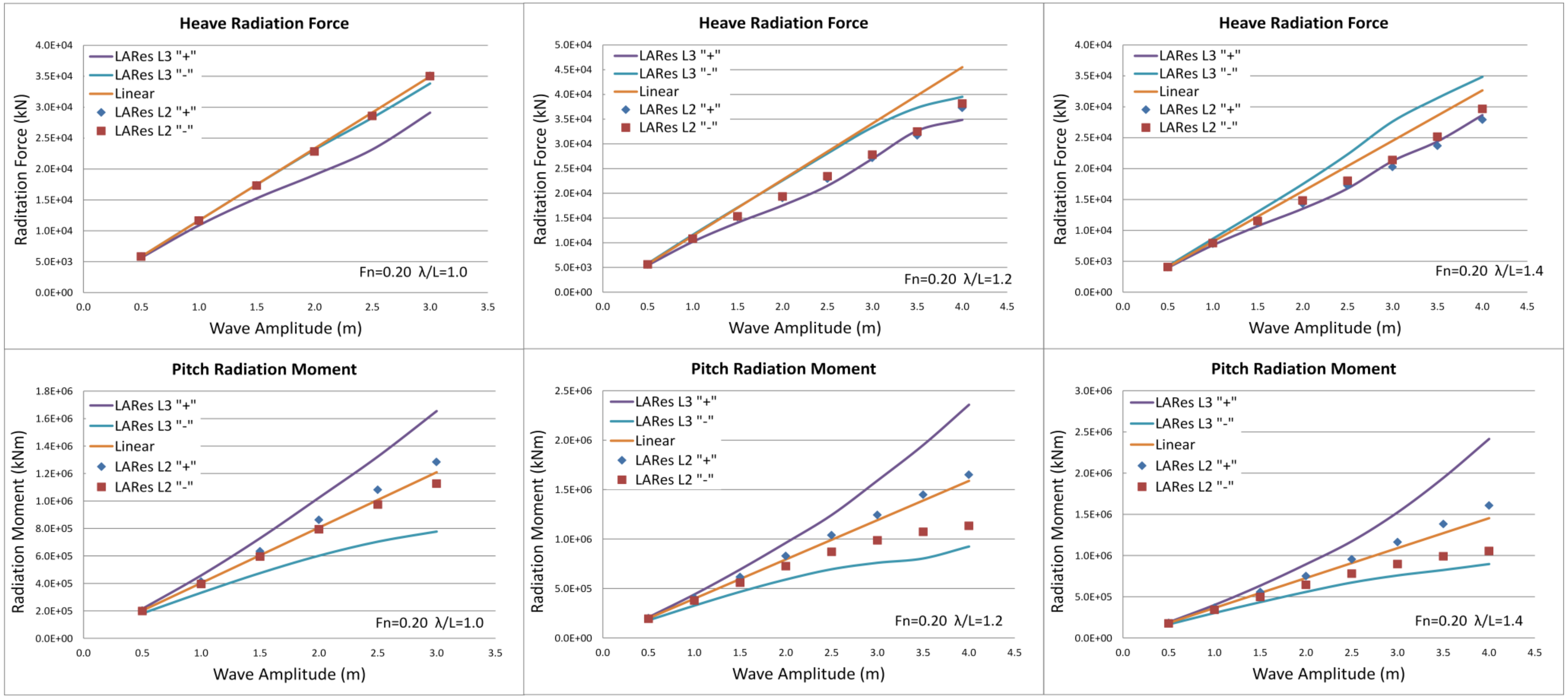

Figure 6.20: Influence of wave length and wave amplitude on the positive and negative peaks of the heave and pitch radiation forces and moments (Fn=0.20, λ/L=1.0,1.2,1.4)

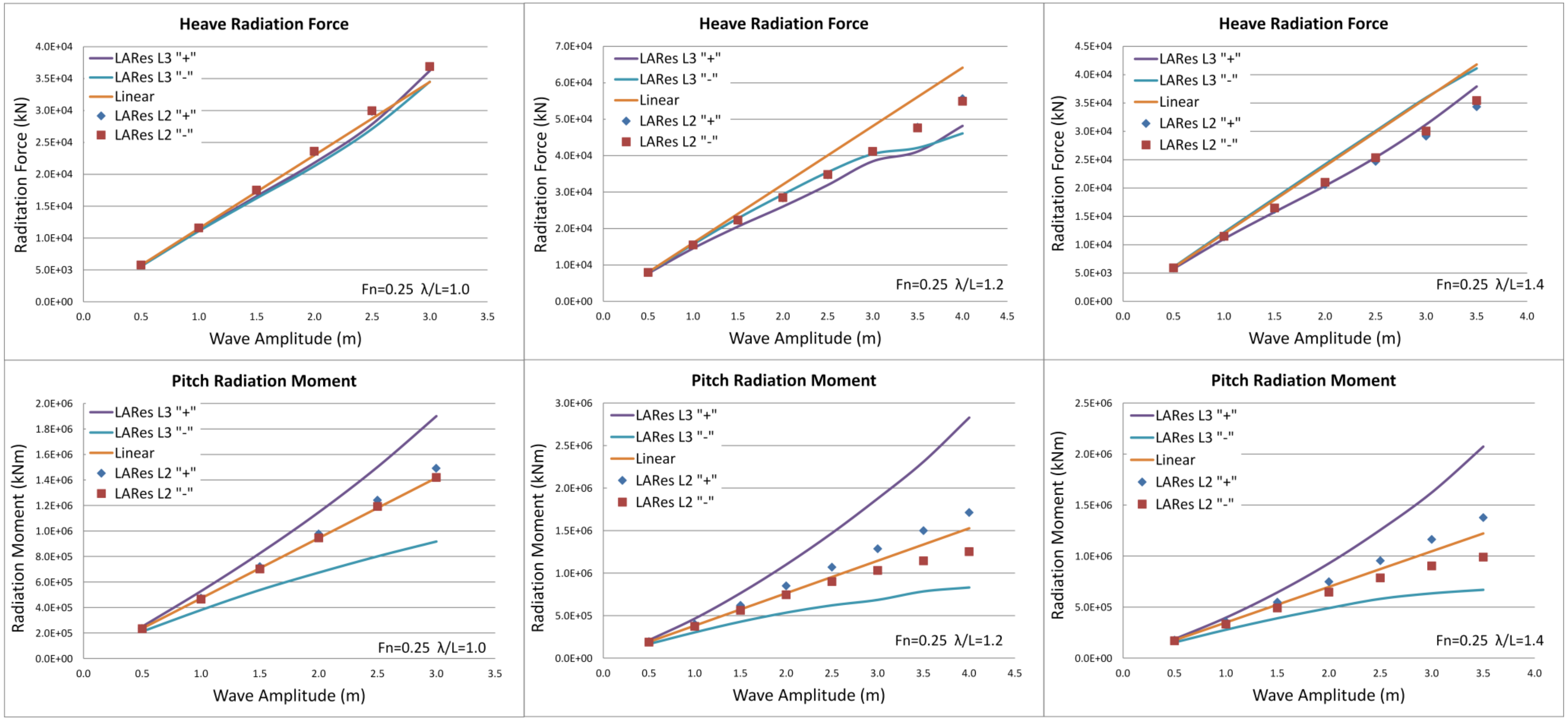

Figure 6.21: Influence of wave length and wave amplitude on the positive and negative peaks of the heave and pitch radiation forces and moments (Fn=0.25, λ/L=1.0,1.2,1.4)

In the pitch radiation moments, the LARes L2 model shows nonlinearity in the positive and negative peaks whereas positive peaks are observed to be larger and negative peaks are smaller than the linear peak points. It is also important to state that in the LARes L2 model, positive peak values show a linear trend while the negative peak values show a decreasing trend with the increasing wave amplitude. This means that negative pitch velocity values are more affected by the nonlinear motions than the positive pitch velocity values. The LARes L3 model predicts the positive radiation moments to be larger and the negative peaks to be smaller than the linear peak values. The increasing wave amplitude increases the asymmetry in the radiation moment peak amplitudes and the largest difference is observed in the resonant frequency case due to the amplified motion responses. Moreover, positive radiation moment amplitudes show higher nonlinearity with the increasing wave amplitude compared to the negative moment amplitude values.

In Figure 6.21 radiation forces and moments at Fn=0.25 and at λ/L_{pp}=1.0, 1.2 and 1.4 are illustrated with respect to the increasing wave amplitude. In the heave radiation forces, the LARes L2 model predicts the positive and negative peak amplitudes to be smaller than the linear peak amplitudes except in the λ/L_{pp}=1.0 case. For the λ/L_{pp}=1.0 case the LARes L2 heave radiation force amplitudes are slightly higher than the linear radiation force amplitudes. The LARes L3 model predicts heave radiation force amplitudes to be smaller than the linear peak amplitudes while the negative peak amplitudes are observed to be larger than the positive amplitudes. In the λ/L_{pp}=1.4 case the LARes L2 negative heave radiation force amplitudes have a linear trend and have nearly identical values to the linear peak amplitudes. It is clear to observe that asymmetric behavior in the radiation force amplitudes is increased at the resonant frequency and with the increase in the wave amplitude. In the pitch radiation moments, the LARes L2 model predicts the amplitude of positive peak values to be larger and the negative peak values to be smaller compared to the linear peak values. For the λ/L_{pp}=1.0 case the LARes L2 model predicts nearly identical values with the linear peak values while in other cases differences between the asymmetric behavior in the nonlinear radiation moments are increased. In general, the LARes L2 model predicts that the amplitude of positive peaks will vary with a linear trend with the increasing wave amplitude while negative peak amplitudes show a decreasing trend with the increase in the wave amplitude. The LARes L3 model predicts the positive peak amplitudes of the radiation moments to be larger than the linear peak amplitudes whereas the negative peak amplitudes are predicted to be smaller than the linear peak amplitudes. The asymmetry between the radiation moment peak amplitudes is amplified at the resonant frequency and when the wave amplitude is increased. Except for the λ/L_{pp}=1.0 case, the mean value of the positive and negative peak amplitudes of the radiation moments is predicted to be larger than the linear estimations. In the λ/L_{pp}=1.0 case mean amplitudes of the peak values are slightly smaller than the linear estimations.

6.7 Summary

In this chapter, effects of the nonlinearity level in the motion responses are investigated using the developed seakeeping models and compared with the experimental data in detail. In order to perform comparisons of different seakeeping models, available experimental results are used and the relative performance of the models is investigated focusing on the level of nonlinearity, forward speed, wave length, maximum and minimum motion amplitude peaks. Moreover, the variation of quasi-non-linear radiation forces with the increasing wave amplitude is investigated in detail.

In general, the LARes L3 results agree better with the experimental results. When the slope of the waves increases, in all models nonlinearity in the responses are increased which led to a decrease in the non-dimensional heave and pitch response amplitudes. At the same speed, maximum difference between the results obtained from the LARes L3 and L2 models are found at λ/L_{pp}=1.0 cases due to the dominancy of the radiation and diffraction forces over the Froude-Krylov and restoring forces. Moreover, for the same wave lengths, the effect of the ship speed on motion responses is investigated and the sensitivity of the motion amplitudes is observed to be decreasing with an increase in the wave slopes. The asymmetry in the maximum and minimum motion response peaks is also investigated. In large amplitude waves, in all models, the S-175 container ship emerges more than it submerges. In pitch motions, in the PRETTI model and experiments, ship's bow emerges more than it submerges whilst in LARes L3 and L2 models, ship's bow submerges more than it emerges. The reason for this difference is attributed to the lack of surge motion influence, frame axis preference and pressure integration techniques in the LARes models.

The influence of wave amplitude on the nonlinear radiation and diffraction forces are investigated in detail. In the F-K nonlinear models, diffraction forces do not show nonlinearity with the increasing wave amplitude due to their direct implementation from the complex linear diffraction forces. However, in the LARes L3 model, especially at the resonant frequency, diffraction forces show highly nonlinear behavior with the increasing wave amplitude. In pitch radiation forces, nonlinearities in the diffraction force amplitudes are observed to be higher than the heave diffraction force amplitudes. The radiation forces are derived from the convolution of the memory functions and the exact ship velocity histories. Therefore, even in the LARes L2 model, heave and pitch radiation forces show nonlinearity by asymmetrical force peaks. In the LARes L3 model, quasi-non-linear radiation forces are used and nonlinearities are observed in the radiation force peak amplitudes. It must be mentioned again that, in pitch radiation forces nonlinearity is observed to be higher than the heave radiation forces with the increasing wave amplitude.

Chapter 7

Application of the Methodology to Predict Internal Load Responses

7.1 Introduction

In this chapter, the effects of nonlinearity level on the vertical load responses using the developed seakeeping models are investigated and compared in detail for the S-175 containership in head seas at Fn=0.25 forward speed. The main aim of the current chapter is to underline the effects of nonlinearity on the Vertical Shear Force (VSF) and Vertical Bending Moment (VBM) responses, and to perform benchmark tests of the in-house developed LARes Level 3 (L3) and LARes Level 2 (L2) models by comparing the internal load results with the experimental results performed by Fonseca and Soares (2004) in large amplitude waves. In order to perform comparisons of different seakeeping models, the available experimental results are used and the relative performance of the models is investigated focusing on the level of nonlinearity, wave length and maximum and minimum peaks of the VSF and VBM responses. The VSF responses at station 15 (1/4 L_{pp} backwards from FP) and VBM responses at station 10 (amidships) and at station 15 are compared with the experiments. The VSF and VBM responses are non-dimensionalized by $\rho g B L_{pp} \zeta a$ and $\rho g B L_{pp}^2 \zeta a$ respectively, where ρ is the fluid specific mass and B is the ship beam amidships, ζa is the wave amplitude and L_{pp} is the length between perpendiculars. In the current thesis, the vertical load values obtained from the still water VSF and VBM values are extracted from the non-linear load responses in order to investigate the effect of the unsteady vertical load responses.

7.2 Effect of the Nonlinearity Level on the Internal Load Responses

In this section, the effects of the nonlinearity level of modelling on the predicted VBM responses of the S-175 containership in large amplitude waves are investigated. Large amplitude vertical load analyses are performed using the LARes L3, L2 and nonlinear PRETTI models, and the results obtained are compared with the available experimental results. The vertical internal load measurements were carried out at station 10 and at station 15 in head seas for three different wave lengths (λ/L_{pp}=1.0, 1.2, 1.4) around the resonant frequency at Fn=0.25 forward speed. VBM responses are calculated in the time domain at the pre-defined positions and compared with the experiments with respect to the wave steepness. In the scope of the current thesis, only the first harmonics of the time-domain vertical internal load responses are investigated and they are obtained by applying Fourier transforms to the VBM response time history. In the experiments, the VSF responses are only investigated for the behavior of the second and third harmonics therefore the first harmonics of the VSF responses are not compared with the predicted numerical models in the current thesis.

Figure 7.1 presents the variation of the VBM response with respect to the wave steepness at station 10. The LARes L3, L2 and PRETTI model VBM estimations are compared with the experimental VBM results at Fn=0.25 forward speed in head seas using three wavelengths (λ/L_{pp}=1.0, 1.2, 1.4). Firstly, at station 10, it is observed that the experimental VBM amplitudes increase slightly with the increasing wave amplitude. Moreover, at the resonant frequency (λ/L_{pp}=1.2), VBM amplitudes are amplified compared to the other wave frequencies due to the resonant frequency of the vertical motions. It must be noted that the magnitude of the VBM estimations is at its highest level at the midship section. It can be seen from the λ/L_{pp}=1.0 case that all of the numerical models agree well with the experimental results up to a wave slope of $k\zeta_a$=0.06, while the PRETTI model results tend to diverge after that wave steepness threshold value. The LARes L2 and L3 VBM estimations generally agree well with the experimental results while the LARes L3 model slightly over estimates the LARes L2 model results. Moreover, the LARes L2 and L3 models show a slight increase with the increasing wave amplitude. In the λ/L_{pp}=1.2 case, all numerical models show an ascending slope with the increase in the predicted VBM responses in the wave amplitude due to the magnification of the vertical motions at this frequency. Again, after a wave slope of $k\zeta_a$=0.08, the PRETTI model VBM estimations tend to diverge from the experimental VBM results. The LARes L2, L3 and PRETTI models underestimate the VBM responses up to a wave steepness of $k\zeta_a$=0.06. The reason for this is attributed to the uncertainties in the longitudinal distribution of mass and therefore the maximum VSF and VBM responses are predicted at slightly higher frequencies than the experimental results (see Chapter 5). In large amplitude waves good agreement in the VBM responses is observed between the LARes L2 and L3 models and the experiments. In the λ/L_{pp}=1.4 case, all numerical models under-predict the VBM results compared to the experimental results. Again, the reason for this is attributed to the forward shift in the maximum VBM frequencies compared to the experimental VBM maximum peak frequency. The PRETTI model shows a divergence compared to the LARes L2 and LARes L3 models at large wave slopes.

Figure 7.2 presents the variation in the VBM response with respect to the wave steepness at station 15. The LARes L3, L2 and PRETTI model VBM estimations are compared with the experimental VBM results at Fn=0.25 forward speed in head seas and for three wavelengths (λ/L_{pp}=1.0, 1.2, 1.4). Firstly, at station 15, it is observed that the experimental VBM amplitudes possess a strong increase with the increasing wave steepness. Although the VBM responses show a high increase with the increasing wave amplitude at station 15, the magnitude of the results is nearly 25% of the VBM results at station 10. It can be seen from the λ/L_{pp}=1.0 case that all of the numerical models over-estimate the experimental results while the PRETTI model shows a divergence after a wave steepness of $k\zeta_a$=0.06.

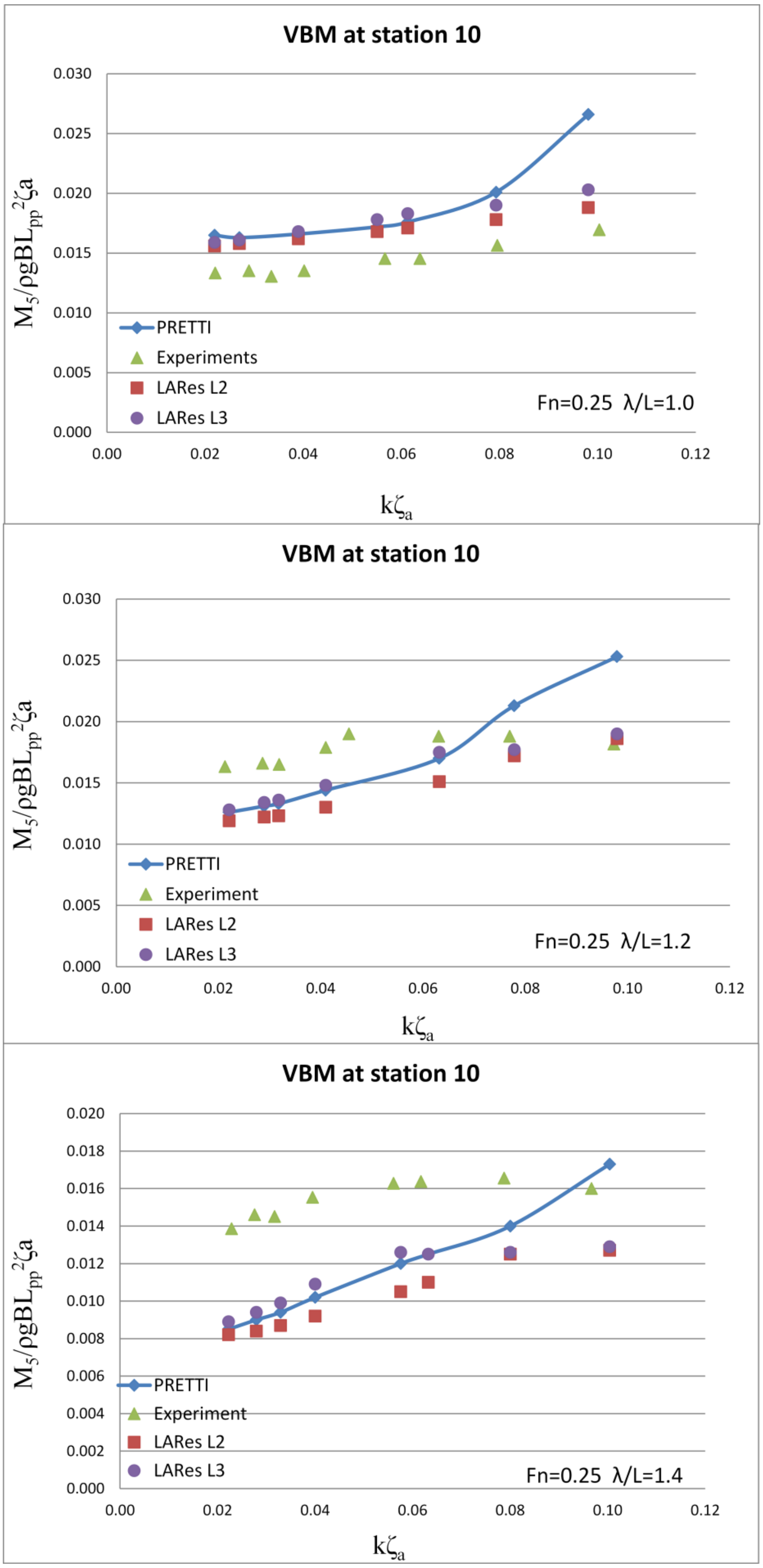

Figure 7.1: Variation of the amplitudes of the VBM amidships with the wave steepness (Fn=0.25, β=180)

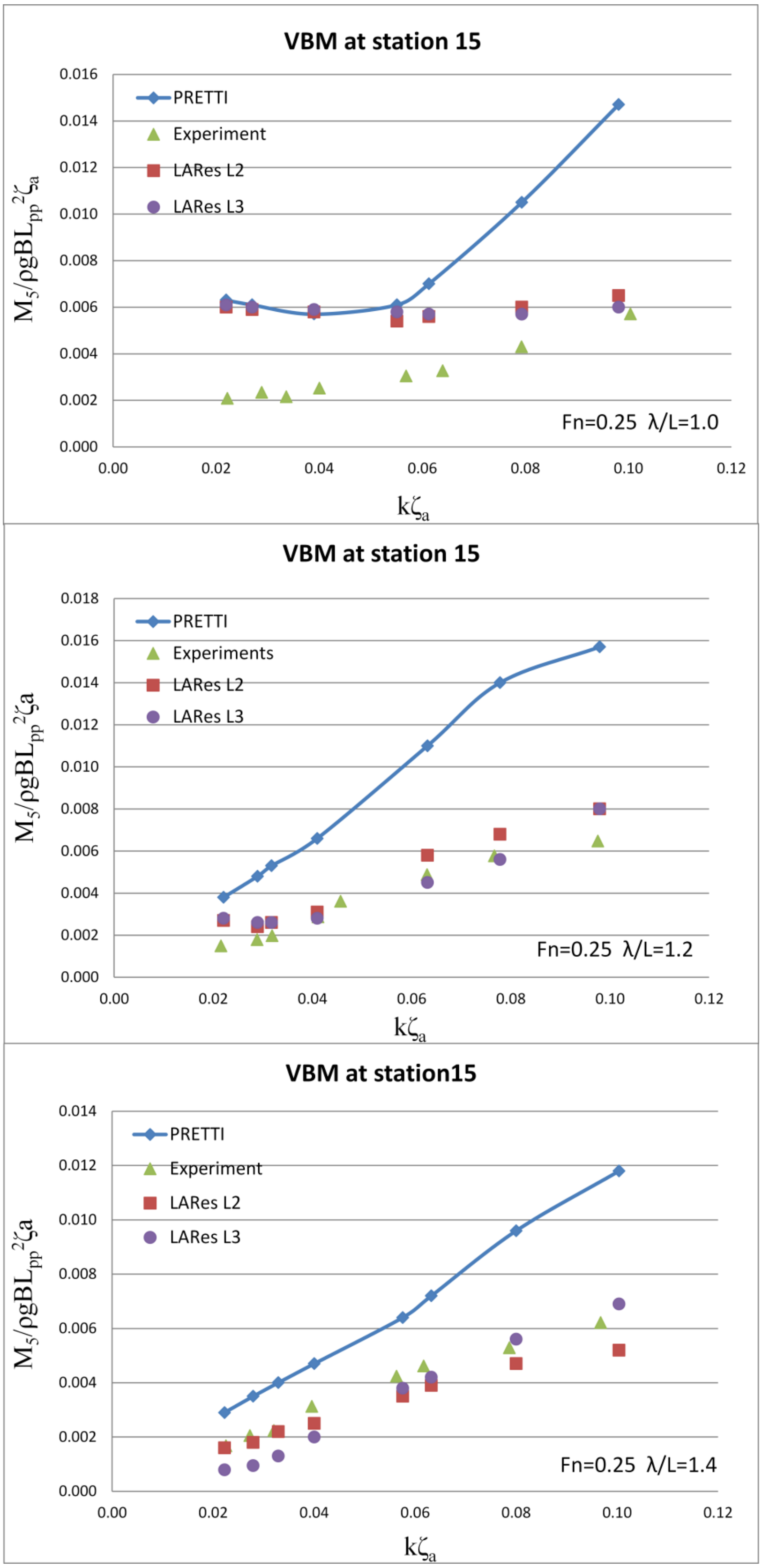

Figure 7.2: Variation of the amplitudes of the VBM at station 15 with the wave steepness (Fn=0.25, β=180)

Although both the LARes L2 and L3 models agree well with the experiments, the LARes L3 model agrees better with the experiments compared to the LARes L2 model at large wave amplitudes. It must be noted that the LARes L2 and L3 model VBM estimations show a constant trend with the increasing wave slope compared to the strong increase in the experimental results. In the $\lambda/L_{pp}=1.2$ case, the PRETTI model over-predicts the VBM results at station 15 compared to the experimental results. The LARes L2 and L3 model VBM estimations agree well with the experimental VBM records at station 15. It must be noted that the LARes L3 model agree better with the experiments when compared to the LARes L2 model due to the sectional quasi-non-linear radiation and diffraction force evaluations. In the $\lambda/L_{pp}=1.4$ case, the PRETTI model over-estimates the VBM responses at station 15 compared to the experimental results. The LARes L2 and L3 results agree perfectly well with the experimental VBM responses, while the LARes L3 model slightly under-estimates the VBM responses in small amplitude waves compared to the LARes L2 model and experiments. Moreover, the LARes L3 model results show an ascending trend compared with the experimental results and do not show a decrease in large amplitude waves. It should be highlighted that the VBM amplitudes which are calculated at station 15 show higher non-linear behavior when compared to results obtained at station 10 with the increase in wave amplitude.

7.3 Nonlinear Behavior in Vertical Load Responses

In this section, the nonlinear behavior in the VSF and VBM responses at station 10 and 15 is investigated in detail in large amplitude waves. It is known from the experimental results that, when a ship is subjected to large amplitude waves, the VSF and VBM responses show highly unsymmetrical positive and negative peak values in the internal loads time histories. The nonlinear behavior in the VSF and VBM responses is identified with the magnitudes of the sagging peaks which are much larger than those of the hogging peaks (Fonseca and Soares, 2004). The sign agreement for the VSF and VBM responses are discussed in Chapter 3 in detail. Due to the asymmetry in the peaks of the VBM responses the mean values of the VBM responses is negative in both at stations, where the asymmetry in the peak values increases with the wave amplitude. In the VSF responses, the magnitude of the positive peaks (sagging) is higher than the negative peaks (hogging) and the asymmetry between the positive and negative peaks increases with the wave amplitude.

Figure 7.3 presents the variation of the positive peaks, negative peaks and mean values of the VBM responses with respect to the wave steepness at station 10. Firstly, it must be noted that the magnitude of the VBM responses is at a maximum level at the midship station. It is observed from the experimental results that there is a strong asymmetry between the positive and negative peaks of the VBM responses during the model tests. It is highlighted that the asymmetry in the results varies partly due to the steady effects and partly due to the unsteady effects arising from the ship motions (Fonseca and Soares, 2004). In the λ/L_{pp}=1.0 case, the PRETTI model over-predicts the negative peaks and under-predicts the positive peaks of the VBM results compared to the experimental results. It is observed that above a wave steepness of $k\zeta_a$=0.06, negative peaks (sagging) in the VBM records at the midship section diverge compared to the experimental results where they show an ascending trend with increasing wave steepness. On the other hand, the positive peaks (hogging) in the VBM responses predicted using the PRETTI model show a descending trend with the increase in the wave steepness. Moreover due to the large negative peak values the mean values also diverge from the experimental data above a wave steepness of $k\zeta_a$=0.06. In the same case, the LARes L3 model shows a better agreement with the experiments compared to the PRETTI model in the positive and negative peaks, and the mean values of the VBM records at the midship section. Again, in the LARes L3 model, the negative peaks of the VBM responses show an ascending trend with the increase in the wave steepness. On the contrary, the LARes L3 model shows an ascending trend in the positive peaks of the VBM results and agrees better with the positive peaks in the experiments compared to the PRETTI model. It is observed that the mean values of the LARes L3 VBM estimations follow the exact trend of the mean values of the VBM records in the experiments.

In the λ/L_{pp}=1.2 case, the PRETTI model over-predicts the negative peaks and under-predicts the positive peaks of the VBM results at station 10 compared to the experimental results. It is observed that above a wave steepness of $k\zeta_a$=0.06, the negative peaks (sagging) of the VBM records at the midship section diverge compared to the experimental results where they showed an ascending trend with the increase in the wave steepness. Again, the positive peaks (hogging) of the VBM responses show a descending trend with the increase in the wave steepness in the PRETTI model but this time the decrease in the responses is strong due to the amplified motion responses for this frequency. In the same case, the LARes L3 results show a better agreement with the experiments compared to the PRETTI results in the positive and negative peaks and the mean values of the VBM records at the midship section. Again, in the LARes L3 model, the negative peaks of the VBM responses show an ascending trend with the increase in the wave steepness. On the contrary, the results obtained from the LARes L3 model show an ascending trend in the positive peaks of the VBM results and agrees better with the positive peaks in the experiments compared to the PRETTI model. It is observed that the mean values of the LARes L3 VBM estimations agree well with the mean values of the VBM records in the experiments. In the λ/L_{pp}=1.4 case, the positive and negative peaks of the experiments at first show an increase with the increase in the wave steepness but then in large amplitude waves show a strong decrease. The PRETTI model predicts the negative peaks well, but under-predicts the positive peaks of the VBM results at station 10 compared to the experimental results. In the PRETTI model, due to the under-prediction of the positive peaks in the VBM responses, the mean values of the VBM estimations are over-predicted compared with the experimental results at the midship section. The LARes L3 model under-predicts the positive and negative peaks of the VBM responses at the midship section compared to the experimental data. On the other hand, the mean values of the estimated VBM responses agree well with the experimental data whilst maintaining a constant trend with respect to the increasing wave steepness. Moreover, the LARes L3 model shows an ascending trend in the positive and negative peaks of the VBM responses with respect to the wave steepness.

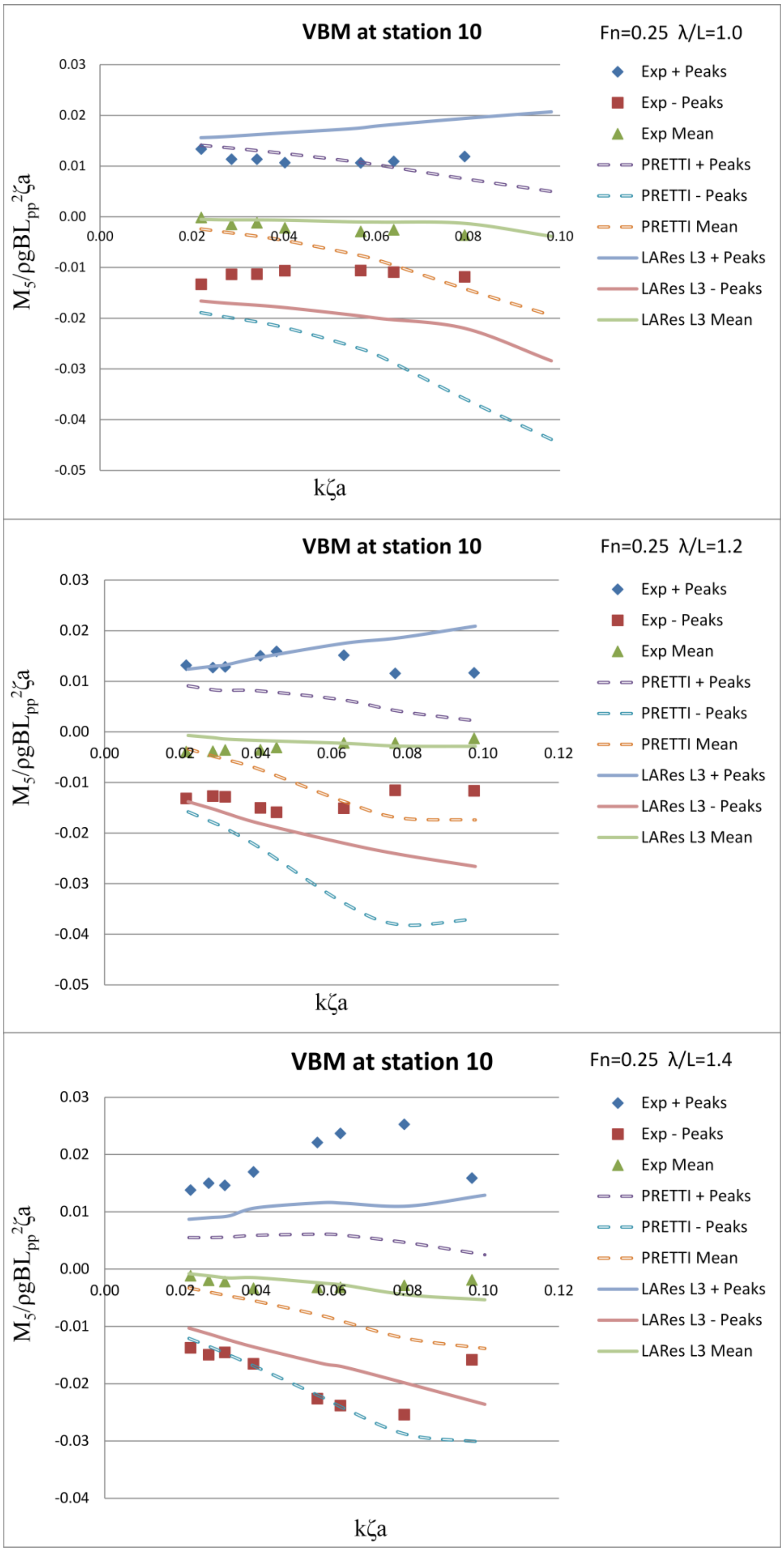

Figure 7.3: Positive, negative peaks and mean values of the VBM amidships as a function of wave steepness (Fn=0.25, λ/L_{pp}=1.0,1.2,1.4, β=180)

Figure 7.4 presents the variation in the positive peaks, negative peaks and mean values of the VBM responses with respect to the wave steepness at station 15. Firstly, the magnitude of the VBM responses is smaller at station 15 than those at the midship station. In the experimental results, the magnitude of the negative peaks is observed to be higher than the predicted magnitude of the negative peaks at station 15. Moreover, the nonlinearity in the trends in the positive and negative peaks of the VBM responses is observed to be higher at station 15 when compared to station 10. In the λ/L_{pp}=1.0 case, the experimental results show a descending trend of negative peaks and a constant trend of positive peaks with respect to the increasing wave steepness. When compared to the experimental results, the PRETTI model results over-predict the positive and negative peaks of the VBM responses while the negative peaks diverge above a wave steepness of $k\zeta_a$=0.06. Due to the over-estimation of the negative peaks after the threshold value of wave steepness, the mean values also tend to diverge from the experimental results. In the same case, the LARes L3 results over-predict the positive peaks of the VBM responses compared to the experiments whilst the agreement with the negative peaks is found to be satisfactory. The mean values of the LARes L3 model VBM responses agree quite well with the experimental mean values however it does over-predict them slightly. In the λ/L_{pp}=1.2 case, the experimental positive and negative peaks show highly non-linear behavior while the negative peaks are much higher than the positive peaks. The PRETTI results under-predict the positive peaks of the VBM responses and over-predict the negative peaks compared to the experimental records. In the PRETTI model, the negative peak values show an ascending trend while the positive peaks show a descending trend with the increasing wave steepness. Due to the over-estimation of the negative peak values, the mean values are also over-predicted compared to the experimental results. In the LARes L3 model, positive peaks in the VBM are over-predicted while the negative peaks are under-predicted compared to the experiments. Positive and negative peaks in the VBM follow the ascending trend of the experiments satisfactorily with respect to the wave steepness. In the λ/L_{pp}=1.4 case, the positive and negative peaks in the experiments show a strong ascending trend with respect to the increasing wave steepness.

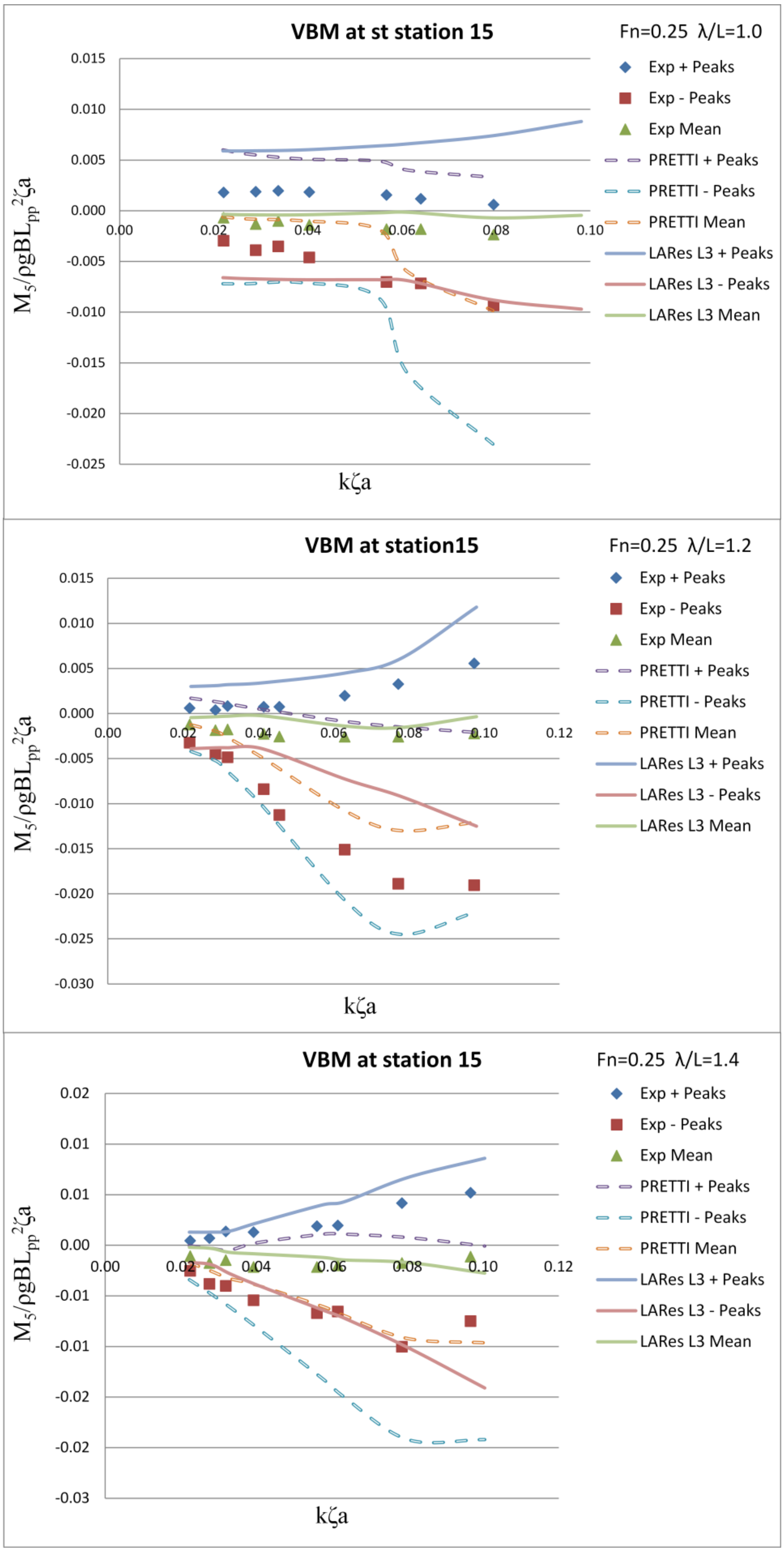

Figure 7.4: Positive, negative peaks and mean values of the VBM at station 15 as a function of wave steepness (Fn=0.25, λ/L_{pp}=1.0,1.2,1.4, β=180)

The PRETTI results under-predict the positive peaks while over-predict the negative peaks compared to the experimental results. In the PRETTI model, the positive peaks of the VBM responses show a nearly constant trend while the negative peaks show an ascending trend with the increasing wave steepness. The LARes L3 results predict the positive and negative peaks of the VBM values well at station 15. The LARes L3 results slightly over-predict the positive peaks of the VBM responses while agreeing satisfactorly with the negative peaks compared to the experiments. It is again observed that the mean values of the VBM responses at station 15 show negative values which mean that the sagging bending moments are higher than the hogging bending moments.

Figure 7.5 presents the variation in the positive peaks, negative peaks and mean values of the VSF responses with respect to the wave steepness at station 15. In the λ/L_{pp}=1.0 case, the positive peaks (hogging) in the experimental results show an ascending trend whilst negative peaks and mean values show a constant trend with respect to the increasing wave steepness. It is observed from the experimental records that the positive peaks are higher than the negative peaks which mean that the sagging VSF responses are higher than the hogging ones in large amplitude waves where the difference between them can reach a factor of two. The PRETTI results show a good agreement with the experiments up to a wave steepness of $k\zeta_a$=0.06 and beyond this they diverge. The PRETTI model predicted positive peaks in the VSF responses which show an ascending trend while under-predicting the experimental results. The negative peak values obtained from the PRETTI model show a slight increase with the wave steepness while the agreement between these values and the experiments is found to be satisfactory. In the LARes L3 model, the positive peaks are under-predicted while the negative peaks are slightly over-predicted compared to the experimental results. In the LARes L3 model, the positive peaks show an ascending trend whilst the negative peaks showed nearly a constant trend with the increasing wave steepness. Moreover, the mean values estimated by the LARes L3 model agree well with the experimental VSF responses at station 15.

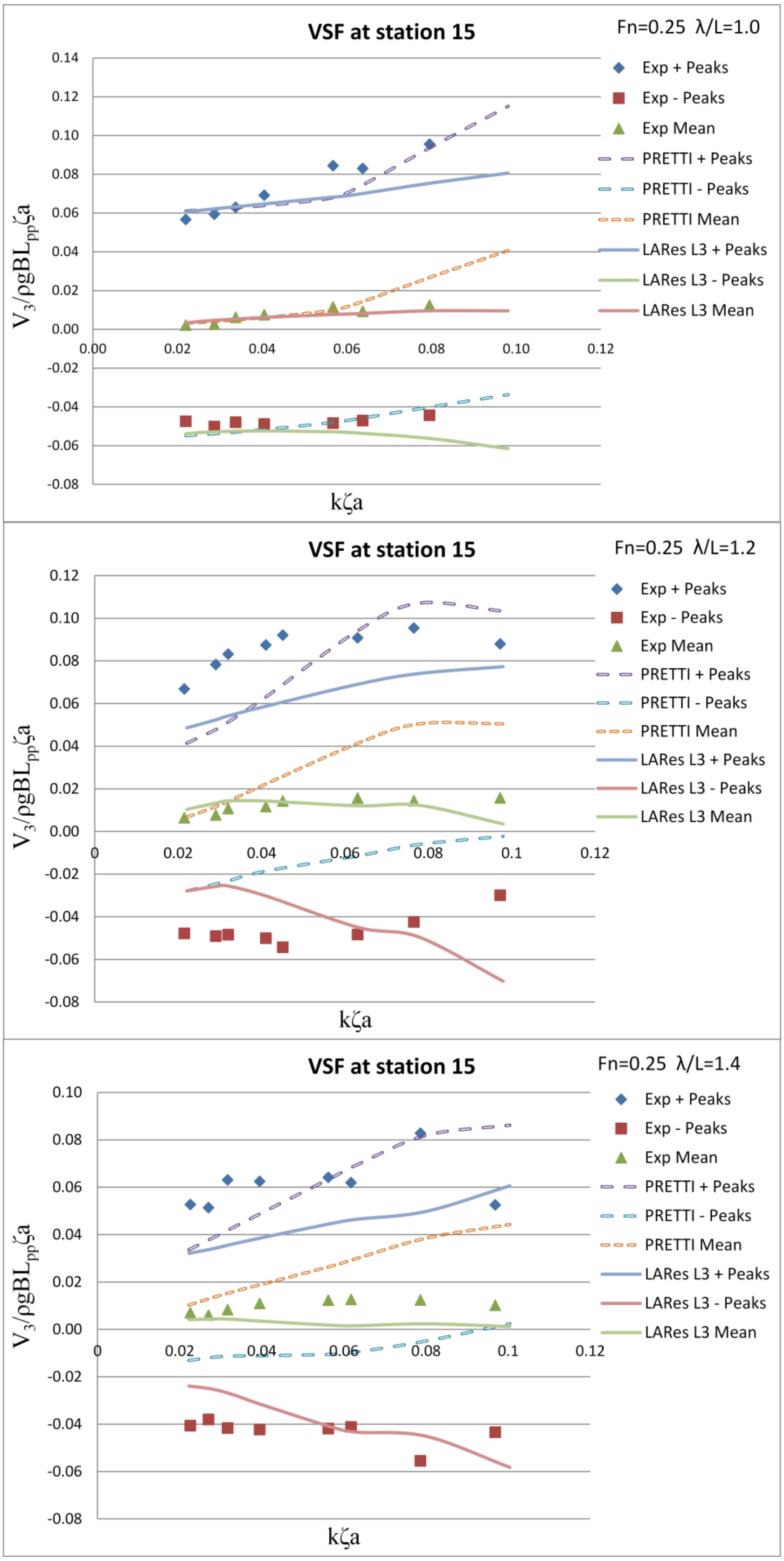

Figure 7.5: Positive, negative peaks and mean values of the VSF at station 15 as a function of wave steepness (Fn=0.25, λ/L_{pp}=1.0,1.2,1.4, β=180)

In the $\lambda/L_{pp}=1.2$ case, in the experimental results, the positive peaks (hogging) of the VSF responses show an ascending trend while the negative peaks show a descending trend and the mean values show a constant trend with respect to the increasing wave steepness. The PRETTI model under-predicts the positive peaks of the VSF responses at station 15 up to a wave steepness of $k\zeta_a=0.06$ and above this threshold slightly over predicts the results compared to the experiments.The negative peak points of the VSF responses are under-predicted compared to the experimental results. The PRETTI model predicted positive peaks in the VSF responses show an ascending trend while the negative peak values of the PRETTI model showed a decrease with the increasing wave steepness. The LARes L3 model predicted positive peaks in the VSF results show an ascending trend with the wave steepness while under-predicting the experimental values. On the contrary, the LARes L3 model negative peaks show an ascending trend which is the opposite of the descending trend observed in the experimental results. Nevertheless, the LARes L3 results showed a good agreement for the mean values while following the exact trend of the experimental results. In the $\lambda/L_{pp}=1.4$ case, in the experimental results, the positive peaks in the VSF response showed an ascending trend whilst the negative peaks and mean values show a constant trend with respect to the increasing wave steepness. The PRETTI model predicted positive peaks agree well, however the negative peaks of the VSF responses are under-predicted compared to the experimental results at station 15. Moreover, the positive peaks in the VSF responses show an ascending trend while the negative ones show a slightly descending trend with respect to the wave steepness. The mean values of the VSF responses are over-predicted by the PRETTI model while showing an increase due to the increase in the positive peak points. In the LARes L3 model, the positive peaks of the VSF results show an ascending trend with the wave steepness, but under-predict the experimental values. The negative peaks show a strongly ascending trend compared to the constant trend observed in the experiments. In the LARes L3 model, the mean values of the VSF results agree well with the experimental results and follow a constant trend.

7.4 Summary

In this chapter, the effects of the nonlinearity level on the VSF and VBM responses are investigated using the developed seakeeping models and compared with the available experimental results in detail. The nonlinearity in the VSF and VBM responses are discussed in detail in order to investigate the effect of large amplitude waves on them. Mainly, this chapter comprises of two sections where the first one investigates the VBM amplitudes and the second one investigates the nonlinear behaviors in the VSF and VBM responses at station 10 and station 15 in large amplitude waves. The relative performance of the models is investigated focusing on the wave length and wave steepness parameters.

In general, the LARes L3 results agree well with the experimental VBM results. In the experiments, at the midship section, the VBM amplitudes do not show significant nonlinearity while at station 15 a strong nonlinearity in the VBM amplitudes is observed with the increasing wave slope. The numerical models show nonlinearity with the increasing wave slope especially in the λ/L_{pp}=1.0 and 1.2 cases. In the λ/L_{pp}=1.0 case, at station 10, all the numerical models over-estimate the results while in the λ/L_{pp}=1.2 and 1.4 cases the numerical models under-estimate the VBM amplitudes compared to the experimental VBM responses. At station 15, PRETTI results over-predicted the VBM amplitudes while the LARes L3 model results agree better with the experiments.

In the second section, the maximum and minimum peaks and the mean values of the VBM and VSF responses at stations 10 and 15 are investigated. In general, at stations 10 and 15, the LARes L3 model VBM responses agree better with the experiments than the PRETTI model responses and they follow the trends of the experiments well. In all the numerical models and in the experiments, the magnitude of the negative peaks (sagging) of the VBM responses is found to be higher than the positive (hogging) ones. The peak values of the VSF responses are investigated only at station 15 and whilst the LARes L3 model results under-predict the peaks especially in the λ/L_{pp}=1.2 and 1.4 cases, it is hard to draw a general conclusion for the PRETTI model. The magnitude of the positive (sagging) VSF peaks is observed to be higher than the negative (hogging) VSF peaks.

In conclusion, it is observed that at station 10 wave steepness does not influence the VBM results at high extents whilst at station 15 a strong nonlinearity is observed. It is hard to draw a general conclusion on the positive and negative peaks of the VBM responses at station 10, but at station 15 peaks of the responses are observed to increase with the increasing wave steepness. Moreover, in general, LARes L3 model VSF and VBM results agree better with the experimental results when compared to the PRETTI model responses due to the implementation of the sectional quasi-non-linear radiation and diffraction forces. It should be highlighted that, in a rigid ship approach, the accuracy of the LARes L3 model VBM responses are mainly related to the accuracy of the motion response predictions.

Chapter 8

Conclusions and Recommendations

8.1 Introduction

The primary objective of the work presented in this thesis was to investigate the effects of large amplitude waves in the ship motion and load responses with a novel time-domain approach. The chapter starts by the novelty of the research and then presents the contributions to the field of study and the research achievements. Finally, the conclusions and recommendations for the future works are outlined.

8.2 Novelty of the Research

The novelty of the current study can be outlined as follows:

- Introduction of a novel body-nonlinearity level (level 3) approach using 3D linear frequency-domain potential diffraction and radiation data and process them in order to evaluate the ship motion and vertical load responses in large amplitude waves, using impulse-response functions. It is believed that, this approach is performed the first in the research field. Nowadays, linear frequency-domain codes are at industrial standard in ship motion and load computations therefore the developed methodology aims to provide an efficient and low cost solution with an acceptable accuracy for ship designers using the pre-calculated frequency-domain data in large amplitude waves. The level 3 model has the capability to investigate the global and sectional quasi-non-linear radiation and diffraction forces with the varying underwater geometry of a moving ship in large amplitude waves. The main aim of the LARes L3 model is to lower the `safety factors` in the ship design cycle in which they are high due to the over-estimation or under-estimation of the motion and load responses in the linear methods. It has been observed that, LARes L3 model predicted closer results to the experiments compared to the LARes L2 model which means ships designers can use smaller safety factors on the new designs and that will provide lighter, more efficient and safe ship designs.

8.3 Contributions to the Research

The main contributions to the research in towards developing a fast and accurate tool to predict the non-linear motion and load responses of ships in large amplitude waves are outlined below:

- The LARes L3 model gives the opportunity to the ship designers and classification societies to investigate the quasi-non-linear radiation and diffraction forces at low cost. The interpolation subroutine was designed for the combination of 120 different position cases therefore it is valid for most of the mono hull vessels in which ship designers do not need an alteration in the code for a special case of time-domain motion and load simulations in head seas. After the generation of the hydrodynamic forces database, unlimited amount of simulations can be performed by the ship designers and classification societies without any modification in the database.
- It has been observed that in large amplitude waves LARes L3 model reduces the heave and pitch motions up to 15% compared to the LARes L2 model and also provides closer results to the experimental data. The reductions on the motion estimations are stronger around the $\lambda/L_{pp}=1.2$ case where the motions are amplified. Moreover, the LARes L3 model did not show divergence in the motion responses like the PRETTI model in very large wave amplitudes

which also proves the stability of the code in severe environmental conditions.

- The non-linearity in the radiation and diffraction forces were investigated in detail and it was observed that they behaved strongly non-linear in large amplitude waves. The magnitude of the positive and/or negative peaks in the quasi-non-linear radiation and diffraction forces in the LARes L3 model reached up to twice of the amplitude of LARes L2 model. It was also observed that, the influence of the radiation and diffraction forces were larger in short waves in which in long waves the F-K and restoring forces were dominant.
- It has been observed that in large amplitude waves LARes L3 model reduces the Vertical Shear Force (VSF) and Vertical Bending Moment (VBM) responses up to 10% compared to the LARes L2 model and in general provided closer results to the experimental data. However, due to the uncertainties in the mass distribution the peak values of the VSF (st 15) and VBM (st 10) responses in the numerical models are found to be shifted to higher frequencies when compared to the experiments. It has been observed that mass distribution is one of the key elements accurate estimation of the in the vertical load response values.
- Introduction of a new multi-dimensional integration and interpolation tool to handle body-nonlinear level motion and internal load calculations. Each level 3 model simulation comprises of a combination of 120 different position cases. One by one, the evaluation of retardation forces and interpolation of the related hydrodynamic forces and coefficients is very costly. In order to eliminate these computational costs a multi-dimensional algorithm is introduced and hence the memory function integrations for all 120 positions can be handled in a single step. The use of multi-dimensional approach provided at least 40% advantage in time consumption during the non-linear motion and internal load solutions.
- The influence of the wave length on the non-linear motion responses were investigated on the S-175 container ship and it was observed that when $\lambda/L_{pp}=1.2$ the motions are amplified, but the influence of the quasi-non-linear

radiation and diffraction forces were observed to be at the highest level at the when $\lambda/L_{pp}=1.0$ due to the dominancy of the radiation and diffraction forces in short wave lengths.

8.4 Achievements

In addition to the contribution to the field, achievements and developments of the current research performed in this research can be summarized as follows:

- Development of a pre-processor, the LARes Mesh Generator (LMG), in order to generate the database of geometries and to overcome the difficulties which were faced in the PRECAL Auto Mesh Generator (AMG) in large displacement cases. The LMG code is designed to generate the underwater and waterplane area (LID) panels using the initial mesh generation of the ship. The AMG can only generate the panels up to the emergence of the bulb and when the bulb is completely emerged AMG code crashes. Moreover, even in small pitch angles AMG code keeps the same amount of vertical mesh properties and this results in panels with high aspect ratios therefore mathematical singularities in the BVP solutions. In order to prevent this, a unique approach of panelization is implemented in to the LMG code where the initial mesh of the ship is direct input to the LMG and ship is translated and rotated and the initial mesh is cutted with respect to the still water level.
- The novelty in the LMG code is, the initial mesh on the ship geometry is input only once into the code while it translates and rotates the ship and intersects the ship with the mean sea level. After the ship and mean sea surface intersection process, the panels close to the waterline level are corrected. It was observed that small panels close to the waterline level cause mathematical singularities in the Boundary Value Problem (BVP) solution. The LMG calculates the properties of each panel after intersection and if a panel has a smaller area than the defined area limit, it merges that panel with the adjacent panel below and eliminates the singularities in the BVP solution automatically. Irregular frequencies in the damping curves are eliminated using the `Lid Panel Method` in which the BVP is solved with the underwater

and water plane panels. The LMG automatically generates the water plane panels after the intersection process between the updated ship position and the mean sea surface for each position of the ship, and then generates the outputs of <>.NOD and <>.FAC files to be used for PRECAL calculations. In the current study, the ship position range scans through 120 different variations of ship position corresponding to ±5m heave displacement and ±5 degrees pitch angle with respect to the mean position of the ship. The range of the pre-calculated ship positions database is directly related to the ship geometry and environmental conditions. In the current analysis, the range of positions includes bulb and propeller emergence conditions. In the Froude-Krylov and restoring force calculations, the actual wetted surface under the wave profile is taken into account without any motion restrictions.

- In the LMG code, LID panels are generated automatically using the contour line of the waterplane area of the ship on the still water level. However, it is a hard decision to make how many panels are needed per metre of ship breadth. It has been observed that when large panels are used the BVP solution takes less time, but the irregular frequencies cannot be suppressed adequately. Moreover, when very small size panels are used in the waterplane area mesh, the irregular frequencies are suppressed successfully, but the BVP solution take longer time. In order to investigate the optimum number of panels on the waterplane area of the vessel, the number of LID panels is optimized to be one panel per ship beam in metres and in this way the BVP solution time is optimized and the irregular frequencies are suppressed properly. The LMG code can automatically generate the PRECAL input files and prepares all panel properties for the hydrodynamic calculations.
- Development of a memory functions integrator for the global and sectional damping coefficients using a multi-dimensional algorithm. All pre-calculated global and sectional damping curves of the different ship positions are stored in a multi-dimensional approach in order to make the process faster. Damping curves are stored in a multi-dimensional array, like internal layers in a cube, therefore the global and sectional memory functions are calculated at the same time without using loops. This algorithm gives an advantage in terms of

computational speed in order to calculate memory functions and gives the user the opportunity to calculate more than one memory function at the same time. In the current study, 120 different variations of positions were calculated. Detailed figures of the analysis flow charts, integration and interpolation figures were provided in the Chapter 4.

- Development of a multi-dimensional interpolation tool in order to interpolate the global and sectional memory functions, diffraction forces, and infinite added mass and damping coefficients for the interim ship positions. The interpolation tool uses the same approach as the integration tool and distributes hydrodynamic input sets like internal layers of a cube. Therefore, the interim position hydrodynamic forces are calculated in one step which eliminates the need for loop structures and reduces the computational cost around 40% compared to the looped structure approach.
- Development of a code in order to scan and read global and sectional damping coefficients from the PRECAL database and write it to excel code to visualize the properties of the damping curves. In order to generate accurate memory functions damping coefficients must be smooth in all ship positions. Developed excel code gives the user the opportunity to eliminate the un-wanted irregular frequencies in the computational database before the generation of quasi-non-linear memory functions. It was observed that irregular frequencies in the damping coefficients cause fluctuations in the memory functions and therefore generate inaccurate radiation forces during the LARes L2 and L3 models.
- Development of the LARes L2 and L3 internal load solver in order to estimate the Vertical Shear Force (VSF) and Vertical Bending Moment (VBM) responses for various cut sections. In order to use the LARes L3 model, all sectional hydrodynamic forces are stored in various ship positions, and multi-dimensional integration and interpolation processes are used for the sectional hydrodynamic properties.
- Development of a 3-D linear time-domain code in order to process frequency domain data and to validate responses compared to the PRETTI model linear calculations. In order to generate radiation forces, memory functions were

evaluated accurately using damping curves corresponding to the underwater part of the ship, taking into account any forward speed effects. The memory functions are validated with the PRETTI model memory functions and they were found to be identical to each other. The accuracy of the memory forces are crucial in the evaluation of quasi-non-linear radiation forces which was used in the body-nonlinear level non-linear time domain code.

- Development of the F-K non-linear time-domain code corresponding to Level 2 (L2) (ISSC, 2012), in order to assess non-linear motion response characteristics. A fast and efficient meshing tool was developed which vectorises the domain of discretized ship geometry, and performs wet/dry panel calculations at each time step on all of the panels on the geometry instead of using loops to calculate each panel’s properties one by one at the same time instant. Due to the vectorisation process, simulations were solved faster with the same accuracy level and it was proven that vectorized approach provided 90% faster results than the looped approach during the evaluation of instantaneous F-K and restoring forces. In the LARes L2 model, motion results were validated by using the S175 hull and experimental data from Fonseca and Soares (2004) in the forward speed case. The predicted results were found to be in good agreement with the experiments. The lack of the surge motions in the level 2 code provided closer results to the experiments compared to the PRETTI model results.
- Development of a non-linear time domain code corresponding to Level 3 (L3) (ISSC, 2012) body nonlinearity level, in order to assess the non-linear effects of radiation and diffraction forces in large amplitude motion simulations. In this body-nonlinear computation level, a database of pre-calculated damping curves, diffraction forces, and infinite added mass and damping coefficients was generated in PRECAL with respect to a pre-calculated range of instantaneous wetted portions of the ship under the still water level. The results of LARes level 3 body nonlinearity calculations were compared with the ITTC (2010) and Fonseca and Soares (2004) experimental results with respect to the increasing wave steepness in various forward speed cases. It was observed that the level 3 formulation predicted motion results agreed

better with the experimental data compared to the level 2 formulations in large amplitude waves due to the quasi-non-linear radiation and diffraction forces. Above a wave steepness of $k\zeta_a$=0.1, the level 2 formulation failed to calculate the motion responses accurately due to the steep waves and this has resulted in large predicted heave responses and divergence from the experimental results.

8.5 Conclusions

The main conclusions of this work in the field of large amplitude wave induced ship motions and loads are summarised in the following.

- For the developed LARes L2 and L3 models, the heave and pitch motion responses were investigated with respect to three different forward speed cases (Fn=0.20, 0.25, 0.275) and also for three different wave length to ship length ratios (λ/L_{pp}=1.0, 1,2, 1.4) around the resonant frequency. The predicted results were compared with the experimental results (ITTC, 2010) and also with the PRETTI results. It was observed that the motion responses were amplified around the λ/L_{pp}=1.2 ratio and nonlinear behavior in the results decreased with the increasing ship speed. The main reason for the decrease was attributed to the Approximate Forward Speed (AFS) Green function method. In order to investigate the forward speed effects properly, one needs to implement Exact Forward Speed (EFS) approach in the linear and non-linear seakeeping calculations.
- In the LARes L3 model, the effect of the large amplitude waves on the non-linear radiation and diffraction forces was investigated and compared with the LARes L2 model. It was discussed in previous chapters that in the level 2 formulations, the diffraction forces are completely linear and are fed from complex diffraction RAO's generated using PRECAL software. The influence of the wave amplitude on the non-linear diffraction force amplitudes was investigated with respect to their positive and negative peak

values and compared with the linear diffraction force amplitudes. In the level 2 model, the positive and negative peaks of the diffraction forces were observed to be identical, but in the level 3 model the diffraction force amplitudes showed highly nonlinear behavior with the increasing wave amplitude. In the level 2 radiation force amplitudes a slight difference between the positive and negative peak points was observed due to the convolution of the memory functions with the exact heave and pitch velocity history. The difference was observed to be higher in the pitch radiation force amplitudes than the heave radiation force amplitudes in the level 2 model. In the level 3 model, the heave and pitch radiation force amplitudes showed highly nonlinear behavior in positive and negative peak amplitudes. Likewise, the pitch radiation moment amplitudes showed stronger non-linear behavior than the heave radiation force amplitudes. The strong nonlinearity in the pitch motions is attributed to the magnitude of the pitch motion force components which are much higher than the heave motion force components. It must be mentioned again that the difference in the radiation and diffraction force amplitude peaks can only be observed using the level 3 formulation due to the quasi-non-linear evaluation of the forces in different ship displacements.

- It has been observed that in large amplitude waves, around the resonant frequency, the LARes L3 model reduces the heave and pitch responses up to 15% and VSF and VBM responses up to 10% compared to the LARes L2 model and also provides closer results to the experimental data. In the internal load simulations, at station 15 (1/4 L_{pp} backwards from FP), nonlinearities in the VSF and VBM responses are more pronounced than the station 10 (amidships). On the contrary, VBM responses are found to be at the maximum level at the station 10. The reductions on the motion and load estimations are stronger around the $\lambda/L_{pp}=1.2$ whilst the largest difference in the radiation and diffraction forces between the LARes L3 and L2 is obtained in the $\lambda/L_{pp}=1.0$ case due to the dominancy of them over other force components. Moreover, the LARes L3 model did not show divergence in the motion responses like the PRETTI model results in very large wave amplitudes which also proves the stability of the code in heavy environmental conditions.

- It has been observed that multi-dimensional integration and interpolation tools reduce the computational cost around 40% compared to the looped structure approach. Interpolation of the hydrodynamic forces and coefficients is more time consuming than the integration of the damping coefficient because during the simulation time at each interim position interpolation needs to be performed whilst integration is performed once in advance to the simulations.

8.6 Recommendations for the future works

The present LARes L3 model can be further improved in several ways:

- In order to improve the accuracy of predictions in large rotational motions, the body-fixed hydrodynamic frame should be taken into account. Especially in bow quartering seas, large roll motions occur and the time domain forces on the exact wetted area of the ship needs to be calculated using the body-fixed hydrodynamic frame. The current model only works in head seas therefore all six degrees of motion solutions should be taken into account in order to perform bow quartering seas analysis.
- In order to be independent from the PRECAL software, an exact forward speed Green function seakeeping code needs be developed in order to predict the forward speed effects to a better accuracy than the AFS formulation. In order to take into account the forward speed influences, steady-unsteady wave interaction problem need to be focused on due to their high importance in BVP solutions, especially in fast forward speed problems. Steady sinkage problems are also important for the ship motion and load estimations in forward speed problems and need to be taken into account in the calculations.
- Viscosity is an important concern in the estimation of the wave induced motions and loads especially in bow quartering seas. In the potential methods, viscosity effects are not taken into account therefore roll motions are over-

estimated in the motion responses. However, the calculation of the viscous forces is very time consuming and completely depend on the experimental investigations and the Computational Fluid Dynamics (CFD) methods. Viscous forces can be calculated using CFD methods and then can be implemented to the potential solvers as an external force. However, it needs to be underlined again that, the solution of this problem can be very costly compared to the practical potential flow solutions.

- Irregular seas analysis is very important for understanding ship behaviour in a real sea environment. Irregular sea analysis should be carried out in order to simulate the real ship motions and loads in a provided sea spectrum.
- In large amplitude waves, ships act as an elastic beam. In the current thesis, ships are assumed to be rigid and elasticity analysis is not implemented into the calculations. Especially for ships with large lengths, the elastic ship approach should be taken into account in order to investigate the influence of the elasticity on the vertical shear forces and bending moments.
- In large amplitude waves, ships are prone to having water on deck and this exerts extra forces on the deck. Although the occurrence of water on deck has a highly nonlinear nature, a simplified approach can be used in the system of equations and the effects of the water on deck can be investigated.
- In the internal load calculations, it is better to use the ship’s mass distribution as a function of ship length, and so for each section the function needs to be cut and integrated for the part forward of the cut section. In PRECAL, the ship’s mass distribution is given in mass points and if a mass point is very close to the cut section, PRECAL translates it slightly backwards and this result in a loss in the inertial forces at the forward part of the section.
- In the internal load calculations, PRECAL checks each panel’s centre point to establish whether it is positioned forward of the cut section or not. In long panels this creates a problem because if the panel’s centre point is positioned forward of the cut, it is completely taken into account. Long panels should be cut by the sections in advance of the hydrodynamic solutions and this will provide more accurate VSF estimations, especially at the midship section.

References

Ando, S., (1999). *Time-domain simulation of nonlinear ship motions and wave loads,* 5th Canadian Marine Hydromechanics and Structures Conference, Newfoundland, Canada.

Ba, M., Guilbaud, M. (1995). A Fast Method of Evaluation for the Translating and Pulsating Green's Function *Ship Technology Research*, **42** (2), 68-80.

Bessho, M. (1977). On the fundamental singularity in the theory of ship motions in a seaway. *Memoirs of the defense academy Japan*, **17** (8), 95-105.

Boin, J.-P., Guilbaud, M., Ba, M. (2003). On the Integration of the Diffraction-Radiation with Forward Speed Green Function. *Ship Technology Research*, **50**, 106-124.

Bruzzone, D., Gironi, C., Grasso, A., (2011). Nonlinear effects on motions and loads using an iterative time-frequency solver, International Journal of Naval Architecture and Ocean Engineering, p. 20.

Bruzzone, D., Grasso, A., (2007). *Time domain evaluation of vertical motions of high-speed displacement hulls,* 2nd Intl Conference on Marine Research and Transportation, Naples,Italy, pp. 253-258.

Buchner, (1995). *The impact of green water on FPSO design*, 27th Offshore Technology Conference, Houston, Texas, pp. 45-57.

Bunnik, T., (1999). *Seakeeping calculations for the ships, taking into account the non-linear steady waves*. Technical University of Delft.

Bunnik, T., van Daalen, E., Kapsenberg, G., Shin, Y., Huijsmans, R., Deng, G., Delhommeau, G., Kashiwagi, M., Beck, B., (2010). *A comparative study on state-of-the-art prediction tools for seakeeping*, Proceedings of the 28th Symposium on Naval Hydrodynamics, , Pasadena, CA.

Chakrabarti, S.K., (1987). Hydrodynamics of Offshore Structures. Computational Mechanics.

Chang, M., (1977). *Computations of three-dimensional ship motions with forward speed*, 2nd Conference on Numerical Ship Hydrodynamics, pp. 124-135.

Chapchap, A., Ahmed, F., Hudson, D., Temarel, P., Hirdaris, S. (2011). The influence of forward speed and nonlinearities on the dynamic behaviour of a container ship in regular waves. *Trans. RINA*, **153** (2), 137-148.

Chen, X., Malenica, Š. (1998). Interaction effects of local steady flow on wave diffraction-radiation at low forward speed. *International Journal of Offshore and Polar Engineering*, **8** (2), 102-109.

Cong, L., Huang, Z., Ando, S., Hsiung, C., (1998). *Time-domain analysis of ship motions and hydrodynamic pressures on a ship hull in waves*, 2nd International Conference on Hydroelasticity in Marine Technology, pp. 485-495.

Cummins, W.E. (1962). The impulse response function and ship motions. *Ship Technology Research*, **9**, 101-109.

Delhommeau, G., Alessandrini, B. (1991). Comparaison de differentes approximations du probleme de diffraction radiation avec vitesse d'avance. *Journees de L'Hydrodynamique*, 3-16.

Fang, C.C., Chan, H.S., Incecik, A. (1997). Investigations of motions of catamarans in regular waves-II. *Ocean Engineering*, **24** (10), 949-966.

Fang, M.C. (2000). The effect of the steady flow potential on the motions of a moving ship in waves. *Journal of ship research*, **44** (1), 14-32.

Fonseca, N., Soares, C.G. (1998). Time-domain analysis of large-amplitude vertical ship motions and wave Loads. *Journal of Ship Research*, **42** (2), 139-153.

Fonseca, N., Soares, C.G. (2002). Comparison of numerical and experimental results of nonlinear wave-induced vertical ship motions and loads. *Journal of Marine Science and Technology*, **6** (4), 193-204.

Fonseca, N., Soares, C.G. (2004). Experimental investigation of the nonlinear effects on the vertical motions and loads of a containership in regular waves. *Journal of Ship Research*, **48** (2), 118-147.

Fonseca, N., Soares, C.G. (2005). Comparison between experimental and numerical results of the nonlinear vertical ship motions and loads on a containership in regular waves. *International shipbuilding progress*, **52** (1), 57-89.

Fossen, T.I., (1994). Guidance and Control of Ocean Vehicles. John Wiley & Sons, Trondheim.

Froude, W. (1861). On the Rolling of Ships. *Trans. RINA*, **2**, 180-229.

Guevel, P., Bougis, J. (1982). Ship motions with forward speed in infinite depth. *International shipbuilding progress,* **29** (332), 103-117.

Haskind, M. (1946). The Hydrodynamic Theory of Ship Oscillations in Rolling and Pitching. *Prikl. Mat. Mekh.*, **2**, 180-229.

Hess, J.L., Smith, A.M.O., (1962). *Calculation of non-lifting potential flow about arbitrarty three-dimensional bodies*.

Hirdaris, S., Bai, W., Dessi, D., Ergin, A., Gu, X., Hermundstad, O., Huijsmans, R., Iijima, K., Nielsen, U., Parunov, J. (2014). Loads for use in the design of ships and offshore structures. *Ocean engineering*, **78**, 131-174.

Huang, Y., Sclavounos, P.D. (1998). Nonlinear Ship Motions. *Journal of Ship Research*, **42** (2), 120-130.

Huang, Z.J., Hsiung, C.C., (1994). *Application of the flux difference splitting method to compute nonlinear shallow water flow on deck,* IWWWFB.

Huang, Z.J., Hsiung, C.C., (1997). *Nonlinear shallow water flow on deck coupled with ship motion*, 21th Symp. on Naval Hydrodynamics. The National Academies Press, Trondheim,Norway.

Inglis, R., Price, W. (1981a). The influence of speed dependent boundary condition in three-dimensional ship motion problems. *Int. Shipbuilding Progress*, **28** (318), 22-29.

Inglis, R., Price, W. (1981e). A three-dimensional ship motion theory: comparison between theoretical predictions and experimental data of the hydrodynamic coefficients with forward speed. *Trans. RINA*, **124**, 141-157.

ISSC, (2009). *17th ISSC Committee 1.2 Load-Technical report*, Seoul, Korea.

ISSC, (2012). *18th ISSC Committee 1.2 Loads-Technical Report*, Hamburg, Germany.

ITTC, (2010). *ITTC Workshop on Seakeeping, in: (ed.), i.Y.K. (Ed.),* ITTC Towing Tank Conference, Seoul, Korea.

ITTC, (2011). *The Seakeeping Committee, Techical Report*, Rio de Janeiro, Brazil.

Iwashita, H., Ito, A. (1998). Seakeeping computations of a blunt ship capturing the influence of the steady flow. *Ship Technology Research*, **45**, 159-171.

Iwashita, H., Ohkusu, M. (1992). The Green function method for ship motions at forward speed. *Ship Technology Research*, **39**, 3-21.

Kim, B., Shin, Y.-S. (2007). Steady flow approximations in three-dimensional ship motion calculation. *Journal of Ship Research*, **51** (3), 229-249.

Kim, Y., Kim, K.-H., Kim, J.-H., Kim, T., Seo, M.-G., Kim, Y. (2011). Time-domain analysis of nonlinear motion responses and structural loads on ships and offshore structures: development of WISH programs. *International Journal of Naval Architecture and Ocean Engineering*, **3** (1), 37.

Ko, K.H., Park, T., Kim, K.H., Kim, Y., Yoon, D. (2011). Development of panel generation system for seakeeping analysis. *Computer-Aided Design*, **43** (8), 848-862.

Korvin-Kroukovsky, B.V. (1955). Investigation of Ship motions in Regular Waves. *Transactions SNAME*, **63**, 386-435.

Kotik, J., Mangulis, V. (1962). On the Kramers-Kronig Relations for Ship Motions. *International Shipbuilding Progress*, **9** (97).

Kring, D., Huang, Y.-F., Sclavounos, P.D., Vada, T., Braathan, A., (1997). *Nonlinear Ship Motions and Wave Induced Loads by a Rankine Method*, 21th Symp. on Naval Hydrodynamics. National Academy Press, Trondheim,Norway, pp. 45-63.

Krylov, A. (1896). A New Theory of the Pitching Motion of Ships on Waves, and on the Stresses Produced by this Motion. *Trans. RINA*, **37**, 326-368.

Kukkanen, T., Matusiak, J. (2014). Nonlinear hull girder loads of a RoPax ship. *Ocean Engineering*, **75**, 1-14.

Lee, C.H., Sclavounos, P.D. (1989). Removing the irregular frequencies from integral equations in wave-body interactions. *J. Fluid Mechanics*, **207**, 393-418.

Liapis, S.J., (1986). *Time-domain analysis of ship motions*, Department of Naval Architecture and Marine Engineering. University of Michigan.

Lin W.M., Yue, D.K.P., (1991). *Numerical Solutions for Large Amplitude Ship Motion in Time Domain*, 18th Symp. on Naval Hydrodynamics. National Academy Press, Washington D.C.,USA, pp. 41-66.

Lin, W.M., Meinhold, M., Salvasen, N., Yue, D.K.P., (1994). *Large Amplitude ship motions and wave loads for ship design*, 20th Symp. on Naval Hydrodynamics. National Academy Press, Santa Barbara, USA, pp. 205-226.

Lin, W.M., Yue, D.K.P., (1991). *Numerical solutions for large amplitude ship motions in the time domain*, 19th Symp. on Naval Hydrodynamics, pp. 41-66.

Lin, W.M., Zhang, S., Weems K.M., Yue, D.K.P., (1999). *A mixed source formulation for nonlinear ship motion and wave load simulations*, 7th Conference on Numerical Ship Hydrodynamics, Nantes,France.

Liu, S., Papanikolaou, A. (2012). On Nonlinear Simulation Methods and Tools for Evaluating the Performance of Ships and Offshore Structures in Waves. *Journal of Applied Mathematics*, **2012**, 21.

McTaggart, K.A., (1996). *SHIPMO7: An updated strip theory program for predicting ship motions and sea loads in waves*, DREA Technical Memorandum TM 96/243.

Molland, A.F., Wellicome, J.F., Temarel, P., Cic, J., Taunton, D.J. (2001). Experimental investigation of the seakeeping characteristics of fast displacement catamarans in head and oblique seas. *Trans. of the RINA*, 78-97.

Nakos, D., Sclavounos, P.D., (1991). *Ship motions by a three-dimensional Rankine panel method*, 18th Symp. on Naval Hydrodynamics, pp. 21-40.

Newman, J.N. (1979). The theory of ship motions. *Advances in applied mechanics*, **18**, 221-283.

Noblesse, F., Chen, X. (1995). Decomposition of free-surface effects into wave and near-field components. *Ship Technology Research*, **42**, 167-185.

O'Dea, J., Powers, E., Zselecsky, J., (1992). *Experimental determination of non-linearities in vertical plane ship motions*, 19th Symp. on Naval Hydrodynamics, Seoul,Korea, pp. 73-91.

Ogilvie, T., (1964). *Recent Progress Toward the Understanding and Prediction of Ship Motions*, 5th Symp. on Naval Hydrodynamics. National Academy Press, Bergen, Norway.

Ogilvie, T.A., Tuck, E.O., (1969). *A Rational Strip Theory of Ship Motions: Part I*. University of Michigan.

Papanikolaou, A.D., Schellin, T.E. (1992). A Three-Dimensional Panel Method for Motions and Loads of Ships with Forward Speed. *Ship Technology Research*, **39**, 147-156.

Pawlowski, J.S., Bass, D.W. (1991). A theoretical and numerical model of ship motions in heavy seas. *SNAME Transactions,* **99**, 319-352.

Rajendran, S., Fonseca, N., Soares, C.G., Clauss, G.F., Klein, M., (2011). *Time domain comparison with experiments for ship motions and structural loads on a container ship in abnormal waves,* 30th International Conference on Ocean, Offshore and Arctic Engineering,OMAE 2011, pp. 919-927.

Rienecker, M.M., Fenton, J.D. (1981). A Fourier approximation method for steady water waves. *Journal of Fluid Mechanics*, **104**, 119-137.

Saad, Y., Schultz, M. (1986). GMRES: A Generalized Minimal Residual Algorithm for Solving Nonsymmetric Linear Systems. *SIAM Journal on Scientific and Statistical Computing*, **7** (3), 856-869.

Salvasen, N., Tuck, E.O., Faltinsen, O.M. (1970). Ship Motions and Sea Loads *SNAME*, **104**, 119-137.

Sen, D. (2002). Time-domain computation of large amplitude 3D ship motions with forward speed. *Ocean Engineering*, **29** (8), 973-1002.

Shin, Y.S., Belenky, V.L., Lin, W.M., Weems, K.M., Engle, A.H. (2003). Nonliner time domain Simulation Technology for seakeeping and Wave-Load Analysis for Modern Ship Design. *Trans. SNAME*, **111**, 257-281.

Singh, S.P., Sen, D. (2007a). A comparative linear and nonlinear ship motion study using 3-D time domain methods. *Ocean Engineering*, **34** (13), 1863-1881.

Singh, S.P., Sen, D. (2007e). A comparative study on 3D wave load and pressure computations for different level of modelling of nonlinearities. *Marine Structures*, **20**, 1-24.

Song, M.-J., Kim, K.H., Kim, Y. (2011). Numerical analysis and validation of weakly nonlinear ship motions and structural loads on a modern containership. *Ocean Engineering*, **38** (1), 77-87.

St Denis, M., Pierson, W. (1953). On the Motion of Ships in Confused Seas. *Trans SNAME*, **61**, 280-354.

Thwaites, B., (1960). Incompressible Aerodynamics. Oxford University Press.

Van't Veer, A.P., (2009). *PRECAL v6.5 Theory Manual*.

Van't Veer, A.P., Van Daalen, E., Willemstein, I.T., (2009). *PRETTI v1.5 Theory Manual*.

Watanabe, I., Uneo, M., Sawada, H. (1989). Effects of bow flare shape on wave loads of a containership. *Journal of the Society of Naval Architects of Japan,* **166**, 259-266.

Weems, K., Lin, W.M., Zhang, S., Treakle, T., (2000). *Time Domain Prediction for Motions and Loads of Ships and Marine Structures in Large Seas Using a Mixed- Singularity Formulation*, 4th Osaka Colloquium on Seakeeping Performance of Ships, Osaka, Japan, pp. 272-280.

Wehausen, J.V., Laitone, C.V., (1960). Surface Waves. Springer Verlag, Berlin.

Wu, G. (1991). A numerical scheme for calculating the m_j-terms in wave-current-body interaction problem. *Applied ocean research*, **13** (6), 317-319.

Wu, G., Taylor, R.E. (1988). Radiation and diffraction of water waves by a submerged sphere at forward speed. *Proceedings of the Royal Society of London. A. Mathematical and Physical Sciences,* **417** (1853), 433-461.

Wu, G., Taylor, R.E., (1989). *The numerical solution of the motions of a ship advancing in waves,* 5th Conference on Numerical Ship Hydrodynamics, Hiroshima, Japan, pp. 529-538.

Wu, G., Taylor, R.E. (1990). The hydrodynamic force on an oscillating ship with low forward speed. *Journal of Fluid Mechanics,* **211**, 333-353.

Zhang, X., Bandyk, P., Beck, R.F. (2010). Seakeeping computations using double-body basis flows. *Applied Ocean Research,* **32** (4), 471-482.

Zhao, R., Faltinsen, O.M., (1990). *Interaction between current, waves and marine structures*, 5th Conference on Numerical Ship Hydrodynamics. The National Academies Press, pp. 513-527.

Zhu, D.X., Katory, M. (1998). A time-domain prediction method of ship motions. *Ocean Engineering*, **25** (9), 781-791.